Developmental transformation of nanodomain coupling between Ca^{2+} channels and release sensors at a central GABAergic synapse

by

Jing-Jing Chen

March, 2024

A thesis submitted to the
Graduate School
of the
Institute of Science and Technology Austria
in partial fulfillment of the requirements
for the degree of
Doctor of Philosophy

Committee in charge:
Professor Mario de Bono, Chair
Professor Peter Jonas (Supervisor)
Professor Ryuichi Shigemoto (Internal)
Professor Hartmut Schmidt (External)

The thesis of Jing-Jing Chen, titled "*Developmental transformation of nanodomain coupling between Ca^{2+} channels and release sensors at a central GABAergic synapse*", is approved by:

Supervisor: Peter Jonas, ISTA, Klosterneuburg, Austria

Signature: _____

Committee Member: Ryuichi Shigemoto, ISTA, Klosterneuburg, Austria

Signature: _____

Committee Member: Hartmut Schmidt, Carl-Ludwig-Institute for Physiology, University of Leipzig, Leipzig, Germany

Signature: _____

Defense Chair: Mario de Bono, ISTA, Klosterneuburg, Austria

Signature: _____

Signed page is on file

ISTA Thesis, ISSN: 2263-337X

I hereby declare that this thesis is my own work and that it does not contain other people's work without this being so stated; this thesis does not contain my previous work without this being stated, and the bibliography contains all the literature that I used in writing the dissertation.

I declare that this is a true copy of my thesis, including any final revisions, as approved by my thesis committee, and that this thesis has not been submitted for a higher degree to any other university or institution.

I certify that any republication of materials presented in this thesis has been approved by the relevant publishers and co-authors.

Signature: _____

Jing-Jing Chen

March, 2024

Signed page is on file

Abstract

The coupling between presynaptic Ca^{2+} channels and release sensors is a key factor that determines speed and efficacy of synapse transmission. At some excitatory synapses, channel–sensor coupling becomes tighter during development, and tightening is often associated with a switch in the reliance on different Ca^{2+} channel subtypes. However, the coupling topography at many synapses remains unknown, and it is unclear how it changes during development. To address this question, we analyzed the coupling configuration at the cerebellar basket cell (BC) to Purkinje cell (PC) synapse at different developmental stages, combining biophysical analysis, structural analysis, and modeling.

Quantal analysis of BC–PC indicated that release probability decreased, while the number of functional sites increased during development. Although transmitter release persistently relied on P/Q-type Ca^{2+} channels in the time period postnatal day 7–23, effects of the Ca^{2+} chelator EGTA and BAPTA applied by intracellular pipette perfusion decreased during development, indicative of tightening of source-sensor coupling. Furthermore, presynaptic action potentials became shorter during development, suggesting reduced efficacy of Ca^{2+} channel activation.

Structural analysis by freeze-fracture replica labeling (FRL) and transmission electron microscopy (EM) indicated that presynaptic P/Q-type Ca^{2+} channels formed nanoclusters throughout development, whereas docked vesicles were only clustered at later developmental stages. The number of functional release sites correlated better with the AZ number early in development, but match better with the Ca^{2+} channel cluster number at later stages.

Modeling suggested a developmental transformation from a more random to a more clustered coupling nanotopography. Thus, presynaptic signaling developmentally approaches a point-to-point configuration, optimizing speed, reliability, and energy efficiency of synaptic transmission.

Acknowledgements

First of all, I would like to thank my supervisor Prof. Peter Jonas for giving me the opportunity to work in his group. Being one of the leading groups that study the mechanism of synaptic transmission, it gave me a thorough background in the current state of the field and the necessary skills to perform research of significance. During the past 6 years, I have been impressed a lot by Prof. Jonas, not only the wide range of knowledge, but also the characteristics that an outstanding scientist has.

Secondly, I would also like to thank Prof. Ryuichi Shigemoto and Prof. Hartmut Schmidt for being my thesis committee members and Prof. Mario de Bono for being the Chair.

During my project, I closely worked with Dr. Walter Kaufmann and Electron Microscope Facility. I therefore appreciated their input very much and have learned a lot from them.

I also want to thank Dr. Alois Schlögl for his excellent programming help. To Dr. Chong Chen, who taught me paired recording at the very beginning. To Dr. Olena Kim, for her help with flash and freeze and freeze substitution experiments. To Drs. Yuji Okamoto and Xiaomin Zhang, for scientific discussion and inspiration. To Drs. Benjamin Sutter and Katharina Lichter for the help of image analysis. To Florian Marr, Christina Altmutter, preclinical facility and machine shop for their generous technical support. To the other Jonas lab members for being such a dynamic team.

Lastly, I would like to thank my family members, who supported me to pursue my research. To my parents, my brother for their understanding and love and to my husband Peng for his unconditional support.

The project received funding from the European Research Council (ERC) under the European Union's Horizon 2020 research and innovation programme (grant agreement No 692692), the Fond zur Förderung der Wissenschaftlichen Forschung (Z 312-B27, Wittgenstein award; P 36232-B), all to P.J., and a DOC fellowship of the Austrian Academy of Sciences to J.-J.C.

About the author

Jing-Jing Chen started her academic journey in the Institute of Brain Science, Fudan University, where she obtained an MSs in neurobiology, after a BSc in biotechnology in China. During her master thesis study, she worked on the role of gap junction Cx26 and Cx43 in the developing neocortex, and published the results on the journal of PNAS (2017, co-first author with equal contribution) and Brain Research (2019, second author). In 2017, she joined ISTA and a year later the group of Prof. Peter Jonas. Since then, she worked on the project of "Developmental transformation of nanodomain coupling between Ca^{2+} channels and release sensors at a central GABAergic synapse", and her research proposal was awarded with a DOC fellowship from the Austrian Academy of Sciences (OeAW). During her PhD thesis, she presented her research in the Austrian neuroscience meeting (ANA) in 2021 and the Federation of European neuroscience society (FENS) in 2022. Besides, she also worked as two teaching assistants in 2019. Subsequently, she published on the journal Neuron in 2024.

List of Collaborators, publications and presentations

Collaborators

Prof. Peter Jonas, performed modeling in Chapter 5.

Prof. Ryuichi Shigemoto, supervised EM experiments and gave advice on analysis.

Dr. Walter Kaufmann, performed all freeze-fracture replica immunolabeling experiments, part of the serial section EM experiments, and gave advice on analysis.

Dr. Chong Chen, provided 7 pairs in Figure 3-4.

Dr. Itaru Aria, provided 13 pairs in Figure 3-3.

Original publication

Chen, J.-J., Kaufmann, W.A., Chen, C., Arai, I., Kim, O., Shigemoto R., and Jonas, P. Developmental transformation of Ca^{2+} channel-vesicle nanotopography at a central GABAergic synapse. **Neuron** (in press).

Posters and presentations

Chen, J.-J., Kaufmann, W.A., Shigemoto, R., and Jonas, P. Developmental reconfiguration of nanodomain coupling between Ca^{2+} channels and release sensors at a GABAergic central synapse. FENS Forum 2022, Pairs, France. (Poster)

Chen, J.-J., Kaufmann, W.A., Shigemoto, R., and Jonas, P. Developmental regulation of coupling between presynaptic Ca^{2+} channels and release sensors at basket cell–Purkinje cell synapses in cerebellum. 17th ANA meeting 2021, Salzburg, Austria. (Poster)

Table of Contents

List of Figures

List of tables

List of abbreviations

AP	Action potential
AZ	Active zone
BAPTA	Ethylenedioxybis-(ophenylenenitrilo)-N,N,N',N'-tetraacetic acid
BC	Basket cell
CaMKII	Ca^{2+}/calmodulin-dependent protein kinase II
cAMP	Cyclic adenosine monophosphate
Cav	Calcium channel (voltage-dependent)
CC	Candelabrum cell
CF	Climbing fiber
CS	Complex spike
DBSCAN	Density-based spatial clustering of application with noise
DCN	Deep cerebellar nuclear
EGTA	Ethylene glycol-bis(β-aminoethyl ether)-N,N,N’,N’-tetraacetic acid
ELKS	Protein rich in the amino acids E, L, K, and S
EM	Electron microscope
FRL	Freeze fracture replica immunolabeling
GABA	γ-aminobutyric acid
GAD67	Glutamate acid decarboxylase 67
GC	Granule cell
GCL	Granule cell layer
GoC	Golgi cell
HCN1	Hyperpolarization-activated cyclic nucleotide-gated potassium channel 1
IO	Inferior olive
IPSC	Inhibitory postsynaptic current
K_V1.1	Voltage-gated potassium channel 1.1
KO	Knock out
LM	Light microscope

ML	Molecular layer
MLI	Molecular layer interneuron
NGS	Normal goat serum
NND	Nearest neighbour distance
PC	Purkinje cell
PCL	Purkinje cell layer
PF	Parallel fiber
PSD95	Postsynaptic density protein 95
RIM	Rab3-interacting molecule
RIM-BP	RIM-binding protein
RRP	the Readily releasable pool
RT	Room temperature
SC	Stellate cell
SEM	Standard error of mean
SNARE	Soluble N-ethylmaleimide-factor attachment receptor
SS	Simple spike
UBC	Unipolar brush cell
VGCC	Voltage-gated calcium channel
WT	Wild type

Chapter 1. Introduction

1.1 The cerebellum and molecular layer interneurons

The cerebellum is localized at the posterior of the brain (above the brainstem), and is involved in motor, cognitive and affective behaviors (Schmahmann, 2019). From the anterior-posterior axis, the cerebellum is divided into three major lobes, anterior lobe (lobe I–lobe V), posterior lobe (lobe VI–IX), and flocculonodular lobe (lobe X), which are split by primary and posterolateral fissures (Figure 1-1A and B; Palay and Chan-Palay, 1974). Since the cerebellum receives multiple inputs and has distinct roles, it is also conventionally divided into three functional subregions: the vestibulorcerebellum, the spinocerebellum, and the cerebrocerebellum. Each of the subregions is involved in different brain functions.

1.1.1 Cerebellar function

The vestibulorcerebellum is the evolutionarily oldest and primitive region of the cerebellum (Kandel et al., 2013). It includes flocculonodular lobe, which receives visual and vestibular inputs, and is responsible for the vestibular reflex, eye movement, and keeping a balance. In behavioral neuroscience, the classical behavioral paradigm, vestibulo-ocular reflex (VOR) adaption has been widely used to study its function (Beekhof et al., 2021).

The spinocerebellum comprises vermis and intermediate parts of the hemisphere (Figure 1-1A) and receives input from the spinal cord and parts of cerebral cortex (Coffman et al., 2011; Kandel et al., 2013). The vermis controls posture and locomotion as well as eye movement. The intermediate parts of the hemisphere receive somatosensory inputs from the limbs (Kandel et al., 2013).

The cerebrocerebellum is composed of the lateral portions of the hemisphere, and receives multiple inputs from the cerebral cortex. These regions are more pronounced in humans and apes compared to monkeys and cats, representing a recent phylogenetic development (Kandel et al., 2013). It plays a pivotal role in various functions, with a primary focus on planning and motor execution.

1.1.2 Cerebellar cell types and circuitry

Although different subregions of the cerebellum receive inputs from various parts of brain and spinal cord and project to different deep cerebellar nuclei (Baumel et al., 2009), the organization of the cerebellum is composed of a series of highly regular, repeating units, each of which contains the same basic microcircuit (Kandel et al., 2013). The similarity of the architecture and physiology in all regions of the cerebellum implies that different cerebellar regions perform similar computational operations upon different inputs (Kandel et al., 2013).

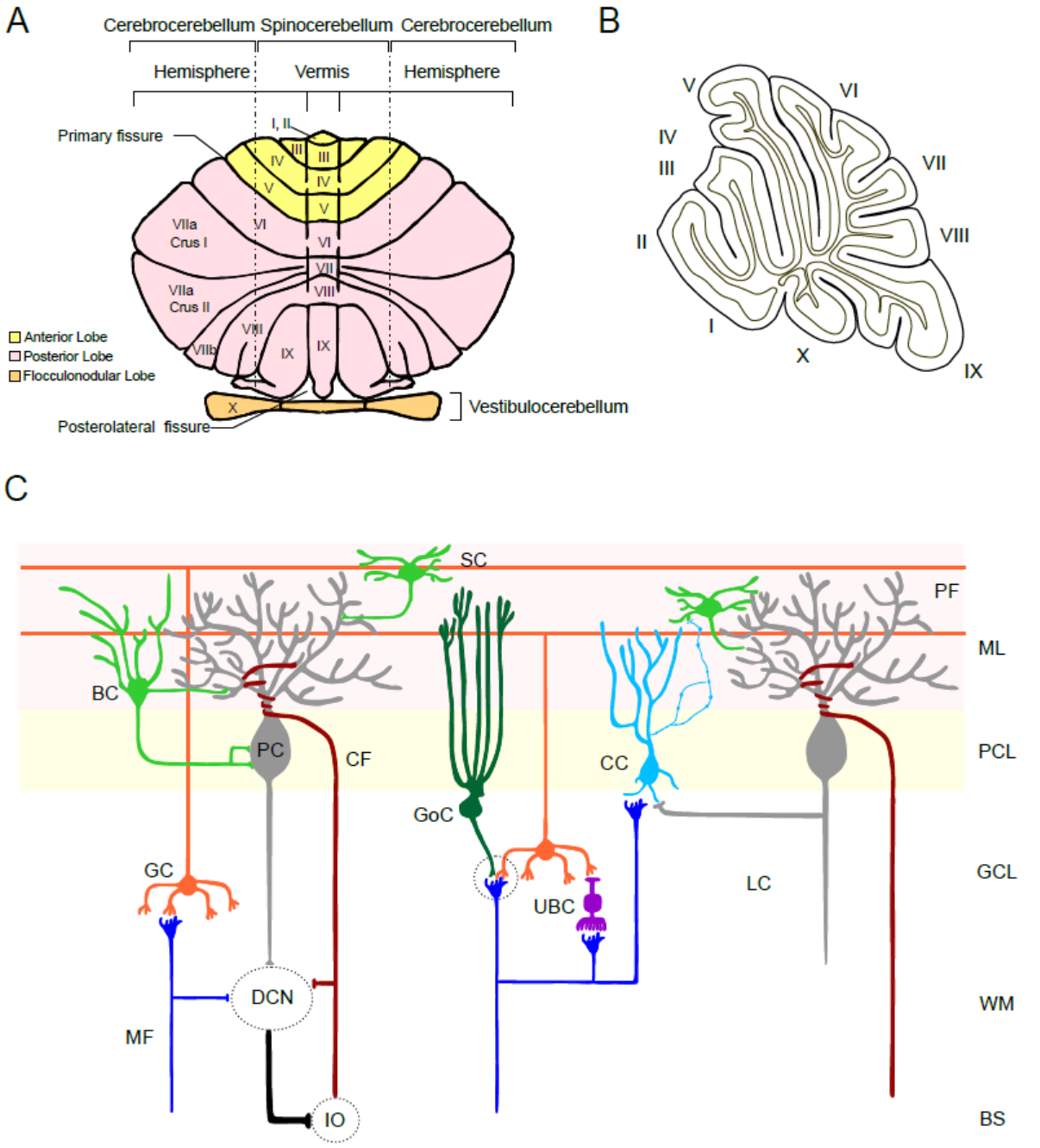

Figure 1-1 Cerebellar anatomy and circuity

(A) Schematic anatomy of the cerebellum from rodents. **(B)** Sagittal view from vermis region of the cerebellum. **(C)** The basic cytoarchitecture of cerebellar cortex. BC, basket cell; PC, Purkinje cell; GC, granule cell; DCN, deep cerebellar nuclear; MF, mossy fiber; IO, inferior olive; CF, climbing fiber; SC, stellate cell; GoC, Golgi cell; UBC, unipolar brush cell; CC, Candelabrum cell; LC, lugaro cell; PF, parallel fiber; ML, molecular layer; PCL, Purkinje cell layer; GCL, granule cell layer; WM, white matter; BS, brain stem. Adapted from Cerminara et al., 2015, and Schmahmann, 2019.

The cerebellar cortex is divided into three distinct layers: the inner or deepest granule cell layer (GCL), the middle Purkinje cell layer (PCL), and the outer molecular layer (ML) (Figure 1-1C; Palay and Chan-Palay, 1974).

The GCL is the input layer, containing a vast number of granule cells (GCs), which are the most numerous neurons in the brain (>50 %; Herculano-Houzel et al., 2006). This layer also contains a few larger Golgi interneurons, Lugaro cells, unipolar brush cells and chandelier cells. The mossy fibers (MFs), one of the two principal afferent inputs to the cerebellum, terminate in this layer. The bulbous terminals of MFs which receive signals from spinal cord and brain stem excite GCs and Golgi neurons in synaptic complexes called cerebellar glomeruli (Palay and Chan-Palay, 1974; Hámori and Somogyi, 1983; Kandel et al., 2013).

The PCL is the sole output layer, and Purkineje cells (PC) project to deep cerebellar and vestibular nuclei. The fan-like dendrites of PCs extend upward to the ML, where they receive inputs from the second major afferent fiber, the climbing fiber (CF) and local interneurons (Kandel et al., 2013). Typically, each PC receives input from a single CF, but this input is extremely strong, consisting of numerous synapses (~300 in frog; Llinas et al., 1969). PCs generate two distinct types of action potentials (APs). Simple spikes (SSs) fire spontaneously and occur at high rates (30–100 Hz; Cerminara et al., 2015). In contrast, complex spikes (CSs), which consist of an initial AP that is usually followed by a series of small spikelets, occur at very low rates (~ 1Hz; Armstrong and Rawson, 1979), and are generated as a result of activity of the inferior olive-CF system (Ito, 1984). In addition, this layer also contains candelabrum cells and Bergmann glia. The candelabrum cells receive excitatory inputs from MFs and GCs, and inhibitory inputs from PCs, and target on ML interneurons. Prolonged candelabrum cells firing disinhibits PCs, and candelabrum cells are thus part of an inhibitory loop between ML interneurons and PCs (Osorno et al., 2022). The Bergmann glias are specialized, unipolar glial cells, whose radial fibers aid the migration of neurons and the elongation of dendrites and axons (Leung and Li, 2018).

The outer ML is an important processing layer. It contains two types of inhibitory interneurons, the extensive dendritic trees of PCs, as well as PFs. PFs are the axons of the GCs, they bifurcate in a T-type manner in ML, and extend several millimeters parallel to the long axis of the folia. The spatially polarized dendrites of PCs cover extensive terrain in the anterior-posterior direction, but a very narrow territory in the medial-lateral direction. The PFs are oriented perpendicular to the dendritic trees of PCs, thus each GC has the potential to form a few synapses with each of a large number of PCs, while making denser connections on a few PC as its axon ascends into the ML (Kandel et al., 2013).

1.1.3 The molecular layer interneurons

The molecular layer interneurons (MLSs) originate from a common precursor pool in the ventricular zone, and they undergo sequential generation throughout embryonic and postnatal stages in an inside-out progression (Leto et al., 2009; Sudarov et al., 2011). Depending on the location, morphology, and type of inhibition, the MLIs are canonically divided into basket cells (BCs) and stellate cells (SCs). The BCs are localized in the inner third

of ML, and form “baskets” of axonal arborization onto the somata of PCs, providing strong perisomatic inhibition. Part of BC axon collaterals wrap around the axon initial segment area of PCs, and form a specialized structure called ‘pinceau’, name for its paintbrush-like structure first described by the modern neuroscience pioneer-Santiago Ramón y Cajal (Cajal, 1911). Several molecules and ion channels have been characterized and accumulated at the pinceau, including membrane-associated adaptor protein ankyrin-G, cell adhesion molecules neurofascin (Buttermore et al., 2012), hyperpolarization-activated cyclic nucleotide-gated potassium channel 1 (HCN1), postsynaptic density protein 95 (PSD95), voltage-gated potassium channels (K_V1.1) and glutamate acid decarboxylase 67 (GAD67, Zhou., et al, 2020). Although pinceau lacks synaptic vesicles or sodium channels (Iwakura et al., 2012), several studies showed that the pinceau inhibits PCs by ephaptic coupling, a mechanism that neurons communicate by extracellular electrical signals, which is a synapse independent way (Bolt and Barbour, 2014; Martin and Kullmann, 2023). The SCs are localized in the upper two thirds of ML, usually have a star-like shape, and form synapses onto PC dendrites. Both BCs and SCs are fast spiking interneurons.

Although MLIs can be divided emphatically, a recent study showed that their genetic expression are heterogenous. Transcriptomic analysis identified two discrete population of MLIs depending on molecular markers. The first population MLI1, expresses *Lypd6*, *Sorcs3*, and *Ptprk*, whereas the second population MLI2 express *Nxph1* and *Cdh22* (Kozareva et al., 2021). On top of that, only MLI1 express *Gjd2*, the gene encoding the main gap junction protein (i.e. connexin36) in interneurons, and the spontaneous firing rate was higher in MLI1 than for MLI2 (Kozareva et al., 2021). Surprisingly, both MLI1 and MLI2 showed a similar continuum in their morphological properties and were distributed throughout the entire ML, which means that the canonical division is not related to the genetic subpopulation.

A recent study selectively depleted GABAergic transmission either in BCs or SCs using genetic inducible fate mapping showed that the MLIs have distinct functions in regulating the spike activity of Purkinje cells *in vivo* (Brown et al., 2019). Inhibiting BCs increase SS firing frequency and decrease CS frequency, whereas inhibition SCs increase the regularity of SC firing and increase the CS firing frequency of Purkinje cell. Since glutamate spillover has been observed from CF onto MLIs both *in vitro* and *in vivo* (Coddington et al., 2013; Arlt and Häusser, 2020; Pennock et al., 2023), one possible explanation is that BCs and SCs provide different inhibition motifs upon PCs which is mediated by CF (Arlt and Häusser, 2020).

1.1.4 $GABA_A$ receptors in ML

γ-aminobutyric acid (GABA) is the dominant inhibitory neurotransmitter in the central nervous system, which is decarboxylated from glutamate by glutamic acid decarboxylase. Upon vesicular release, GABA diffuses across synaptic cleft and activates ionotropic receptors ($GABA_A$ receptors) and/or metabotropic GABA receptors ($GABA_B$ receptors).

$GABA_A$ receptors are hetero-pentameric ligand-gated Cl^- channels (Fritschy and Panzanelli, 2014; Marvin et al., 2019), and are formed from 19 subunits (α1–α6, β1–β3, γ1–γ3, δ, ε, π, Θ, and ρ1–ρ3; Ghit et al., 2021). However, in the cerebellum, the expression of subunit of $GABA_A$ receptor in Purkinje cells is limited, with α1, β2, β3, and γ2 subunits being detected (Laurie et al., 1992; He et al., 2015). In addition, the majority of $GABA_A$ receptors are assembled by two α subunits, two β subunits, and one γ subunit. Therefore, it has been largely assumed that BC or SC derived synaptic $GABA_A$ receptors are composed of α1β2γ2, α1β2β3γ2, or α1β3γ2 in Purkinje cells.

Rebound potentiation or long-term potentiation of GABAergic MLI–PC synapses is one form of neural plasticity described in the cerebellum (Kano et al., 1992; Hansel et al., 2001). PC depolarization (either by repetitive CF stimulation or current injection) can activate postsynaptic voltage-gated calcium channels (VGCCs), and the resulting Ca^{2+} influx therefore activates Ca^{2+}/calmodulin-dependent protein kinase II (CaMKII), and cAMP-dependent protein kinase. Subsequently, activation of these protein kinases increases synaptic $GABA_A$ receptor numbers, resulting in an augmentation of inhibitory postsynaptic current (IPSC) amplitude. A recent study showed that the β2 subunit from BCs participate in this interneuron input-specific plasticity (He et al., 2015). Induced IPSC was significantly reduced and rebound potentiation was absent in $\beta2^{-/-}$ mice compared to wild type (WT) mice. As β2 subunits have several phosphorylation sites (Nakamura et al., 2015), interactions between CaMKII and the β2 subunit would possibly enhance receptor recruitment.

1.2 Synaptic transmission

The human brain comprises of approximately 100 billion neurons (Kandel et al., 2003; Herculano-Houzel, 2009). What is even more remarkable is that the number of synapses, which is approximately 10000 times greater than the number of neurons themselves (Tang et al., 2001). Synaptic transmission is the basic process by which one neuron “talks” to another. Disentangling the rules that govern this basic process is of central importance to understand the brain and its higher function, such as learning, memory formation, cognition, and etc.

Synaptic transmission consists of a series of highly sophisticated events. When an AP arrives in the presynaptic terminal, VGCCs open, leading to an increase in the local Ca^{2+} concentration. These calcium ions, upon binding to Ca^{2+} sensors, trigger exocytosis, causing synaptic vesicles to fuse with the presynaptic membrane. Subsequently, transmitters diffuse across the synaptic cleft and activate postsynaptic receptors, resulting in the alterations in the activity of postsynaptic neuron.

Synaptic vesicle exocytosis is restricted to the small section of the presynaptic plasma membrane which has an electron-dense material, i.e., the presynaptic active zone (AZ; Couteaux and Pécot-Dechavassine, 1970). The morphology and organization of presynaptic

AZs have been characterized by various imaging techniques, which are crucial to understand the function of synapses.

1.2.1 Molecular organization of presynaptic AZ

AZ proteins shape the spatial and temporal properties of neurotransmitter release. There are five evolutionary conserved proteins–Rab3-interacting molecules (RIMs), RIM-binding proteins (RIM-BPs), Munc13s, α-liprin, and protein rich in the amino acids E, L, K, and S (ELKS)–that form the core of AZs (Figure 1-2; Südhof, 2012; Emperador-Melero and Kaeser, 2020). In this section of the introduction, multidomain proteins RIMs, RIM-BPs, and Munc13s will be discussed in detail.

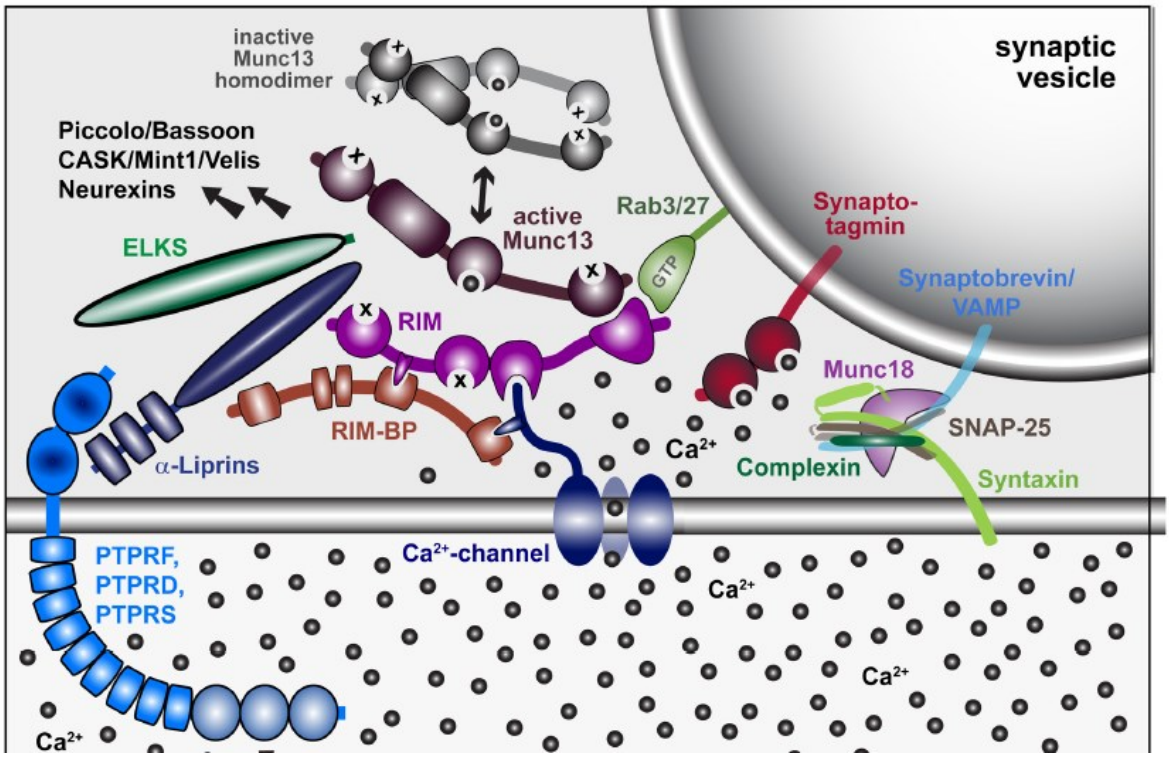

Figure 1-2 Organization of presynaptic active zone.
Schematic of molecular organization of the active zone, adapted from Südhof, 2012.

1.2.1.1 RIMs

Among the five conserved AZ proteins, RIM plays a pivotal role in interacting with other AZ proteins. In vertebrates, RIM has 7 isoforms and is encoded by four genes: *RIM1* (RIM1α and RIM1β), *RIM2* (RIM2α, RIM2β, and RIM2γ), *RIM3* (RIM3γ), and *RIM4* (RIM4γ) (Wang and Südhof, 2003; Kaeser et al., 2008). Only the isoforms RIM1α and RIM2α have full domains, which will be discussed in detail (Figure 1-3). In RIM1α and RIM2α, from the N-terminal to the C-terminal, the domains are α-helically wrapped zinc finger, PDZ domain, C2A domain, proline-rich sequence, and C2B domain. As a central protein for AZ organization, RIM binds

to other AZ proteins. Through the zinc finger domain, RIM binds to Rab3 and the C2A domain from Munc13. In addition, its PDZ domain binds to VGCCs, thus recruiting Ca channels to AZ (Kaeser et al., 2011). The proline-rich sequence interacts with SH-3 domain from RIM-BP. Although the two C2 domains lack of Ca binding sites, the C2B domain binds to α-liprins (Schoch et al., 2002).

The physiological role of RIM has been examined in numerous synapses. In Calyx of Held, RIM1 and RIM2 enrich Ca^{2+} channels at active zones and determine vesicle docking (Han et al., 2011). Removal of RIM1/2 reduces Ca^{2+} channel currents in presynaptic terminals, and slower the kinetics of vesicle release, suggesting an increased coupling distance between Ca^{2+} channel and vesicles in RIM1/2 knockout (KO) synapses. In the hippocampus, the long-term potentiation is abolished in RIM1α KO mossy fiber synapses (Castillo et at., 2002). Subsequent ultrastructure analysis showed that the number of tightly docked synaptic vesicles was reduced, in parallel with the increased AZ size and vesicle pool delocalization in RIM1α KO mossy fiber terminals (Lichter et al., 2022). Therefore, RIMs play a pivotal role in synaptic transmission and plasticity.

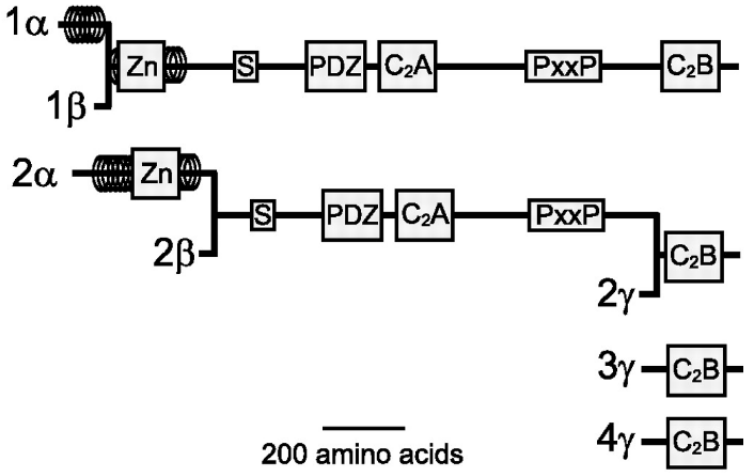

Figure 1-3 RIM isoforms in vertebrates
Schematic of RIM isoforms, adapted from Kaeser et al., 2008. Zn, zinc finger domain; PDZ, PDZ domain; C2A, C2A domain; PxxP: proline-rich sequence; C2B, C2B domain.

1.2.1.2 RIM-BPs

RIM-BPs are large multidomain proteins and are encoded by three genes, two of which (RIM-BP1 and RIM-BP2) are primarily synthesized inside the brain (Mittelstaedt and Schoch, 2007). RIM-BPs have similar domain structures, with their major SH3 domains binding to proline-rich sequences of VGCCs and RIMs (Kaeser et al., 2011). Conditional deletion of RIM-BP1 and RIM-BP2 impedes the coupling probed by exogeneous slow Ca^{2+} chelator experiments, and impairs the timing of synaptic transmission both in cultured hippocampal neurons and the Calyx of held synapses (Acuna et al., 2015). A subsequent study showed that RIM-BP2 is the

dominating RIM-BP isoform in regulation the Ca^{2+} nanodomain by positioning Ca channels close to synaptic vesicles release sites (Grauel et al., 2016). Therefore, RIM-BPs are essential for tight coupling of presynaptic calcium channels to release machinery.

1.2.1.3 Munc13s

Munc13 proteins are the mammalian homologous of the *Caenorhabditis elegans* Unc13 proteins, and play an important role in the regulation of synaptic vesicle priming and fusion (Augustin et al., 1999; Richmond et al., 1999). There are three Munc13 isoforms–Munc13-1, Munc13-2, and Munc13-3–that are involved in vesicle exocytosis (Brose et al., 1995; Shin et al., 2010), whereas two ubiquitous expressed isoforms (BAP-3 and Munc13-4) are expressed outside of the brain which are related to synaptic-independent exocytosis (Figure 1-4).

In Munc13-1, from N-terminal to C-terminal, the domains are C2A domain, C1 domain, C2B domain, MUN domain, and C2C domain. Munc13 plays an important role in the process of priming. The Munc13-1 and ubMunc13-2 are inactivated in homodimer form by C2A domain, which constrains the MUN domain. When the RIM Zinc-finger domain binds to the C2A domain of Munc13, it disrupts the homodimers, leading to an activation of Munc13 (Deng et al., 2011). Subsequently, the free MUN domain from Munc13 together with Munc18 executes the priming function by opening the closed form of the soluble N-ethylmaleimide-factor attachment receptors (SNARE) protein syntaxin-1, thereby facilitating the SNARE complex formation (Richmond et al., 2001; Ma et al., 2011).

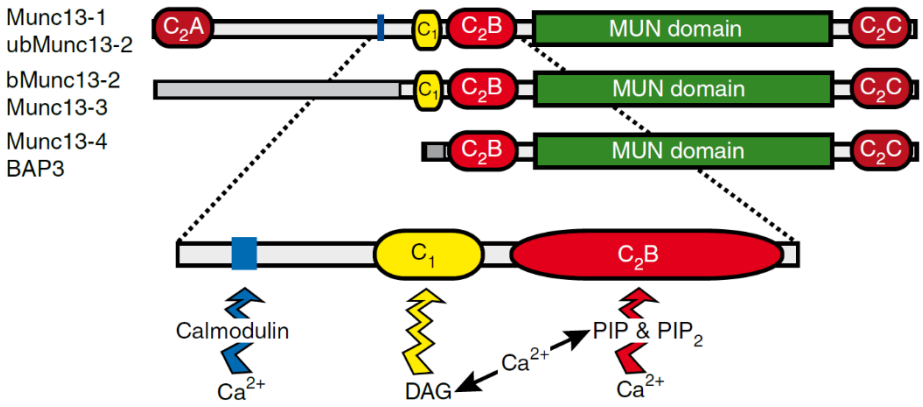

Figure 1-4 Munc13 isoforms and domains
C2 domains, MUN domains, C1 domains, and Ca^{2+}/Calmodulin binding sites are illustrated in red, green, yellow, and blue respectively. Munc13-2 has two isoforms: ubiquitous expressed ubMunc13-2 and brain-specific bMunc13-2. Adapted from Shin et al., 2010.

1.2.2 Release machinery

Central components of release machinery are the SNAREs: synaptobrevin on SVs, SNAP-25, and syntaxin at the AZ plasma membrane. As described before, Munc13-1 plays a major role in priming (Figure 1-5). After vesicle priming, fusion is executed by complete zippering of

SNAREs into a four alpha-helical bundle to fuse the vesicle in the target membranes. Several proteins can activate the fusion by interfering with SNAREs. The SV protein synaptotagmin-1 acts as the dominant calcium sensor that triggers fast synchronous release through a combination of interactions with the SNARE complex and plasma membrane (Fernández-Chacón et al., 2001; Chang et al., 2018). In addition, complexin also binds tightly to SNAREs and stabilizes its primed state, which is critical for efficient Ca^{2+}-triggered neurotransmitter release (Chen et al., 2002).

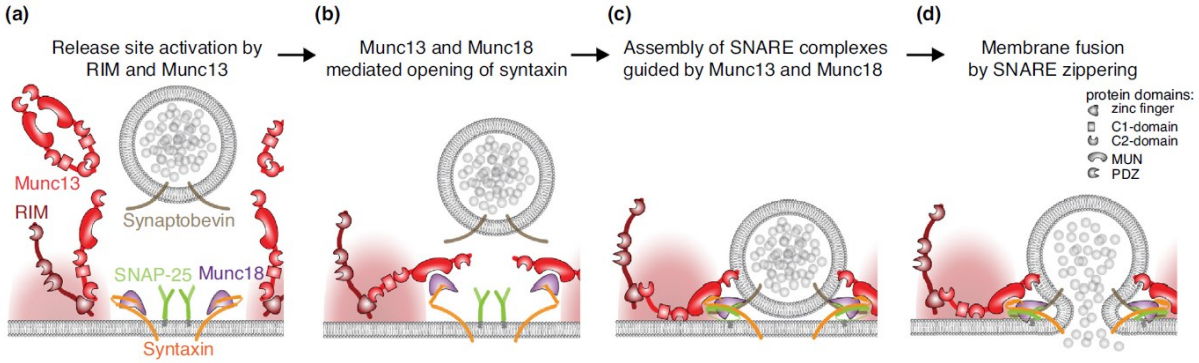

Figure 1-5 Sequential steps for Munc13 centered vesicle fusion and release

1. After Munc13's C2A domain binding to the RIM's zinc finger domain, the MUN domain from Munc13 is activated. 2. Through MUN domain, Munc13 and Munc18 together mediate opening of syntaxin. 3. SNARE complex (synaptobrevin, SNAP-25, and syntaxin) are assembled guided by Munc13 and MUnc18. 4. Zippering of SNARE complex lead to membrane fusion. Adapted from Kaeser and Regehr, 2017.

Release is highly Ca^{2+} dependent and involves a series of sophisticated dynamic events (Figure 1-6). Therefore, it is of significant importance to know the kinetics of vesicle release, and whether a rate-limiting step exists. In this regard, a recent three-step model has been proposed by experimental based simulation (Neher and Brose, 2018). First of all, vesicles are loosely tethered and docked at AZ, forming the SNAREs assembly, which is a state called "loose docking" (LS). Secondly, the loosely docked vesicles get tightened to the AZ by association of additional proteins and partial SNAREs zippering, a state called "tight docking" (TS). Last but not least, TS vesicles fuse to the plasma membrane of AZ upon Ca^{2+} influx. Above all, the first step is a rate-limiting step, which can proceed within 10–50 ms, whereas the other two steps occur on a millisecond or sub-millisecond timescale. Although research on the single glutamatergic synapse (i.e. cerebellar PF–MLI) suggested a two-step model, where both vesicle priming (LS→TS transition) and fusion can occur in rapid succession (Miki et al., 2018), the sequential progression of fusion brought the notion that vesicles have distinct states prior to fusion.

1.2.4 Voltage-gated calcium channels and coupling distance

VGCCs normally comprised a pore-forming α1 subunit and two auxiliary subunits (β and α2δ), they interact directly or indirectly with a diverse array of proteins that regulate their

localization, function and modulation within the presynaptic active zone (Dolphin and Lee, 2020). The main VGCC involved in synaptic transmission in the central nervous systems are Ca_v2 channels, including $Ca_v2.1$ (P/Q-type), $Ca_v2.2$ (N-type) and $Ca_v2.3$ (R-type) channels (Li et al., 2007), but could undergo switch in subtypes during development (Fedchyshyn and Wang, 2005; Bornschein et al., 2019). In the neocortical layer 5 pyramidal cell synapses, transmission relies on both P/Q- and N- type calcium channels at young synapses (P8–10), whereas release exclusively depends on P/Q-type calcium channels at mature synapses (P21–24; Bornschein et al., 2019). Developmental switch is also found in the Calyx of Held synapse (Fedchyshyn and Wang, 2005), and usually associated with the tightening of coupling distance.

The coupling distance between presynaptic Ca^{2+} channels and the Ca^{2+} sensors is a key factor that determine the efficacy and speed of synaptic transmission (Eggermann et al., 2012). Experiments with exogenous Ca^{2+} chelators (EGTA and BAPTA) indicated that the average coupling distance varies among synapses (Table 1). In the mature brain, loose coupling was reported for low release probability synapses with plasticity (Vyleta and Jonas, 2014), and tight coupling at many inhibitory synapses with speed and efficacy (Bucurenciu et al., 2008; Arai and Jonas, 2014). As mentioned above, the coupling distance is not static, but undergoes substantial reorganization during developmental maturation. At excitatory synapses, coupling tightened during development, including the Calyx of Held (Fedchyshyn and Wang, 2005; Nakamura et al., 2015), layer 5 neocortical synapses (Bornschein et al., 2019), and cerebellar parallel fiber synapses (Baur et al., 2015). However, it remains unclear whether developmental tightening of coupling represents a general rule, especially to the inhibitory synapses.

Table 1. Different coupling distance at various synapses

Synapse	Brain area	Coupling Distance (linearized model)	Reference
BC–PC	Cerebellum (P14–16)	Tight coupling (10–20 nm)	Arai and Jonas, 2014
PC–PC	Cerebellum (P7–12)	Tight coupling (25–30 nm)	Bornschein et al., 2013
PF–PC	Cerebellum (P21–27)	Tight coupling (<30 nm)	Schmidt et al., 2013
BC–GC	Hippocampus (P18–21)	Tight coupling (10–20 nm)	Bucurenciu et al., 2008
Calyx of Held	Brain stem (P7–21)	Tight coupling (<30 nm)	Nakamura et al., 2015

L5 pyramidal neuron	Neocortex (P21–24)	Tight coupling (7–15 nm)	Bornschein et al., 2019
L5 pyramidal neuron	Neocortex (P8–10)	Loose coupling (>40 nm)	Bornschein et al., 2019
GC–CA3	Hippocampus (P20–23)	Loose coupling (80 nm)	Vyleta and Jonas, 2014

1.2.5 Topography of presynaptic organization

Although coupling distance can be probed by exogenous Ca^{2+} chelator experiments and have been already investigated in some synapses (Table 1), the spatial organization of Ca^{2+} channels and synaptic vesicles still remain largely elusive in most synapses. By a combination of freeze-fracture replica labeling (FRL), serial-section electron microscope (EM), and modeling, several different topographical models have been suggested.

In the Calyx of Held, the exclusion zone model in which Ca^{2+} channels were randomly positioned around docked vesicles with a minimum radius of around ~30 nm (Keller et al., 2015), and the perimeter release model in which Ca^{2+} channels were localized near clusters of Ca^{2+} channels (Nakamura et al., 2015) have been proposed. A recent study showed different coupling topographies can co-exist in the same circuit, in which cerebellar PF–MLI synapses utilized exclusion zone model, whereas the SC synapses employed perimeter release model (Rebola et al., 2019). Different Ca^{2+} channel-synaptic vesicle arrangement not only explained functional difference of synapse, but also suggested distinct molecular mechanism in establishing the ultrastructure of AZ (e.g. putative repulsive or spacer molecules vs. adhesive molecules). Therefore, it is crucial to characterize the coupling topography in order to gain a deep understanding of diversity and function of a synapse.

1.2.6 Quantal analysis of synaptic transmission

The function of a synapse can be quantified based on the quantal theory of transmission (Katz, 1969). Fluctuation in the amplitude of a synaptic response were first reported at the neuromuscular junction (del Castillo and Katz, 1954). The similarity between the incremental amplitude of these fluctuation and the amplitude of spontaneous miniature synaptic events, let to the development of the ‘quantal’ hypothesis of transmitter release. The quantal theory was subsequently extended to synapses and ion channels in the central nervous system, and has been applied and developed in many studies. They include stationary fluctuation analysis of the variance and mean of postsynaptic responses recorded at different release probability conditions (also known as “multiple-probability fluctuation analysis”; Silver et al., 1998; Clements and Silver, 2000; Silver, 2003) and analysis of mean, variance, and covariance of

nonstationary trains of postsynaptic responses (Scheuss and Neher, 2001; Meyer et al., 2001; Scheuss et al., 2002). In the following paragraph, variance and mean analysis will be introduced in detail, since this method has been widely used and require minimal assumptions.

In a given synapse, there are three key parameters that describe its function: the average amplitude of the postsynaptic response to a packet of transmitter (Q), the average probability of transmitter release across release sites (p_R), and the number of independent release sites that make up synaptic contacts (N). Given the binomial model of synaptic transmission, these quantal parameters can be computed based on the relationship between the variance and mean over a wide range of release probabilities by fitting a parabolic function. Although this model is highly applicable in many studies, there are several assumptions and restrictions.

The assumptions first came from the binomial model that include: (1) N operates independently; (2) release is synchronous; (3) p_R and Q are uniform within intrasites and across intersites (Silver, 2003). Extra models will be applied if release did not fulfill the previous assumptions (e.g. a multinomial model is used if release is asynchronous). In addition, caution needs to be taken whether postsynaptic receptor saturation or desensitization occurs especially under high release probability condition (multivesicular release or transmitter spillover), by examining the blocking effect of the postsynaptic currents by low affinity competitive antagonists.

Overall, the variance and mean analysis is a powerful tool to study the function of a synapse, especially during development. Since the N is quite a fuzzy concept (Pulido and Marty, 2017), it is of significant importance to disentangle its structural correlation.

1.3 Developmental regulation of synaptic transmission

It is widely believed that synapses and synaptic transmission undergo developmental reorganization upon maturation. This process is fundamentally crucial for higher network and normal brain function. Developmental impairments or disorders in the neural system (e.g. schizophrenia or autism spectrum disorder) are often associated with abnormal synaptic function. Therefore, characterizing the developmental properties of synapses is highly required to understand the brain.

Although numerous studies have been focused on excitatory synapses (Fedchyshyn and Wang, 2005; Bornschein et al., 2019), little is known about how inhibitory synapses are developed during maturation. An early paired recoding study between single MLI and PC showed that there is a decrement in the amplitude of unitary inhibitory postsynaptic currents

(IPSC; Pouzat and Hestrin, 1997), but the mechanism underlying the reduced IPSC is uncovered.

In addition, the BC–PC synapse shows a particularly tight coupling between Ca^{2+} channels and synaptic vesicles at the age of P14–16 (Arai and Jonas, 2014). Whether the tightening of coupling which have been found in many excitatory synapses is applied to inhibitory synapses is a significant question in neuroscience.

1.4 Aims of the study

The main goal of this project is to systematically study how the functional and morphological properties of BC–PC synapse evolve as a function of age. In addition, the coupling distance and topographical arrangement of Ca^{2+} channels to synaptic vesicles were investigated for the first time during inhibitory synaptic maturation. In order to achieve these goals, biophysical analysis (paired recording, presynaptic recording, and pipette perfusion), structural measurements (EM and FRL), and in silico simulation of Ca^{2+} diffusion were combined together.

First of all, chapter 3 provides the most detailed information in regard to the functional changes in BC–PC synapse during development. Cutting-edge inhibitory bouton patch clamp recording and subcellular calcium imaging shed lights on the AP shape and Ca^{2+} channel open probability in the small presynaptic terminals. The decent presynaptic pipette perfusion of exogenous Ca^{2+} chelator (EGTA and BAPTA) experiments give the most accurate estimation of coupling distance, which helps to alleviate washout of mobile endogenous buffers (i.e. PV).

In addition, chapter 4 offers a thorough picture on the distribution properties of docked vesicles and Ca^{2+} channels with a nanoscale resolution. Reconstruction of the whole bouton showed that GABAergic boutons contain one to three AZs independently of developmental stage. FRL revealed that the Ca^{2+} channels were clustered throughout development, whereas the docked vesicles illustrated from serial EM were only clustered at later developmental stage.

Last but not least, based on the real AZ morphologies, the Ca^{2+} channel distribution properties, and the experimentally extracted synaptic functional properties, chapter 5 simulation gives a clear picture on how the Ca^{2+} domains developed and how the coupling topography is transformed during synaptic maturation.

Chapter 2. Material and methods

2.1 Experimental animal procedures

2.1.1 Animals

C57BL/6J mice were used for this study. Experiments were performed in strict accordance with institutional, national, and European guidelines for animal experimentation and were approved by the Bundesministerium für Bildung, Wissenschaft und Forschung (A. Haslinger, Vienna).

2.1.2 Cerebellar slice preparation

Slices were cut from the cerebellum of C57BL/6J mice of either sex in three age groups (7–9 days, 14–16 days, and 21–23 days). After decapitation, the brain was rapidly dissected out and immersed in ice-cold slicing solution containing: 87 mM NaCl, 25 mM $NaHCO_3$, 2.5 mM KCl, 1.25 mM NaH_2PO_4, 10 mM D-glucose, 75 mM sucrose, 0.5 mM $CaCl_2$, and 7 mM $MgCl_2$ (pH 7.4 in 95% O_2 / 5% CO_2, ~325 mOsm). Parasagittal 250-µm-thick cerebellar slices from the vermis region were cut using a VT1200 vibratome (Leica Microsystems). After ~20 min incubation at ~35°C, the slices were stored at room temperature (Arai and Jonas, 2014). Slices were used for maximally 5 hours after dissection. Experiments were performed at 21–24°C.

2.2 Electrophysiology

2.2.1 Pair recording

During experiments, slices were superfused with a bath solution containing: 125 mM NaCl, 2.5 mM KCl, 25 mM $NaHCO_3$, 1.25 mM NaH_2PO_4, 25 mM D-glucose, 2 mM $CaCl_2$, and 1 mM $MgCl_2$ (pH 7.4 in 95% O_2 / 5% CO_2, ~325 mOsm). Paired recordings from synaptically connected BCs and PCs were performed as described previously (Pouzat and Hestrin, 1997; Caillard et al., 2000; Sakaba, 2008; Eggermann and Jonas, 2012; Arai and Jonas, 2014). Intracellular solution used for presynaptic BCs contained: 125 mM K-gluconate, 20 mM KCl, 10 mM HEPES, 10 mM phosphocreatine, 2 mM $MgCl_2$, 0.1 mM ethylene glycol-bis(β-aminoethyl ether)-*N*,*N*,*N*′,*N*′-tetraacetic acid (EGTA), 2 mM ATP, 0.4 mM GTP, and 0.2% biocytin (pH adjusted to 7.28 with KOH, ~310 mOsm). Presynaptic pipette resistance was 8–10 MΩ. Intracellular solution for postsynaptic PCs contained: 140 mM KCl, 10 mM HEPES, 2 mM MgCl2, 10 mM EGTA, 2 mM ATP, and 2 mM QX-314 (pH adjusted to 7.28 with KOH, ~313 mOsm). To achieve minimal postsynaptic series resistance, leaded glass (PG10165-4, WPI) was used to fabricate large tip-sized recording pipettes. Postsynaptic pipette resistance was 0.8–1.5 MΩ, resulting in a series resistance of 3–8 MΩ. Experiments in which series resistance changed by > 3 MΩ were discarded. BCs were recorded under current clamp conditions. For P7–9 synapses, no holding current was applied. For P14–16 and P21–23 age groups, a

hyperpolarizing holding current of ~–50 pA was injected to maintain the resting membrane potential at ~–65 mV and to avoid spontaneous AP generation. PCs were recorded in the voltage-clamp configuration with a holding potential of –70 mV. To evoke presynaptic APs, single pulses or trains of 10 pulses at 50 Hz (400 pA, 4 ms) were injected into the presynaptic BC every 4 s or 20 s, respectively. Miniature IPSCs (mIPSCs, Table 2) were recorded in pharmacological isolation in the presence of 1 µM TTX, 10 µM CNQX, and 20 µM D-AP5.

2.2.1.1 Variance and mean experiments

To investigate the relationship between IPSC peak amplitude and $[Ca^{2+}]_o$, different combinations of $[Ca^{2+}]_o/[Mg^{2+}]_o$ were used (0.7/2.3, 2/1, 4/1, and 10/1 mM). In the age group of 21–23 days, 1 mM TEA and 0.05 mM 4-AP were added to the 10/1 mM combination of $[Ca^{2+}]_o/[Mg^{2+}]_o$ to further enhance release probability. In a subset of variance-mean analysis experiments, 300 µM of the low-affinity competitive $GABA_A$ receptor antagonist TPMPA was added to the bath solution. As TPMPA has fast binding and unbinding rates (kon ~ $5 \times 106\ M^{-1}\ s^{-1}$; koff ~ $2000\ s^{-1}$), this is expected to minimize receptor saturation and desensitization (Jones et al., 2001).

2.2.1.2 Pharmacological experiments of peptide toxins

Peptide toxins were applied using a recirculation system with a peristaltic pump (Ismatec, Germany). The total volume of the system was ~5 ml, and the solution was equilibrated with 95% O_2 / 5% CO_2. Bovine serum albumin (BSA, Sigma-Aldrich, St. Louis, MI) was added at a concentration of 0.5 mg ml^{-1} to prevent adsorption of peptides to the surfaces of the perfusion system. ω-agatoxin IVa and ω-conotoxin GVIa were from Bachem (Switzerland), and SNX-482 was from Peptides International.

2.2.1.3 Presynaptic patch pipette perfusion

For experiments using Ca^{2+} chelators, 0.1 mM EGTA was replaced by 10 mM EGTA or 10 mM BAPTA; the concentration of K-gluconate was reduced accordingly to maintain osmolarity (Bucurenciu et al., 2008).

Ca^{2+} chelators were loaded into presynaptic BCs by pipette perfusion, as described previously (Bucurenciu et al., 2008), using a custom-made two-port pipette holder and parts of the 2PK+ pipette perfusion kit (ALA Scientific Instruments, Westbury, NY; Figure 2). Presynaptic pipettes were filled with a small volume (2–4 µl) of intracellular solution. Chelators were applied through one port via a flexible quartz tubing (100 µm outer diameter) coated with polyamide (Bucurenciu et al., 2008). To avoid the long antenna inside the pipette and electrical noise, the silver wire was coated with Teflon. To minimize exchange times, the end of the tubing was positioned closely to the pipette tip. The other end was connected to a ~0.6 ml reservoir with chelator-containing solution. To deliver the chelators to the pipette,

positive pressure was applied to the reservoir and a compensatory negative pressure was applied at the second port of the pipette holder (which was also used for suction during seal formation and transition from cell-attached into whole-cell mode). Both positive and negative pressure were generated by a pressure/vacuum pump system and precisely controlled using two independent pressure regulators (2–5 mm Hg; Bucurenciu et al., 2008). To ensure stable long-term recordings, 3 mM GABA was added to the presynaptic internal solution (Yamashita et al., 2018). Control experiments with mock application of a solution with 0.1 mM EGTA revealed that the rundown of evoked IPSCs during long-lasting recordings was only minimal (to 100.4% of control value; Figure 3-10C and D). Given the small magnitude of rundown, no correction was made. To minimize diffusion time, pipette perfusion experiments were made from closely spaced pairs (BC–PC intersomatic distance <50 µm).

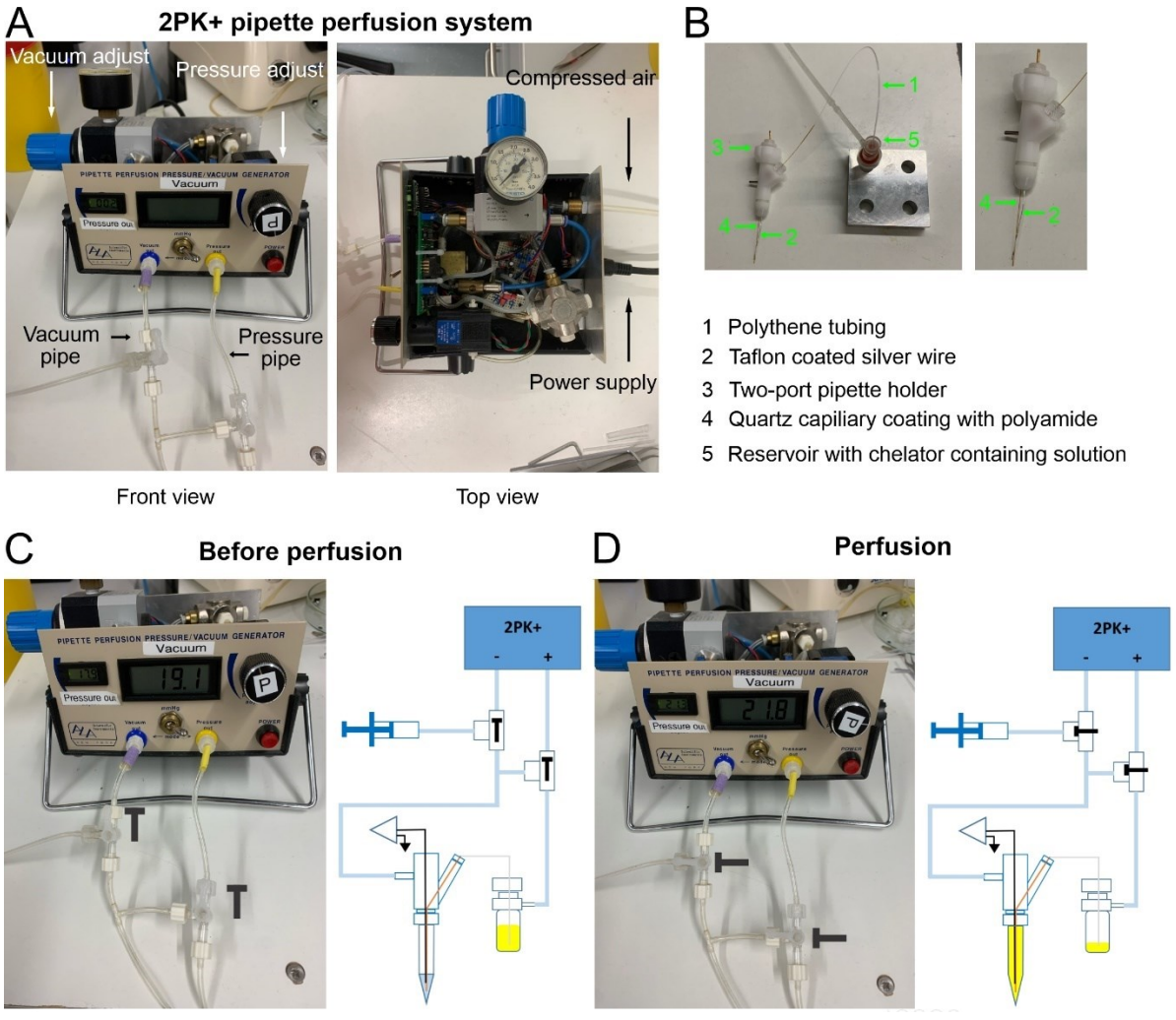

Figure 2 2PK+ whole-cell/patch pipette perfusion kit

(A) Front view and top view of 2PK+ pressure/vacuum controller connected with compressed air. Vacuum is created by a venturi pump (positive air flow creates vacuum discovered by 18th century physicist Giovanni Battista Venturi). The vacuum pressure regulator adjusts the air flow into the venturi tube which regulates the vacuum pressure. Both pressure and vacuum can be adjusted with great sensitivity using the corresponding knobs. **(B)** Custom-made two-port pipette holder with accessories. **(C)** Vacuum pipe is connected to the standard vacuum port on the pipette holder during formation of whole-cell configuration. Note the three-way valves

position before perfusion. Original internal solution inside the pipette is shown in light blue, whereas the chelator containing solution in the reservoir is shown in yellow. **(D)** Chelator containing solution is driven into the pipette holder and then into the pipette by application of both vacuum and pressure. Forces are balanced to minimize turbulence and likelihood of disruption of the whole-cell configuration.

2.2.2 Presynaptic terminal recording

BC boutons were patched using the following experimental strategy (Sasaki et al., 2012; Hu and Jonas, 2014). First, a somatic whole-cell recording was obtained, using BC internal solution containing Alexa Fluor 488 (100 µM, Invitrogen). Second, after ~20 min of recording, the fluorescently labeled boutons were visualized in the PC layer with a Leica TCS SP5 confocal microscope (equipped with a DFC365FX camera, a Leica HCX APO L 20x/1.0W objective, and an argon laser, excitation wavelength of 488 nm). Exposure time was minimized to avoid phototoxicity and photobleaching. The bouton pipettes were coated with BSA Alexa Fluor 488 conjugate (0.02%, Invitrogen) solution for ~20 s while keeping a positive intrapipette pressure during vertical dipping to prevent the pipette tips from clogging. Finally, confocal and infrared differential interference contrast (IR-DIC) images were compared and boutons were patched in the cell-attached configuration guided by confocal images.

2.2.3 Data acquisition and analysis

Data were acquired with a Multiclamp 700B amplifier (Axon Instruments / Molecular Devices), low-pass filtered at 10 kHz, and sampled at 20 or 50 kHz using a CED 1401plus interface (Cambridge Electronic Design). Data were analyzed with Stimfit 0.15.8, Igor Pro 6.3 (Wavemetrics), Mathematica 13.2 (Wolfram Research), or R 4.1.0 (the R project for statistical computing). For BC recording, resting membrane potential was determined immediately after transition into the whole-cell configuration. Single AP parameters (peak amplitude, half-duration, and maximal rate of rise and decay) were measured from the AP threshold determined as the first point in the voltage trajectory in which the slope exceeded 20 V s^{-1}. Membrane potentials reported in the text were not corrected for liquid junction potentials. For BC–PC recording, functional properties of unitary IPSCs were determined from averages of 10–50 individual traces including failures. Synaptic latency (from the peak of the presynaptic AP to the onset of the IPSC), rise time (20–80% of IPSC peak amplitude), and the proportion of failures were determined from 100 to 800 traces using Stimfit software (Guzman et al., 2014). The IPSC decay time constant (single-exponential fit) was determined from single IPSCs. To quantify multiple-pulse depression, traces were averaged and the amplitude of each IPSC in a train was measured from the baseline directly preceding the rising phase. mIPSCs (Table 2) were detected using a template matching algorithm and verified by visual inspection (Pernía-Andrade et al., 2012). For analysis of quantal parameters, multiple probability fluctuation analysis was used (Clements and Silver, 2000). Mean and variance of

IPSC peak amplitude were determined from stationary epochs. Variance-mean data were then fit with the equation

$$\boldsymbol{\sigma^2 = Iq - I^2/N}, \qquad \text{(Eq. 1a)}$$

where $\boldsymbol{\sigma^2}$ is variance, I is mean current, q is quantal size, and N is the number of functional release sites. Variance-mean data were also fit with equations including type 1 (intrasite) and type 2 (intersite) quantal variability

$$\boldsymbol{\sigma^2 = \left(Iq - \frac{I^2}{N}\right)\left(1 + CV_{q2}^2\right) + IqCV_{q1}^2 = Iq\left(1 + CV_{q1}^2 + CV_{q2}^2\right) - (1 + CV_{q2}^2)I^2/N}, \qquad \text{(Eq. 1b)}$$

where CV_{q1} and CV_{q2} represent the coefficients of variation of type 1 and type 2 variability, respectively (Silver et al., 1998). Thus, the basic structure of the variance-mean relation was maintained, with linear scaling factors for q ($1 + CV_{q1}^2 + CV_{q2}^2$) and N ($(1 + CV_{q2}^2)^{-1}$). As corrections were relatively small for plausible values of CV, and N was only affected by CV_{q2}, Eq. 1a was used for final analysis. Additionally, variance-mean data were also fit with equations using a baseline noise term. As introducing this term gave only minimal differences in the estimated parameters and the best-fit value was close to 0, it was omitted in the final analysis. Finally, release probability at 2 mM $[Ca^{2+}]_o$ was computed as $pR = I_{2\ mM} / (N\ q)$. To determine the time course of quantal release, average unitary IPSCs were deconvolved from average quantal IPSCs (Hefft and Jonas, 2005; Arai and Jonas, 2014). Quantal events were detected in the decay phase after a train of 10 APs using the template matching procedure, and converted into an idealized waveform with instantaneous rise and exponential decay. Time course of quantal release was computed by dividing the Fourier transforms of unitary and quantal IPSCs, and computing the inverse Fourier transform (Figure 3-2). To determine vesicular pool size and refilling rate, IPSC amplitudes during a 100-Hz train of 50 stimuli were subjected to cumulative release analysis (Schneggenburger et al., 1999). IPSC values were normalized by $IPSC_1$, averaged across cells, and cumulatively plotted against stimulus number. The last ten data points were fit by linear regression. The size of the readily releasable pool (RRP) was determined from intersection of the regression line with the ordinate, whereas refilling rate was determined from the slope (Schneggenburger et al., 1999). For obtaining absolute numbers of RRP size and refilling rate, estimated values were multiplied by the quantal content of $IPSC_1$. For P7–9 and P14–16 synapses, the depression under control conditions was > 50%, fulfilling a previously specified criterion for this analysis (Neher, 2015). For P21–23 synapses, however, the extent of depression was less; thus, pool analysis was performed in high-pR conditions with 4 mM extracellular Ca^{2+} (Figure 3-7).

2.3 Bouton calcium imaging

Imaging of BC boutons was performed using a Leica TCS SP5 confocal microscope (equipped with a Leica HCX APO L 20x/1.0W objective). First, BCs were filled with Fluo-5F (200 µM) and Alexa Fluor 594 (80 µM) via somatic whole-cell patch pipettes. To allow for a proper equilibration of the dyes, fluorescent signals were measured ~40 min after break-in. Excitation wavelength was 488 nm (argon laser, intensity was set at 0.5%) for Fluo-5F and 561 nm for Alexa Fluor 594 (diode pumped solid state laser, intensity was set at 0.05%). Fluorescence signals were detected by two photomultiplier tubes (PMTs) at fixed PMT voltages, and detection range was 500–550 nm for Fluo-5F and 600–650 nm for Alexa Fluor 594. Boutons were searched in PC layer and were identified as varicosities with diameter >2 times that of the adjacent axons. Line scan imaging was performed in the center of boutons, and the zoom factor was set such that pixel size was 90 nm. To enable simultaneous measurements from boutons at slightly different focal planes, the pinhole size was increased to 2 Airy units. Fluorescent transients were elicited by single APs evoked by brief somatic current pulses and recorded in line scans at 700 Hz temporal resolution. Each bouton was recorded 3 to 5 times. Intracellular Ca^{2+} transients were extracted with Fiji (Schindelin et al., 2012) and further analyzed with custom-made Matlab code (Matlab 2020, Mathworks). The Ca^{2+}-dependent green fluorescence was normalized to the Ca^{2+}-insensitive red fluorescence and expressed as $\Delta G(t)/R$, where G(t) is the fluorescence in the green channel for each time point and R is the mean fluorescence signal in the red channel over each recording epoch. Baseline fluorescence was measured in a 50-ms time window before stimulation, and peak fluorescence was determined in a 10-ms time window after stimulation. Care was taken to avoid phototoxic damage; experiments in which the resting green fluorescence increased by > 20% during recording were excluded from analysis. As background was minimal, no correction was performed. Ca^{2+} transients shown in figures represent averages of 5 individual consecutive line scans. The decay phase of the Ca^{2+} transients was fit by a double-exponential function, and the time constant was given as amplitude-weighted average decay time constant; components with negative amplitudes were set to 0. The average decay time constant of the Ca^{2+} transients was ~100 ms, consistent with the relatively low affinity of Fluo-5F (Mishra et al., 2016).

2.4 Immunohistochemistry

After recording, slices were fixed by immersion in phosphate buffer (PB; 0.1 M, pH 7.4) containing 4% formaldehyde at 4°C overnight. After 3 times wash in PB, slices were embedded in 4% agarose and further sectioned into 50-µm-thick slices. For cryoprotection, slices were immersed in 30% sucrose in PB for 2 hours at 4°C. Slices were further frozen above liquid nitrogen and thawed in PB to increase penetration of reagents. For immunolabeling, slices were first washed 3 times in PB and immersed in 10% normal goat serum (NGS) and 0.4% Triton X-100 in PB for 1 hour at RT to block nonspecific binding. The slices were then incubated in rabbit polyclonal anti- $GABA_A$ receptor α1 primary antibody (5 µg ml^{-1}, Synaptic Systems,

cat# 224 203) and guinea pig polyclonal anti-VGAT primary antibody (1:200, Synaptic Systems, cat# 131 004) for 48 hours at 4°C in PB with 5% NGS and 0.4% Triton X-100. After washing 3 times in PB, slices were further incubated in PB containing 5% NGS, 0.4% Triton X- 100, streptavidin Alexa Fluor 647 conjugate (4 µg ml^{-1}, Invitrogen, cat# S32357), goat anti-rabbit Alexa 488 (10 µg ml^{-1}, Invitrogen, cat# A-11034), and goat anti-guinea pig Alexa Fluor 405 (10 µg ml^{-1}, Abcam, cat# ab175678) for 2 hours at RT. Slices were then washed in PB and mounted in Prolong Gold antifade embedding medium (Invitrogen). Fluorescence images were acquired using a Zeiss LSM 800 inverted microscope with sequential scanning of fluorescence signals using an oil objective (63x/1.4). Confocal images were analyzed with Fiji.

2.5 Sample preparation for EM experiments

2.5.1 Sample preparation for serial-section EM

For the analysis of the number of AZs per bouton, brains of animals (C57BL/6 mice P7–9, n = 4; P14–16, n = 4; P21–23, n = 4) were perfusion-fixed with PB containing 2% formaldehyde, 2.5% glutaraldehyde, and 15% saturated picric acid solution. Serial sagittal sections from the cerebellum were sliced at 50 µm with a VT1200 vibratome and processed according to a previously published protocol (Starborg et al., 2013) with modifications. Briefly, sections were washed in PB and treated with 0.2% tannic acid in PB two times 45 min each at RT. Sections were postfixed and stained with 2% osmium tetroxide in PB for 40 min at RT and 1% uranyl acetate in water overnight at 4°C. They were further contrast-enhanced with Walton's lead aspartate for 30 min at 60°C, dehydrated in graded ethanol and anhydrous acetone, and embedded in epoxy resin following the manufacturer's instructions (Durcupan ACM, Sigma-Aldrich).

For the analysis of the number of docked vesicles per AZ, high-pressure freezing (HPF) of acute slice preparations was performed with a Leica EM ICE high pressure freezing apparatus (Leica Microsystems) as previously described (Borges-Merjane et al., 2020). After slicing and recovery, slices were mounted in sapphire-metal ring sandwiches. For mounting, a bottom sapphire disk (diameter 6 mm, thickness 120 µm; Wohlwend, Sennwald, Switzerland) was placed on the middle plate of a clear cartridge. Next, a spacer ring (outer diameter 6 mm, inner diameter 4 mm; thickness 200 µm) was put on top of the sapphire disk, adding a drop of extracellular bath solution containing 15% of the cryoprotectant polyvinylpyrrolidone. Subsequently, the tissue sample was transferred using a paintbrush. Finally, a second sapphire disk with identical dimensions was put on top to form a sandwich. Freeze substitution and embedding were done as previously described (Borges-Merjane et al., 2020).

For serial sectioning, samples were sliced at either 40 nm (number of docked vesicle analysis in cryofixed samples) or 80 nm (number of AZ analysis in chemically fixed samples) using a UC7 ultramicrotome (Leica Microsystems) and a 4-mm Ultra 35° diamond knife

(Diatome). Ribbons of sections were mounted onto Formvar-coated copper slot grids, and examined in a Tecnai 10 transmission electron microscope (T10 TEM; Thermo Fisher Scientific) operated at 80 kV accelerating voltage. Images were recorded with a Megaview III CCD camera and Radius acquisition software (both EMSIS).

2.5.2 Freeze-fracture replica immunolabeling (FRL)

FRL was performed with some modifications to the original method (Fujimoto, 1995; Kaufmann et al., 2021). Brains of animals (C57BL/6 mice P7–9, n = 3; P14–16, n = 3; P21–23, n = 3) were perfusion-fixed with PB containing 2% formaldehyde and 15% saturated picric acid solution. Sagittal sections from the cerebellum were cut at 140 µm with a VT1200 vibratome and cryoprotected by immersion in 30% glycerol in PB overnight at 4°C. Samples were rapidly frozen by use of the high-pressure freezing machine HPM 010 and fractured by a double-replica method in the freeze-etching device BAF 060 (Leica Microsystems) as described before (Möbius et al., 2010). In brief, fractured faces were replicated by evaporation of carbon (rotating) by means of an electron beam gun positioned at a 90° angle to a thickness of 5 nm for immobilization of macromolecules (Kaufmann et al., 2013). They were then shadowed unidirectionally with platinum-carbon at a 60° angle (thickness 2 nm) and strengthened by evaporation of carbon to a thickness of 20 nm from a 90° angle (rotating). Samples were brought to atmospheric pressure and thawed to RT in Tris-buffered saline (TBS; 50 mM, 0.9% NaCl, pH 7.4). Tissue not immobilized in the replica membrane was solubilized in a medium containing 2.5% sodium dodecyl sulfate (SDS) and 20% sucrose in 15 mM TBS, pH 8.3, on a shaking platform for 48 h at 60°C. Replicas were treated for another 12 h at 37°C and kept at RT in the same solution (Kaufmann et al., 2013).

For immunolabeling, replicas were washed in TBS and incubated in 5% BSA in TBS for 1 h at RT to block nonspecific binding. Subsequently, antibodies were applied sequentially in TBS containing 2% BSA. Replicas were first incubated with guinea pig polyclonal anti-$Ca_v2.1$ α-1A primary antibodies (2 µg ml^{-1}; Synaptic Systems, cat# 152 205), and reacted with goat anti-guinea pig secondary antibodies conjugated to 10-nm gold particles. Replicas were then incubated with a cocktail of AZ marker proteins including rabbit polyclonal anti-RIM1/2 antibodies (2 µg ml^{-1}; Synaptic Systems, cat# 140 203), rabbit polyclonal anti-ELKS antibodies (2 µg ml^{-1}; provided by Akari Hagiwara and Toshihisa Ohtsuka, Yamanashi University Medical School, Japan), and rabbit polyclonal anti-neurexin antibodies (1 µg ml^{-1}; provided by Masahiko Watanabe, Hokkaido University School of Medicine, Japan), and reacted with goat anti-rabbit secondary antibodies conjugated to 2-nm gold particles (Miki et al., 2017). Finally, replicas were incubated with mouse monoclonal anti-VGAT antibodies (4 µg ml^{-1}; Synaptic Systems cat# 131 011), and reacted with goat antimouse secondary antibodies conjugated to 15-nm gold particles. All primary antibodies and gold-conjugated secondary antibodies (1:30, BBI Solutions) were each applied overnight at 15°C. The specificity of the $Ca_v2.1$ antibody was

confirmed by testing cerebellar tissue samples from $Ca_v2.1$ α1A −/− mice. Replicas were then washed in water, mounted onto Formvar-coated 100-line copper grids, and examined in a Tecnai 12 TEM (Thermo Fisher Scientific) operated at 120 kV and equipped with a Veleta CCD camera (EMSIS). Images were acquired and analyzed using Radius (EMSIS) and Fiji software (distributed under the General Public License, GPL).

Labeling efficacy of the $Ca_v2.1$ antibody used in the present study was estimated in control experiments at hippocampal mossy fiber synapses, in which direct presynaptic Ca^{2+} current recordings (Li et al., 2007), serial-section EM data (Rollenhagen et al., 2007), and FRL data (O.K., unpublished) are all available (Eguchi et al., 2022). Functional analysis revealed 2007 Ca^{2+} channels of all types and 1324 P/Q-type Ca^{2+} channels per mossy fiber terminal (Li et al., 2007). Serial-section EM gave a total AZ area of 3.33 μm^2, a total presynaptic surface area of 75.5 μm^2, and an extrasynaptic surface area of 72.2 μm^2 (75.5 μm^2 − 3.33 μm^2; P28; Rollenhagen et al., 2007). Finally, FRL analysis revealed $Ca_v2.1$ particle densities of 279 μm^{-2} inside the AZ and 1.36 μm^{-2} outside the AZ (O.K., unpublished). Taken together, this gives a total number of P/Q immunoparticles of 1027 per mossy fiber terminal (AZ density × AZ area + extrasynaptic density × extrasynaptic area), corresponding to a labeling efficiency of 77.6% (1027 / 1324). This is higher than a previous estimate based on optical fluctuation analysis (~40%; Rebola et al., 2019).

2.6 Ultrastructural analysis of bouton, active zone, docked vesicles, and Ca channels

2.6.1 Bouton and active zone reconstructions from serial-sections

BC boutons and AZs were selected for three-dimensional reconstruction from serial section electron micrographs based on completeness and optimal angle of sectioning. Serial images were aligned and relevant structures were traced and measured with Fiji/TrakEM2 software (Cardona et al., 2012). Perimeters of AZs were drawn according to close and parallel apposition of the pre- and postsynaptic membrane, and presence of amorphous electron-dense material in the cleft. Three-dimensional reconstruction of AZs was performed using custom-made Matlab software. Vesicles were classified as docked when the distance between vesicular and presynaptic plasma membrane was < 5 nm, consistent with previous criteria for classification of vesicular pools (Borges-Merjane et al., 2020). Three-dimensional reconstruction of boutons was performed using the ETomo software of the IMOD software package, version IMOD 4.11 (Kremer et al. 1996). For model scaling, the z scale was set as the section thickness divided by the pixel size of the respective electron micrograph. For calculation of the AZ surface area, the object was meshed within the 3Dmod software using the standard parameters.

2.6.2 Active zone demarcation from FRL samples

For identification of BC AZs, we set the following criteria: (1) presence of immunoparticles labeling AZ marker proteins (2 nm) and VGAT (15 nm; min. 2 particles), (2) aggregates of intramembrane particles, and (3) direct proximity to postsynaptic PC plasma membrane. AZs were delineated according to the following principles: (1) demarcation of AZs drawing a polygon based on the outmost immunoparticles for $Ca_v2.1$ (10-nm gold particles) and RIM-ELKS-neurexin (2-nm gold particles; Miki et al., 2017). (2) Inclusion of an outer rim of 20 nm as antibodies can freely rotate around the epitope (Kaufmann et al., 2021). The dimension of this rim results from the size of antibodies applied (IgGs with approximately 8 nm each) and the size of the immunoparticle itself (radius of the gold particle). (3) Elimination of cases where a single gold particle or the center of an individual particle cluster was >100 nm away from the nearest particle cluster to avoid spurious delineation of AZs by isolated RIM-ELKS-neurexin particles. The threshold of 100 nm was derived from the longest distance between neighboring RIM-ELKS-neurexin clusters inside AZs. Distances were calculated using macros in R 4.1.0 (the R project for statistical computing). The X and Y coordinates of immunoparticles were recorded and extracted in Fiji**.**

2.6.3 Ca channel and docked vesicle cluster analysis

2.6.3.1 Nearest neighbour distance analysis

The distances from each particle to every other particle were calculated, and the smallest value was assigned as the NND for each particle. Clustering of particles or docked vesicles were analyzed by comparing cumulative distributions of NNDs between real data from experimental measurements and simulated data generated by a random point process. Statistical significance was assessed using a Wilcoxon-Mann-Whitney test.

2.6.3.2 Ripley's analysis

Clustering of particles was analyzed using the Ripley method (Ripley, 1977; Rebola et al., 2019). Ripley's K function was computed as:

$$\boldsymbol{K(r) = \lambda^{-1} \sum_{i \neq j} \omega_{i,j}^{-1} I(d_{i,j} < r)/N,} \qquad \text{(Eq.2)}$$

where λ is average point density, $\omega_{i,j}$ is a weight factor for edge correction, I is an indicator function that counts the number of points within a radius r (taking a value of 1 if its operand is true and 0 otherwise), and N is number of points in the pattern. After correction for edge effects, H(r) was computed from K(r) as $H(r) = \sqrt{\boldsymbol{K(r)/\pi}} - \boldsymbol{r}$. Values H(r) > 0 may indicate clustering, while values H(r) < 0 may suggest dispersion. H(r) curves were first obtained for individual AZs and then pooled for all AZs of each developmental time period. Statistical significance was assessed using a maximum deviation test, comparing experimental against Monte Carlo-simulated data (Rebola et al., 2019). To specifically test for clustering, only

positive deviations were considered. For random positioning of Ca^{2+} channels, points were simulated on the AZ plane with 10 nm minimal distance. For random positioning of vesicles, spheres were distributed within single sections with 30 nm minimal distance.

2.6.3.3 Density-based spatial clustering of applications with noise (DBSCAN)

To define clusters of particles, we applied DBSCAN to our replica data (Ester et al., 1996). To obtain quantitative criteria for separating particles in the same versus different clusters, we plotted, for each particle, the 2-nearest neighbor graph for an individual AZ, and then identified the onset point of each graph as ε. We found that most of the ε were located in the range between mean + 2 SD and mean + 3 SD of the NND. The mean ε was 40.3 nm, 41.1 nm, and 40.9 nm for the P7–9, P14–16, and P21–23 age groups, respectively. The minimal number of points in each cluster was set to 3, based on the $Ca_V2.1$ particle background labeling on knockout mice tissue (Miki et al., 2017; Figure 4-4). The NND between clusters was estimated by determining the shortest distance between cluster centers.

2.7 Modeling of nanodomain coupling based on realistic coupling topographies

Ca^{2+} diffusion and binding to buffers was modeled solving the full set of partial differential equations of the reaction-diffusion problem in three dimensions, including all necessary boundary and initial conditions (Smith, 2001; Bucurenciu et al., 2008; Eggermann et al., 2012, Vyleta and Jonas, 2014; Nakamura et al., 2018). The main partial differential equations were

$$\frac{\partial[\mathrm{Ca}]}{\partial t} = \boldsymbol{D_{Ca}}\left(\frac{\partial^2[\mathrm{Ca}]}{\partial x^2} + \frac{\partial^2[\mathrm{Ca}]}{\partial y^2} + \frac{\partial^2[\mathrm{Ca}]}{\partial z^2}\right) - \boldsymbol{k_{on}}\,[\mathrm{Ca}][\boldsymbol{B_i}] + \boldsymbol{k_{off}}([\boldsymbol{B_i}]_{\boldsymbol{tot}} - [\boldsymbol{B_i}]), \qquad \text{(Eq. 3)}$$

$$\frac{\partial[B_i]}{\partial t} = \boldsymbol{D_B}\left(\frac{\partial^2[B_i]}{\partial x^2} + \frac{\partial^2[B_i]}{\partial y^2} + \frac{\partial^2[B_i]}{\partial z^2}\right) - \boldsymbol{k_{on}}\,[\mathrm{Ca}]\,[\boldsymbol{B_i}] + \boldsymbol{k_{off}}([\boldsymbol{B_i}]_{\boldsymbol{tot}} - [\boldsymbol{B_i}]), \qquad \text{(Eq. 4)}$$

and

$$\frac{\partial[B_{fix}]}{\partial t} = -\boldsymbol{k_{on}}\,[\mathrm{Ca}]\,[\boldsymbol{B_{fix}}] + \boldsymbol{k_{off}}\left([\boldsymbol{B_{fix}}]_{\boldsymbol{tot}} - [\boldsymbol{B_{fix}}]\right), \qquad \text{(Eq. 5)}$$

where [Ca] is the free Ca^{2+} concentration, *t* is time, *x*, *y*, and *z* are spatial coordinates, and D_{Ca} is the diffusion coefficient for Ca^{2+}. Furthermore, $[B_i]$ is the free mobile buffer concentration, k_{on} the binding rate, k_{off} the unbinding rate, $[B_i]_{tot}$ the total mobile buffer concentration, and D_B the diffusion coefficient of the buffer. Finally, $[B_{fix}]$ is the free fixed buffer concentration, and $[B_{fix}]_{tot}$ is the total fixed buffer concentration.

Near the Ca^{2+} sources, the boundary conditions were given as

$$\frac{\partial[\mathrm{Ca}]}{\partial z} = \boldsymbol{D_{Ca}}\,\sigma(\boldsymbol{t}, \boldsymbol{x}, \boldsymbol{y}) \text{ for } z \rightarrow 0, \qquad \text{(Eq. 6)}$$

where $\sigma(t, x, y)$ is the flux density.

Otherwise, the boundary conditions were

$$\frac{\partial[\mathrm{Ca}]}{\partial x} = \frac{\partial[B_i]}{\partial x} = \mathbf{0} \text{ for } x \rightarrow x_{min} \text{ or } x_{max}, \quad \text{(Eq. 7a)}$$

$$\frac{\partial[\mathrm{Ca}]}{\partial y} = \frac{\partial[B_i]}{\partial y} = \mathbf{0} \text{ for } y \rightarrow y_{min} \text{ or } y_{max}, \quad \text{(Eq. 7b)}$$

$$\frac{\partial[\mathrm{Ca}]}{\partial z} = \frac{\partial[B_i]}{\partial z} = \mathbf{0} \text{ for } z \rightarrow z_{max}, \quad \text{(Eq. 7c)}$$

and

$$\frac{\partial[B_i]}{\partial z} = \mathbf{0} \text{ for } z \rightarrow 0. \quad \text{(Eq. 7d)}$$

This set of partial differential equations was numerically solved with NDSolve of Mathematica 11.3, 12.2, 13.0, or 13.1 running under a Windows 10 operating system, using the IDA method and the GMRES implicit solver of Mathematica. The spatial grid resolution was 5 nm, and the total number of grid points was 1,295,061. For analysis of multiple random Ca^{2+} channel activation patterns and AZs, computations were performed on a high-performance computing cluster (ISTA-HPC), using x86_64 (64bit Intel/AMD) CPUs, GNU/Linux Debian11 operating system, and Mathematica 13.0.

Ca^{2+} influx during an AP was represented by a Gaussian function. The standard deviation was set according to the shape of the presynaptic APs and the gating properties of presynaptic P/Q-type Ca^{2+} channels (Li et al., 2007; Figure 5-2). APs were simulated using a Wang-Buzsáki excitability model of GABAergic interneurons (Wang and Buzsáki, 1996), with gating scaling factors Φ and K^+ conductance $\overline{g_K}$ varied over a wide range. Simulated APs were applied as stimuli to models of P/Q-type Ca^{2+} channels, and Ca^{2+} current half-duration was plotted against AP half-duration and analyzed by linear regression. The peak amplitude of the current through a single Ca^{2+} channel was set to 0.13 pA (Li et al., 2007; Weber et al., 2010; Sheng et al., 2012). The diffusion coefficient for Ca^{2+} was assumed as D_{Ca} = 220 µm^2 s^{-1} throughout.

The standard parameters of our model were as follows (Table 5): for the fixed buffer, the rates were chosen as $k_{on} = 1 \times 10^8$ M^{-1} s^{-1} and k_{off} = 10,000 s^{-1}; the total concentration was set to 4 mM (Nakamura et al., 2015). For the endogenous mobile buffer (with ATP-like binding properties), the rates were chosen as $k_{on} = 5 \times 10^8$ M^{-1} s^{-1} and k_{off} = 100,000 s^{-1}, the concentration was set to 0.27 mM, and the diffusion coefficient was D_B = 200 µm^2 s^{-1}. For the exogenous buffer EGTA, the rates were assumed as $k_{on} = 1 \times 10^7$ M^{-1} s^{-1} and k_{off} = 0.7 s^{-1} (affinity 70 nM); for the exogenous buffer BAPTA, the rates were taken as $k_{on} = 4 \times 10^8$ M^{-1} s^{-1}

and k_{off} = 88 s^{-1} (affinity 220 nM; Meinrenken et al., 2002; Naraghi and Neher, 1997; Neher, 1998; Nägerl et al., 2000). The diffusion coefficient was set as $D_{EGTA} = D_{BAPTA}$ = 220 μm^2 s^{-1}.

Buffer concentrations were assumed to be uniform. The resting Ca^{2+} concentration was set to 40 nM (Collin et al., 2005). Initial conditions were calculated according to mass action law. Ca^{2+} channels were represented as disks with 5 nm radius. Cytoplasmic volume around an AZ was represented as a cuboid with 0.68 µm × 0.68 µm width and 0.34 µm height (Figure 5-1B). Experimentally determined Ca^{2+} channel coordinates were shifted and rotated to optimize insertion into the cuboid. Mathematically, a system in which a single AZ is surrounded by a small volume with reflective boundaries would be equivalent to a system in which multiple AZs are surrounded by a larger volume without boundaries. Thus, the model was consistent with our morphological data. Ca^{2+} extrusion mechanisms were not modeled, since the kinetics of these processes is more than an order of magnitude slower than the fast Ca^{2+} transients following single APs examined here. As BCs express the Ca^{2+}-binding protein PV, a buffer with PV-like properties (Collin et al., 2005; Eggermann and Jonas, 2012) was added in a subset of simulations (Figure 5-3). As simulations were computationally expensive and differences were minimal, we have not routinely included PV-like buffers in our model.

Finally, the release rate was computed using an allosteric model of transmitter release, previously established at the calyx of Held (Lou et al., 2005). As both BC–PC and calyx synapses involve synaptotagmin-2 as a Ca^{2+} sensor (Sun et al., 2007; Chen et al., 2017a, b), the use of a model from a different synapse was justified, although subtle developmental differences in affinity cannot be excluded (Kochubey et al., 2009). Total simulation time was 10 ms.

The occupancies for the different states of the model were obtained by solving the corresponding first-order ordinary differential equations with a Q matrix approach. The location of the Ca^{2+} sensor was varied in x and y direction, whereas in z direction the sensor was placed 5 nm below the surface of the plasma membrane. For simulation of fixed Ca^{2+} channel activation patterns (P7–9), a single pattern of Ca^{2+} channel activation was used together with 100 patterns of random synaptic vesicle placement. For simulation of stochastic Ca^{2+} channel activation (P14–16 and P21–23), 10 random activation patterns were combined with 10 random patterns of synaptic vesicle placement for each representative example AZ (Nakamura et al., 2015). For simulation of all AZs (67, 69, and 81 AZs), 5 random synaptic vesicle placement patterns were generated. Vesicles were randomly placed on cluster areas, cluster perimeters, AZs, and presynaptic membrane, using the Random Point function of Mathematica. For CA and CP model, the area of a circle with double radius was subtracted for each positioned vesicle, and vesicle positioning was iteratively continued until the available

area was empty. The mean number of attached vesicles was 22 and 19, 37 and 31, and 42 and 34, respectively. For RAZ and RPM model, the same number of vesicles as in the CA model was distributed over a larger area. Finally, a likelihood score was determined, which describes the probability of a model given the experimental data. Specifically, the minus log-likelihood score was computed as

$$L = -\ln \Pi P(x_{mod} \mid x_{exp}) = -\ln [P(r_{EGTA,\,mod} \mid r_{EGTA,\,exp}) \times P(r_{BAPTA,\,mod} \mid r_{BAPTA,\,exp}) \times P(p_{R,\,mod} \mid p_{R,\,exp}) \times P(\delta_{tcr,\,mod} \mid \delta_{tcr,\,exp}) \times P(\tau_{tcr,\,mod} \mid \tau_{tcr,\,exp})], \quad \text{(Eq. 8)}$$

where x is a given synaptic parameter, mod indicates modeling data, exp denotes experimental values, r_{EGTA} and r_{BAPTA} are chelator-to-control current ratios, δ_{tcr} is the delay, and τ_{tcr} is the decay time constant of the time course of release. P distributions $P(x_{mod} \mid x_{exp})$ were represented by normal distributions based on experimental data (means taken from each age group; standard deviations averaged across age groups; peaks normalized to 1). Release probability p_R was computed as $p_R = \xi_{max} / I_+ f^5$ (Lou et al., 2005; Table 5), where ξ_{max} is maximal release rate. Delay δ_{tcr} was measured from peak of Ca^{2+} flux to peak of release. τ_{tcr} was obtained by fitting a monoexponential function to the decay of the release period. Weights were set to 1 for r_{EGTA} and r_{BAPTA}, and 0.5 for p_R, δ, and τ_{tcr} to account for smaller reliability in kinetic measurements. *L* values were computed for each random pattern in each model, and cumulative distributions were compared between models using a Wilcoxon-Mann-Whitney test.

To determine the mean topographical coupling distance, the following procedure was used (Figure 5-4D, left). For each channel-vesicle pair, the physical distance in x-y plane was measured, resulting in a distance matrix. Each channel's fractional contribution to the release rate was probed by either activating the channel (if closed) or inactivating the channel (if open), resulting in a release relevance matrix. Finally, the weighted mean distance was computed, using the release relevance matrix to derive the weight factors. Thus, the topographical coupling distance was obtained as $\sum_{i=1}^{m}\sum_{j=1}^{n} r(i,j)\, d(i,j) \;/ \sum_{i=1}^{m}\sum_{j=1}^{n} r(i,j)$, where r(i, j) is the fractional contribution of Ca^{2+} channel i to the release of vesicle j, d(i, j) is the distance in x-y plane between Ca^{2+} channel i and vesicle j, m is the total number of Ca^{2+} channels, and n is the total number of vesicles.

2.8 Statistical analysis

All values were reported as mean ± standard error of the mean (SEM). Statistical significance was tested using a Kruskal-Wallis test, followed by a Wilcoxon rank sum test / Mann-Whitney U-test with Bonferroni correction, unless specified differently. Differences with $P < 0.05$ were considered significant. In the text, P values indicate the results from Kruskal-Wallis test. In the figures, brackets with *, **, and *** labels indicate the results from Wilcoxon-Mann-Whitney test (representing $P < 0.05$, $P < 0.01$, and $P < 0.001$, respectively). In the tables, both values are given. Throughout the paper, P7– 9 data are indicated in gray, P14–16 data in red, and P21–23 data in cyan. In bar graphs, circles represent data from individual experiments, and bars indicate mean ± SEM, unless specified differently. In total, data included in the present paper were from 197 BC–PC paired recordings, 5 BC soma-soma recordings, and 15 BC bouton-soma recordings. 13 recordings at P14 were taken from a previously publication (Arai and Jonas, 2014).

Chapter 3. Functional characterization of BC–PC synapse during development

3.1 Basic synaptic transmission properties at BC–PC synapses

To study how the synaptic transmission properties evolve as a function of age, we performed paired recordings between BCs and PCs in the vermis region (lobe V and lobe VI) of parasagittal cerebellar acute slices at three developmental age groups, postnatal day (P) 7–9, P14–16, and P21–23. After establishing whole-cell current clamp recording of BC, a series of squared pulses (starting from -100 to 350 pA, with 50 pA increment) were injected to test the firing property of BC. BCs show fast spiking firing property, with a maximum frequency up to 156.9 ± 6.45 Hz at the age of P21–23. In addition, the half-duration of somatic AP decreased from 1.11 ± 0.05 at P7–9 to 0.99 ± 0.11 at P14–16 and 0.75 ± 0.02 at P21–23 (15 recordings per age group; $P < 0.0001$; Table 2). Thus, the somatic AP undergoes substantial shortening during development.

To test the synaptic connection between BCs and PCs, trains of stimuli (10 pulses at 50 Hz) were applied to BCs and simultaneous IPSC of PCs were recorded (Figure 3-1). The peak amplitude of IPSC was significantly reduced (Figure 3-1D), consistent with a previous observation (Pouzat and Hestrin, 1997). In addition, the proportion of failures increased slightly from 1.36% ± 0.62% at P7–9 to 1.47% ± 1.05 % at P14–16 and 1.55% ± 0.69% at P21–23, although there is no significant difference among groups ($P = 0.6686$; Table 2). The latency measured between the peak of AP from presynaptic BC and the onset of IPSC from postsynaptic PC were decreased from 0.75 ± 0.03 at P7–9 to 0.66 ± 0.04 at P14–16 and 0.59 ± 0.03 at P21–23 during development (Figure 3-1E). In parallel, the 20–80% rise time of IPSC was also declined from 0.72 ± 0.03 at P7–9 to 0.62 ± 0.05 at P14–16 and 0.58 ± 0.05 at P21–23 (Figure 3-1F). These results indicate an increase in speed and temporal precision of synaptic transmission. In addition, the pair pulse ratio measured as $IPSC_2/IPSC_1$ (Figure 3-1G) and depression ratio measured as $IPSC_{10}/IPSC_1$ (Figure 3-1H) were increased significantly during synaptic transmission, indicating increased reliability during repetitive activity. On the contrary, the half duration and decay time constant of IPSC were only changed minimally with no significant difference between groups (Table 2), suggesting constant properties of postsynaptic $GABA_A$ receptors.

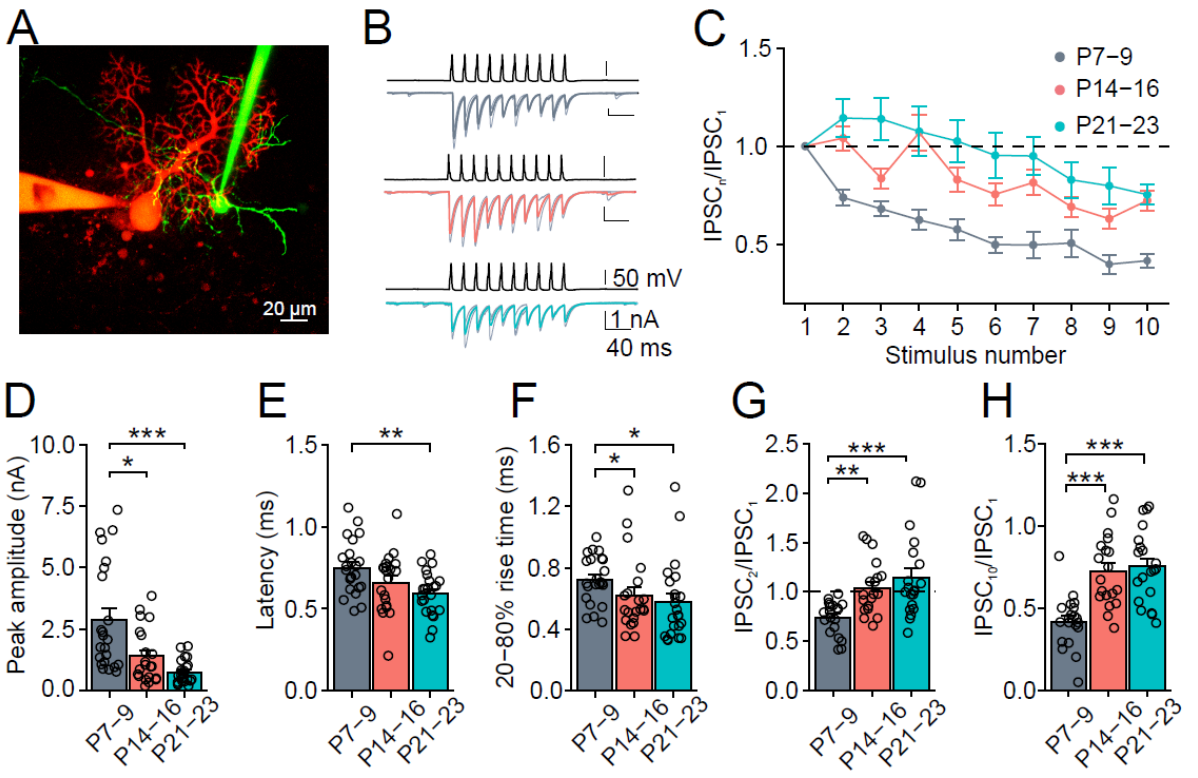

Figure 3-1 Kinetics and efficiency of synaptic transmission at BC–PC synapse during development
(A) Confocal maximum intensity projection of synaptically connected BC filled with Alexa Fluor 488 and PC filled with Alexa Fluor 594 during recording at P14. **(B)** Representative IPSC from BC–PC recordings at postnatal days (P) 7, P14, and P21. Top traces represent presynaptic APs evoked by trains of 10 stimuli, bottom traces are individual IPSCs (light gray) and average IPSCs (gray, red, and cyan) from 3 consecutive traces. (**C)** Plot of normalized IPSC amplitude ($IPSC_n/IPSC_1$) against stimulus number (n) for P7–9, P14–16, and P21–23 age groups, respectively. **(D–H)** Summary bar graphs of IPSC peak amplitude (D), latency (E), 20–80% rise time (F), paired-pulse ratio ($IPSC_2/IPSC_1$; G), and multiple-pulse ratio ($IPSC_{10}/IPSC_1$; H). Circles represent data from individual experiments, and bars indicate mean ± SEM.

3.2 Time course of quantal release at BC–PC synapse

To study the release kinetics in more detail, we analyzed the time course of quantal release by deconvolution (Hefft and Jonas, 2005; Pernía-Andrade, et al., 2012). Averaged unitary IPSCs during the train were deconvolved from average quantal IPSC after the train. Quantal events were detected in the decay phase using a template matching procedure, and converted into a waveform with instantaneous rise and exponential decay. Time course of quantal release was computed by dividing the Fourier transforms of unitary and quantal IPSCs, and computing the inverse Fourier transform (Figure 3-2A). We found that the peak-to-peak interval between the peak of AP and the peak of release became significantly shorter during development (Figure 3-2B), which is in consistent with the reduction in the synaptic latency (Figure 3-1E). In parallel, the decay time constant of quantal release became shorter. Taken together, these results demonstrate that quantal release at the BC–PC synapse becomes

significantly faster during synaptic maturation, suggesting an increase in the speed and temporal precision of synaptic transmission.

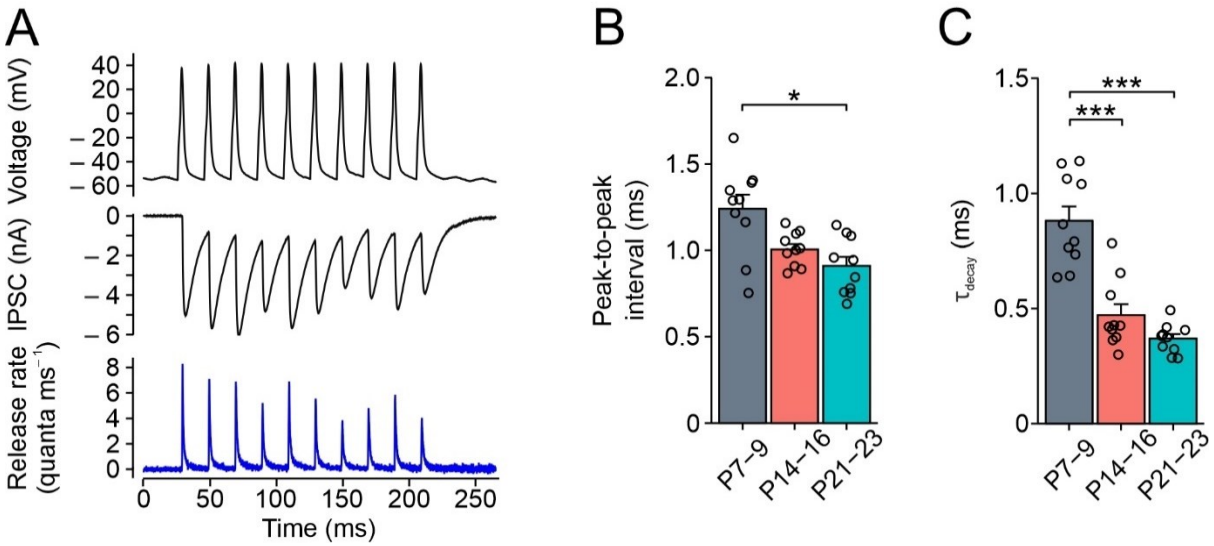

Figure 3-2 Time course of release of synaptic transmission at BC–PC synapse
(A) Presynaptic AP (top), evoked IPSCs (center), and release rate (bottom) obtained by deconvolution. **(B and C)** Summary bar graphs of time interval between peak of AP and peak of release (B) and decay time constant of release (C) at P7–9 (gray), P14–16 (red), and P21–23 (cyan).

3.3 Constant reliance of P/Q-type Ca^{2+} channels

To probe whether there is a switch in the type of Ca^{2+} channel underlies synaptic transmission at presynaptic BC, we applied different Ca^{2+} channel specific blockers to examine their roles on synaptic transmission. In addition, to avoid possible peptides absorption effect at the bath solution surfaces, 0.5 mg ml^{-1} BSA were applied in the ~ 5 ml system. The contribution of P/Q-type Ca^{2+} channels were tested by 1 µM ω-agatoxin IVa, a concentration expected to completely block both P- type and Q- type Ca^{2+} channels. We found that ω-agatoxin IVa almost completely blocked synaptic transmission at all developmental stages tested. The residual evoked IPSC 10 to 20 minutes after toxin application was 3.4 ± 1.6% of the control value at P7–9, 4.5 ± 2.0% at P14–16, and 3.1 ± 1.0% at P21–23 (mean ± SEM; 5, 4, and 5 pairs, respectively; $P < 0.05$). In contrast, 1 µM ω-conotoxin GVIa, a selective blocker of N-type channels, and 500 nM SNX-482, a blocker of R-type channels, had only minimal effects on unitary IPSCs in all age groups (ω-conotoxin GVIa: 86.2 ± 5.9% at P7–9, 93.2 ± 10.8% at P14–16, and 113.3 ± 14.4% at P21–23; SNX-482: 108.4 ± 8.9% at P7–9, 106.8 ± 6.1% at P14–16, and 99.6 ± 14.5% at P21–23; $P > 0.5$; Figure 3-3). These results indicate that transmitter release at cerebellar BC synapses exclusively relies on P/Q-type Ca^{2+} channels throughout the entire developmental period examined, different from the calyx of Held (Iwasaki and Takahashi, 1998) or neocortical pyramidal synapse (Bornschein et al., 2019).

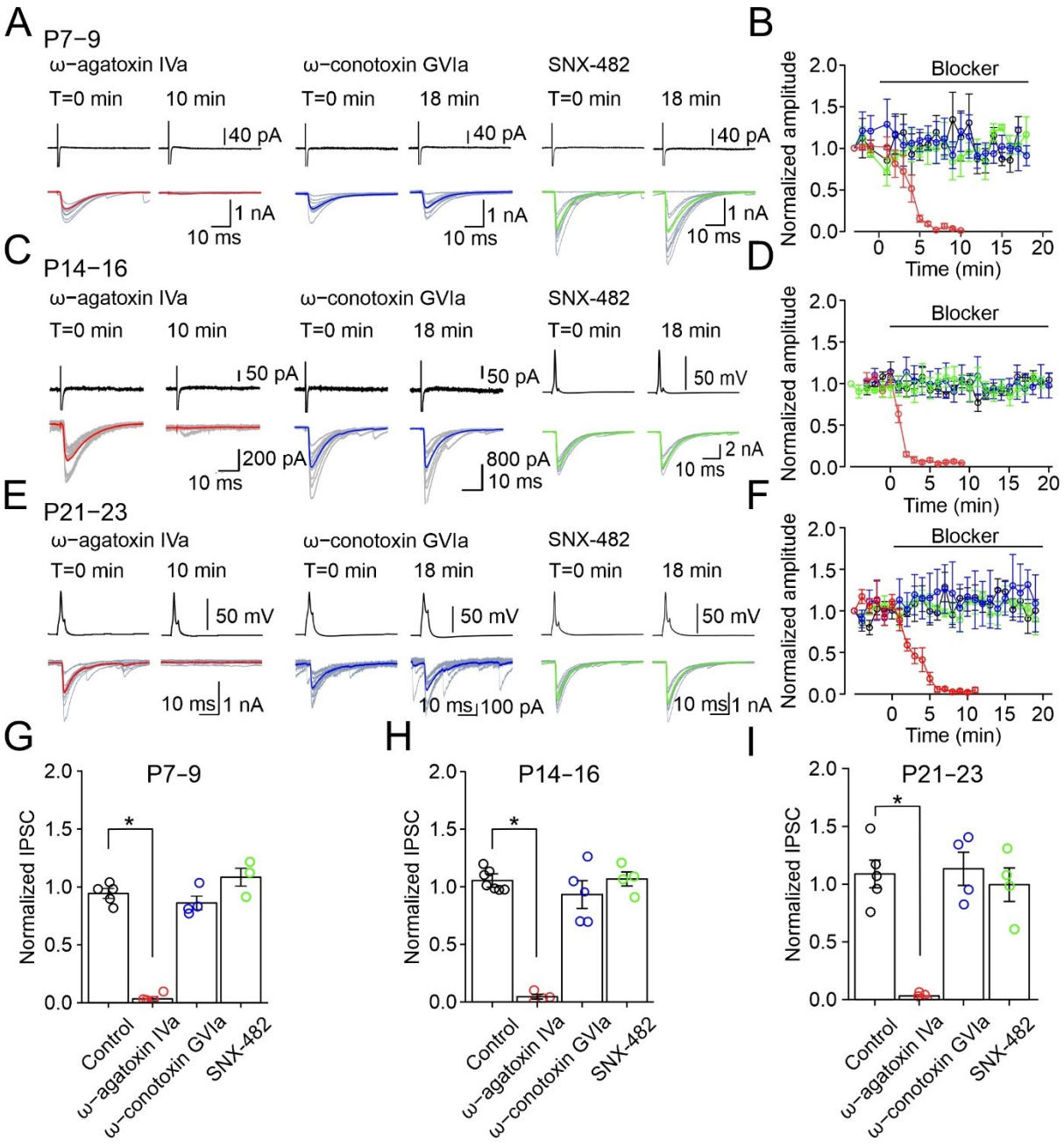

Figure 3-3 Transmitter release constantly relies on P/Q-type Ca^{2+} channels during development

(A) IPSCs in BC–PC pairs before and after application of 1 µM of the selective P/Q-type Ca^{2+} channel blocker ω-agatoxin Iva (left), 1 µM of the selective N-type Ca^{2+} channel blocker ω-conotoxin Iva (middle), and 0.5 µM of the selective R-type Ca^{2+} channel blocker SNX-482 (right) at P7–9 synapses. **(B)** Plot of IPSC peak amplitude, normalized to control value, against experimental time during application of ω-agatoxin IVa (red), ω-conotoxin GVIa (blue), SNX-482 (green), and mock application of control solution (black) at P7–9 synapses. **(C and D)** Same in (A) and (B), but performed at P14–16 synapses. **(E and F)** Same in (A) and (B), but performed at P21–23 synapses. **(G–I)** Summary bar graphs of the effects of Ca^{2+} channel blockers. Circles represent data from individual experiments, and bars indicate mean ± SEM.

3.4 Quantal parameters of synaptic transmission

Early work shows that the amplitude of IPSC undergo substantial reduction during development in rats (Pouzat and Hestrin, 1997). However, little is known about how the quantal parameters change during development. According to the quantal theory of synaptic transmission, the average amplitude of single IPSC is the product of release probability (p_R), the number of functional release sites (N), and the quantal size (Q), given as IPSC = p_R N Q. To determine how quantal parameters change during development, we performed multiple-probability fluctuation analysis of evoked IPSCs (Silver, 2003). The extracellular Ca^{2+} concentration was changed between 0.7 and 10 mM (Figure 3-4A–C). Variance and mean were determined from stationary periods after the Ca^{2+} concentration change, and variance was plotted against mean for individual experiments. In the P21–23 age group, the potassium channel blocker tetraethylammonium (TEA, 1 mM) and 4-aminopyridine (4-AP, 0.05 mM) were added to further enhance release.

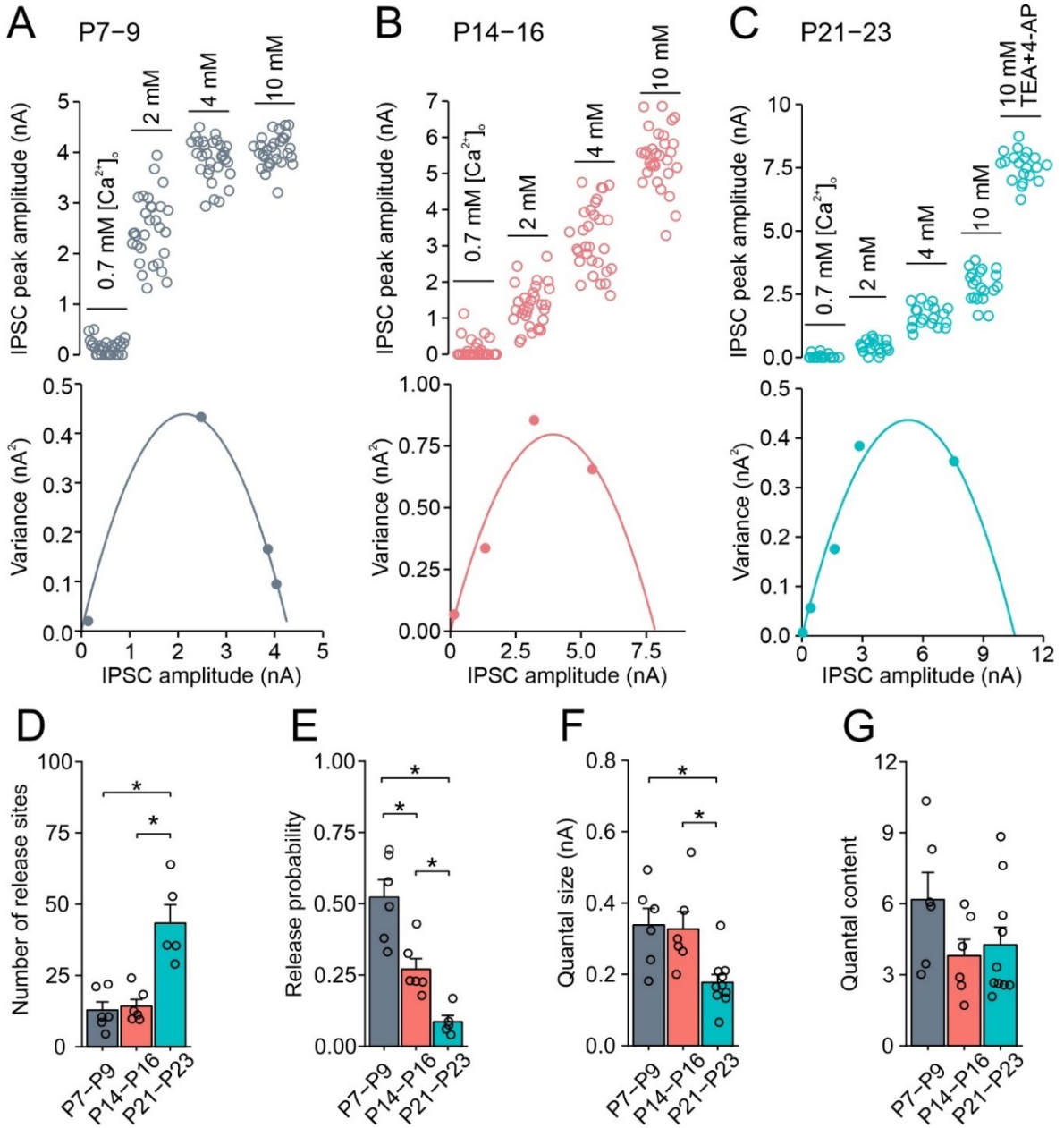

Figure 3-4 Reciprocal increase in number of functional release sites and decrease in release probability during development at BC–PC synapses

(A–C) Example variance-mean measurements of evoked IPSC amplitudes at varying external Ca^{2+} concentrations in BC–PC synapses at P9 (A), P14 (B), and P21 (C). The values for release probability and quantal size were calculated according to the equations $\sigma^2 = I\,q - I^2/N$ and $I = p_R\,N\,q$, with I being the average IPSC amplitude, p_R release probability, N the number of functional release sites, and q quantal size. **(D–G)** Summary bar graphs of number of functional release sites (D), release probability at 2 mM $[Ca^{2+}]_o$ (E), quantal size (F), and quantal content (G). Circles represent data from individual experiments, and bars indicate mean ± SEM.

To first rule out the possibility that the TEA and 4-AP application affected the quantal parameter estimates, we compared the results from variance-mean analysis at P7–9 synapses in the absence and presence of TEA and 4-AP (Figure 3-5A–F). No significant differences were detected, validating the use of these blockers in our analysis ($P > 0.2$).

Variance-mean analysis revealed that release probability at 2 mM extracellular Ca^{2+} decreased from 0.52 ± 0.06 at P7–9 to 0.27 ± 0.04 at P14–16 and 0.09 ± 0.02 at P21–23 (6, 6, and 5 pairs, respectively; $P = 0.0013$; Figure 3-4D). Here, the release probability refers to the averaged vesicle release probability, since there is no significant difference in the failure rate of synaptic transmission (Table 2). Consistent with a reduction of p_R, the Ca^{2+} dependence of transmitter release shifted to higher concentrations during synaptic maturation (Figure 3-6). The number of functional release sites increased in parallel, from 12.8 ± 2.9 at P7–9 to 14.3 ± 2.4 at P14–16 and 43.3 ± 6.5 at P21–23 ($P = 0.0061$; Figure 3-4E). These results suggest a major reorganization of the release mechanism at BC–PC synapses during development. While p_R decreased, N became progressively larger during synaptic maturation. In parallel, the quantal size significantly declined during synaptic maturation (from 338.5 ± 46.6 pA at P7–9 to 327.1 ± 49.0 pA at P14–16 and 177.3 ± 22.2 pA at P21–23; $P = 0.0066$; Figure 3-4F). In contrast, the quantal content ($p_R \times N$) was only slightly, but not significantly reduced, implying that the changes in p_R and N largely compensated each other ($P = 0.13$; Figure 3-4G).

In addition, to exclude the possibility that saturation or desensitization of postsynaptic receptors confounded the variance-mean analysis, additional experiments were performed in the presence of a low-affinity competitive $GABA_A$ receptor antagonist (1,2,5,6-tetrahydropyridin-4-yl) methylphosphinic acid (TPMPA; 300 µM) and a $GABA_B$ receptor antagonist (CGP 55845; 1 µM); CGP 55845 was added to rule out possible effects of TPMPA on presynaptic $GABA_B$ receptors. In the presence of TPMPA and CGP 55845, q significantly decreased ($P = 0.016$), showing the effectiveness of the $GABA_A$ receptor antagonist, whereas p_R and N remained constant (Figure 3-5G–L). Thus, postsynaptic receptor saturation or desensitization are unlikely to affect our measurements. Taken together, these results corroborate our observations of reciprocal changes in p_R and N during development.

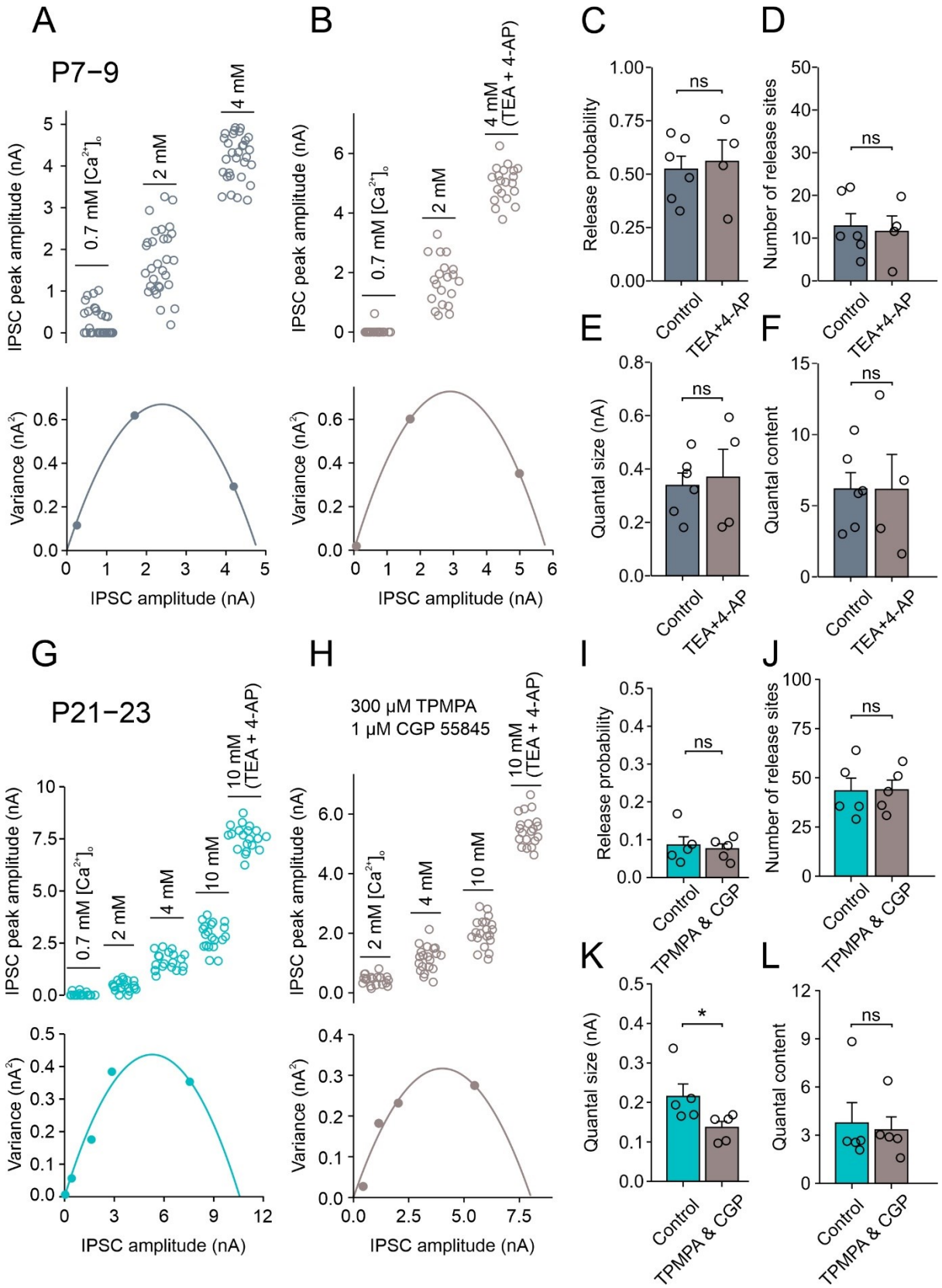

Figure 3-5 Analysis of release probability and number of functional release sites in the presence of K^+ channel blockers and low-affinity competitive antagonist

(A) Example variance-mean measurements of evoked IPSC amplitudes at varying external Ca^{2+} concentrations at a P7–9 synapse. **(B)** Same as (A), but with application of 1 mM TEA and 0.05 mM 4-AP at 4 mM $[Ca^{2+}]_o$ in a

different experiment at P7–9 synapse. **(C–F)** Summary bar graphs of release probability at 2 mM $[Ca^{2+}]_o$ (C), number of functional release sites (D), quantal size (E), and quantal content (F). **(G)** Example variance-mean measurements of evoked IPSC amplitudes at varying external Ca^{2+} concentrations at a P21–23 synapse. **(H)** Same as (G), but with application of 300 µM TPMPA and 1 µM CGP 55845 in a different experiment. **(I–L)** Summary bar graphs of release probability at 2 mM $[Ca^{2+}]_o$ (I), number of functional release sites (J), quantal size (K), and quantal content (L). Circles represent data from individual experiments, and bars indicate mean ± SEM.

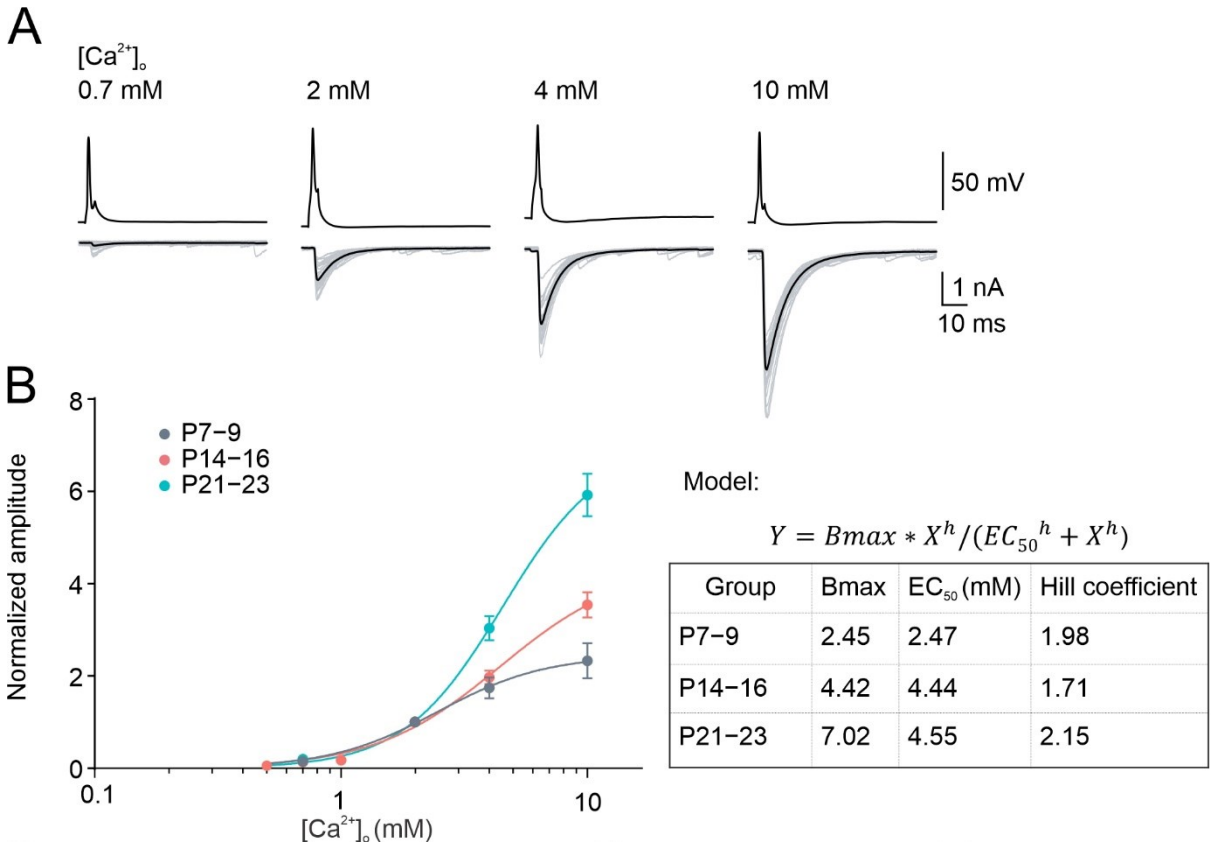

Group	Bmax	EC_{50} (mM)	Hill coefficient
P7–9	2.45	2.47	1.98
P14–16	4.42	4.44	1.71
P21–23	7.02	4.55	2.15

Figure 3-6 Dependence of transmitter release at BC–PC synapse on extracellular Ca^{2+} concentration
(A) Presynaptic AP (top) and evoked IPSCs (bottom) in different extracellular Ca^{2+} concentrations $[Ca^{2+}]_o$. 10 consecutive individual traces (gray) and the corresponding average (black) are shown superimposed. **(B)** Plot of IPSC peak amplitude, normalized to the value at 2 mM $[Ca^{2+}]_o$, against $[Ca^{2+}]_o$ at logarithmic scale, at P7–9 (gray), P14–16 (red), and P21–23 (cyan). Data were fit with a Hill equation. Right table shows the best-fit parameter values of the Hill equation.

3.5 The readily releasable pool

To probe developmental changes in the vesicular pool, we performed cumulative release analysis (Figure 3-7). Synapses were stimulated repetitively, normalized IPSC values were cumulatively plotted against stimulus number, and the size of the readily releasable pool (RRP) was determined by linear regression (train method). As the release probability is low and depression ratio is high in the P21–23 age group, RRP tends to be underestimated (Kaeser and Regeher, 2017) by using the normal $[Ca^{2+}]_o$. Therefore, we performed experiments in high $[Ca^{2+}]_o$ to meet the standard of depression ratio (Neher, 2015). We found that RRP size increased during development, from 37.4 ± 5.3 quanta at P7–9 to 51.6 ± 8.1 quanta at P14–

16 and 72.6 ± 13.1 quanta at P21–23 (P = 0.028; Figure 3-7E). Thus, the vesicular pool size was developmentally upregulated.

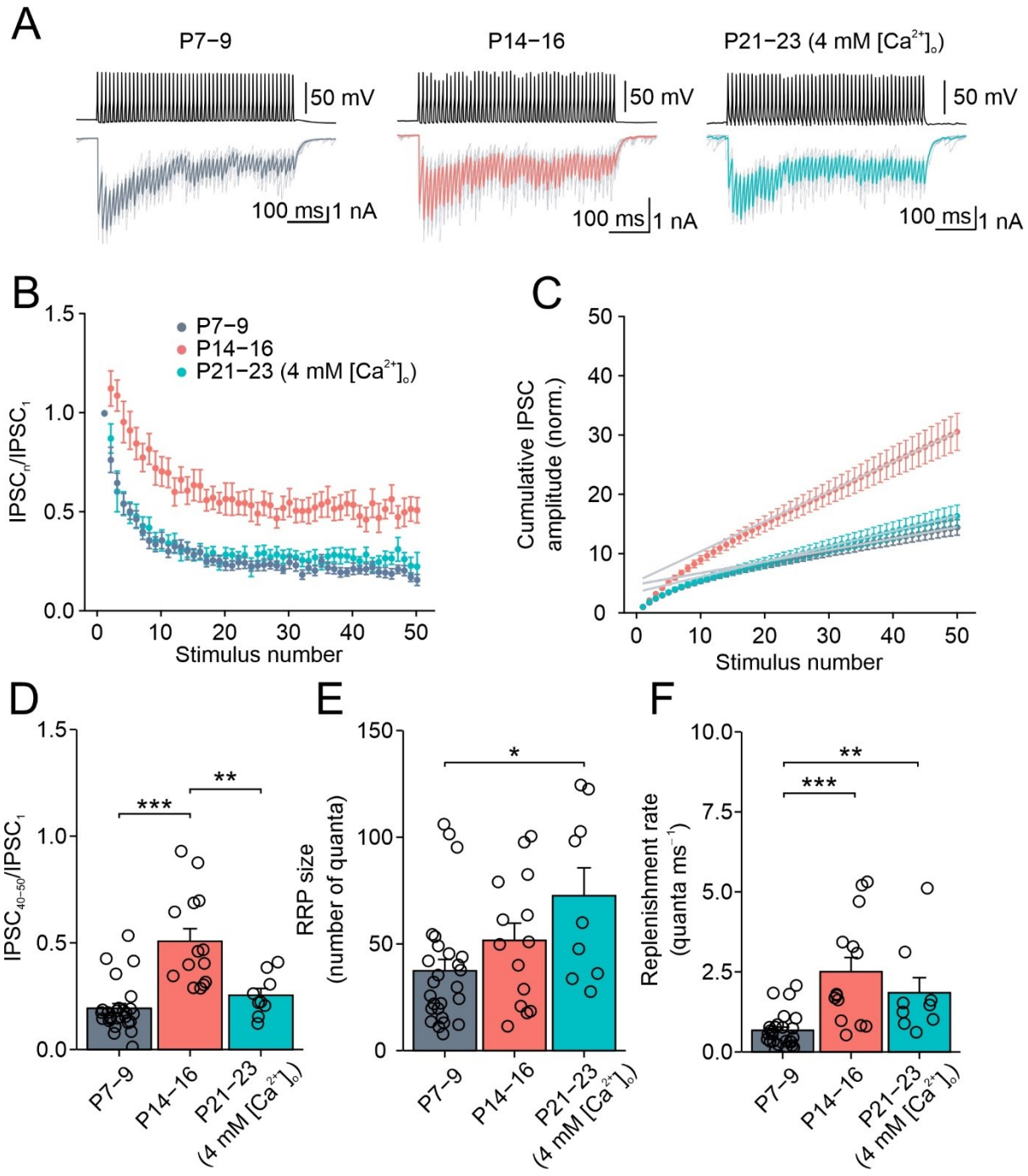

Figure 3-7 Pool size determined by cumulative IPSC analysis

(A) IPSCs evoked by trains of 50 APs at P7–9, P14–16, and P21–23. **(B and C)** Plot of IPSC peak amplitude (B) and cumulative IPSC (C), normalized by $IPSC_1$ and plotted against stimulus number, at P7–9 (gray), P14–16 (red), and P21– 23 (cyan). **(D–F)** Summary bar graphs of multiple-pulse ratio ($IPSC_{40–50}$ / $IPSC_1$, D), readily releasable pool (RRP) size (E), and replenishment rate (F). Data in P21–23 synapses were recorded in 4 mM $[Ca^{2+}]_o$ to increase depression.

3.6 Shortening of presynaptic action potential during development

As variance-mean analysis shows a significant reduction in the release probability during synaptic maturation, we then tried to obtain insight into the mechanism underlying the development change. In the Calyx of Held, the presynaptic AP duration undergoes substantial shortening during development (Nakamura et al., 2015). Therefore, we first analyzed the shape of the presynaptic AP.

A somatic whole-cell recording was obtained from a BC, the neuron was filled with Alexa Fluor 488, and the axon arbor including presynaptic terminals surrounding PC somata was visualized using confocal microscopy (Figure 3-8A). Subsequently, a cell-attached configuration was obtained from a BC presynaptic terminal, and the extracellular AP current were recoded upon somatic stimulation.

We used the peak-to-peak duration as a proximal estimation of half-duration of AP. To confirm this assumption, we performed double-somatic whole cell – cell-attached recordings (Figure 3-8E–G). The intracellular AP (iAP) was measured in whole-cell current-clamp configuration whereas the extracellular AP (eAP) was measured in cell-attached voltage-clamp configuration. eAPs are theoretically believed to be the first derivatives of iAPs under biophysical ideal conditions. However, under actual experimental conditions, eAPs were more likely a mixture of negative iAPs and their derivatives (Sasaki et al., 2011). The results demonstrate a close agreement between half-duration of the action potential (whole-cell, iAP) and peak-to-peak time of the action current (cell-attached, eAP), which is also validated by a previous finding (Rowan et al., 2014).

Analysis of the peak-to-peak duration of the presynaptic action current, revealed a marked change in duration, from 2.24 ± 0.33 ms at P7–9 to 0.99 ± 0.11 ms at P14–16 and 0.59 ± 0.07 ms at P21–23 (5 presynaptic recordings per age group; P = 0.0025; Figure 3-8D). This huge reduction of AP half-duration in presynaptic terminal is more prominently than the reduction in somatic AP half-duration (Table 2), which suggesting that the voltage-gated potassium channel expression is differently regulated between somata and bouton. Thus, the presynaptic AP undergoes substantial shortening during development. Together with the constant reliance of transmitter release on P/Q-type Ca^{2+} channels, these results suggest a reduced efficacy of opening of these channels by the presynaptic AP.

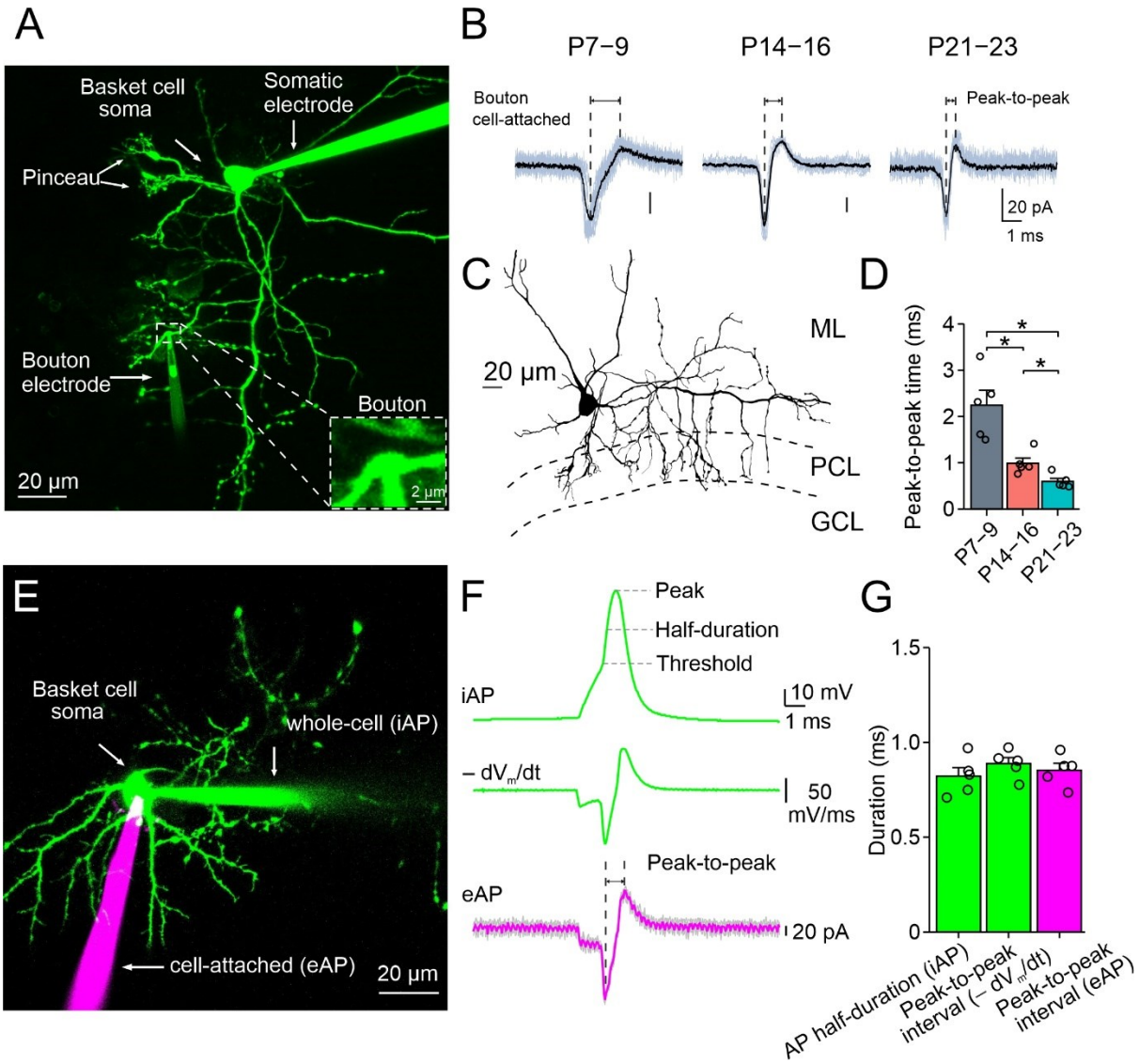

Figure 3-8 Shortening of AP in presynaptic terminal during development

(A) Confocal maximum intensity projection of BC filled with Alexa Fluor 488 during recording through a somatic patch pipette. Somatic recording electrode is located on the top right, presynaptic recording electrode is visible at the bottom. **(B)** Cell-attached voltage-clamp recordings from putative presynaptic terminals. Gray, individual traces; black, average trace. 10 individual traces superimposed. **(C)** Reconstruction of BC after recording. ML, molecular layer; PCL, Purkinje cell layer, GCL, granule cell layer. **(D)** Summary bar graph of AP half-duration measured from presynaptic terminal. Half-duration of the presynaptic AP was quantified as the time difference between negative and positive peaks of presynaptic action current. Data from 5 (P7–9), 5 (P14–16), and 5 (P21–23) bouton recordings. **(E)** Confocal maximum intensity projection of BC filled with Alexa Fluor 488. The intracellular AP (iAP) was measured in whole-cell current-clamp configuration through a patch pipette (shown in green). The extracellular AP (eAP) was measured in cell-attached voltage-clamp configuration through a patch pipette (shown in magenta). **(F)** Top, whole-cell current clamp iAP; center, negative derivative of iAP; bottom, cell-attached voltage-clamp eAP. **(G)** Summary bar graph of AP half-duration measured from different waveforms.

3.7 Decrease in presynaptic peak Ca^{2+} transients

To further test this hypothesis, we measured presynaptic Ca^{2+} transients in BC terminals (Figure 3-9). BCs were filled with Fluo-5F (200 µM) and Alexa Fluor 594 (80 µM), Ca^{2+} transients were evoked by single APs, and ratiometric imaging was performed. Peak amplitudes of Ca^{2+} transients became significantly smaller during development (Figure 3-9C). In parallel, decay time constants became shorter. As parvalbumin has slow binding kinetics, which does not significantly reduce the peak amplitude of Ca^{2+} transient but rather accelerate the decay (Lee et al., 2000; Collin et al., 2005; Müller et al., 2007), these results suggesting that the amplitude reduction was generated by reduced Ca^{2+} inflow rather than increased Ca^{2+} buffering. Consistent with this conclusion, application of K^+ channel blocker (1 mM TEA) significantly increased the peak amplitude of Ca^{2+} transients at P21–23, but not in the P7–9 and the P14–16 age groups (Figure 3-9E). These results provide converging evidence that the efficacy of presynaptic Ca^{2+} channel opening decreases during development.

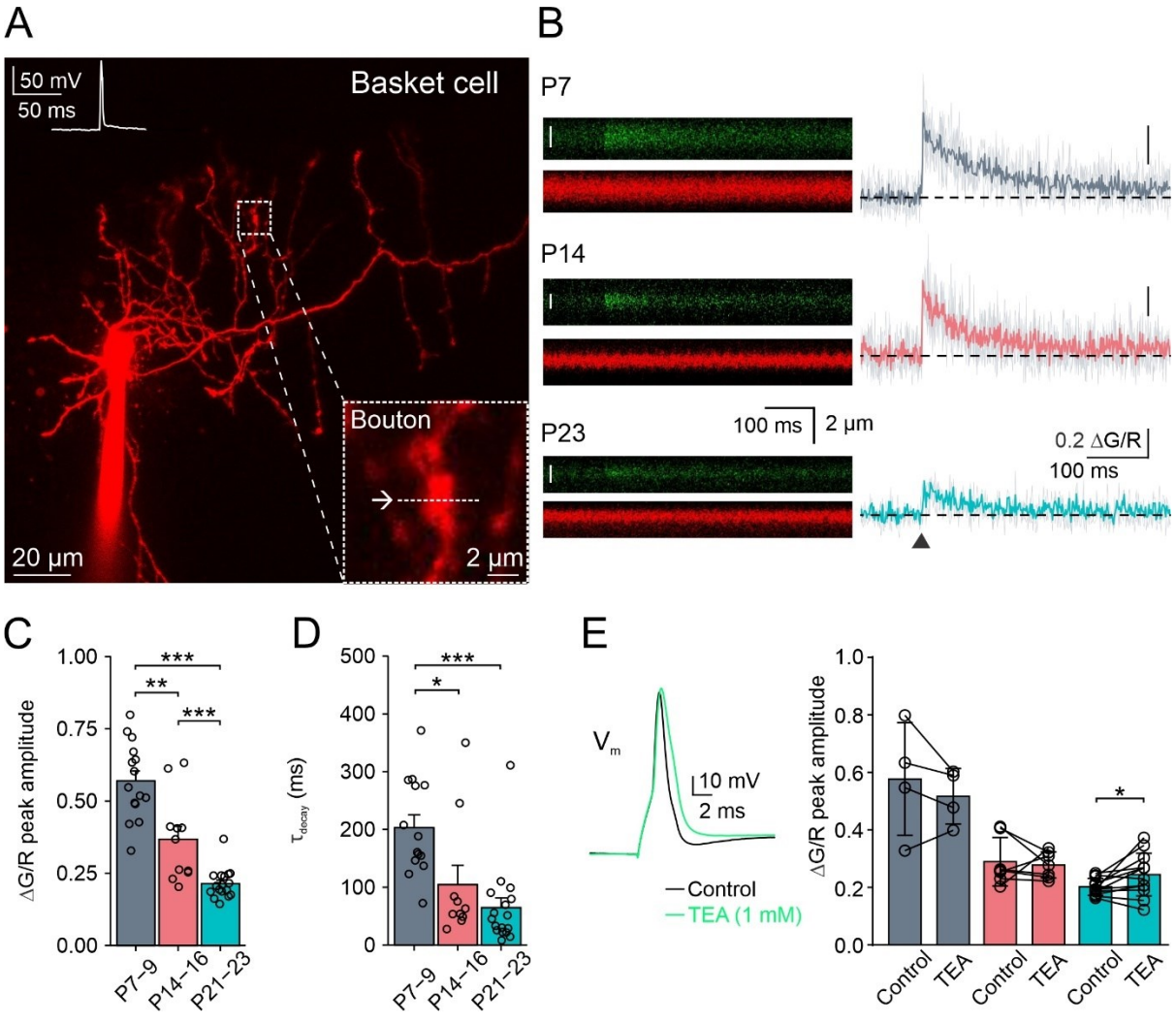

Figure 3-9 Substantial reduction of Ca^{2+} transient in presynaptic terminals during development

(A) Confocal maximum intensity projection of BC filled with Alexa Fluor 594 during recording through a somatic patch pipette. Somatic recording electrode is located on the left. Bouton Ca^{2+} transients were recorded using line scan (dashed line). **(B)** Left: Representative line scans of Fluo-5F (green, 200 µM) and Alexa Fluor 594 (red, 80 µM) fluorescence recorded from three boutons at P7, P14, and P23 following single AP initiation by short

somatic current pulses. Right: Averaged ΔG/R signals (gray, red, and cyan) from 3–5 traces (light gray). White lines indicate the region of interest for fluorescence analysis and arrowhead indicates the time point of somatic stimulation. **(C and D)** Summary bar graphs of ΔG/R peak amplitude (C) and decay time constant (D). Circles indicate data from individual boutons, bars represent mean ± SEM. In total, 43 boutons from 20 BCs were analyzed. **(E)** Left: Somatic AP (V_m) in the absence (black) and presence of 1 mM TEA (green). Right: Summary bar graph of ΔG/R peak amplitude in control and TEA. Circles indicate data from individual BCs, bars represent mean ± SEM, data from the same experiments are connected by lines.

3.8 Reduced coupling distance between Ca^{2+} channels and release sensors

At several excitatory synapses, the coupling between Ca^{2+} channels and release sensors becomes progressively tighter during development (Table 1). However, in all of these cases, reliance on the Ca^{2+} channel subtype changes during maturation, making it difficult to distinguish direct effects of coupling from indirect effects of changes in Ca^{2+} channel subtype. To probe the channel–sensor coupling distance at the BC–PC synapse at different developmental time points, we first infused 10 mM of the slow Ca^{2+} chelator ethylenglycol-bis(β-aminoethylether)-N,N,N’,N’-tetraacetic acid (EGTA) into the presynaptic terminals by pipette perfusion (Figure 3-10). Pipette perfusion provides a quantitatively controlled way of probing the chelator sensitivity, minimizing any confounding effects of wash-in of anions or wash-out of mobile endogenous buffers, such as parvalbumin (PV). In P7–9 synapses, infusion of 10 mM of the slow Ca^{2+} chelator EGTA gradually suppressed synaptic transmission (Figure 3-10B–D). In contrast, at P21–23 synapses, infusion of 10 mM EGTA had only minimal effects ($P = 0.0127$; Figure 3-10 E and F; Table 2). In P14–16 synapses, the effects of EGTA were also minimal, confirming the previous conclusion that transmitter release at this developmental stage is triggered by nanodomain coupling (Figure 3-10E and F; Arai and Jonas, 2014). In contrast to EGTA, infusion of 10 mM of the fast Ca^{2+} chelator ethylenedioxybis-(ophenylenenitrilo)-N,N,N',N'-tetraacetic acid (BAPTA) strongly suppressed synaptic transmission at all developmental stages (Figure 3-10G and H). Taken together, our results suggest developmental tightening of channel–sensor coupling independently of any switch in Ca^{2+} channel subtype.

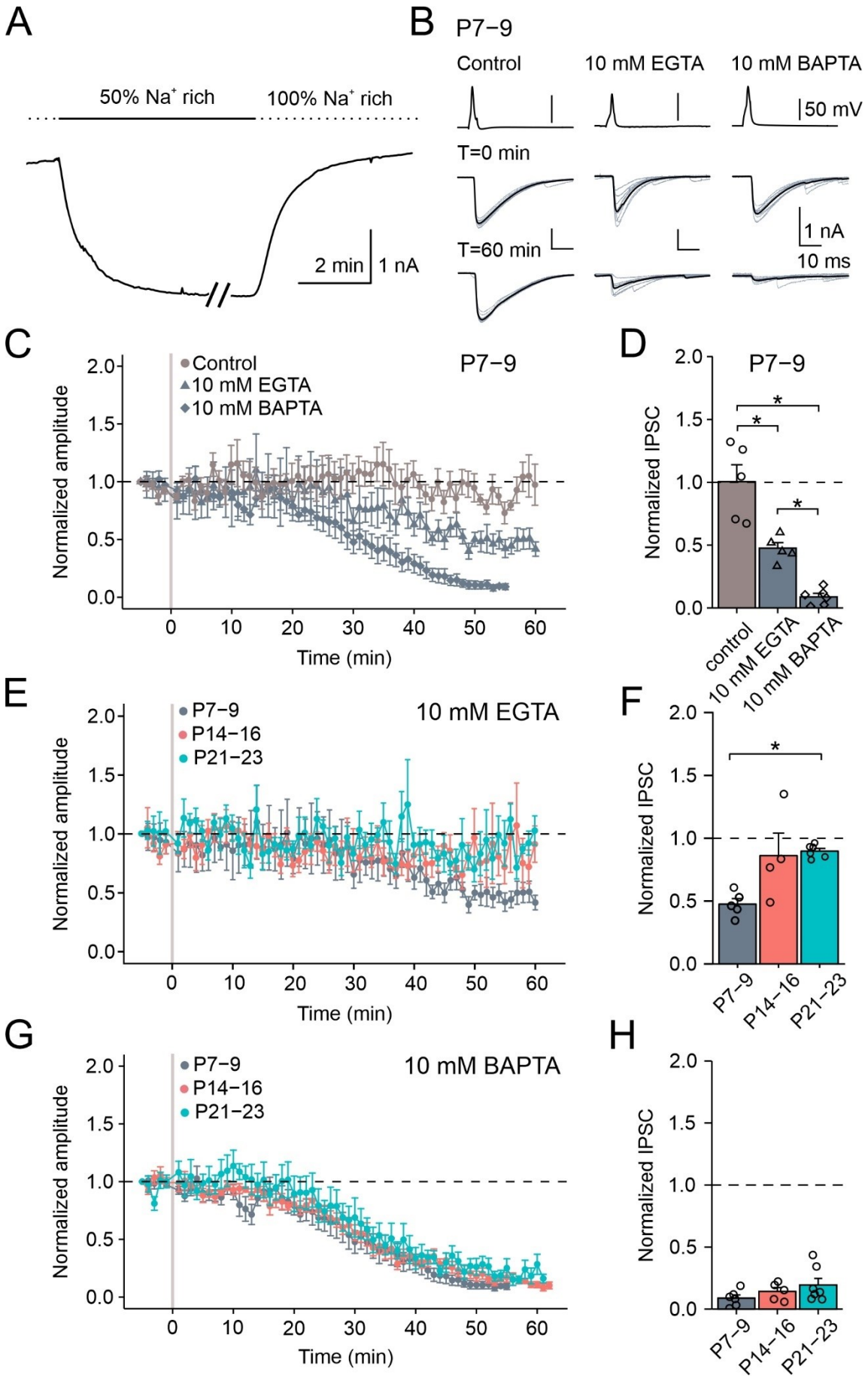
A
50% Na+ rich
100% Na+ rich
2 min
1 nA
B
P7–9
Control
10 mM EGTA
10 mM BAPTA
50 mV
T=0 min
T=60 min
1 nA
10 ms
C
P7–9
Control
10 mM EGTA
10 mM BAPTA
Normalized amplitude
Time (min)
D
P7–9
Normalized IPSC
control
10 mM EGTA
10 mM BAPTA
E
10 mM EGTA
P7–9
P14–16
P21–23
Normalized amplitude
Time (min)
F
Normalized IPSC
P7–9
P14–16
P21–23
G
10 mM BAPTA
P7–9
P14–16
P21–23
Normalized amplitude
Time (min)
H
Normalized IPSC
P7–9
P14–16
P21–23

Figure 3-10 Decrease of exogenous Ca^{2+} chelator sensitivity during development

(A) Speed of solution exchange by pipette perfusion, measured as a change in junction current in an open patch pipette during a solution change from 100% Na^+-rich to 50% Na^+-rich solution and back. **(B)** IPSCs in a BC–PC synapse under control conditions (left), loading presynaptic terminals with 10 mM EGTA (middle), and loading presynaptic terminals with 10 mM BAPTA (right) at P9. Top traces represent APs; center traces represent IPSC amplitudes before loading; bottom traces represent IPSC amplitudes 60 min after loading. **(C)** Plot of IPSC peak amplitude against experimental time for control, 10 mM EGTA, and 10 mM BAPTA loading by pipette perfusion in P7–9 synapses. Gray vertical bar indicates the time when loading starts. **(D)** Summary bar graph of the effects of EGTA and BAPTA on synaptic transmission at P7–9 synapses. **(E and G)** Plots of IPSC peak amplitude against experimental time for 10 mM EGTA and 10 mM BAPTA loading by pipette perfusion in P7–9 (gray), P14–16 (red), and P21–23 synapses (cyan). **(F and H)** Summary bar graphs of the effects of EGTA and BAPTA on synaptic transmission at BC–PC synapses at different developmental stages.

Table 2. Functional properties of cerebellar BC–PC synapses at different developmental stages

Parameter	P7–9	P14–16	P21–23	P[1]
IPSC latency (ms)	0.75 ± 0.03 (23)	0.66 ± 0.04 (21)	0.59 ± 0.03 (23)	0.0079 (0.4010; 0.4595; 0.0041)
IPSC 20–80% rise time (ms)	0.72 ± 0.03 (23)	0.62 ± 0.05 (21)	0.58 ± 0.05 (23)	0.0072 (0.0460; 1.0000; 0.0130)
IPSC peak amplitude (nA)	2.88 ± 0.45 (23)	1.40 ± 0.24 (21)	0.74 ± 0.10 (23)	< 0.0001 (0.0240; 1.0000; < 0.0001)
IPSC half duration (ms)	8.36 ± 0.51 (23)	8.17 ± 0.42 (21)	7.73 ± 0.58 (23)	0.3794 (1.0000; 0.7300; 0.8200)
CV of peak amplitude[2]	0.29 ± 0.04 (23)	0.30 ± 0.03 (21)	0.34 ± 0.03 (23)	0.2438 (1.0000; 1.0000, 0.2500)
CV of latency	0.12 ± 0.01 (23)	0.17 ± 0.02 (21)	0.13 ± 0.01 (23)	0.0960 (0.1100; 0.6000; 0.9500)
IPSC decay time constant	7.41 ± 0.49 (12)	7.83 ± 0.33 (12)	7.29 ± 0.32 (14)	0.4500 (1.0000; 0.8200; 1.0000)
Paired-pulse ratio $IPSC_2$ / $IPSC_1$	0.74 ± 0.04 (20)	1.04 ± 0.06 (19)	1.14 ± 0.10 (20)	0.0002 (0.0010; 1.0000; 0.0003)
Multiple-pulse ratio $IPSC_{10}$ / $IPSC_1$	0.42 ± 0.04 (20)	0.72 ± 0.05 (19)	0.75 ± 0.05 (20)	< 0.0001 (< 0.0001; 1.0000; < 0.0001)
Proportion of failure (%)	1.36 ± 0.62 (20)	1.47 ± 1.05 (20)	1.55 ± 0.69 (20)	0.6686 (1.0000; 1.0000; 1.0000)
Miniature IPSC frequency (Hz)	2.20 ± 0.28 (11)	7.57 ± 0.74 (3)	4.82 ± 0.76 (6)	0.0019 (0.0165; 0.2857; 0.0092)
Miniature IPSC peak amplitude (pA)	250.8 ± 22.0 (11)	121.3 ± 7.1 (3)	88.0 ± 6.8 (6)	0.0005 (0.0165; 0.1429; 0.0005)

AP peak-to-peak duration at BC bouton (ms)	2.24 ± 0.33 (5)	0.99 ± 0.11 (5)	0.59 ± 0.07 (5)	0.0025 (0.0240; 0.0480; 0.0240)
AP half-duration at BC soma (ms)	1.11 ± 0.05 (15)	0.78 ± 0.03 (15)	0.75 ± 0.02 (15)	< 0.0001 (0.0001; 1.0000; < 0.0001)
IPSC amplitude in 10 mM EGTA (% of control)	47.6 ± 4.4 (5)	86.2 ± 18.0 (4)	89.7 ± 2.1 (6)	0.0127 (0.1900; 1.0000; 0.0130)
IPSC amplitude in 10 mM BAPTA (% of control)	8.8 ± 2.6 (6)	14.2 ± 3.2 (5)	19.5 ± 5.3 (7)	0.2606 (0.9900; 1.0000; 0.4100)
Release probability at 2 mM $[Ca^{2+}]_o$	0.52 ± 0.06 (6)	0.27 ± 0.04 (6)	0.09 ± 0.02 (5)	0.0013 (0.0260; 0.0130; 0.0130)
Number of functional release sites	12.83 ± 2.90 (6)	14.26 ± 2.37 (6)	43.34 ± 6.47 (5)	0.0061 (1.0000; 0.0130; 0.0130)
Quantal size (pA)	338.5 ± 46.6 (6)	327.1 ± 49.0 (6)	177.3 ± 22.2 (10)	0.0066 (1.0000; 0.0220; 0.0220)
Quantal content	6.18 ± 1.14 (6)	3.80 ± 0.69 (6)	4.26 ± 0.75 (10)	0.1315 (0.2800; 1.0000; 0.2800)
Time course of release, latency (ms)	1.24 ± 0.08 (10)	1.01 ± 0.03 (10)	0.91 ± 0.05 (10)	0.0064 (0.0560; 0.5480; 0.0190)
Time course of release, decay τ (ms)	0.88 ± 0.06 (10)	0.47 ± 0.05 (10)	0.37 ± 0.02 (10)	< 0.0001 (0.0010; 0.1573; < 0.0001)
Number of vesicles in the readily releasable pool per connection	37.41 ± 5.31 (26)	51.59 ± 8.10 (14)	72.55 ± 13.12 (9)	0.0280 (0.4870; 0.6730; 0.0270)
ΔG/R peak amplitude	0.57 ± 0.03 (15)	0.37 ± 0.04 (11)	0.21 ± 0.01 (17)	< 0.0001 (0.0031; 0.0006; < 0.0001)
ΔG/R decay time constant (ms)	203 ± 22 (14)	104 ± 34 (10)	65 ± 17 (17)	0.0001 (0.018; 0.6130; < 0.0001)

Mean ± SEM (number of experiments in parenthesis).

[1] P values outside the parenthesis indicate results from Kruskal-Wallis test. P values inside the parenthesis indicate results from Wilcoxon-Mann-Whitney test with Bonferroni correction. The order of pairwise comparisons is P7–9 vs. P14–16; P14–16 vs. P21–23; and P7–9 vs. P21–23, respectively.

[2] As the quantal content is constant, the CV of IPSC peak amplitude would be expected to be approximately constant.

Chapter 4. Structural characterization of BC–PC synapse during development

We next attempted to obtain insight into the mechanisms underlying changes in the number of functional release sites, N. Although the functional release site is a widely used concept, the structural correlate remains elusive (Pulido and Marty, 2017). To examine the structural properties of BC–PC synapses during synaptic maturation, we combined light microscopy (LM) and EM analysis. Analysis was performed at P7–9, P14–16, and P21–23, developmental time points identical to those used in our biophysical experiments.

4.1 The number of bouton measurements by LM

We first determined the number of boutons per connection, using a triple labeling procedure (Figure 4-1). BCs were filled with biocytin via whole-cell recording and labeled with Alexa Fluor-conjugated streptavidin (5, 5, and 6 biocytin-filled BCs, respectively). Synaptic contacts were identified using antibodies against vesicular GABA transporters (VGAT) and postsynaptic $GABA_A$ receptor subunits ($GABA_A\alpha1$). LM analysis including both somata and proximal dendrites of PCs revealed that the number of boutons per connection increased from 6.55 ± 0.64 at P7–9 to 8.40 ± 1.09 at P14–16, and 9.00 ± 0.95 at P21–23 (11, 10, and 10 PCs; P = 0.1126). Thus, the BC–PC synapse is a multi-bouton connection throughout development (Figure 4-1D).

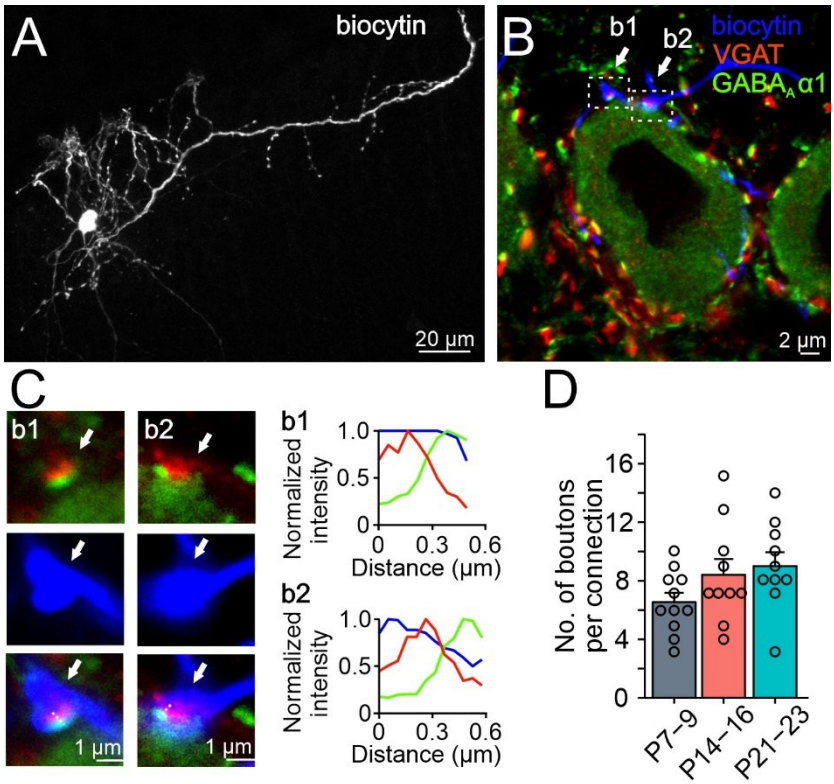

Figure 4-1 The number of boutons per connection measurement

(A) Confocal maximum intensity projection of BC at P14 filled with biocytin during recording and labeled using Alexa Fluor-conjugated streptavidin. **(B)** Example confocal fluorescence micrographs of biocytin-labeled BC

terminals and immunolabeling for VGAT and $GABA_A$ α1 subunit in a BC–PC synapse at P14. White arrows indicate two boutons. Boutons were identified by double labeling with VGAT antibody and fine alignment with $GABA_A$ α1 subunits in the perisomatic PC region. Individual fluorescent signals were converted into red, green, and blue pseudocolors to improve clarity. **(C)** Zoomed images from the rectangular boxes in panel B. Dashed lines indicate pixels used for intensity profile plots (right). **(D)** Summary bar graph of the number of boutons emerging from a single BC and terminating in the perisomatic area of a single PC. Circles represent data from individual boutons. Bars indicate mean ± SEM.

4.2 The number of AZs per bouton and the number of docked vesicles per AZ measurements by serial-section EM

Next, we determined the number of AZs per bouton, using serial-section EM on perfusion-fixed brain samples (Figure 4-2A–C). BC–PC synapses were unequivocally identified, based on their morphological characteristics and location. Evaluation of the AZ number in fully reconstructed boutons revealed 1.87 ± 0.22 AZs per bouton at P7–9, 2.00 ± 0.33 AZs per bouton at P14–16, and 2.16 ± 0.19 AZs per bouton at P21–23 (15, 10, and 19 fully reconstructed boutons; P = 0.5371). Thus, the majority of GABAergic boutons contained one to three AZs, independently of the developmental stage (Table 3).

Finally, we analyzed the nanoscopic structure of the AZs in more detail (Figure 4-2D–H). To accurately determine the number of docked vesicles, we performed cryofixation of acute brain slices, which avoids confounding effects of chemical fixation, and reconstructed entire AZs using serial section EM. The number of docked vesicles per AZ substantially increased during development, from 10.2 ± 1.4 at P7–9 to 14.1 ± 2.9 at P14–16, and 25.1 ± 2.0 at P21–23 (16, 10, and 14 AZs). The AZ area also significantly increased, from 0.15 ± 0.02 μm^2 at P7–9 to 0.17 ± 0.04 μm^2 at P14–16, and 0.21 ± 0.02 μm^2 at P21–23 (9, 8, and 22 AZs; P = 0.0474). In parallel, the density of docked vesicles significantly increased from 48.0 ± 5.1 μm^{-2} at P7–9 to 64.9 ± 10.1 μm^{-2} at P14–16, and 90.9 ± 10.0 μm^{-2} at P21–23 (P = 0.0082). This indicates that the increase in the total number of docked vesicles per AZ is caused by a combination of both increase in AZ area and increase in vesicle density. Finally, we found that the diameter of synaptic vesicles decreased slightly, but significantly, during synaptic maturation (Figure 4-2H), which may explain the declining quantal size (Table 2).

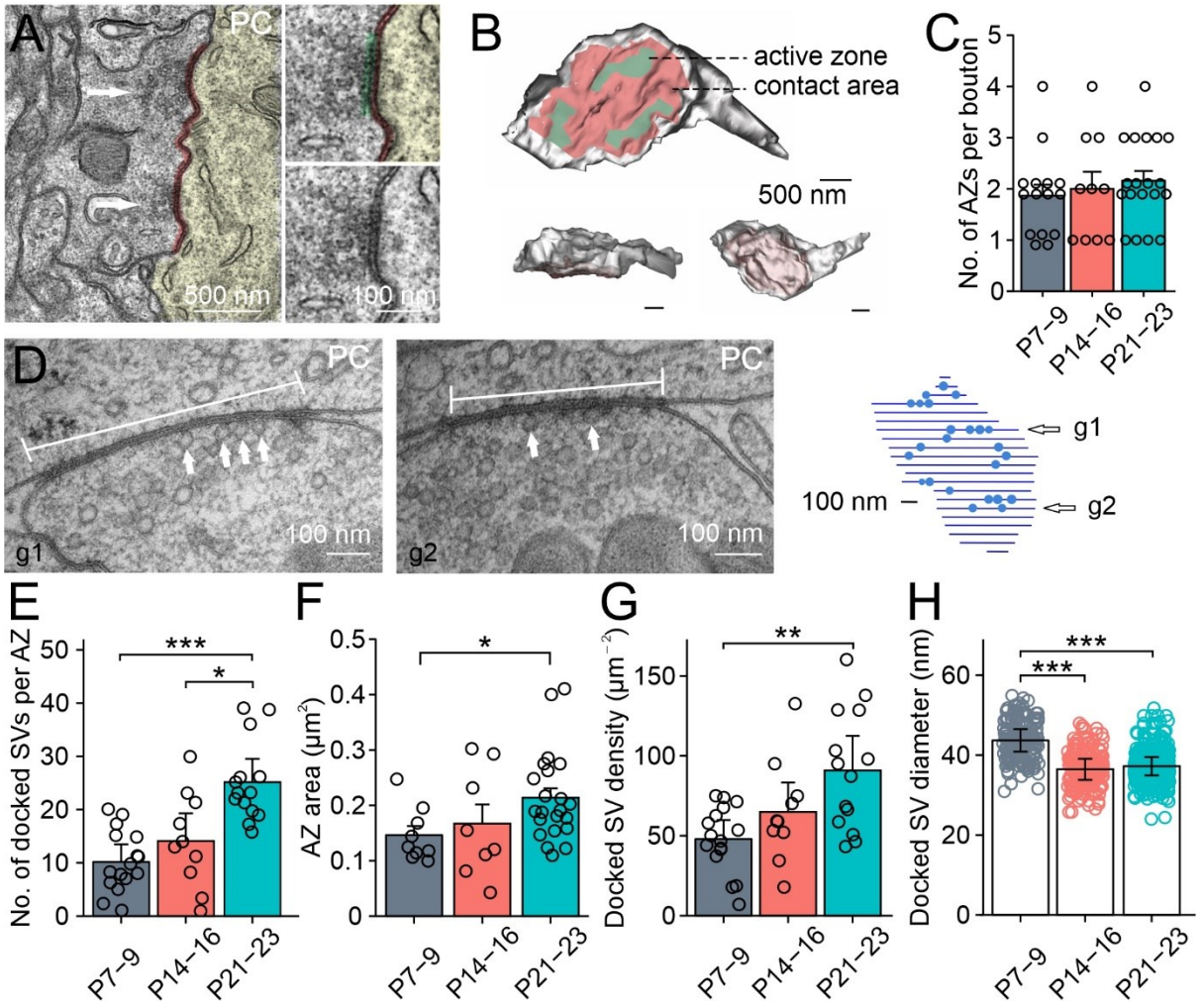

Figure 4-2 The number of AZs per bouton and the number of docked vesicles per AZ measurement
(A) Transmission electron micrograph of a BC bouton at P14. White arrows indicate AZs. **(B)** 3D reconstruction of a BC bouton at P9 shown in gray. The contact area between BC terminal and PC soma is depicted in pink, and the AZs are shown in green. **(C)** Summary bar graph of the number of AZ pers bouton. **(D)** Transmission electron micrographs (left) and corresponding reconstruction of synaptic vesicle distribution from serial sections (right, blue circles) of an AZ of a BC– PC synapse at P21. Sections (left) correspond to arrows g1 and g2 (right). **(E–H)** Summary bar graphs of number of docked synaptic vesicles per AZ (E), AZ area (F), docked synaptic vesicle density (G), and docked synaptic vesicle diameter (H) at P7–9, P14–16, and P21–23 respectively. Circles represent data from individual AZs, or vesicles. Bars indicate mean ± SEM.

4.3 Distribution property analysis of docked synaptic vesicles in AZs

To determine the distribution of docked vesicles within AZs, we analyzed nearest neighbor distance (NND) distributions of docked synaptic vesicles, and compared them to simulated random distributions (Figure 4-3A–C). For random positioning of vesicles, spheres were distributed within single sections with 30 nm minimal distance, which is close to real experiments (AZ reconstruction from serial sections). NND analysis revealed that vesicles were non-randomly distributed at all three developmental stages ($P < 0.001$; Figure 4-3A–D).

To distinguish between clustering and dispersion, we performed Ripley's H(r) function analysis (Figure 4-3 E and F). At both P7–9 and P14–16, maximal H(r) values were not significantly different in measured and randomized data (15 and 9 AZs; P = 0.39 and 0.59, respectively), and the proportion of individual AZs with significant maximal H(r) was small (13.3% for P7–9 and 22.2% for P14–16). In contrast, at P21–23 synapses, maximal H(r) values were significantly higher than in randomized data (15 AZs; P = 0.04), and the proportion of individual AZs with significant vesicle clustering was much larger (60.0%; P < 0.05; Figure 4-3 F). These results suggest that the distribution of docked synaptic vesicles at AZs changes from a more random to a more clustered configuration during development (Figure 4-3 E–G).

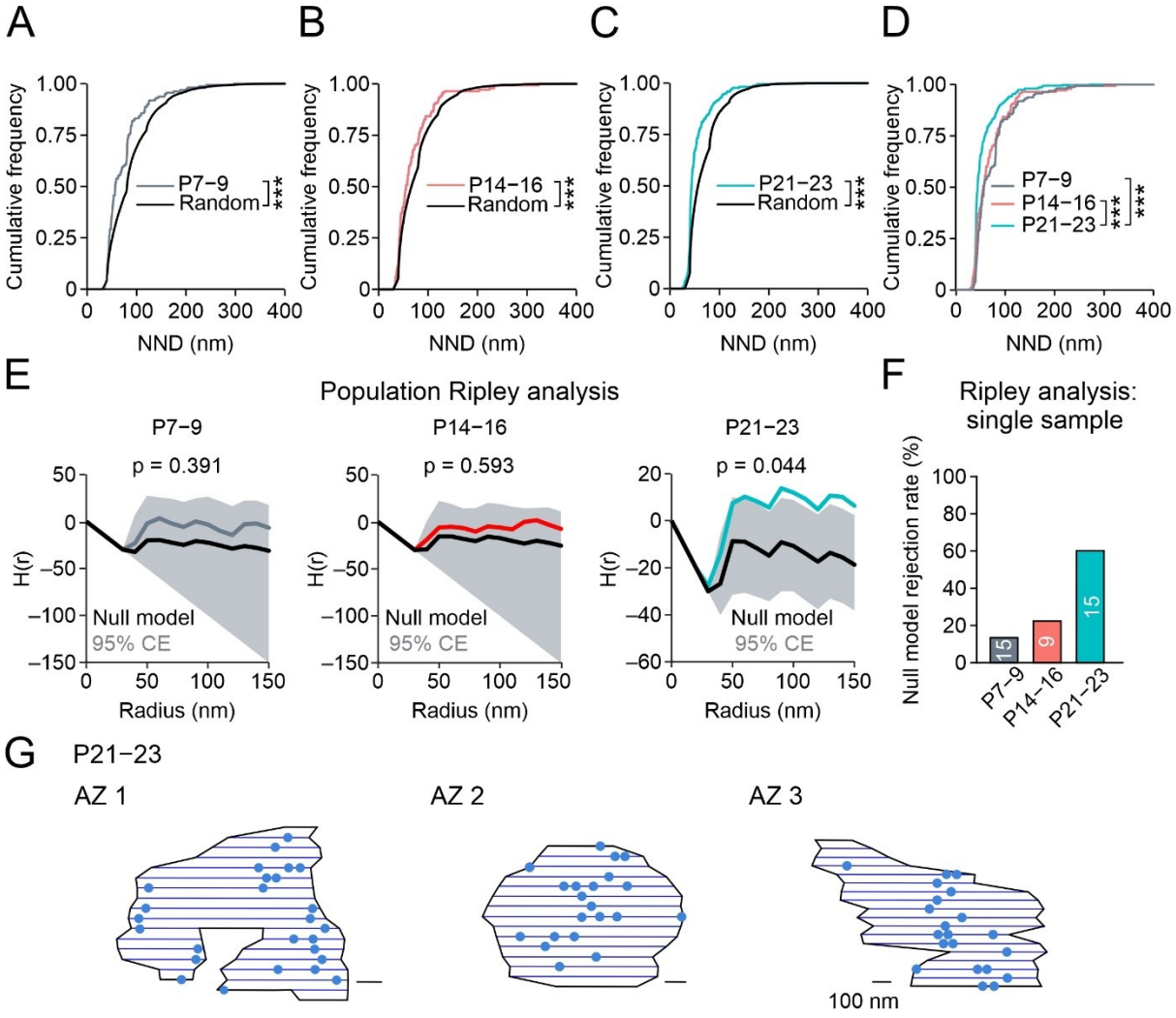

Figure 4-3 The NND analysis and Ripley's analysis of docked synaptic vesicles

(A–C) Cumulative distribution of NND of docked vesicles for experimental data (gray, red, and cyan curves), compared with a null model in which the same numbers of docked vesicles were distributed within single sections with 30 nm minimal distance 100 times. The distances between docked vesicles were calculated using their centers as reference points. **(D)** Overlay of cumulative distributions of NND for P7–9, P14–16, and P21–23 age groups. **(E)** Ripley H-function analysis of docked vesicle distribution in individual AZs for P7–9 (left), P14–16 (center) and P21–23 age groups (right) AZs. Gray, red, and cyan curves represent the edge-corrected H(r) function for 15, 9, and 15 AZs, respectively. The black line represents the mean H(r) function calculated from

100 null model point pattern simulations from each AZ. The gray shaded area represents the 95% confidence envelope (CE). Population P value was calculated using a maximum difference test. **(F)** Ripley H-function analysis of docked vesicle distribution in individual AZs revealed that the null model was rejected (maximum difference test) for 13.3% of P7–9, 22.2% of P14–16, and 60.0% of P21–23 AZs. **(G)** Three AZ reconstructions of docked synaptic vesicles (blue dots) from serial sections (blue lines) at P21–23, suggesting that vesicles form clusters within AZs (black polygons).

4.4 The Ca channel clustering analysis

To determine the coupling nanotopography, we analyzed the distribution of presynaptic Ca^{2+} channels by means of FRL, a diffusion-free method with single- molecule resolution and unique sensitivity. BC–PC synapses were ideal for this analysis, because transmitter release was exclusively mediated by P/Q-type Ca^{2+} channels, allowing us to quantitatively determine presynaptic Ca^{2+} channel numbers by immunolabeling with $Ca_v2.1$ α1A-specific antibodies. Correlated immunolabeling and Ca^{2+} current recording (Li et al., 2007) revealed that the antibody labeling efficiency was 77.6% (Methods), showing that a major fraction of presynaptic Ca^{2+} channels can be detected under the conditions applied. Immunosignals were almost absent in $Ca_v2.1$ $\alpha1A^{-/-}$ mice, validating the specificity of the antibody (Figure 4-4).

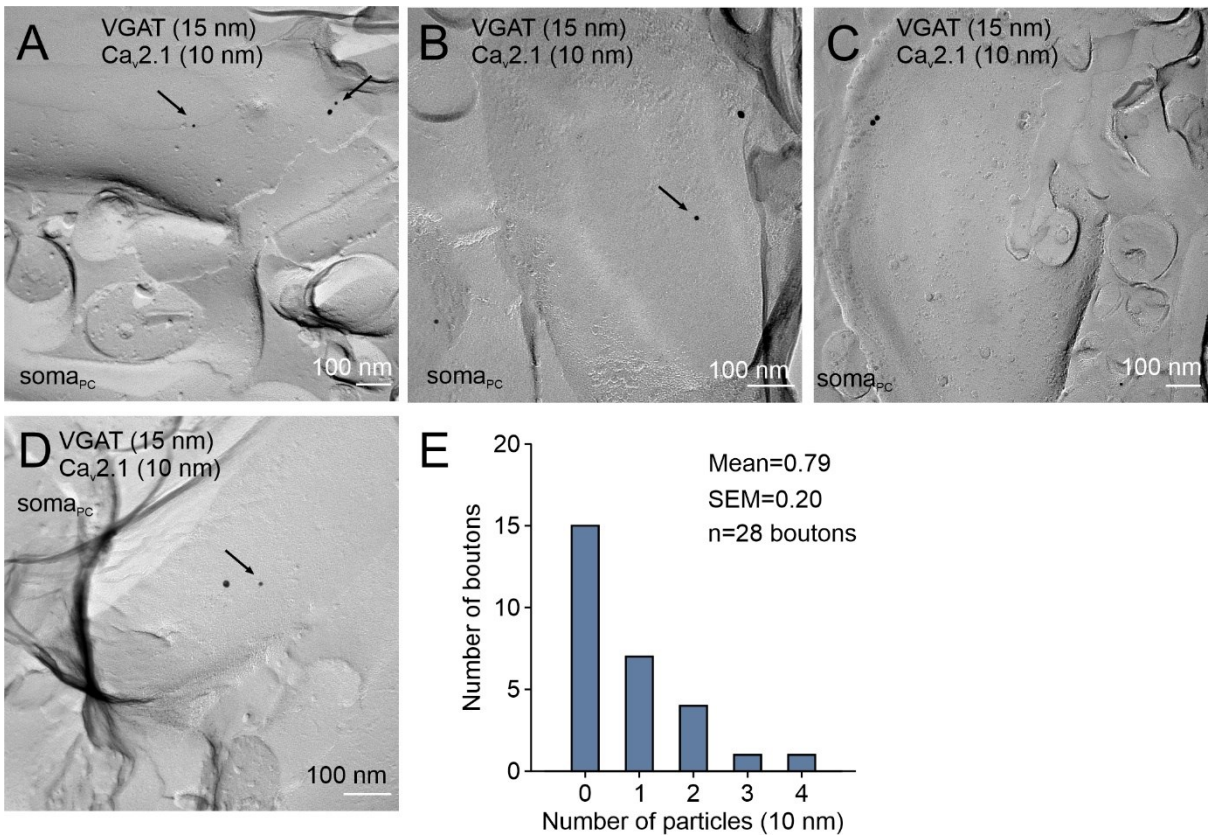

Figure 4-4 Specificity of the $Ca_v2.1$ antibody in FRL at cerebellar BC terminal from $Ca_v2.1$ knockout mice ($Ca_v2.1$-α1A$^{-/-}$)

(A–D) Representative images on FRL of presynaptic Ca^{2+} channels at boutons from $Ca_v2.1$ knockout tissue samples. 15-nm gold particles represent VGAT immunoreactivity, 10-nm gold particles label presynaptic $Ca_v2.1$

Ca^{2+} channels. Black arrows indicate $Ca_V2.1$ gold particles. **(E)** Distribution histogram for the number of $Ca_V2.1$ gold particles per bouton. 28 boutons from two $Ca_V2.1$-α1A$^{-/-}$ mice at P14 were analyzed.

GABAergic synapses were reliably identified by immunolabeling for VGAT, which was detected, albeit with low density, in the plasma membrane of GABAergic, but not glutamatergic terminals (Figure 4-5). This is particularly important early in development, when glutamatergic axons occasionally form synapses with PC somata (Ichikawa et al., 2011). For the identification and reliable delineation of AZs, we applied antibodies against the AZ marker proteins Rab3a-interacting molecule (RIM), E-, L-, K-, and Srich protein (ELKS), and neurexin in a mix (Methods). AZs were delineated drawing a polygon around the outermost immunoparticles for both $Ca_V2.1$ and the AZ marker proteins (Figure 4-5).

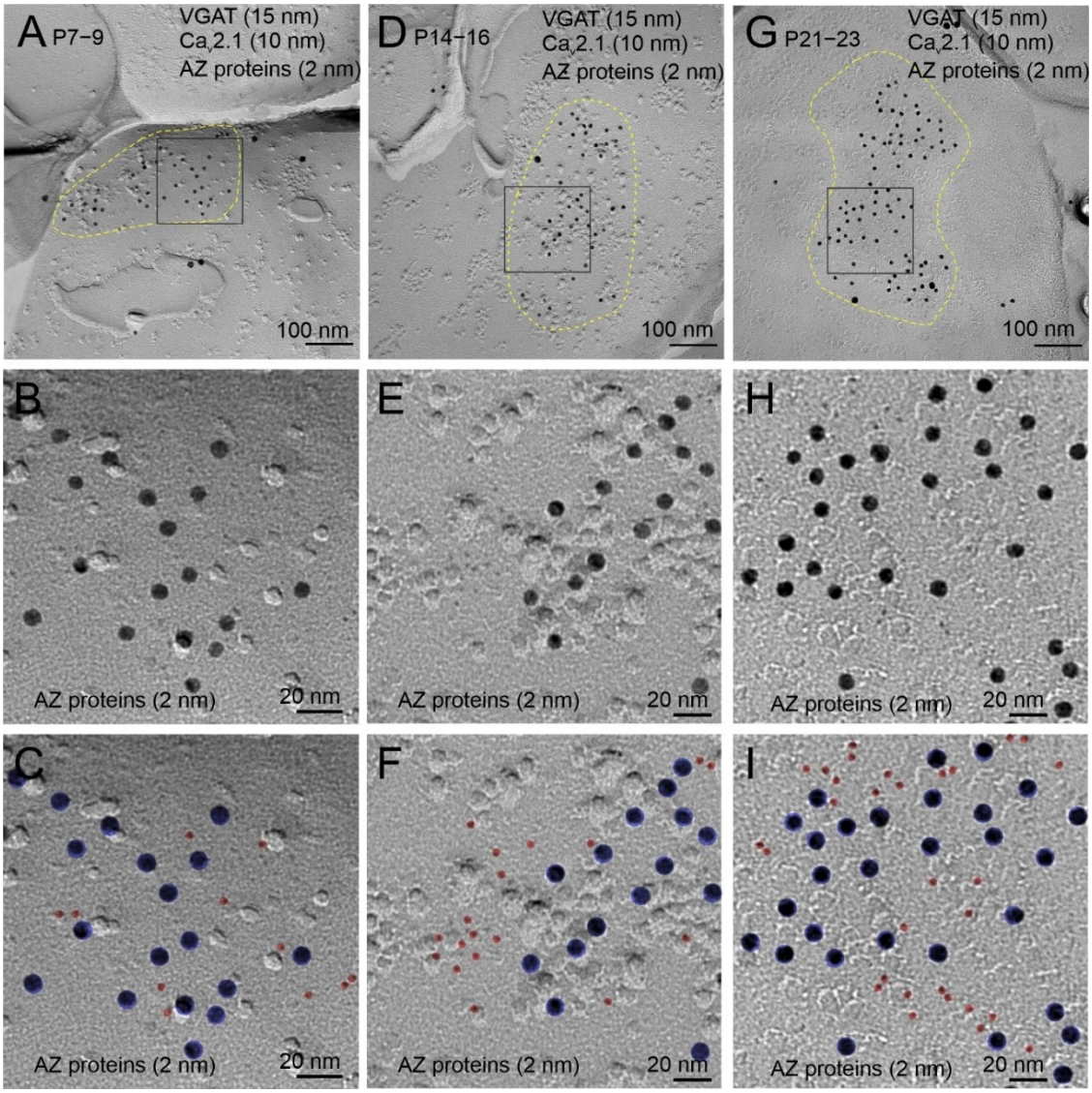

Figure 4-5 AZ demarcation and AZ protein visualization

(A) FRL of presynaptic Ca^{2+} channels at AZs from a representative synapse from the P7–9 age group. 15-nm gold particles represent VGAT immunoreactivity, 10-nm gold particles label presynaptic $Ca_V2.1$ Ca^{2+} channels. **(B)** Zoomed image from the black rectangular box in (A). Note that the 2-nm gold particles represent AZ proteins

RIM, ELKS, and neurexin. **(C)** 2-nm gold particles were overlaid by red dots, and 10-nm gold particles were overlaid by purple circles. **(D–F)** Same as in (A–C), but for an AZ in the P14–16 age group. **(G–I)** Same as in (A–C), but for an AZ in the P21–23 age group.

FRL analysis revealed that the number of particles per AZ significantly increased during maturation (Figure 4-6D). In parallel, the AZ area increased as well (Figure 4-6E), resulting in similar particle densities throughout development (Figure 4-6F). These results reveal a largely constant Ca^{2+} channel density in AZs of GABAergic BC–PC synapses.

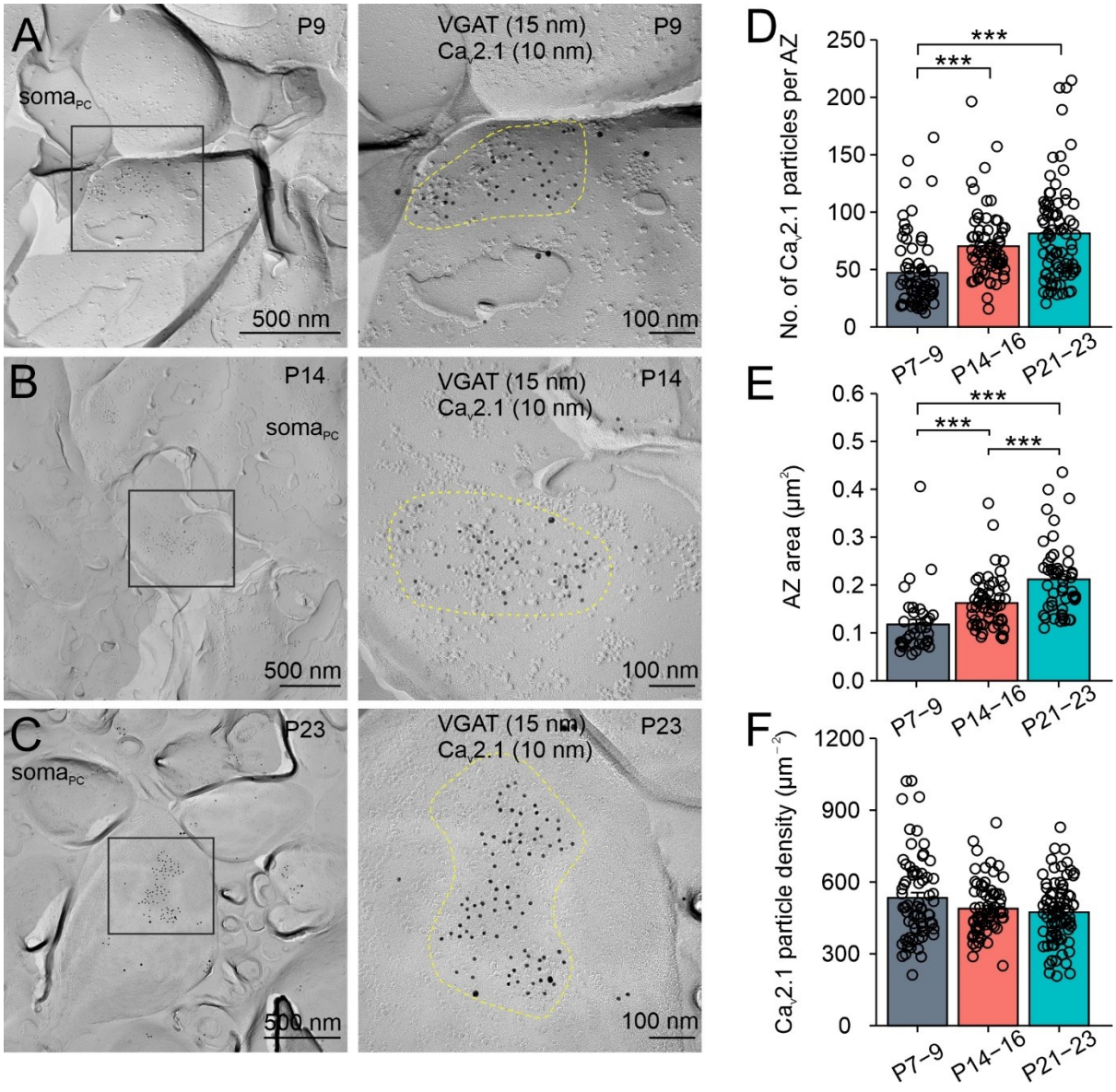

Figure 4-6 $Ca_V2.1$ particle quantification in AZs of BC terminals by FRL

(A–C) FRL of presynaptic Ca^{2+} channels in AZs at P9 (A), P14 (B), and P23 (C), respectively. 15-nm gold particles represent VGAT immunoreactivity, 10-nm gold particles label presynaptic $Ca_V2.1$ Ca^{2+} channels. BC terminals were identified by location near PC soma and VGAT expression. Putative AZ boundaries are indicated by yellow dashed lines. Right panels, zoomed images from the black rectangular boxes in left panels. **(D–F)** Summary bar graphs of number of $Ca_V2.1$ particles per AZ (D), putative AZ area (E), and corresponding Ca^{2+} channel density in

AZs (F). 10-nm gold particle labeling patterns suggest that presynaptic $Ca_v2.1$ Ca^{2+} channels form nanoclusters in presynaptic AZs. Circles represent data from individual AZs, bars indicate mean ± SEM.

To determine the distribution of Ca^{2+} channels within AZs, we analyzed NND distributions of $Ca_v2.1$ particles, and compared them to simulated random distributions (Figure 4-7A–C). The measured NND was significantly smaller than the corresponding simulated value, suggesting clustering of the channels ($P < 0.001$). To further evaluate this, we performed Ripley's H(r) function analysis (Figure 4-7D and E). Population analysis revealed a prominent positive peak and a significant difference from the null model for all developmental stages (67, 69, and 81 AZs; $P = 0.007$, 0.001, and 0.002, respectively). Analysis of null model rejection rate in individual AZs corroborated this conclusion (rejection for > 80% of AZs at three developmental stages; $P < 0.05$). Thus, presynaptic Ca^{2+} channels in BC–PC synapses were significantly clustered at all developmental time points.

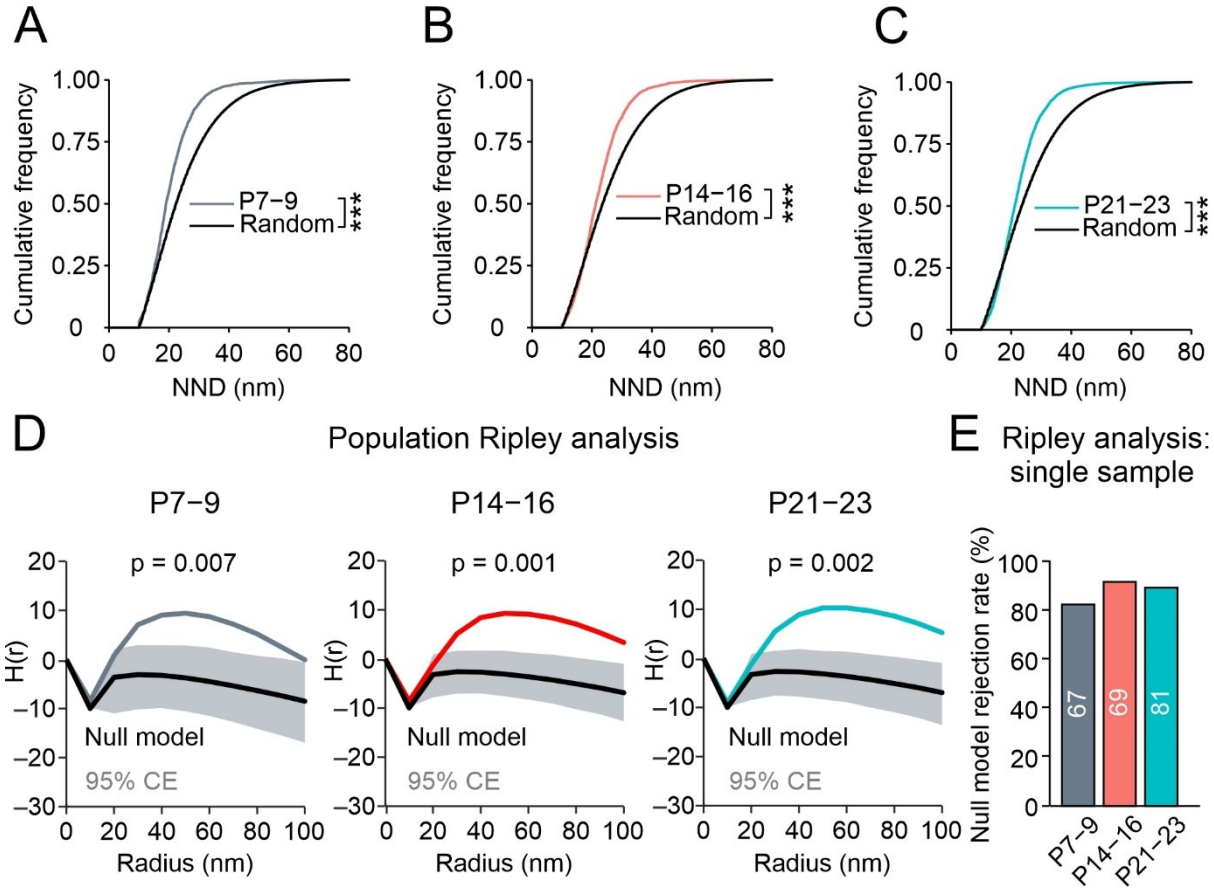

Figure 4-7 The NND analysis and Ripley's analysis for $Ca_v2.1$ particles

(A–C) Cumulative distribution of NNDs for experimental data (gray, red, and cyan curves), compared with a model in which the same numbers of channels were distributed on the same AZ area with random localization for P7–9 (A), P14–16 (B), and P21–23 age groups (C). The random distributions were generated by first counting the number of $Ca_v2.1$ particles in each AZ. Then the same numbers of particles were randomly distributed with an exclusion zone of 10 nm around each particle to account for steric hindrance within each AZ 100 times. **(D)** Ripley H-function analysis of $Ca_v2.1$ gold particles distribution across the population of P7–9 (left), P14–16 (center), and P21–23 AZs (right). Gray, red, and cyan curves represent the edge-corrected H(r) function for 67,

69, and 81 AZs, respectively. The black line represents the mean H(r) function calculated from 100 null model point pattern simulations from each AZ. The gray shaded area represents the 95% confidence envelope (CE). Population P value was calculated using a maximum difference test. **(E)** Ripley H-function analysis of $Ca_V2.1$ gold particles distribution in individual AZs revealed that the null model was rejected (maximum difference test) for 82.1% of P7– 9, 91.3% of P14–16, and 88.9% of P21–23 AZs.

To determine the number of Ca^{2+} channel clusters and analyze their properties, we used a "density-based spatial clustering of applications with noise" (DBSCAN) algorithm (Figure 4-8). We found that the number of clusters per AZ increased significantly during development (2.91 ± 0.19 at P7–9, 4.38 ± 0.23 at P14–16, and 4.64 ± 0.23 at P21–23; 67, 69, and 81 AZs; $P < 0.001$; Figure 4-8G–I and M), whereas the average number of particles per cluster remained almost constant (15.6 ± 1.1 at P7–9, 15.4 ± 1.0 at P14–16, and 16.9 ± 1.0 at P21–23; 194, 299, and 373 clusters; $P = 0.44$; Figure 4-8J–L and N). The spacing of channels within clusters, as quantified by NND, was 20.86 ± 0.29 nm at P7–9, 22.90 ± 0.25 nm at P14–16, and 23.27 ± 0.21 nm at P21–23 (Figure 4-8O). In contrast, the distance between adjacent clusters was much wider, 143.7 ± 3.5 nm at P7–9, 146.2 ± 2.7 nm at P14–16, and 159.8 ± 3.1 nm at P21– 23 (Figure 4-8P). Thus, whereas individual channels within a given cluster were tightly packed, clusters within the same AZ were widely separated.

Analysis of EM and FRL data allowed us to further compute the stoichiometric ratios of the channel-vesicle coupling. On average, the number of docked vesicles associated with a Ca^{2+} channel cluster was 3.50 at P7–9, 3.22 at P14–16, and 5.42 at P21–23. Hence, BC–PC synapses show an increasing excess of the number of docked synaptic vesicles over the number of Ca^{2+} channel clusters.

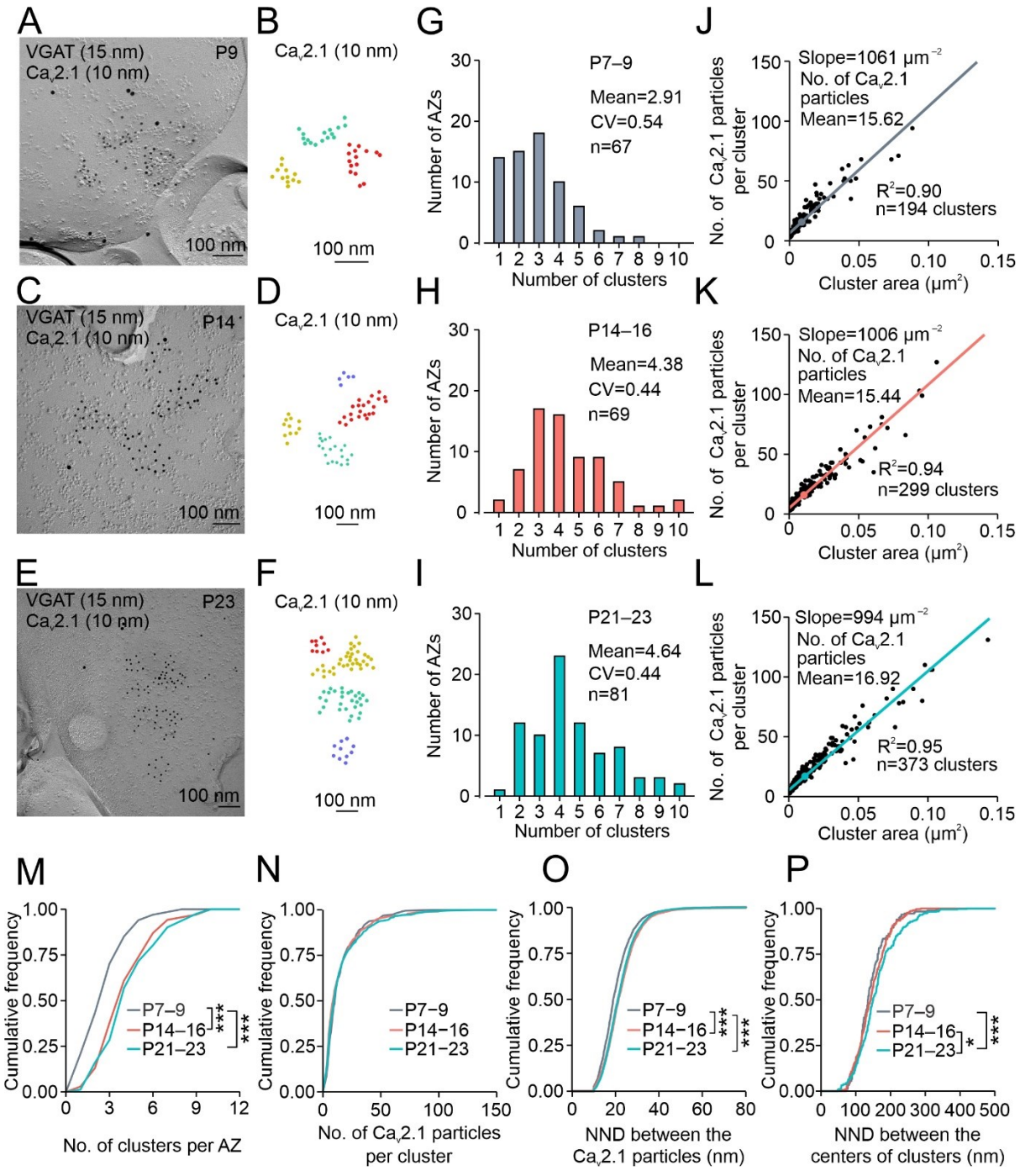

Figure 4-8 DBSCAN clustering analysis for $Ca_V2.1$ particles in AZs of BC terminals by FRL

(A–F) Distributions of $Ca_V2.1$ clusters in representative AZs from the P7–9 (A and B), P14–16 (C and D), and P21–23 age groups (E and F). Original EM micrographs (A, C, and E) and positions of gold particles labeling $Ca_V2.1$, color-coded according to cluster allocation (B, D, and F). Single scattered particles not allocated to clusters were omitted from the analysis. **(G–I)** Distribution histograms for the number of $Ca_V2.1$ clusters per AZ at P7–9 (G), P14–16 (H), and P21–23 age groups (I). **(J–L)** Plots of $Ca_V2.1$ gold particle number per cluster against cluster area at P7–9 (J), P14–16 (K), and P21–23 age groups (L). Gray, red, and cyan filled circles indicate mean values. **(M and N)** Cumulative distributions of the number of $Ca_V2.1$ clusters per AZ (M) and the number of $Ca_V2.1$ particles per cluster (N) for P7–9 (gray), P14–16 (red), and P21–23 age groups (cyan). **(O and P)** Cumulative distributions of nearest neighbor distance (NND) values between $Ca_V2.1$ particles within a cluster (O) and between the centers

of $Ca_v2.1$ clusters (P) for P7–9 (gray), P14–16 (red), and P21–23 age groups (cyan), respectively. The NND between the centers of clusters was calculated by averaging coordinates of all particles in individual clusters.

Table 3. Structural properties of cerebellar BC–PC synapses at different developmental stages

Parameter	P7–9	P14–16	P21–23	P[1]
Number of boutons per connection	6.55 ± 0.64 (11)	8.40 ± 1.09 (10)	9.00 ± 0.95 (10)	0.1126 (0.7200; 1.0000; 0.1300)
Number of AZs per bouton	1.87 ± 0.22 (15)	2.00 ± 0.33 (10)	2.16 ± 0.19 (19)	0.5371 (1.0000; 1.0000; 0.7800)
AZ area (μm^2)[2]	0.15 ± 0.02 (9)	0.17 ± 0.04 (8)	0.21 ± 0.02 (22)	0.0474 (1.0000; 0.711; 0.031)
Number of docked vesicles per AZ[2]	10.2 ± 1.4 (16)	14.1 ± 2.8 (10)	25.1 ± 2.0 (14)	< 0.0001 (0.7350; 0.0230; < 0.0001)
Docked vesicle density (μm^{-2})	47.96± 5.14 (16)	64.87 ± 10.08 (10)	90.92 ± 9.98 (14)	0.0082 (0.6016; 0.4622; 0.0045)
Docked vesicle diameter (nm)	43.68 ± 0.38 (163)	36.45 ± 0.35 (167)	37.23 ± 0.19 (417)	< 0.0001 (< 0.0001; 0.1600; < 0.0001)
Number of $Ca_v2.1$ particles per AZ	47.3 ± 4.0 (67)	70.3 ± 3.6 (69)	81.5 ± 4.8 (81)	< 0.0001 (< 0.0001; 0.5900; < 0.0001)
Number of Ca^{2+} channel clusters per AZ	2.91 ± 0.19 (67)	4.38 ± 0.23 (69)	4.64 ± 0.23 (81)	< 0.0001 (< 0.0001; 1.0000; < 0.0001)
Number of $Ca_v2.1$ particles per cluster	15.6 ± 1.1 (194)	15.4 ± 1.0 (299)	16.9 ± 1.0 (373)	0.4394 (0.6000; 1.0000; 1.0000)
NND between Ca^{2+} channels within cluster (nm)	20.9 ± 0.3 (194)	22.9 ± 0.2 (299)	23.3 ± 0.2 (373)	< 0.0001 (< 0.0001; 1.0000; < 0.0001)
NND between Ca^{2+} channel clusters (nm)	143.7 ± 3.5 (181)	146.2 ± 2.7 (300)	159.8 ± 3.1 (375)	0.0018 (1.0000; 0.0325; 0.0031)
Ratio number of vesicles to number of Ca^{2+} channel clusters	3.50	3.22	5.42	N/A

Mean ± SEM (number of measurements in parenthesis).

[1] P values outside the parenthesis indicate results from Kruskal-Wallis test. P values inside the parenthesis indicate results from Wilcoxon-Mann-Whitney test with Bonferroni correction. The order of pairwise comparisons is P7–9 vs. P14–16; P14–16 vs. P21–23; and P7–9 vs. P21–23, respectively.

[2] AZ area was determined from chemically fixed tissue, number of docked vesicles was measured from cryofixed tissue.

Chapter 5. Bridge the gap between functional properties and structural features of the BC–PC synapse by computational modeling

Our results provide detailed information about p_R, sensitivity of release to Ca^{2+} chelators, type and distribution of presynaptic Ca^{2+} channels, and numbers of synaptic vesicles. Taken together, these data constrain the coupling configuration.

5.1 Change from Ca^{2+} microdomain to Ca^{2+} nanodomain during development

To fully exploit this information, we generated a realistic model of Ca^{2+} diffusion and sensor activation at BC terminals (Figure 5-1). Duration and amplitude of the presynaptic Ca^{2+} flux was constrained by our presynaptic recordings and previous analysis of gating and single-channel conductance of P/Q-type Ca^{2+} channels (Figure 5-2). Buffered diffusion of Ca^{2+} was modeled by numerical solution of the full set of partial differential equations in three dimensions, assuming a fixed Ca^{2+} buffer, a low-affinity endogenous mobile Ca^{2+} buffer, and a high-affinity exogenous mobile Ca^{2+} buffer (EGTA or BAPTA). Finally, transmitter release was computed using a Ca^{2+} sensor model for synaptotagmin-2, the putative Ca^{2+} sensor of exocytosis at the BC–PC synapse.

First, we simulated Ca^{2+} domains around Ca^{2+} channels assuming realistic distributions, including their non-random localization (Figure 5-1A). Intracellular Ca^{2+} concentration was plotted in two dimensions parallel to the AZ. Presynaptic Ca^{2+} flux was represented by Gaussian functions with standard deviations σ of 1.38 ms, 0.56 ms, and 0.3 ms, to account for differences in presynaptic AP shape (Figure 5-2). Peak open probability of presynaptic Ca^{2+} channels was assumed as 1, 0.3, and 0.1, respectively (Figure 5-2).

We found that in young synapses Ca^{2+} domains around individual Ca^{2+} channels and Ca^{2+} channel clusters were merged, whereas in mature synapse individual Ca^{2+} domains were much better separated (Figure 5-1D–F). On average, the width of Ca^{2+} domains at half-maximal amplitude decreased from 83.4 ± 4.5 nm (P7–9) to 58.5 ± 10.2 nm (P14–16), and 19.6 ± 2.1 nm (P21–23; Figure 5-1G). These results indicate a switch from merged Ca^{2+} microdomains, which cover the entire AZ, to isolated Ca^{2+} nanodomains, which are spatially more confined. Thus, the assumed reduction of Ca^{2+} channel open probability, suggested by the reduction in presynaptic AP duration, markedly changed the shape of the Ca^{2+} domains (Figure 5-1D–F, bottom).

Next, we simulated the effects of these different Ca^{2+} domains on transmitter release (Figure 5-1H and I). Vesicles were put at random locations at Ca^{2+} channel clusters (corresponding to a cluster area “CA” model), and the Ca^{2+} concentration at the corresponding location was used to drive the release sensor model (Figure 5-1H). Simulations were performed in control conditions (0.1 mM EGTA), and in the presence of 10 mM EGTA

and 10 mM BAPTA to predict the effects of the Ca^{2+} chelators. Furthermore, the simulated release rates with 0.1 mM EGTA were used to estimate release probability, delay, and decay time constant of transmitter release. Although the model was highly constrained, it reasonably predicted both EGTA sensitivity and release probability (Figure 5-1J and K).

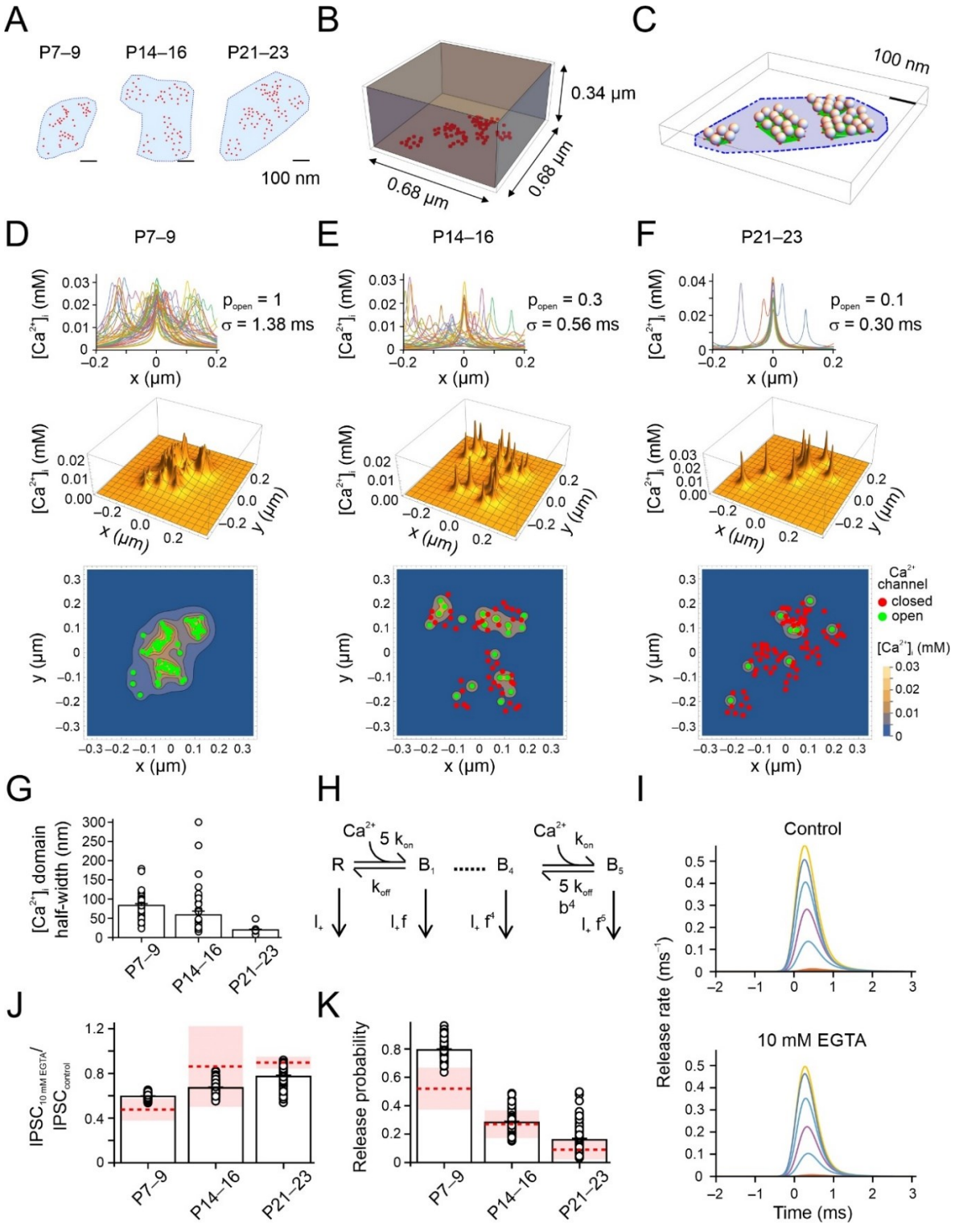

Figure 5-1 Sharpening of Ca^{2+} domains in cerebellar BC terminals during development

(A) Topography of three representative AZs from the P7–9, P14–16, and P21–23 age groups (P8, P14, and P23, respectively). Blue, AZ area; red, presynaptic Ca^{2+} channels. **(B)** Schematic illustration of simulations of buffered diffusion of Ca^{2+}. The full set of partial differential equations was solved assuming a three dimensional spatial grid with 5 nm resolution. Gray cube, simulated volume. **(C)** Model of AZ in which vesicles were attached to the presynaptic membrane opposite to nanoclusters of presynaptic Ca^{2+} channels. Spheres, synaptic vesicles; red dots, presynaptic Ca^{2+} channels; green areas, convex hull around Ca^{2+} channel clusters. Vesicles were attached at 5 nm vertical distance from the plasma membrane, consistent with the distance of docked vesicles. **(D–F)** Intracellular Ca^{2+} concentration 5 nm away from the plasma membrane and 0.2 ms after the peak of the presynaptic Ca^{2+} inflow for P7–9 (D), P14–16 (E), and P21–23 (F) AZs. Top, "line scans" of Ca^{2+} concentration through all Ca^{2+} channels in the x direction (y = 0, z = 5 nm), with x = 0 corresponding to the channel center. Different colors indicate different Ca^{2+} channels. Center, 3D plots of Ca^{2+} domains. Bottom, contour plots of Ca^{2+} concentration; points indicate Ca^{2+} channels (red, closed; green, activated). Presynaptic Ca^{2+} flux was represented by a Gaussian function with standard deviation σ of 1.38 ms, 0.56 ms, and 0.3 ms. Open probability of presynaptic Ca^{2+} channels was assumed as 1, 0.3, and 0.1, respectively. Note that individual Ca^{2+} domains merge in the young synapse, but are separated in the mature synapse, due to reduced opening of adjacent Ca^{2+} channels (properties of the endogenous Ca^{2+} buffers were the same). **(G)** Summary bar graph of width of Ca^{2+} domains at half-maximal amplitude for the example AZs from the P7–9, P14–16, and P21–23 age groups. Circles, individual Ca^{2+} domains; bars, mean ± SEM. Note that half-widths of Ca^{2+} domains become significantly shorter during synaptic maturation ($P < 0.001$; n = 49, 38, and 16). **(H and I)** Random positioning of synaptic vesicles opposite to Ca^{2+} channel clusters explains nanodomain coupling and developmental changes. Transmitter release rate was computed using the Ca^{2+} sensor-release model of Lou et al., 2005 (H). Release rate was computed in control (I, top) and in 10 mM EGTA (I, bottom) for a representative synapse from the P21–23 age group. Different colors represent release rates for individual vesicles at different locations. **(J and K)** Summary bar graphs of simulated EGTA effects (J) and release probability (K) for representative AZs from the P7–9, P14–16, and P21–23 age groups. Data in P7–9 were generated by 100 random vesicle placement patterns, data in P14–16 and P21–23 were generated by 10 random channel activation patterns combined with 10 random vesicle placement patterns (CA model). Circles, individual instances of random positioning; bars, mean ± SEM. Red dashed lines, mean experimental values; light red shaded area, 95% confidence band.

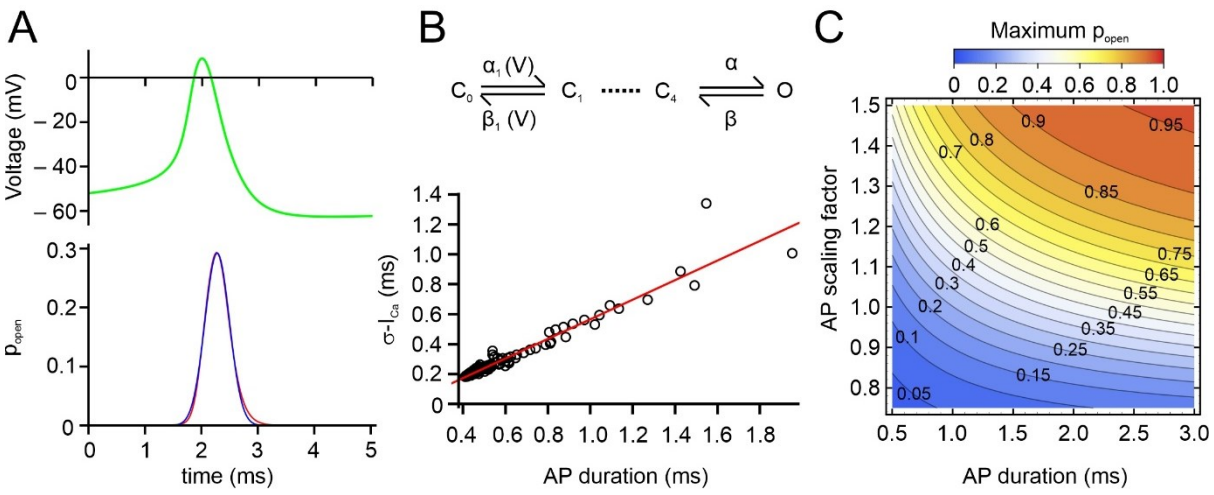

Figure 5-2 Relation between peak open probability of P/Q-type Ca^{2+} channels and half-duration of presynaptic AP

(A) Simulated AP (top) and corresponding Ca^{2+} channel open probability (bottom). The AP was simulated using the Wang-Buzsáki model of interneuron excitability. The Ca^{2+} channel open probability was computed using the Li et al. model of presynaptic P/Q-type Ca^{2+} channel gating (Li et al., 2007). ϕ = 1 .. 10 (default ϕ = 5); $\overline{g_K}$ = 3 ..

30 mS cm^{-2} (default $\overline{g_K}$ = 9 mS cm^{-2}). **(B)** Plot of width of Ca^{2+} current (σ) against AP duration. Red line represents linear regression. AP duration was measured from the steepest point in the rise to the steepest point in decay of the AP, permitting direct comparison with experimental eAPs. **(C)** Contour plot illustrating peak open probability of P/Q-type Ca^{2+} channels (contour lines) versus scaling factors for AP duration (horizontal axis) and AP peak amplitude (vertical axis). APs were simulated with the Wang-Buzsáki model, arbitrarily scaled in time (from peak time) and amplitude (from −65 mV resting potential), and applied to the Ca^{2+} channel gating model. Color scale bar indicates peak open probability. Note that the assumed p_{open} values (0.1, 0.3, and 1) are well covered by the parameter space.

In addition, we also examined the parvalbumin (PV) effect in the model simulation. PV is an endogenous mobile buffer with slow Ca^{2+} binding kinetics similar to EGTA (Müller et al., 2007), and is substantially upregulated during development. In cerebellar ML, PV was detected at P5, and increased approximately 5 folds between P10 and P20 (Collin et al., 2005). To explore this complex situation and to provide an upper limit estimate of the PV effect, we have added a high concentration of PV (500 µM PV) both to young and mature synapses. We found that PV has little effect on the Ca^{2+} domain structure and the amount of transmitter release (Figure 5-3). As simulations were computationally expensive and differences were minimal, we have not routinely included PV-like buffers in our model.

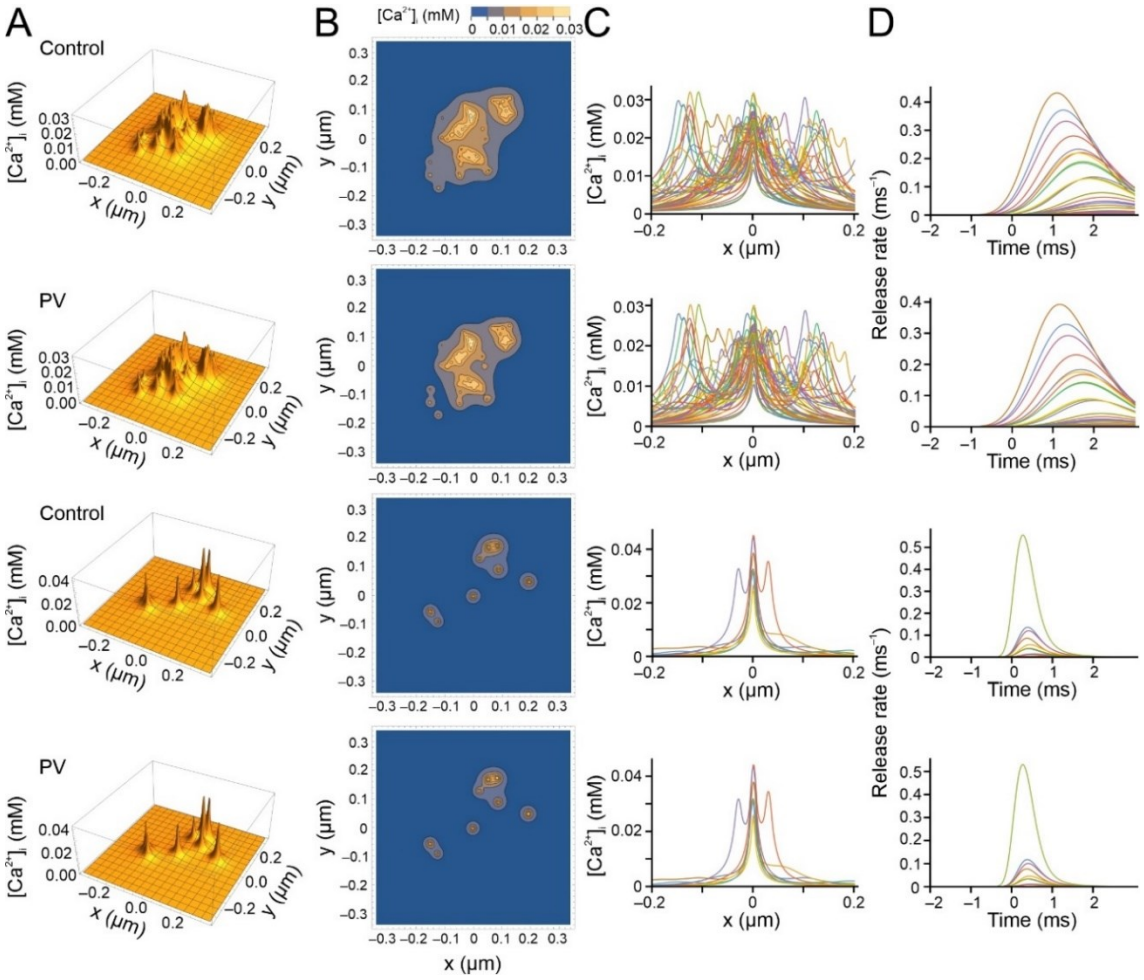

Figure 5-3 Effects of parvalbumin on the shape of Ca^{2+} domains in the models based on experimentally measured channel topography

(A) Intracellular Ca^{2+} concentration plotted in two dimensions parallel to the AZ, 5 nm away from the plasma membrane and 0.2 ms after the peak of the presynaptic Ca^{2+} inflow. All buffer parameters were assumed to be at default values. 1st panel from top, P7–9 control, 2nd panel from top, P7–9 with 1 mM PV buffer, 3rd panel from top, P21–23 control; bottom, P21–23 with 1 mM PV buffer. As PV has two putative Ca^{2+}-binding sites, 1 mM of PV buffer concentration corresponds to 500 µM PV protein concentration, close to experimentally determined values in cerebellar BCs (Eggermann and Jonas, 2012). **(B)** Similar plot as in (A), with contour plot representation of Ca^{2+} domains. Note that Ca^{2+} domains become slightly sharper in the presence of PV. **(C)** "Line scans" through centers of Ca^{2+} channels with similar conditions as in (A) and (B). Note that Ca^{2+} domains are slightly sharper in the presence of PV. **(D)** Release rates at individual docked synaptic vesicles. Note that release rate of more loosely coupled vesicles is slightly reduced in the presence of 1 mM PV buffer.

5.2 Developmental transformation of coupling nanotopography

To examine the coupling topography, we quantitatively compared the ability of several Ca^{2+} channel-vesicle coupling models to describe our experimental observations (including EGTA, BAPTA, p_R, delay, and decay time constant from time course of release data). Ca^{2+} channel-vesicle models used here are CA, CP, RAZ, RPM, CAEZ, RAZEZ, and RPMEZ (Table 4).

Table 4. Various Ca^{2+} channel-vesicle models

Model	Description
CA	Vesicles were positioned on top of Ca^{2+} channel clutser areas.
CP	Vesicles were positioned along Ca^{2+} channel cluster perimeters.
RAZ	Vesicles were randomly positioned over the entire AZ.
RPM	Vesicles were randomly positioned over the entire presynaptic membrane.
CAEZ	Vesicles were positioned on top of Ca^{2+} channel clutser areas, with a 5-nm exclusion redius to the Ca^{2+} channels.
RAZEZ	Vesicles were randomly positioned over the entire AZ, with a 5-nm exclusion redius to the Ca^{2+} channels.
RPMEZ	Vesicles were randomly positioned over the entire presynaptic membrane, with a 5-nm exclusion redius to the Ca^{2+} channels.

To assess the ability of the models to reproduce the experimental data, we selected a representative AZ from each age group, and simulated 100 AZ configurations with stochastic Ca^{2+} channel activation and random vesicle positioning. We then compared the distributions of the minus log-likelihood values, providing a metric of the ability of the model to describe the experimental observations. Whereas the CP model resembles the previously described perimeter model, the RAZEZ model shows similarities to the previously used exclusion zone model (Rebola et al., 2019).

In the representative AZ from the P7–9 age group, the RAZEZ model best described the experimental data, followed by RAZ, CP, CAEZ, CA, RPM, and RPMEZ models ($P < 0.001$; Figure 5-4B, left; Figure 5-5). In contrast, in the AZ from the P21–23 age group, the CP model produced the best fit, followed by CA, CAEZ, RAZ, RAZEZ, RPM, and RPMEZ models ($P < 0.001$; Figure 5-4B, right; Figure 5-5). In the P14–16 age group, the distribution was more similar to the P21–23 than to the P7–9 age group (Figure 5-4B, center), suggesting that a substantial transformation in coupling topography may occur between the young and medium age groups (i.e. in the range P10–13).

The results derived from three representative AZs suggest a developmental change in the coupling configuration. To test this hypothesis more generally, we simulated Ca^{2+} domains and transmitter release in all morphologically analyzed AZs, and determined the best-fit model in each case (67, 69, and 81 AZs, respectively; Figure 5-4 C). In the P7–9 age group, the RAZEZ often provided the best fit, whereas the other models did less frequently (Figure 5-4C, left). In the P21–23 age group, the CP showed highest frequency (Figure 5-4C, right). In the P14–16 age group, the distribution was more similar to the P21–23 than to the P7–9 age group. Distributions of best-fit models were significantly different among age groups ($P < 0.001$). Collectively, structural and modeling results suggest that developmental processes not only result in a reduction in average coupling distance, but also in coupling nanotopography.

Modeling also allowed us to determine the topographical coupling distance between Ca^{2+} channels and synaptic vesicles in the three age groups (Figure 5-4D and E). For each channel-vesicle pair in each model, we first determined the coupling distance in x-y dimension, resulting in a “distance matrix”. We then determined the contribution of each channel to the release of each vesicle by channel silencing or activation, resulting in a “release relevance matrix” (Figure 5-4D, right). Finally, we determined the mean topographical coupling distance, multiplying each distance value with the corresponding release relevance as a weight factor. We found that the average topographical coupling distance was 63.5 ± 0.5 nm at P7–9, 36.4 ± 0.4 nm at P14–16, and 26.3 ± 0.5 nm at P21–23 ($P < 0.001$ for all models; Figure 5-4E). Thus, our combined functional–structural–computational approach directly demonstrates shortening of the topographical coupling distance during development.

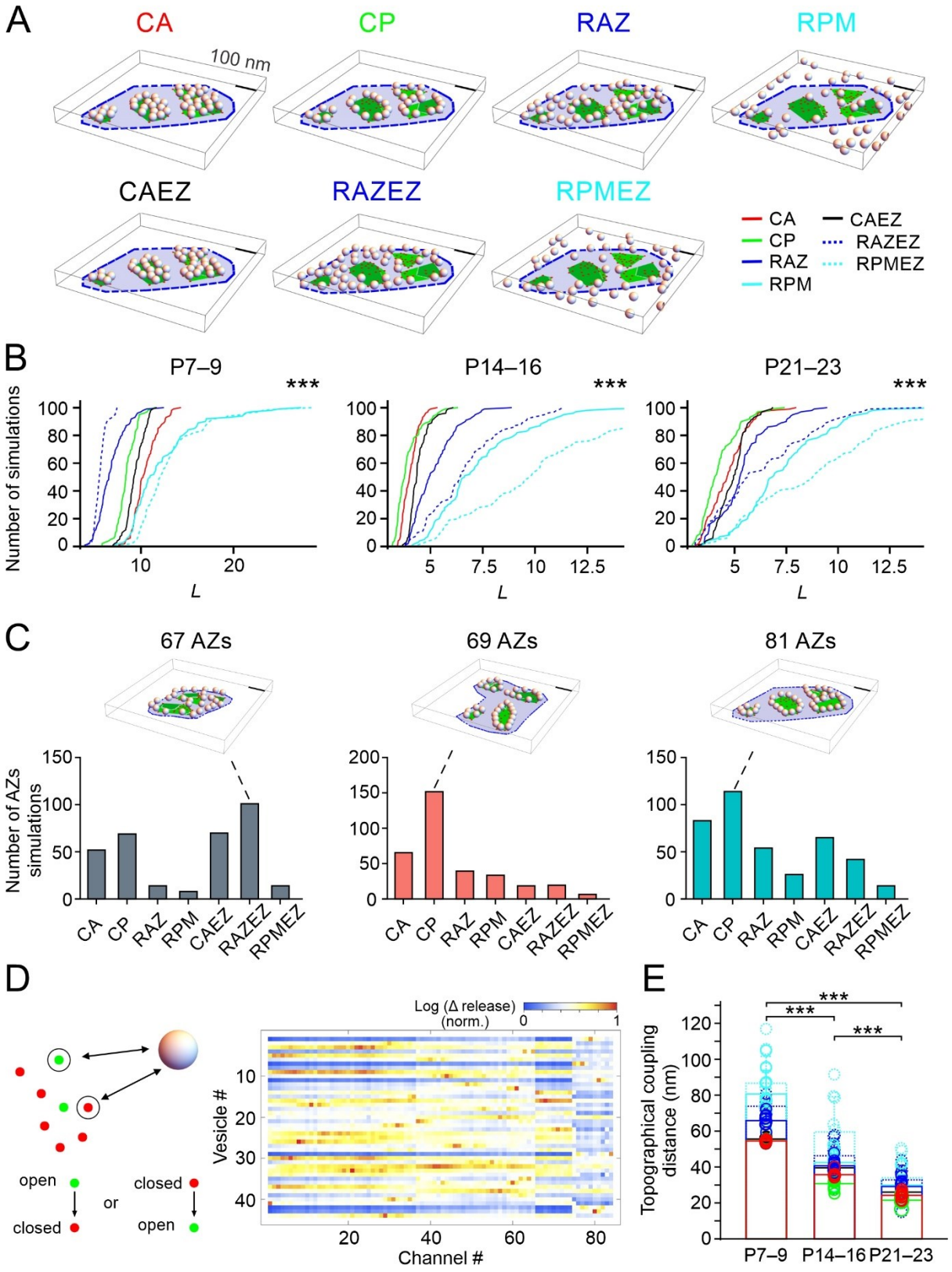

Figure 5-4 Change of Ca^{2+} channel-vesicle coupling from random to clustered nanotopography during development

(A) Three-dimensional depiction of different Ca^{2+} channel-vesicle coupling models. CA, vesicle attachment to the entire Ca^{2+} channel cluster area; CP, vesicle attachment to cluster perimeters; RAZ, vesicle attachment to whole AZ; RPM, vesicle attachment to entire presynaptic membrane; CAEZ, vesicle attachment to cluster area with exclusion zone (5 nm around each channel); RAZEZ, vesicle attachment to AZ with exclusion zone; RPMEZ, vesicle attachment to presynaptic membrane with exclusion zone. Red, Ca^{2+} channels; green, Ca^{2+} channel cluster area; blue, AZ area. AZ from P21–23 age group. **(B)** Comparison of coupling topography models in P7–9 (left), P14–16 (center), and P21–23 age groups (right). Cumulative distribution of minus log-likelihood score (including EGTA, BAPTA, p_R, delay, and time course of release); lower values indicate better fit. Red, CA model; green, CP model; blue, RAZ model; cyan, RPM model; black, CAEZ model; blue dashed, RAZEZ model; cyan dashed, RPMEZ model. **(C)** Histograms of the best-fit model in P7–9 (left), P14–16 (center), and P21–23 age groups (right). Histograms show the distribution for the entire set of reconstructed active zones (67, 69, and 81 AZs). For each AZ, 5 random synaptic vesicle placement patterns were simulated. Insets on top show the models with the highest abundance in the histograms. Note that the nanotopography switches from more random to more clustered. **(D)** Direct estimation of "topographical coupling distance". Left, schematic illustration of the approach. For each channel-vesicle pair, the physical distance in x-y plane was measured, resulting in a distance matrix. Each channel's fractional contribution to the release rate was probed by either activating the channel (if closed) or inactivating the channel (if open), resulting in a relevance matrix. Finally, the weighted mean distance

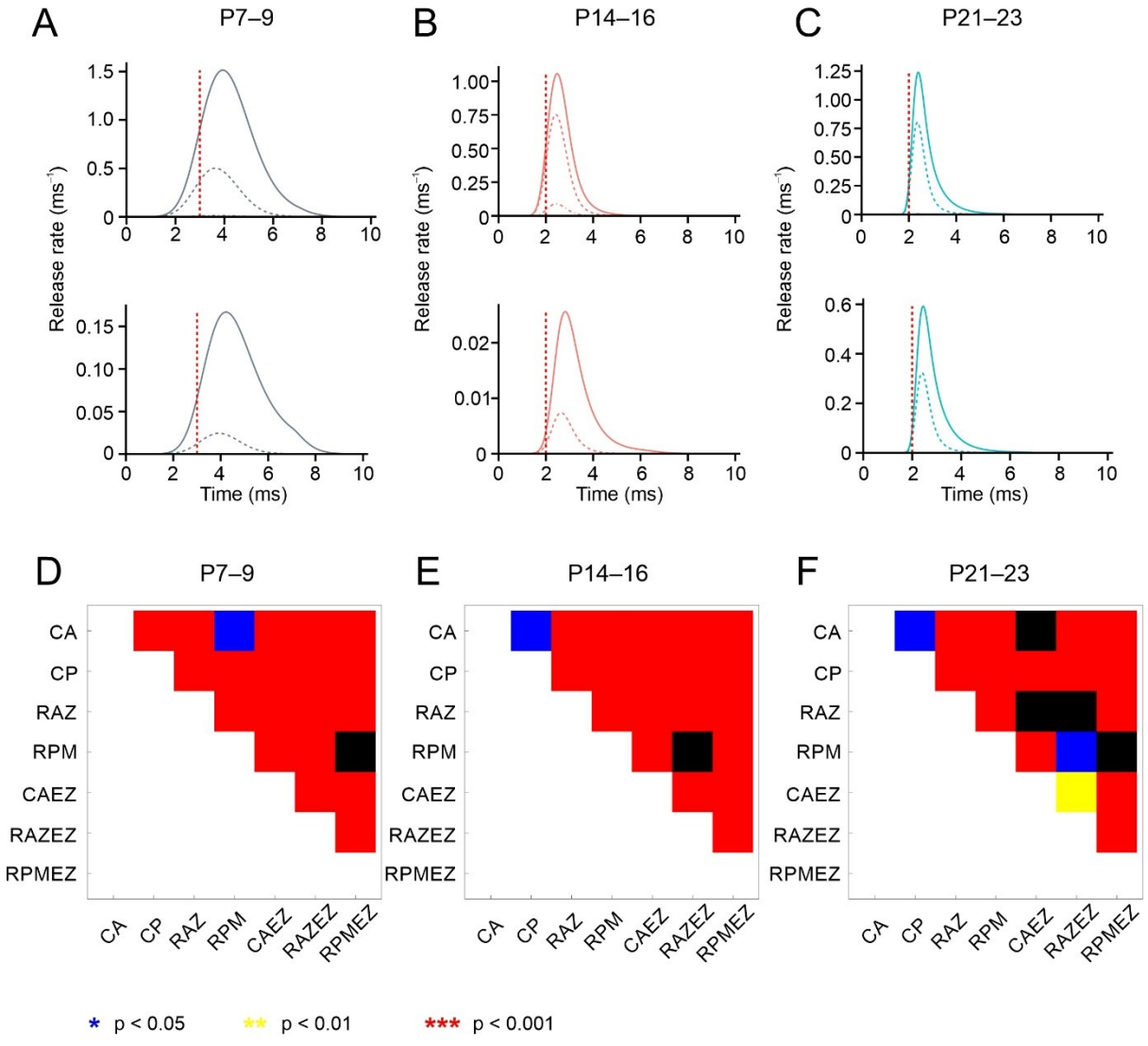

Figure 5-5 Statistical comparison of different coupling models

(A–C) Simulated release rate traces in AZs from the P7–9 (A), P14–16 (B), and P21– 23 age group (C). Continuous, control (0.1 mM EGTA); dashed, 10 mM EGTA; dashed dotted, 10 mM BAPTA. Top, example with best-fit model (RAZEZ, CP, and CP, respectively); bottom, example with worst-fit model (RPMEZ). Dashed vertical red line at 2 or 3 ms indicates peak of Ca^{2+} inflow. Note the better model provides a better description of the chelator sensitivity and timing of release. Traces were computed as the sum of release rates of all vesicles. **(D–F)** Statistical comparison of the 7 coupling topography models. Comparisons were made using a Wilcoxon-Mann-Whitney test with Bonferroni correction for multiple comparisons in AZs from the P7–9 (D), P14–16 (E), and P21–23 age group (F). Corresponding L distributions are shown in Figure 8B, left, center, and right, respectively. Color code: Blue, $P < 0.05$; yellow, $P < 0.01$; red, $P < 0.001$; black, $P \geq 0.05$ (not significant).

Table 5. Parameters of model of Ca^{2+} diffusion, buffering, and release sensor

Parameter		**P7–9**	**P14–16**	**P21–23**	**Reference**
Half-duration Ca^{2+} flux, σ (ms)		1.376 ms	0.559 ms	0.297 ms	Figure 5-2 B
p_{open}	Presynaptic Ca^{2+} channels	1	0.3	0.1	Figure 5-2 C
Ca^{2+} inflow per channel		0.25×10^{-15} M			
$[Ca^{2+}]_{rest}$		40 nM			Collin et al., 2005
k_{on}	Mobile buffer	5×10^8 M^{-1} s^{-1}			
k_{off}	Mobile buffer	100,000 s^{-1}			
[B] total	Mobile buffer	0.27 mM			
k_{on}	Fixed buffer	1×10^8 M^{-1} s^{-1}			Nakamura et al., 2015; Xu et al., 1997; Eggermann and Jonas, 2012
k_{off}	Fixed buffer	10,000 s^{-1}			
[B] total	Fixed buffer	4 mM			
EGTA k_{on}	Exogenous buffer	1×10^7 M^{-1} s^{-1}			Naraghi and Neher, 1997; Neher, 1998; Nägerl et al., 2000; Meinrenken et al., 2002
EGTA k_{off}	Exogenous buffer	0.7 s^{-1}			
BAPTA k_{on}	Exogenous buffer	4×10^8 M^{-1} s^{-1}			
BAPTA k_{off}	Exogenous buffer	88 s^{-1}			
D_{Ca}		220 μm^2 s^{-1}			
D_B	Mobile buffer	200 μm^2 s^{-1}			
$D_{EGTA} = D_{BAPTA}$	Exogenous buffer	220 μm^2 s^{-1}			
k_{on}	Ca^{2+} sensor	1×10^8 M^{-1} s^{-1}			Lou et al., 2005
k_{off}	Ca^{2+} sensor	4,000 s^{-1}			Lou et al., 2005

b	Ca^{2+} sensor cooperativity factor	0.5	Lou et al., 2005
l_+	Ca^{2+} sensor	$2 \times 10^{-4}\ s^{-1}$	Lou et al., 2005
f	Ca^{2+} sensor	31.3	Lou et al., 2005

Chapter 6. Conclusion and discussion

To determine the nanotopography and stoichiometry of coupling at an inhibitory synapse, we combined biophysical analysis (pair recording, presynaptic recording, and pipette perfusion), structural analysis (LM, serial-section EM, and FRL), and modeling of Ca^{2+} diffusion and release sensor activation. This combined approach offered unprecedented insights into the relation between structure and function of a GABAergic central synapse. Our results suggest that developmental processes not only result in a quantitative reduction of the source-sensor coupling distance, but rather in a qualitative transformation in the coupling nanotopography from more random to more clustered. Thus, presynaptic signaling developmentally approaches a point-to-point configuration, optimizing speed, reliability, and energy efficiency of synaptic transmission.

6.1 Substantial reorganization in release machinery

Variance and mean analysis showed that there is a huge reorganization in release machinery during synaptic maturation, which occurred both in presynaptic (reduction in p_R and increase in N) and postsynaptic (reduction in Q) compartments. In addition, cumulative of release (train method) showed an increased RRP size. Efforts have been made to investigate the mechanisms.

6.1.1 Reduction in p_R and its underlying mechanism

The p_R of BC–PC synapse was significantly decreased during development, and it is in accordance with the increased paired pulse ratio (from short-term depression to short-term facilitation). However, the mechanism is elusive.

We first measured the coupling distance between Ca^{2+} channels and synaptic vesicles by perfusing the presynaptic terminals with exogeneous Ca^{2+} chelator (EGTA and BAPTA). Intuitively, the reduced p_R would associate with an increase in the coupling distance. However, we found that the coupling distance decreased during development, which means that the altered coupling distance can't explain the reduced p_R.

We then attempted to examine the AP shape, another factor that would interfere with p_R. We found that the mean half-duration from the BC somata was reduced by 33%, whereas the reduction percentage from the presynaptic terminals was even more profound (73%). Therefore, the huge decrement in the AP duration from the terminal would affect the Ca^{2+} channel open probability (will be discussed in detail in paragraph 6.2), and strongly decrease the p_R in the end.

Why the reduction percentage in AP duration is more prominent in boutons than somata? One possible mechanism is the different expression pattern of voltage-gated K^+ channels. Studies from SC, a closely related cell-type to BC in the cerebellar ML, showed that K_V3 channels were clustered at boutons rather than shafts (Rowan et al., 2016), and K_V3

channels participated in AP repolarization in boutons (Rowan et al., 2014). While our electrophysiology data revealed a pharmacological broadening of somatic APs by TEA throughout development, Ca^{2+} imaging data from boutons demonstrated a significant increase in Ca^{2+} transients only in the mature age group, rather than younger age groups. These data suggested an increased expression of K^+ channels (probably K_v3) in boutons upon synaptic maturation, to faithfully and accurately transmit APs, preventing use-dependent inactivation, especially during high-frequency firing (Rowan et al., 2014).

6.1.2 Increase in N and its structural correlates

The concept of functional release sites is fuzzy (Pulido and Marty, 2017). Various studies have been attempted to correlate its structural properties. At the beginning, it was thought that the functional release sites represent the synaptic contacts (i.e. boutons) based on the analysis from motoneurons (Redman, 1990). In addition, it has been suggested that the functional release sites represent the AZ based on the analysis of hippocampal excitatory synapses (Schikorski and Stevens, 1997). Furthermore, there are also well-documented multivesicular release from singe AZs (Rudolph et al., 2015; Holler et al., 2021), raising the importance of unveiling the substructural organization of AZ. A recent study based on the cerebellar PF–MLI synapse (a simple glutamatergic synapse) showed that the number of functional docking sites matched the number of presynaptic Ca^{2+} channel clusters (Miki et al., 2017), which again challenged the “one site-one vesicle” hypothesis, and drew interest and attention on the ultrastructure analysis of presynaptic AZ (e.g. Ca^{2+} channels, docking sites, or priming sites).

To correlate the functional release sites, we systematically investigated the potential morphological structures including the number of boutons, the number of AZs, the number of docked vesicles, and the number of Ca^{2+} clusters at BC–PC synapses during development (Table 6). We found that early in development, the number of N correlates with the total number of AZs. However, later in development, the number of N exceeds the total number of AZs, and coincides better with the total number of presynaptic Ca^{2+} channel clusters. Therefore, the structural correlate of the functional release sites is not static, but may change during development.

Ca^{2+} domain modeling results may also help to convince our conclusion. Early in development, Ca^{2+} microdomains are wide, and the loosely coupled vesicles may “see” Ca^{2+} inflow throughout the entire AZ, so that the AZ may function as a unit. In contrast, later in development, Ca^{2+} nanodomains are sharp, and the tightly coupled vesicles may selectively sense Ca^{2+} inflow from the nearest Ca^{2+} channels or Ca^{2+} channel clusters, so that the release in the AZ is more fragmented, leading to multiple release sites in one AZ.

6.1.3 Decrease in Q

Variance and mean analysis also showed a decrease in Q during development. Traditionally, the Q is more correlated to postsynaptic compartments (i.e. postsynaptic receptors). Although we can't rule out the possibility of postsynaptic developmental change, the decrease in the diameter of docked vesicles would possibly result in the declined Q.

Future studies should prioritize an in-depth examination of the postsynaptic $GABA_A$ receptors. Currently, little is known concerning the receptor's expression subtype, composition, quantitative expression level, and topographical localization during development. In addition, whether release sits at BC–PC synapses aligned with postsynaptic $GABA_A$ receptors to form "nanocolumn" is elusive (Tang et al., 2016). Exploring these aspects is crucial to enhance our understanding on the inhibitory synapse.

6.1.4 Increase in RRP size and the docked vesicles

The RRP is functionally defined as a subset of vesicles that is more readily released than other vesicles. However, the relationship between functionally derived RRP and structurally defined vesicles is fuzzy. There are three possibilities: (1) all docked vesicles are part of the RRP; (2) only a subset of docked vesicles is RRP; (3) RRP contains part of docked vesicles and part of undocked vesicles which can be rapidly recruited to empty, activated sites (Kaeser and Regehr, 2017).

We used the back extrapolation method on the cumulative release data to determine RRP (Schneggenburger et al., 1999). The RRP estimate represents ''pool decrement'' rather than absolute pool size (Neher, 2015). Errors in the estimation of RRP are generated if the stimulus may be too weak to deplete the whole pool (assumption 1) and/or depletion may take long enough that an appreciable component of release stems from newly recruited vesicles (assumption 2). In order to try to completely delete the pool to fulfill assumption 1, we performed trains of 50 stimuli at 100 Hz. In addition, at the P21-23 age group, we applied high extracellular Ca^{2+} concentration to fulfill the IPSC depression rate larger than 50% (Neher, 2015). In addition, errors which link to assumption 2 may be quite small (Lee et al., 2012). Thanawata and Regehr (2013) suggested corresponding errors on the 10–20% level. Taken together, although we can't obtain the true RRP size, our estimation represents a close approximation of RRP.

We found that the RRP size increased during development, which is in parallel with the increased number of docked vesicles (Table 6). The number of docked vesicles significantly exceeds the RRP size at all developmental stages, which excludes the possibility that not all docked vesicles are part of RRP. Although we can't rule out the third scenario, our results suggested that only a subset of docked vesicles contribute to RRP at BC–PC synapses.

Several molecular mechanisms could possibly regulate RRP. Analysis on mutant mice for Munc13, SNAP-25, syntaxin-1, and synaptobrevin2 had strong reduction on the tightly docked vesicles, whereas the number of vesicles 5–20 nm away from AZ was increased (Imig

et al., 2014). Therefore, these Munc13 and SNARE proteins, which are essential for vesicle fusion, would possibly regulate RRP size. In addition, a report showed that ELKS enhances RRP at hippocampal excitatory synapses, not at inhibitory synapses (Held et al., 2016). Hence, the specific mechanism in regulating RRP at inhibitory synapses need to be further investigated.

In conclusion, our structural analysis aligns well with our functional findings, providing underlying mechanisms for the substantial reorganization of the release machinery during synaptic maturation.

6.2 Reduction in Ca^{2+} channel open probability

Our results illustrated that synaptic transmission constantly rely on P/Q-type Ca^{2+} channels throughout development, with no switch in Ca^{2+} channel subtypes. In addition, presynaptic terminal recording provides accurate information regarding the duration of AP. Taken together, the efficacy of activation of Ca^{2+} channels can be roughly estimated by simulation.

Simulated results suggested that the presynaptic Ca^{2+} channel open probability decreased during synaptic maturation, which is further confirmed by the reduced Ca^{2+} peak transients in presynaptic terminals.

Why immature synapses have a high open probability and mature synapses have a low open probability? With high open probability of Ca^{2+} channels, the immature synapses Ca^{2+} channels are opened largely deterministically, whereas in the mature synapses Ca^{2+} channels are activated more stochastically. Stochastic Ca^{2+} channel activation in the mature synapse may explain why only few Ca^{2+} channels are necessary to trigger transmitter release (Bucurenciu et al., 2010; Scimemi and Diamond, 2012).

6.3 Developmental transformation of Ca^{2+}-vesicle coupling nanotopography

6.3.1Tightening in the coupling distance and reliance on Ca^{2+} channel subtype

Developmental tightening of coupling distance has been found in several excitatory synapses, and tightening is often associated with the switch of Ca^{2+} channel subtypes. In the calyx of Held synapse, transmitter release sensitivity to slow Ca^{2+} chelator EGTA significantly reduced during synaptic maturation (Fedchyshyn and Wang, 2005; Nakamura et al., 2015), suggesting tightening of coupling distance. In addition, transmitter release reliance developed from both N- and P/Q- type Ca^{2+} channels early at P7-12 synapse to P/Q-type Ca^{2+} channel specific at P14-18 synapse (Fedchyshyn and Wang, 2005; Nakamura et al., 2015). In the neocortical layer 5 pyramidal synapse, developmental tightening of coupling has also been found by probing the effect of both slow Ca^{2+} chelator EGTA and fast Ca^{2+} chelator BAPTA on transmitter release, and Ca^{2+} channel subtype reliance changed from P/Q- and N- to P/Q- specific (Bornschein et al., 2019). However, whether it represents a general developmental rule applied to other synapses, particularly the inhibitory synapse, is unclear.

We found that in cerebellar BC–PC synapse, transmitter release exclusively relies on P/Q-type Ca^{2+} channels, without any switch in Ca^{2+} subtype. The sensitivity of release to EGTA

and BAPTA reduced during development, and the coupling distance between Ca^{2+} channels and vesicles become tightened by simulation results. Therefore, our findings revealed a reduction in coupling distance upon synaptic maturation, providing insights into the developmental rule of inhibitory synapses.

6.3.2 Transformation of Coupling nanotopography

In addition to our finding on reduced coupling distance, simulation on real AZs also allowed us to disentangle the developmental topography between Ca^{2+} channels and vesicles. To determine the precise coupling configuration, we compared different models against the experimental data. In mature synapses, the CP model, in which vesicles were attached to cluster perimeters, provided the best fit to our experimental observations, although the variability among AZs was substantial. In contrast, in young synapses the RAZEZ model, in which vesicles were put to entire AZs with an exclusion zone, was superior. Taken together, our results suggest that developmental processes not only result in a reduction of the coupling distance, but rather in a transformation in the coupling topography from more random to more clustered.

6.3.3 Potential molecular mechanism in regulating nanotopography

Our findings have implications for the molecular interactions between Ca^{2+} channels and release sensors. Attractive forces may be explained by the AZ protein RIM, which binds to the vesicle protein Rab3 via Zn-finger domains and to the C-terminus of presynaptic Ca^{2+} channels via PDZ domains (Kaeser et al., 2011; Han et al., 2011). Furthermore, RIM-BPs bind to both RIM and the Ca^{2+} channel C-terminus.

Recent work suggested different machineries for clustering of Ca^{2+} channels and synaptic vesicles. Whereas RIM and RIM-BP are critically important for Ca^{2+} channel clustering, Liprin-α and the protein tyrosine phosphatase PTPσ seem to be more relevant for vesicle docking and priming (Emperador-Melero et al., 2023). Thus, a developmental sequence of expression of these proteins may contribute to the transformation of the coupling configuration.

6.3.4 Functional significance of coupling nanotopography

Inhibitory synapses play a key role in several higher network functions, such as feedforward and feedback inhibition, pattern separation by winner-takes-all computations (Guzman et al., 2021), and fast rhythmic activity, such as network oscillations in the gamma frequency range (Hu et al., 2014). For all these functions, the speed of inhibition is critically important. Furthermore, speed and efficiency have to be maintained during high-frequency activity, a hallmark property of GABAergic neurons *in vivo* (Lapray et al., 2012; Jörntell and Ekerot, 2003). How the requirements for speed and efficacy at inhibitory synapses can be integrated into single AZs remains enigmatic.

Our results suggest that the coupling nanotopography may explain how these requirements are implemented. In the mature synapse, clustered configurations (CA and CP) may offer functional advantages over random configurations (RPM and RPMEZ). The clustered nanotopography enables tight coupling between vesicles and the nearest neighbor Ca^{2+} channels, which maximizes the speed of inhibitory synaptic transmission (Bucurenciu et al., 2008). Furthermore, the clustered nanotopography allows to accommodate a large number of vesicles to their docking sites, leading to a high vesicle-to-channel stoichiometric ratio. Large numbers of docked vesicles will be important to ensure fast and sustained transmitter release during in vivo-like repetitive activity at GABAergic synapses (Lapray et al., 2012; Jörntell and Ekerot, 2003). Additionally, stochastic Ca^{2+} channel activation in combination with low Ca^{2+} channel numbers will minimize multivesicular release at single AZs or single Ca^{2+} channel clusters (Rudolph et al., 2015). This may save vesicles, contributing to both sustained efficacy and energy efficiency of synaptic transmission (Taschenberger et al., 2002). Finally, stochastic Ca^{2+} channel activation will minimize presynaptic Ca^{2+} inflow, further contributing to the energy efficiency. Thus, clustered nanotopography at mature GABAergic synapses provides unique functional advantages to inhibitory synaptic transmission, explaining its critical contribution to higher-order network computations.

Table 6. Comparison of number of functional release sites with estimated number of AZs and Ca^{2+} channel clusters per connection

	Parameter	P7–9	P14–16	P21–23	Reference
1	Number of boutons per connection	6.55	8.40	9.00	Figure 4-1
2	Number of AZs per bouton	1.87	2.00	2.16	Figure 4-2 C
3	Number of Ca^{2+} channel clusters per AZ	2.91	4.38	4.64	Figure 4-8 G, H, I
4	Number of docked vesicles per AZ	10.2	14.1	25.1	Figure 4-2 E
5	Number of AZs per connection	12.2	16.8	19.4	1 × 2
6	Number of Ca^{2+} channel clusters per connection	35.6	73.5	90.2	1 × 2 × 3
7	Number of docked vesicles per connection	124.5	236.9	488.3	1 × 2 × 4
8	Number of functional release sites per connection	12.83	14.26	43.34	Figure 3-4 D
9	Number of vesicles in the readily releasable pool per connection[2]	37.41	51.59	72.55[1]	Figure 3-7 E

[1] As the amount of depression was < 0.5 in control conditions, these experiments were performed in 4 mM extracellular Ca^{2+}.

[2] Note that the number of vesicles in the RRP is larger than the number of functional release sites, as suggested previously at other synapses (Tanaka et al., 2021).

References:

Acuna, C., Liu, X., Gonzalez, A., and Südhof, T.C. (2015). RIM-BPs mediate tight coupling of action potentials to Ca2+-triggered neurotransmitter release. Neuron *87*, 1234–1247.

Arai, I., and Jonas, P. (2014). Nanodomain coupling explains Ca^{2+} independence of transmitter release time course at a fast central synapse. eLife *3*, e04057.

Arlt, C., and Häusser, M. (2020). Microcircuit rules governing impact of single interneurons on Purkinje cell output *in vivo*. Cell Rep. *30*, 3020–3035.

Armstrong, D. M., and Rawson, J. A. (1979). Activity patterns of cerebellar cortical neurones and climbing fibre afferents in the awake cat. J. Physiol. *289*, 425–448.

Augustin, I., Rosenmund, C., Südhof, T.C, and Brose, N. (1999). Munc13-1 is essential for fusion competence of glutamatergic synaptic vesicles. Nature *400*, 457–461.

Baumel, Y., Jacobson, G.A., and Cohen, D. (2009). Implications of functional anatomy on information processing in the deep cerebellar nuclei. Front. Cell. Neurosci. *3*, 14.

Baur, D., Bornschein, G., Althof, D., Watanabe, M., Kulik, A., Eilers, J., and Schmidt, H. (2015). Developmental tightening of cerebellar cortical synaptic influx-release coupling. J. Neurosci. *35*, 1858–1871.

Beekhof, G.C., Osório, C., White, J.J., van Zoomeren, S., van der Stok, H., Xiong, B., Nettersheim, I.H., Mak, W.A., Runge, M., Fiocchi, M.M., Boele, H.-J., Hoebeek, F.E., and Schonewille, M. (2021). Differential spatiotemporal development of Purkinje cell populations and cerebellum-dependent sensorimotor behaviors. eLife *10*, e63668.

Blot, A., and Barbour, B. (2014). Ultra-rapid axon-axon ephaptic inhibition of cerebellar Purkinje cells by the pinceau. Nat. Neurosci. *17*, 289–295.

Borges-Merjane, C., Kim, O., and Jonas, P. (2020). Functional electron microscopy, ‘‘Flash and Freeze,’’ of identified cortical synapses in acute brain slices. Neuron *105*, 992–1006.e6.

Bornschein, G., Eilers, J., and Schmidt, H. (2019). Neocortical high probability release sites are formed by distinct Ca^{2+} channel-to-release sensor topographies during development. Cell Rep. *28*, 1410–1418.e4.

Bornschein, G., Arendt, O., Hallermann, S., Brachtendorf, S., Eilers, J., and Schmidt, H. (2013). Paired-pulse facilitation at recurrent Purkinje neuronsynapses is independent of calbindin and parvalbuminduring high-frequency activation. J. Physiol. *591*, 3355–3370.

Brose, N., Hofmann, K., Hata, Y., and Südhof, T.C. (1995). Mammalian homologues of caenorhabditis elegans unc-13 gene define novel family of C2-domain proteins. Journal of Biological Chemistry *270*, 25273–25280.

Brown, A.M., Arancillo, M., Lin, T., Catt, D.R., Zhou, J., Lackey, E.P., Stay, T.L., Zuo, Z., White, J.J., and Sillitoe R. (2019). Molecular layer interneurons shape the spike activity of cerebellar Purkinje cells. Sci. Rep. *9*, 1742.

Bucurenciu, I., Bischofberger, J., and Jonas, P. (2010). A small number of open Ca2+ channels trigger transmitter release at a central GABAergic synapse. Nat Neurosci *13*, 19–21.

Bucurenciu, I., Kulik, A., Schwaller, B., Frotscher, M., and Jonas, P. (2008). Nanodomain coupling between Ca^{2+} channels and Ca^{2+} sensors promotes fast and efficient transmitter release at a cortical GABAergic synapse. Neuron *57*, 536–545.

Buttermore, E.D., Piochon, C., Wallace, M.L., Philpot, B.D., Hansel, C., and Bhat, M.A. (2012) Pinceau organization in the cerebellum requires distinct functions of neurofascin in Purkinje and basket neurons during postnatal development. J Neurosci. *32*, 4724–4742.

Caillard, O., Moreno, H., Schwaller, B., Llano, I., Celio, M.R., and Marty, A. (2000). Role of the calcium-binding protein parvalbumin in short-term synaptic plasticity. Proc. Natl. Acad. Sci. USA *97*, 13372–13377.

Castillo, P., Schoch, S., Schmitz, F., Südhof, T.C., and Malenka, R.C. (2002). RIM1α is required for presynaptic long-term potentiation. Nature *415*, 327–330.

Cajal, S.R.y. (1911). Histologie Du Système Nerveux De L'homme & Des Vertébrés.

Cardona, A., Saalfeld, S., Schindelin, J., Arganda-Carreras, I., Preibisch, S., Longair, M., Tomancak, P., Hartenstein, V., and Douglas, R.J. (2012). TrakEM2 software for neural circuit reconstruction. PLoS ONE *7*, e38011.

Cerminara, N.L., Lang, E.J., Sillitoe, R.V., and Apps, R. (2015). Redefining the cerebellar cortex as an assembly of non-uniform Purkinje cell microcircuits. Nat. Rev. Neurosci. *16*, 79–93.

Change, S., Trimbuch, T., and Rosenmund C. (2018). Syanptotagming-1 drives synchronous Ca2+-triggered fusion by C2B-domiant mediated synaptic-vesicle-membrane attachment. Nat. Neurosci. *21*, 33–40.

Chen, C., Arai, I., Satterfield, R., Young, S.M. Jr, and Jonas, P. (2017a). Synaptotagmin 2 is the fast Ca2+ sensor at a central inhibitory synapse. Cell Rep. *18*, 723–736.

Chen, C., Satterfield, R., Young, S.M. Jr, and Jonas, P. (2017b). Triple function of Synaptotagmin 7 ensures efficiency of high-frequency transmission at central GABAergic synapses. Cell Rep. *21*, 2082–2089.

Chen, X., Tomchick, D.R., Kovrigin, E., Araç, D., Machius, M., Südhof, T.C., and Rizo, J. (2002). Three-dimensional structure of the complexin/SNARE complex. Neuron *33*, 397–409.

Clements, J. D., and Silver, R.A. (2000). Unveiling synaptic plasticity: a new graphical and analytical approach. Trends Neurosci., *23*, 105–113.

Coddington, L.T., Rudolph, S., Lune, P.V., Overstreet-Wadiche, L., and Wadiche, J.I. (2013). Spillover-mediated feedforward inhibition functionally segregates interneuron activity. Neuron *78*, 1050–1062.

Coffman, K.A., Dm, R.P., and Strick, P.L. (2011). Cerebellar vermis is a target of projections from the motor areas in the cerebral cortex. Proc. Natl. Acad. Sci. USA *108*, 16068–16073.

Collin, T., Chat, M., Lucas, M.G., Moreno, H., Racay, P., Schwaller, B., Marty, A., and Llano, I. (2005). Developmental changes in parvalbumin regulate presynaptic Ca2+ signaling. J. Neurosci. *25*, 96–107.

Couteaux, R. and Pécot-Dechavassine, M. (1970). Synaptic vesicles and pouches at the level of "active zones" of the neuromuscular junction. C R Acad. Hebd. Seances Acad. Sci. D *271*, 2346–2349.

Del Castillo, J. and Katz, B. (1954). Quantal components of the end plate potential. J. Physiol. *124*, 560–573.

Deng, L., Kaeser, P.S., Xu, W., and Südhof, T.C. (2011). RIM proteins activate vesicle priming by reversing autoinhibitory homodimerization of Munc13. Neuron *69*, 317–331.

Dolphin, A.C., Lee, A. (2020). Presynaptic calcium channels: specialized control of synaptic neurotransmitter release. Nat. Rev. Neurosci. *21*, 213–229.

Eggermann, E., Bucurenciu, I., Goswami, S.P., and Jonas, P. (2012). Nanodomain coupling between Ca2+ channels and sensors of exocytosis at fast mammalian synapses. Nat. Rev. Neurosci. *13*, 7–21.

Eguchi, K., Montanaro J., Le Monnier E., and Shigemoto, R. (2022). The number and distinct clustering patterns of voltage-gated calcium channels in nerve terminals. Front. Neuroanat. *16*, 846615.

Emperador-Melero, J., Andersen, J.W., Metzbower, S.R., Levy, A.D., Dharmasri, P.A., de Nola, G., Blanpied, T.A., and Kaeser, P.S. (2023). Molecular definition of distinct active zone protein machineries for Ca^{2+} channel clustering and synaptic vesicle priming. bioRxiv 2023.10.27.564439; doi: https://doi.org/10.1101/2023.10.27.564439

Emperador-Melero, J., and Kaeser, P.S. (2020). Assembly of the presynaptic active zone. Curr. Opin. Neurobio. *63*, 95–103.

Ester, M., Kriegel, H.P., Sander, J., and Xu, X. (1996). A density-based algorithm for discovering clusters in large spatial databases with noise. Proc. 2nd Int. Conf. KDD. AAAI Press, 226–231.

Fedchyshyn, M.J., and Wang, L.Y. (2005). Developmental transformation of the release modality at the calyx of Held synapse. J. Neurosci. *25*, 4131–4140.

Fernández-Chacón, R., Königstorfer, A., Gerber, S., García, J., Matos, M.F., Stevens C.F., Brose, N., Rizo, J., Rosenmund, C., and Südhof, T.C. (2001). Synaptotagmin I functions as a calcium regulator of release probability. Nature *410*, 41–49.

Fritschy, J.M. and Panzanelli, P. (2014). GABAA receptors and plasticity of inhibitory neurotransmission in the central nervous system. Eur J Neurosci. *39*, 1845–1865.

Fujimoto, K. (1995). Freeze-fracture replica electron microscopy combined with SDS digestion for cytochemical labeling of integral membrane proteins. Application to the immunogold labeling of intercellular junctional complexes. J. Cell Sci. *108*, 3443–3449.

Ghit, A., Assal, D., Al-Shami, A.S., and Hussein, D.E.E. (2021). GABAA receptors: structure, function, pharmacology, and related disorders. J Genet Eng Biotechnol. *19*, 123.

Grauel, M.K., Maglione, M., Reddy-Alla, S., Willmes, C.G., Brockmann, M.M., Trimbuch, T., Rosenmund, T., Pangalos, M., Vardar, G., Stumpf, A., Walter, A.M., Rost, B.R., Eickholt, B.J., Haucke, V., Schmitz, D., Sigrist, S.J., and Rosenmund, C. (2016). RIM-binding protein 2 regulates release probability by fine-tuning calcium channel localization at murine hippocampal synapses. Proc. Natl. Acad. Sci. USA *113*, 11615–11620.

Guzman, S.J., Schlögl, A., and Schmidt-Hieber, C. (2014). Stimfit: quantifying electrophysiological data with Python. Front. Neuroinform. *8*, 16.

Guzman, S.J., Schlögl, A., Espinoza, C., Zhang, X., Suter, BA, and Jonas P. (2021). How connectivity rules and synaptic properties shape the efficacy of pattern separation in the entorhinal cortex–dentate gyrus–CA3 network. Nat. Comput. Sci. *1*, 830–842.

Hámori, J. and Somogyi, J. (1983). Differentiation of cerebellar mossy fiber synapse in the rat: a quantitative electron microscope study. J. Comp. Neurol. *220*, 365–377.

Han, Y., Kaeser, P.S., Südhof, T.C., and Schneggenburger, R. (2011). RIM determines Ca2+ channel density and vesicle docking at the presynaptic active zone. Neuron *69*, 304–316.

Hansel, C., Linden, D.J., and D'Angelo, E. (2001). Beyond parallel fiber LTD: the diversity of synaptic and non-synaptic plasticity in the cerebellum. Nat. Neurosci. *4*, 467–475.

He, Q., Duguid, I., Clark, B., Panzanelli, P., Patel, B., Thomas, P., Fritschy J.-M., and Smart, T.G. (2015). Interneuron- and GABAA receptor- specific inhibitory synaptic plasticity in cerebellar Purkinje cells. Nat. Commun. *6*, 7364.

Hefft, S., and Jonas, P. (2005). Asynchronous GABA release generates long-lasting inhibition at a hippocampal interneuron-principal neuron synapse. Nat Neurosci *8*, 1319–1328.

Held, R.G., Liu, C., and Kaeser, P.S. (2016). ELKS controls the pool of readily releasable vesicles at excitatory synapse through its N-terminal coiled-coil domains. eLife *5*, e14862.

Herculano-Houzel, S. (2009). The human brain in numbers: a linearly scaled-up primate brain. Front Hum Neurosci. *9*, 3–31.

Herculano-Houzel, S., Mota, B., and Lent, R. (2006). Cellular scaling rules for rodent brains. Proc. Natl. Acad. Sci. USA. *103*, 12138–12143.

Holler, S., Köstinger, G., Martin, K.A., Schuhknecht, G.F., and Stratford K.J. (2021). Structure and function of a neocortical synapse. Nature *591*, 111–116.

Hu, H., and Jonas, P. (2014). A supercritical density of Na+ channels ensures fast signaling in GABAergic interneuron axons. Nat. Neurosci. *17*, 686–693.

Hull, C., Regehr, W.G. (2022). The cerebellar cortex. Annu. Rev. Neurosci. *45*,151–75.

Ichikawa, R., Yamasaki, M., Miyazaki, T., Konno, K., Hashimoto, K., Tatsumi, H., Inoue, Y., Kano, M., and Watanabe, M. (2011). Developmental switching of perisomatic innervation from climbing fibers to basket cell fibers in cerebellar Purkinje cells. J. Neurosci. *31*, 16916–16927.

Imig, C., Min, S.W., Krinner, S., Arancillo, M., Rosenmund, C., and Südhof, T.C. (2014). The morphological and molecular nature of synaptic vesicle prming at presynaptic active zone. Neuron *84*, 416–431.

Ito, M. (1984). The modification neuronal network of the cerebellum. J. Physiol. *34*, 781–792.

Iwakura, A., Uchigashima, M., Miyazaki, T., Yamasaki, M., and Watanabe, M. (2012). Lack of molecular–anatomical evidence for GABAergic influence on axon initial segment of cerebellar Purkinje cells by the pinceau formation. J. Neurosci. *32*, 9438–9448.

Iwasaki, S., and Takahashi, T. (1998). Developmental changes in calcium channel types mediating synaptic transmission in rat auditory brainstem. J. Physiol. *509*, 419–423.

Jones, M.V., Jonas, P., Sahara, Y., and Westbrook, G.L. (2001). Microscopic kinetics and energetics distinguish GABAA receptor agonists from antagonists. Biophys J. *81*, 2660–2670.

Kaeser, P.S., Deng, L., Wang, Y., Dulubova, I., Liu, X., Rizo, J., and Südhof, T.C. (2011) RIM proteins tether Ca^{2+} channels to presynaptic active zones via a direct PDZ-domain interaction. Cell *144*, 282–295.

Kaeser, P.S., Kwon, H.-B., Chiu, C.Q., Deng, L., Castilo, P.E., and Südhof, T.C. (2008). RIM1α and RIM1β are synthesized from distinct promoters of *RIM1* gene to mediate differential but overlapping synaptic function. J. Neurosci. *28*, 13435–13447.

Kaeser, P.S., and Regehr, W.G. (2017). The readily releasable pool of synaptic vesicles. Curr. Opin. Neurobio. *43*, 63–70.

Kandel, E.R., Schwartz, J.H., Jessell, T.M., Siegelbaum, S.A., and Hudspeth, A.J. (2013). Principles of neural science (5th ed.). McGraw-Hill Companies. Part VI, 42, 960–982.

Kano, M., Rexhausen, U., Dreessen, J., and Konnerth, A. (1992). Synaptic excitation produces a long-lasting rebound potentiation of inhibitory synaptic signals in cerebellar Purkinje cells. Nature *356*, 601–604.

Katz, B. (1969). The Release of Neural Transmitter Substances (Liverpool University Press).

Kaufmann, W.A., Kleindienst, D., Harada, H., and Shigemoto, R. (2021). High-resolution localization and quantitation of membrane proteins by SDS-digested freeze-fracture replica labeling (SDS-FRL). In: Receptor and ion channel detection in the brain. Neuromethods *169*, 267–283.

Kaufmann, W.A., Matsui, K., Jeromin, A., Nerbonne, J.M., and Ferraguti, F. (2013). Kv4.2 potassium channels segregate to extrasynaptic domains and influence intrasynaptic NMDA receptor NR2B subunit expression. Brain Struct Funct *218*, 1115–1132.

Keller, D., Babai, N., Kochubey, O., Han, Y., Markram, H., Schürmann, F., and Schneggenburger, R. (2015). An exclusion zone for Ca^{2+} channels around docked vesicles explains release control by multiple channels at a CNS synapse. PLoS Comput. Biol. *11*, e1004253.

Kochubey, O., Han, Y., and Schneggenburger, R. (2009). Developmental regulation of the intracellular Ca2+ sensitivity of vesicle fusion and Ca2+-secretion coupling at the rat calyx of Held. J. Physiol. *587*, 3009–3023.

Kozareva, V., Martin, C., Osorno, T., Rudolph, S., Guo, C., Vanderburg, C., Nadaf, N., Regev, A., Regehr, W.G., and Macosko, E. (2021). A transcriptomic atlas of mouse cerebellar cortex comprehensively defines cell types. Nature *598*, 214–219.

Kremer, J.R., Mastronarde, D.N., and Mclntosh, J. R. (1996). Computer visualization of three-dimensional image data using IMOD. J. Struct. Biol. *116*, 71–76.

Laurie, D.J., Wisden, W., and Seeburg, P.H. (1992). The distribution of thirteen GABAA receptor subunit mRNAs in the rat brain. III. Embryonic and postnatal development. J. Neurosci. 12, 4151–4172.

Lee, J.S., Ho, W.K., and Lee, S.H. (2012). Actin-dependent rapid recruitment of reluctant synaptic vesicles into a fast-releasing vesicle pool. Proc. Natl. Acad. Sci. USA *109*, E765–E774.

Lee, S.H., Schwaller, B., and Neher, E. (2000). Kinetics of Ca^{2+} binding to parvalbumin in bovine chromaffin cells: implications for [Ca^{2+}] transients of neuronal dendrites. J Physiol. *525*, 419–432.

Leto, K., Bartolini, A., Yanagawa, Y., Obata, K., Magrassi, L., Schilling, K., and Rossi, F. (2009). Laminar fate and phenotype specification of cerebellar GABAergic interneurons. J. Neurosci. *29*, 7079–7091.

Leung, A.W., and Li, J.Y.H. (2018). The molecular pathway regulating bergmann glia and folia generation in the cerebellum. Cerebellum *17*, 42–48.

Li, L., Bischofberger, J., and Jonas, P. (2007). Differential gating and recruitment of P/Q-, N-, and R-type Ca^{2+} channels in hippocampal mossy fiber boutons. J. Neurosci. *27*, 13420–13429.

Lichter, M., Paul, M.M, Pauli, M., Schoch, S., Kollmannsberger, P., Stigloher, C., Heckmann, M., and Sirén, A.L. (2022). Ultrastructural analysis of wild-type and RIM1α knockout active zones in a large cortical synapse. Cell Rep. *40*, 111382.

Llinas, R., Bloedel, J. R., and Hillman, D. E. (1969). Functional characterization of neuronal circuitry of frog cerebellar cortex. J. Neurophysiol. *32*, 847–870.

Lou, X., Scheuss, V., and Schneggenburger, R. (2005). Allosteric modulation of the presynaptic Ca2+ sensor for vesicle fusion. Nature *435*, 497–501.

Ma, C., Li, W., Xu, Y., and Rizo, J. (2011). Munc13 mediates the transition from the closed syntaxin-Munc18 complex to the SNARE complex. Nat. Struct. Mol. Biol. *18*, 542–549.

Martin, H.G.S., and Kullmann, D.M. (2023). Basket to Purkinje cell inhibitory ephaptic coupling is abolished in episodic ataxia type 1. Cells *12*, 1382.

Marvin, J.S., Shimoda, Y., Magloire, V., Leite, M., Kawashima, T., Jensen, T.P., Kolb, I., Knott, E.L., Novak, O., Podgorski, K., Leidenheimer, N.J., Rusakov, D.A., Ahrens, M.B., Kullmann D.M., and Looger, L.L. (2019). A genetically encoded fluorescent sensor for in vivo imaging of GABA. Nat. Methods *16*, 763–770.

Meinrenken, C.J., Borst, J.G.G., and Sakmann, B. (2002). Calcium secretion coupling at calyx of Held governed by nonuniform channel-vesicle topography. J. Neurosci. *22*, 1648–1667.

Meyer, A.C., Neher, E., and Schneggenburger, R. (2001). Estimation of quantal size and number of functional active zones at the Calyx of Held synapse by nonstationary EPSC variance analysis. J. Neurosci. *21*, 7889–7900.

Miki, T., Nakamura, Y., Malagon, G., Neher, E., and Marty, A. (2018). Two-component latency distributions indicate two-step vesicular release at simple glutamatergic synapses. Nat. Commun. *9*, 3943.

Miki, T., Kaufmann, W.A., Malagon, G., Gomez, L., Tabuchi, K., Watanabe, M., Shigemoto, R., and Marty, A. (2017). Numbers of presynaptic Ca^{2+} channel clusters match those of functionally defined vesicular docking sites in single central synapses. Proc. Natl. Acad. Sci. USA *114*, E5246–E5255.

Mishra, R.K., Kim, S., Guzman, S.J., and Jonas, P. (2016). Symmetric spike timing-dependent plasticity at CA3-CA3 synapses optimizes storage and recall in autoassociative networks. Nat. Commun. *7*, 11552.

Mittelstaedt, T., and Schoch, S. (2007). Structure and evolution of RIM-BP genes: Identification of a novel family member. Gene *403*, 70–79.

Möbius, W., Cooper, B., Kaufmann, W.A., Imig, C., Ruhwedel, T., Snaidero, N., Saab, A.S., and Varoqueaux, F. (2010). Electron microscopy of the mouse central nervous system. Methods Cell Biol. *96*, 475–512.

Müller, M., Felmy, F., Schwaller, B., and Schneggenburger, R. (2007). Parvalbumin is a mobile presynaptic Ca^{2+} buffer in the calyx of Held that accelerates the decay of Ca^{2+} and short-term facilitation. J Neurosci. *27*:2261–71.

Nakamura, Y., Darnieder, L.M., Deeb, T.Z., and Moss, S.J. (2015). Regulation of GABAARs by phosphorylation. Adv Pharmacol. *72*, 97–146.

Nakamura, Y., Harada, H., Kamasawa, N., Matsui, K., Rothman, J.S., Shigemoto, R., Silver, R.A., DiGregorio, D.A., and Takahashi, T. (2015). Nanoscale distribution of presynaptic Ca^{2+} channels and its impact on vesicular release during development. Neuron *85*, 145–158.

Nakamura, Y., Reva, M., and DiGregorio, D.A. (2018). Variations in Ca^{2+} Influx can alter Ca^{2+}-chelator-based estimates of Ca^{2+} channel-synaptic vesicle coupling distance. J. Neurosci. *38*, 3971–3987.

Nägerl, U.V., Novo, D., Mody, I., and Vergara, J.L. (2000). Binding kinetics of calbindin-D28k determined by flash photolysis of caged Ca2+. Biophys. J. *79*, 3009–3018.

Naraghi, M., and Neher, E. (1997). Linearized buffered Ca2+ diffusion in microdomains and its implications for calculation of [Ca2+] at the mouth of a calcium channel. J. Neurosci. *17*, 6961–6973.

Neher, E. (1998). Usefulness and limitations of linear approximations to the understanding of Ca++ signals. Cell Calcium *24*, 345–357.

Neher, E. (2015). Merits and limitations of vesicle pool models in view of heterogeneous populations of synaptic vesicles. Neuron *87*, 1131–1142.

Neher, E., and Brose, N. (2018). Dynamically primed synaptic vesicle states: key to understand synaptic short-term plasticity. Neuron *100*, 1283–1291.

Osorno, T., Rudolph, S., Nguyen, T., Kozavera, V., Nadaf, N.M., Norton, A., Macosko, E.Z., Lee, W.-C.A., and Regehr, W.G. (2022). Candelabrum cells are ubiquitous cerebellar cortex interneurons with specialized circuit properties. Nat. Neurosci. *25*, 702–713.

Palay, S.L., and Chan-Palay, V. (1974). Cerebellar Cortex. Springer Berlin, Heidelberg.

Pennock, R.L., Coddington., L.T., Yan, X., Overstreet-Wadiche, L., and Wadiche, J.I., (2023). Afferent convergence to a shared population of interneuron AMPA receptors. Nat. Commun. *14*, 3113.

Pernía-Andrade, A.J., Goswami, S.P., Stickler, Y., Fröbe, U., Schlögl, A., and Jonas P. (2012). A deconvolution-based method with high sensitivity and temporal resolution for detection of spontaneous synaptic currents in vitro and in vivo. Biophys. J. *103*, 1429–1439.

Pouzat, C., and Hestrin, S. (1997). Developmental regulation of basket/stellate Cell →Purkinje Cell Synapses in the Cerebellum. J. Neurosci. *17*, 9104–9112

Pulido, C., and Marty, A. (2017). Quantal fluctuations in central mammalian synapses: Functional role of vesicular docking sites. Physiol. Rev. *97*, 1403–1430.

Quade, B., Camacho, M., Zhao, X., Orlando, M., Trimbuch, T., Xu, J., Li, W., Nicastro, D., Rosenmund, C., and Rizo, J. (2019). Membrane bridging by Munc13-1 is crucial for neurotransmitter release. eLife *8*, e42806.

Rebola, N., Reva, M., Kirizs, T., Szoboszlay, M., Lőrincz, A., Moneron, G., Nusser, Z., and DiGregorio, D.A. (2019). Distinct nanoscale calcium channel and synaptic vesicle topographies contribute to the diversity of synaptic function. Neuron *109*, 3178.

Redman, S. (1990). Quantal analysis of synaptic potentials in neurons of the central nervous system. Physiol. Rev. *70*, 165–198.

Richmond, J.E, Davis, W.S., and Jorgensen, E.M. (1999). UNC-13 is required for synaptic vesicle fusion in C. elegans. Nat. Neurosci. *2*, 959–964.

Richmond, J.E., Weimer, R.M., and Jorgensen, E.M. (2001). An open form of syntaxin bypasses the requirement for UNC-13 in vesicle priming. Nature *412*, 338–341.

Ripley, B.D. (1977). Modelling spatial patterns. J. R. Stat. Soc. B *39*, 172–192.

Rollenhagen, A., Sätzler, K., Rodríguez, E.P., Jonas, P., Frotscher, M., and Lübke, J.H.R. (2007). Structural determinants of transmission at large hippocampal mossy fiber synapses. J. Neurosci. *27*, 10434–10444.

Rosenmund, C., and Stevens, C.F. (1996). Definition of the readily releasable pool of vesicles at hippocampal synapses. Neuron *16*, 1197–1207.

Rowan, M.J., DelCanto, G., Yu, J.J., Kamasawa, N., and Christie, J.M. (2016). Synapse-level determination of action potential duration by K^+ channel clustering in axons. Neuron *91*, 370–383.

Rowan, M.J., Tranquil, E., and Christie, J.M. (2014). Distinct Kv channel subtypes contribute to differences in spike signaling properties in the axon initial segment and presynaptic boutons of cerebellar interneurons. J. Neurosci. *34*, 6611–6623.

Rudolph, S., Tsai, M.C., von Gersdorff, H., and Wadiche, J.I. (2015). The ubiquitous nature of multivesicular release. Trends Neurosci. *38*, 428–438.

Sakaba, T. (2008). Two Ca2+-dependent steps controlling synaptic vesicle fusion and replenishment at the cerebellar basket cell terminal. Neuron *57*, 406–419.

Sasaki, T., Matsuki, N., and Ikegaya, Y. (2012). Targeted axon-attached recording with fluorescent patch-clamp pipettes in brain slices. Nat. Protoc. *7*, 1228–1234.

Scheuss, V. and Neher, E. (2001). Estimating synaptic parameters from mean, variance, and covariance in trains of synaptic responses. Biophys. J. *81*, 1970–1989.

Scheuss, V., Schneggenburger, R., and Neher, E. (2002). Separation of presynaptic and postsynaptic contributions to depression by covariance analysis of successive EPSCs at the Calyx of Held synapse. J. Neurosci. *22*, 728–739.

Schikorski, T., and Stevens, C.F. (1997). Quantitative ultrastructural analysis of hippocampal excitatory synapses. J. Neurosci. *17*, 5858–5867.

Schindelin, J., Arganda-Carreras, I., Frise, E., Kaynig, V., Longair, M., Pietzsch, T., Preibisch, S., Rueden, C., Saalfeld, S., Schmid, B., Tinevez, J.Y., White, D.J., Hartenstein, V., Eliceiri, K., Tomancak, P., and Cardona, A. (2012). Fiji: an open-source platform for biological-image analysis. Nat. Methods. *9*, 676–682.

Schmahmann, J.D. (2019). The cerebellum and cognition. Neuroscience Letters *688*, 62–75.

Schmidt, H., Brachtendorf, S., Arendt, O., Hallermann, S., Ishiyama, S., Bornschein, G., Gall, D., Schiffmann, S.N., Heckmann, M., and Eilers, J. (2013). Nanodomain coupling at an excitatory cortical synapse. Curr. Biol. *23*, 244–249.

Schneggenburger, R., Meyer, A.C., and Neher, E. (1999). Released fraction and total size of a pool of immediately available transmitter quanta at a calyx synapse. Neuron *23*, 399–409.

Schoch, S., Castillo, P.E., Jo, T., Mukherjee, K., Geppert, M., Wang, Y., Schmitz, F., Malenka, R.C., and Südhof, T.C. (2002). RIM1α forms a protein scaffold for regulating neurotransmitter release at the active zone. Nature *415*, 321–326.

Scimemi, A., and Diamond, J.S. (2012). The number and organization of Ca^{2+} channels in the active zone shapes neurotransmitter release from Schaffer collateral synapses. J. Neurosci. *32*, 18157–18176.

Sheng, J., He, L., Zheng, H., Xue, L., Luo, F., Shin, W., Sun, T., Kuner, T., Yue, D.T., and Wu, L.G. (2012). Calcium-channel number critically influences synaptic strength and plasticity at the active zone. Nat. Neurosci. *15*, 998–1006.

Shin, O.H., Lu, J., Rhee, J.S., Tomchick, D.R., Pang, Z.P., Wojcik, S.M., Camacho-Perez, M, Brose, N., Machius, M., Rizo, J., Rosenmund, C., and Südhof, T.C. (2010). Munc13 C2B domain is an activity-dependent Ca^{2+} regulator of synaptic exocytosis. Nat. Struct. Mol. Biol. *17*, 280–288.

Silver, R.A. (2003). Estimation of nonuniform quantal parameters with multiple-probability fluctuation analysis: theory, application and limitations. J. Neurosci. Methods *130*, 127–141.

Silver, R.A., Momiyama, A., Cull-Candy, S.G. (1998). Locus of frequency-dependent depression identified with multiple-probability fluctuation analysis at rat climbing fiber-Purkinje cell synapses. J. Physiol. *510*, 881–902.

Smith, G.D. (2001). Modeling local and global calcium signals using reaction-diffusion equations. In Computational Neuroscience, E. de Schutter, ed. (Boca Raton, FL, CRC Press), pp. 49–85.

Starborg, T., Kalson, N.S., Lu, Y., Mironov, A., Cootes, T.F., Holmes, D.F., and Kadler, K.E. (2013). Using transmission electron microscopy and 3View to determine collagen fibril size and three-dimensional organization. Nat. Protoc. *8*, 1433–1448.

Sudarov, A., Turnbull, R., Kim, E.J., Lebel-Potter, M., Guillemot, F., and Loyner, A.L. (2011). *Ascl1* genetics reveals insight into cerebellum local circuit assembly. J. Neurosci. *31*, 11055–11069.

Südhof, T.C. (2012). The presynaptic active zone. Neuron *75*, 11–25.

Sun, J., Pang, Z.P., Qin, D., Fahim, A.T., Adachi, R., and Südhof, T.C. (2007). A dual- Ca2+-sensor model for neurotransmitter release in a central synapse. Nature *450*, 676–682.

Tang, A.H., Chen, H., Li, T., Metzbower, S.R., MacGillavry, H.D., and Blanpied T.A. (2016). A trans-synaptic nanocolumn aligns neurotransmitter release to receptors. Nature *536*, 210–214.

Tang, Y., Nyengaard, J.R., De Groot, D.M., and Gundersen, H.J. (2001). Total regional and global number of synapses in the human brain neocortex. Synapse *41*, 258–273.

Thanawala, M.S., and Regehr, W.G. (2013). Presynaptic calcium influx controls neurotransmitter release in part by regulating the effective size of the readily releasable pool. J. Neurosci. *33*, 4625–4633.

Vincent, P., and Marty, A. (1996). Fluctuation of inhibitory postsynaptic currents in Purkinje cells from rat cerebellar slices. J. Physiol. *494*, 183–199.

Vyleta, N.P., and Jonas, P. (2014). Loose coupling between Ca^{2+} channels and release sensors at a plastic hippocampal synapse. Science *343*, 665–670.

Wang, X.J., Buzsáki, G. (1996). Gamma oscillation by synaptic inhibition in a hippocampal interneuronal network model. J. Neurosci. *16*, 6402–6413.

Wang Y., and Südhof T.C. (2003). Genomic definition of RIM proteins: evolutionary amplification of a family of synaptic regulatory proteins. Genomics *81*, 126–137.

Weber, A.M., Wong, F.K., Tufford, A.R., Schlichter, L.C., Matveev, V., and Stanley, E.F. (2010). N-type Ca2+ channels carry the largest current: implications for nanodomains and transmitter release. Nat. Neurosci. *13*, 1348–1350.

Yamashita, M., Kawaguchi, S.Y., Hori, T., and Takahashi, T. (2018). Vesicular GABA uptake can be rate limiting for recovery of IPSCs from synaptic depression. Cell Rep. *22*, 3134–3141.

Zhou, J., Brown, A.M., Lackey, E.P., Arancillo, M., Lin, T., and Sillitoe, R.V. (2020) Purkinje cell neurotransmission patterns cerebellar basket cells into zonal modules defined by distinct pinceau sizes. eLife *9*, e55569.

Neuron

Article

Developmental transformation of Ca^{2+} channel-vesicle nanotopography at a central GABAergic synapse

Highlights

- Reciprocal changes in release probability and release site number during development
- Maintained reliance on P/Q-type Ca^{2+} channels, but reduced sensitivity to Ca^{2+} chelators
- Ca^{2+} channel clusters throughout development, docked vesicle clusters at later stages
- Developmental transformation from more random to more clustered coupling nanotopographies

Authors

Jing-Jing Chen, Walter A. Kaufmann, Chong Chen, Itaru Arai, Olena Kim, Ryuichi Shigemoto, Peter Jonas

Correspondence

peter.jonas@ist.ac.at

In brief

Chen et al. combine paired recordings, structural analysis, and modeling to examine the coupling between presynaptic Ca^{2+} channels and release sensors in an inhibitory GABAergic synapse at different developmental time points. The results reveal a developmental transformation from more random organization to precise point-to-point synaptic transmission at the nanometer scale.

Chen et al., 2024, Neuron *112*, 755–771
March 6, 2024
https://doi.org/10.1016/j.neuron.2023.12.002

CellPress

Neuron

CellPress
OPEN ACCESS

Article

Developmental transformation of Ca^{2+} channel-vesicle nanotopography at a central GABAergic synapse

Jing-Jing Chen,[1,4] Walter A. Kaufmann,[1,4] Chong Chen,[1,2] Itaru Arai,[1,3] Olena Kim,[1] Ryuichi Shigemoto,[1] and Peter Jonas[1,5,*]

[1]Institute of Science and Technology Austria (ISTA), Am Campus 1, 3400 Klosterneuburg, Austria
[2]Present address: Department of Cell Biology and Physiology, University of North Carolina at Chapel Hill, 116 Manning Dr., Chapel Hill, NC 27599, USA
[3]Present address: Department of Physiology, Keio University School of Medicine, 35 Shinanomachi, Shinjuku-ku, Tokyo 160-8582, Japan
[4]These authors contributed equally
[5]Lead contact
*Correspondence: peter.jonas@ist.ac.at
https://doi.org/10.1016/j.neuron.2023.12.002

SUMMARY

The coupling between Ca^{2+} channels and release sensors is a key factor defining the signaling properties of a synapse. However, the coupling nanotopography at many synapses remains unknown, and it is unclear how it changes during development. To address these questions, we examined coupling at the cerebellar inhibitory basket cell (BC)-Purkinje cell (PC) synapse. Biophysical analysis of transmission by paired recording and intracellular pipette perfusion revealed that the effects of exogenous Ca^{2+} chelators decreased during development, despite constant reliance of release on P/Q-type Ca^{2+} channels. Structural analysis by freeze-fracture replica labeling (FRL) and transmission electron microscopy (EM) indicated that presynaptic P/Q-type Ca^{2+} channels formed nanoclusters throughout development, whereas docked vesicles were only clustered at later developmental stages. Modeling suggested a developmental transformation from a more random to a more clustered coupling nanotopography. Thus, presynaptic signaling developmentally approaches a point-to-point configuration, optimizing speed, reliability, and energy efficiency of synaptic transmission.

INTRODUCTION

Synapses are key sites of exchange and storage of information in neuronal circuits.[1–4] Although all synapses are assembled from similar building blocks, their functional properties differ substantially. However, the mechanisms underlying synaptic diversity are incompletely understood. A key factor defining the signaling properties of a synapse is the coupling between presynaptic Ca^{2+} channels and release sensors.[5–7] Experiments with exogenous Ca^{2+} chelators[8] indicated that the average coupling distance varies among synapses, with tighter "nanodomain" coupling at many inhibitory GABAergic synapses[6,9] and looser "microdomain" coupling at several excitatory glutamatergic synapses.[7,10,11] Nanodomain coupling conveys various functional advantages, including speed and efficacy of synaptic transmission. Conversely, microdomain coupling permits the regulation of release probability via presynaptic plasticity.[7] Thus, channel-vesicle coupling sets the speed, efficacy, and plasticity of synaptic signaling.[3]

Although the Ca^{2+} chelator approach allows precise biophysical measurement of the average coupling distance,[8] the exact topography and stoichiometry of channel-vesicle coupling remains unknown. At the calyx of Held, a biophysically well-characterized synapse, several topographies have been proposed based on freeze-fracture replica labeling (FRL), serial-section electron microscopy (EM), and modeling data. These include random localization of Ca^{2+} channels and synaptic vesicles,[12] random placement of Ca^{2+} channels with an exclusion zone around synaptic vesicles,[13] ring models in which Ca^{2+} channels surround synaptic vesicles,[14] and perimeter models in which synaptic vesicles are positioned near clusters of Ca^{2+} channels.[15] Recent work suggested different coupling topographies at cerebellar parallel fiber synapses (exclusion zone coupling) and stellate cell synapses (perimeter coupling) in the same circuit.[16] However, whether these topographies represent canonical coupling motifs used in other synapses remains unclear.

Coupling between Ca^{2+} channels and release sensors not only differs between synapses but also changes during development.[15,17–19] Developmental tightening of coupling has been reported at several excitatory synapses, including the calyx of Held,[17,20,21] cerebellar parallel fiber synapses,[18] and layer 5 neocortical synapses.[19] However, the corresponding changes in nanotopography have not been defined. At the calyx of Held, developmental tightening of the coupling is associated with a reduction in release probability and an increase in the size of the releasable pool.[22–24] This implies that during

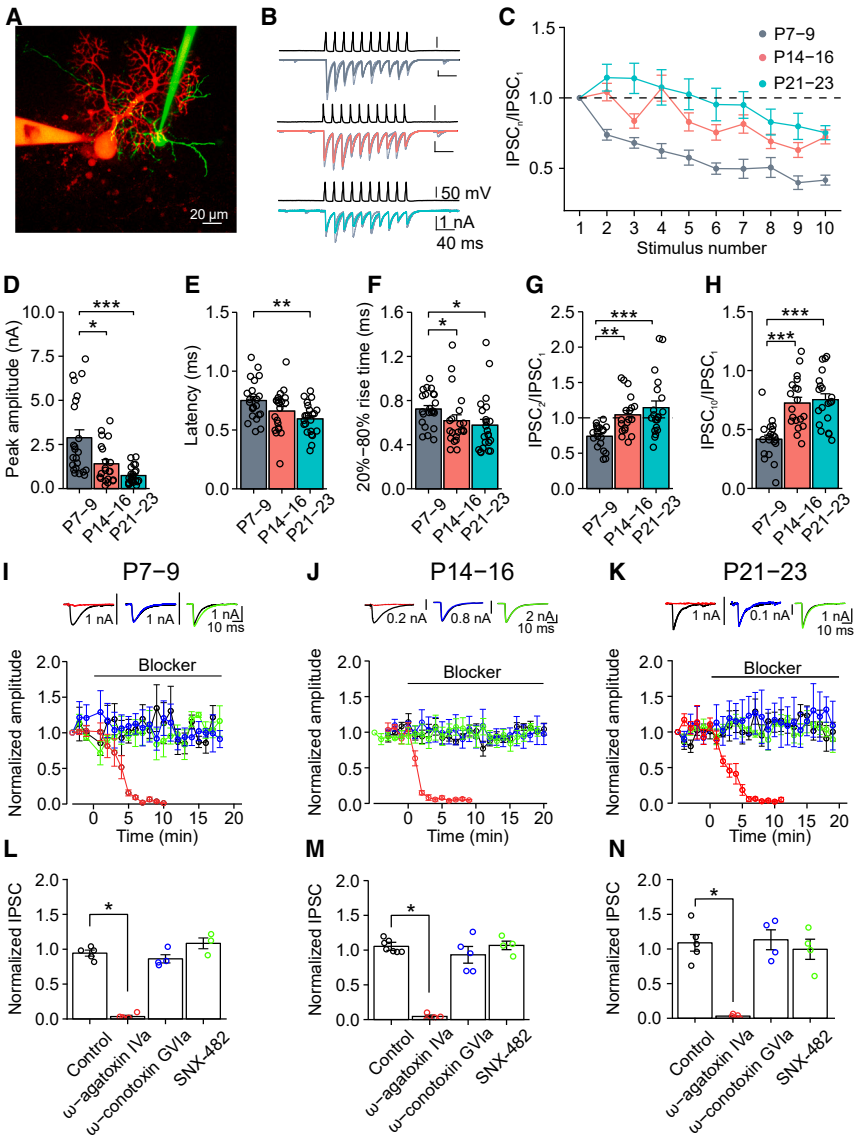

Figure 1. Kinetics, efficacy, and reliance of transmission on P/Q-type Ca^{2+} channels at BC-PC synapses during development

(A) Confocal maximum intensity projection of a basket cell (BC) filled with Alexa Fluor 488 and a synaptically connected Purkinje cell (PC) filled with Alexa Fluor 594 during recording at postnatal day (P) 14.

(B) Representative unitary inhibitory postsynaptic current (IPSC) recordings at the BC-PC synapse at P7, P14, and P21. Top traces represent presynaptic action potentials (APs) evoked by trains of 10 stimuli. Bottom traces are individual IPSCs (light gray) and average IPSCs (gray, red, and cyan) from 3 consecutive traces.

(C) Plot of normalized IPSC amplitude ($IPSC_n$/$IPSC_1$) against stimulus number (n) for P7–9, P14–16, and P21–23 age groups, respectively.

(D–H) Summary bar graphs of IPSC peak amplitude (D), latency measured from the peak of the presynaptic AP to the onset of the IPSC (E), 20%–80% rise time (F), paired-pulse ratio ($IPSC_2$/$IPSC_1$; G), and multiple-pulse ratio ($IPSC_{10}$/$IPSC_1$; H).

(I–K) Transmitter release constantly relies on P/Q-type Ca^{2+} channels during development. Top: Average IPSCs in BC-PC pairs before and after application of 1 µM ω-agatoxin IVa (left), 1 µM ω-conotoxin GVIa (center), and 0.5 µM SNX-482 (right) for P7–9 (I), P14–16 (J), and P21–23 synapses (K). Bottom: Plot of IPSC peak amplitude, normalized to control value, against experimental time during application of 1 µM ω-agatoxin IVa (red), 1 µM ω-conotoxin GVIa (blue), 0.5 µM SNX-482 (green), and mock application of control solution (black).

(L–N) Summary bar graphs of the effects of Ca^{2+} channel blockers at P7–9 (L), P14–16 (M), and P21–23 (N). ω-agatoxin IVa: 5, 4, and 5 pairs; ω-conotoxin GVIa: 4, 5, and 4 pairs; SNX-482: 3, 4, and 4 pairs; control: 5, 7, and 5 pairs, respectively. See also Figures S1–S5 and Table S1.

development, an increasing number of vesicles needs to be coupled to presynaptic Ca^{2+} channels with increasing tightness. How this exactly affects the coupling topography remains enigmatic. To analyze the nanotopography of Ca^{2+} channel-release sensor coupling at GABAergic synapses, we focused on the cerebellar basket cell (BC)-Purkinje cell (PC) synapse.[9,25–27] This synapse is not only a classical inhibitory synapse in the brain[28] but also a particularly suitable model for the analysis of developmental changes.

RESULTS

Developmental changes in synaptic efficacy and kinetics despite constant reliance on Ca^{2+} channel subtype

To probe developmental changes in biophysical properties at an identified GABAergic synapse, we performed paired recordings between synaptically connected BCs and PCs. We first compared the basic transmission properties at three developmental age groups, postnatal day (P) 7–9, P14–16, and P21–23 (Figure 1; Table S1). During development, the peak amplitude of unitary inhibitory postsynaptic currents (IPSCs) declined (Figure 1D), consistent with previous observations.[25] In parallel, both synaptic latency and 20%–80% rise time of IPSCs significantly shortened ($p = 0.0079$ and 0.0072, respectively; Figures 1E and 1F), indicating an increase in speed and temporal precision of synaptic transmission. Furthermore, paired-pulse ratio ($IPSC_2$/$IPSC_1$) and multiple-pulse ratio ($IPSC_{10}$/$IPSC_1$) increased during synaptic maturation (Figures 1G, 1H, and S1), demonstrating increased reliability of transmission during repetitive activity. In contrast, IPSC half-duration and decay time constant changed minimally, suggesting constant properties of postsynaptic $GABA_A$ receptors ($p = 0.38$ and 0.45, respectively; Table S1). These results demonstrate that both efficiency and kinetic properties of BC-PC synapses change during development.

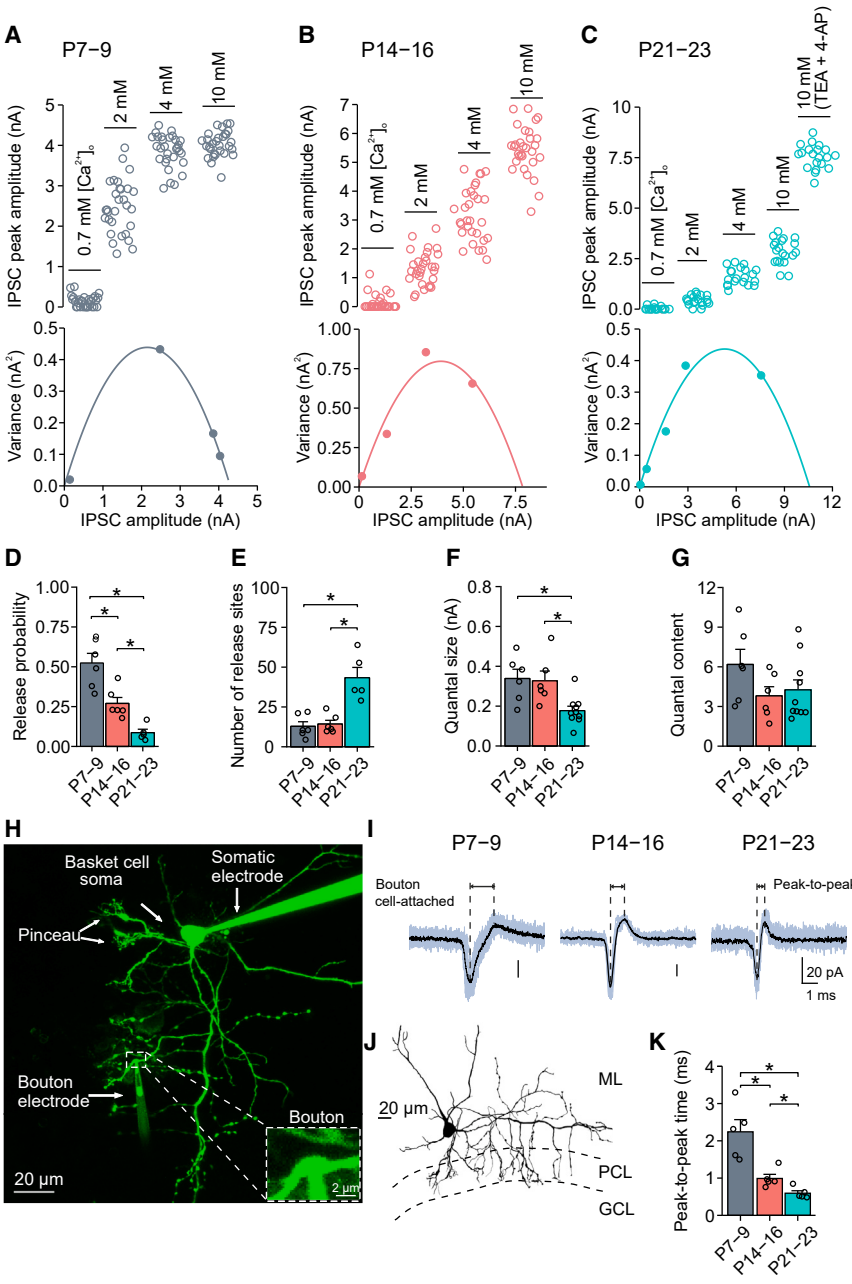

Figure 2. Reciprocal changes in release probability, functional release site number, and presynaptic AP duration during development

(A–C) Example variance-mean measurements of evoked IPSC amplitudes at varying outer Ca^{2+} concentrations ($[Ca^{2+}]_o$) in BC-PC synapses at P9 (A), P14 (B), and P21 (C). Curves represent fits with Equation 1a (STAR Methods).

(D–G) Summary bar graphs of release probability at 2 mM $[Ca^{2+}]_o$ (D), number of functional release sites (E), quantal size (F), and quantal content (G).

(H–K) Changes in presynaptic AP duration during development. (H) Confocal maximum intensity projection of BC filled with Alexa Fluor 488 during recording through a somatic patch pipette. Somatic recording electrode is located on the top right, presynaptic recording electrode is visible at the bottom. (I) Cell-attached voltage-clamp recordings from putative presynaptic terminals. Gray, individual traces; black, average trace. 10 individual traces superimposed. (J) Reconstruction of BC after recording. ML, molecular layer; PCL, Purkinje cell layer, GCL, granule cell layer. (K) Summary bar graph of AP half-duration measured from presynaptic terminal. Half-duration of the presynaptic AP was quantified as the time difference between negative and positive peaks of presynaptic action current. Data are from 5 (P7–9), 5 (P14–16), and 5 (P21–23) bouton recordings. See also Figures S1–S5 and Tables S1 and S3.

At all previously investigated synapses, transmitter release relies on P/Q-, N-, and R-type channels early in development but switches to P/Q-type channels at later time points.[19,23,29] Therefore, we examined the reliance of transmitter release on different types of presynaptic Ca^{2+} channels at the BC-PC synapse (Figures 1I–1N). To determine the contribution of P/Q-type Ca^{2+} channels, we applied 1 µM of the selective P/Q-type Ca^{2+} channel blocker ω-agatoxin IVa, a concentration expected to completely block both P- and Q-type channels.[30] Surprisingly, ω-agatoxin IVa almost completely blocked synaptic transmission at all developmental stages. The residual evoked IPSC 10–20 min after toxin application was 3.4% ± 1.6% of the control value at P7–9, 4.5% ± 2.0% at P14–16, and 3.1% ± 1.0% at P21–23 (mean ± SEM; 5, 4, and 5 pairs, respectively; $p < 0.05$). In contrast, 1 µM ω-conotoxin GVIa, a selective blocker of N-type channels, and 500 nM SNX-482, a blocker of R-type channels, had only minimal effects on unitary IPSCs in all age groups (ω-conotoxin GVIa: 86.2% ± 5.9% at P7–9, 93.2% ± 10.8% at P14–16, and 113.3% ± 14.4% at P21–23; SNX-482: 108.4% ± 8.9% at P7–9, 106.8% ± 6.1% at P14–16, and 99.6% ± 14.5% at P21–23; $p > 0.5$; Figures 1L–1N). These results indicate that, throughout the developmental period examined, transmitter release at cerebellar BC-PC synapses exclusively relies on P/Q-type Ca^{2+} channels.

Changes in release probability, number of functional release sites, and vesicle pool size

According to the quantal theory of synaptic transmission, the average amplitude of single IPSCs is given as IPSC = $p_R \times N \times q$, where p_R is release probability, N is number of functional release sites, and q is quantal size.[31] To determine how quantal parameters at the BC-PC synapse change during development, we performed nonstationary fluctuation analysis of evoked IPSCs at different developmental time points (Figure 2).[32] The extracellular Ca^{2+} concentration was changed between 0.7 mM and 10 mM.

Variance and mean of IPSC peak amplitudes were determined from stationary periods after the Ca^{2+} concentration change, and variance was plotted against mean for individual experiments. In a subset of experiments with 10 mM Ca^{2+}, the K^+ channel blockers tetraethylammonium (TEA, 1 mM) and 4-aminopyridine (4-AP, 0.05 mM) were added to maximally enhance release.[33,34]

Variance-mean analysis revealed that release probability at 2 mM extracellular Ca^{2+} decreased from 0.52 ± 0.06 at P7–9 to 0.27 ± 0.04 at P14–16, and 0.09 ± 0.02 at P21–23 (6, 6, and 5 pairs, respectively; p = 0.0013; Figure 2D). Consistent with a reduction of p_R, the Ca^{2+} dependence of transmitter release shifted to higher concentrations during synaptic maturation (Figure S1). The number of functional release sites increased in parallel, from 12.8 ± 2.9 at P7–9 to 14.3 ± 2.4 at P14–16, and 43.3 ± 6.5 at P21–23 (p = 0.0061; Figure 2E). These results suggest a major reorganization of the release mechanism at BC-PC synapses during development. While p_R decreased, N became progressively larger during synaptic maturation. In parallel, the quantal size significantly declined during synaptic maturation (from 338.5 ± 46.6 pA at P7–9 to 327.1 ± 49.0 pA at P14–16, and 177.3 ± 22.2 pA at P21–23; p = 0.0066; Figure 2F). In contrast, the quantal content (p_R × N) was only slightly but not significantly reduced, implying that the changes in p_R and N largely compensated for each other (p = 0.13; Figure 2G).

To probe developmental changes in the vesicular pool, we performed cumulative release analysis (Figure S2).[35,36] Synapses were stimulated repetitively, normalized IPSC peak amplitude values were cumulatively plotted against stimulus number, and the size of the readily releasable pool (RRP) was determined by linear regression (STAR Methods). RRP size increased during development, from 37.4 ± 5.3 quanta at P7–9 to 51.6 ± 8.1 quanta at P14–16, and 72.6 ± 13.1 quanta at P21–23 (p = 0.028; Figure S2). Thus, the vesicular pool size was developmentally upregulated.

To exclude that TEA and 4-AP affected our quantal parameter estimates, we compared the results from variance-mean analysis at P7–9 synapses in the absence and presence of TEA and 4-AP. No significant differences were detected, validating the use of these blockers in our analysis (p > 0.2; Figures S3A–S3F). To exclude the possibility that saturation or desensitization of postsynaptic receptors confounded the variance-mean analysis, additional experiments were performed in the presence of a low-affinity competitive $GABA_A$ receptor antagonist (1,2,5,6-tetrahydropyridin-4-yl) methylphosphinic acid (TPMPA; 300 μM)[37] and a $GABA_B$ receptor antagonist (CGP 55845; 1 μM); CGP 55845 was added to rule out possible effects of TPMPA on presynaptic $GABA_B$ receptors.[38] In the presence of TPMPA and CGP 55845, q significantly decreased (p = 0.016), showing the effectiveness of the $GABA_A$ receptor antagonist, whereas p_R and N remained constant (Figures S3G–S3L). Thus, postsynaptic receptor saturation or desensitization are unlikely to affect our measurements. These results corroborate our observations of reciprocal changes in p_R and N during development.

Shortening of the presynaptic action potential (AP) in BC terminals

To obtain insight into the mechanisms underlying developmental changes in p_R, we analyzed the shape of the presynaptic AP that initiates transmitter release (Figures 2H–2K). A somatic whole-cell recording was obtained from a BC, the neuron was filled with Alexa Fluor 488, and the axon arbor including presynaptic terminals surrounding PC somata was visualized using confocal microscopy (Figure 2H). Subsequently, a cell-attached recording was obtained from a BC presynaptic terminal. Analysis of the peak-to-peak duration of the presynaptic action current, a proxy of the half-duration of the presynaptic AP (Figures S4A–S4C), revealed a marked change in duration, from 2.24 ± 0.33 ms at P7–9 to 0.99 ± 0.11 ms at P14–16, and 0.59 ± 0.07 ms at P21–23 (5 presynaptic recordings per age group; p = 0.0025; Figure 2K). In contrast, the half-duration of the somatic AP decreased less prominently, from 1.11 ± 0.05 ms at P7–9 to 0.78 ± 0.03 ms at P14–16, and 0.75 ± 0.02 ms at P21–23 (15 somatic recordings per age group; p < 0.001; Table S1). Thus, the presynaptic AP undergoes substantial shortening during development. Together with the constant reliance of transmitter release on P/Q-type Ca^{2+} channels (Figures 1I–1N), these results suggest a reduced efficacy of opening of these channels by the presynaptic AP.

To further test this hypothesis, we measured presynaptic Ca^{2+} transients in BC terminals (Figure S5). BCs were filled with Fluo-5F (200 μM) and Alexa Fluor 594 (80 μM), Ca^{2+} transients were evoked by single APs, and ratiometric imaging was performed. Peak amplitudes of Ca^{2+} transients became significantly smaller during development (Figure S5C). In parallel, decay time constants became shorter, suggesting that the amplitude reduction was generated by reduced Ca^{2+} inflow rather than increased Ca^{2+} buffering.[39] Consistent with this conclusion, application of K^+ channel blockers significantly increased the peak amplitude of Ca^{2+} transients at P21–23, but not in the P7–9 and the P14–16 age groups (Figure S5E). These results provide converging evidence that the efficacy of presynaptic Ca^{2+} channel opening decreases during development.

Tightening of coupling between Ca^{2+} channels and release sensors

At several excitatory synapses, the coupling between Ca^{2+} channels and release sensors becomes progressively tighter during development.[17–21] However, in all of these cases, reliance on the Ca^{2+} channel subtype changes during maturation, making it difficult to distinguish direct effects of coupling from indirect effects of changes in Ca^{2+} channel subtype. To probe the channel-sensor coupling distance at the BC-PC synapse at different developmental time points, we infused 10 mM of the slow Ca^{2+} chelator ethyleneglycol-bis(β-aminoethylether)-N,N,N′,N′-tetraacetic acid (EGTA) into the presynaptic terminals by pipette perfusion (Figure 3).[6,21] Pipette perfusion provides a quantitatively controlled way of probing the chelator sensitivity, minimizing any confounding effects of wash-in of anions[40] or wash-out of mobile endogenous buffers, such as parvalbumin (PV).[27,41] In P7–9 synapses, infusion of 10 mM EGTA gradually suppressed synaptic transmission (Figures 3B–3D). In contrast, at P21–23 synapses, infusion of 10 mM EGTA had only minimal effects (p = 0.0127; Figures 3E and 3F; Table S1). In P14–16 synapses, the effects of EGTA were also minimal, confirming the previous conclusion that transmitter release at this developmental stage is triggered by nanodomain coupling (Figures 3E and 3F).[9] In contrast to EGTA, infusion of 10 mM of the fast Ca^{2+} chelator ethylenedioxybis-(*o*-phenylenenitrilo)-N,N,N′,N′-tetraacetic acid (BAPTA) strongly suppressed

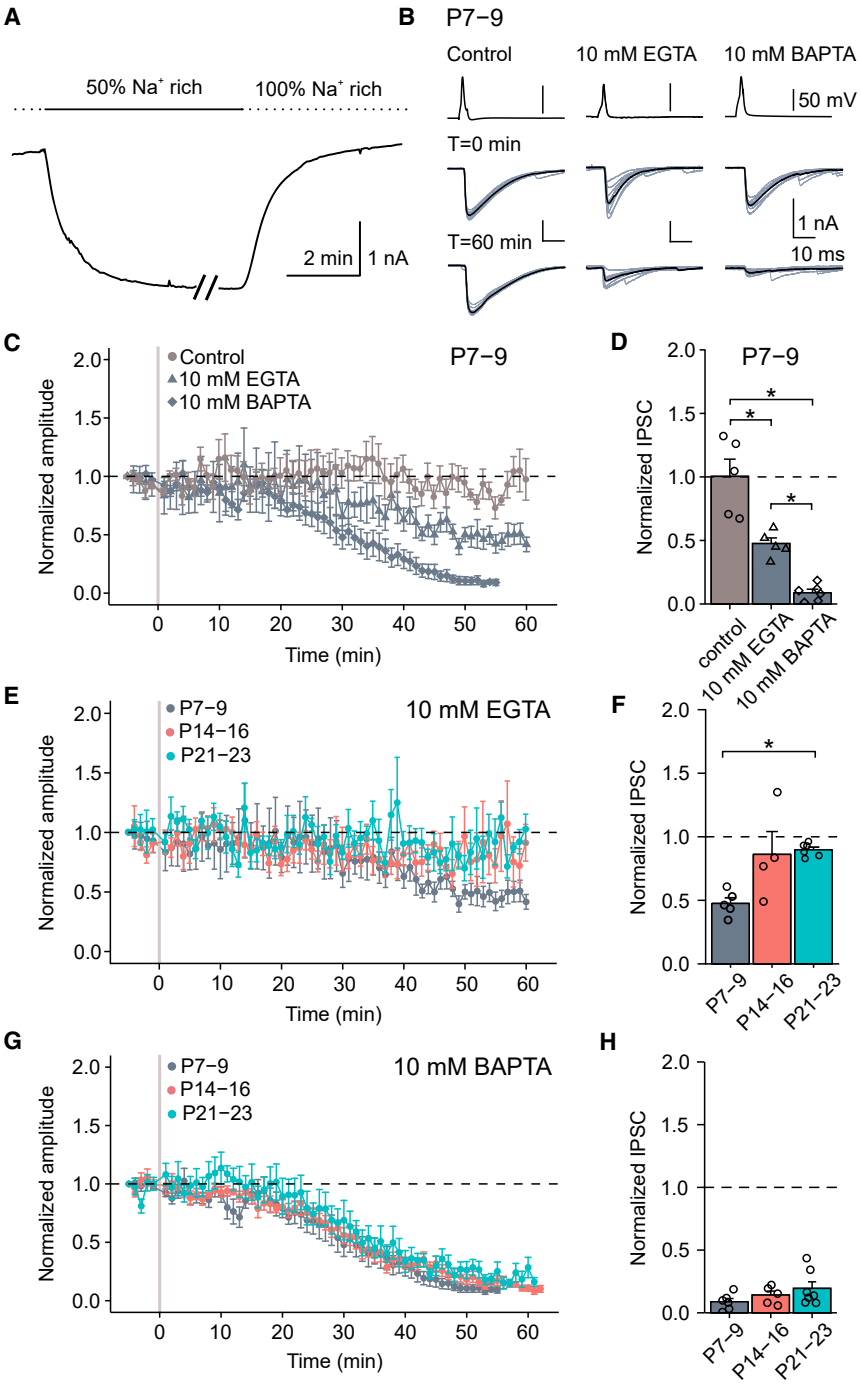

Figure 3. Decrease of exogenous Ca^{2+} chelator sensitivity during development

(A) Speed of solution exchange by pipette perfusion, measured as a change in junction current in an open patch pipette during a solution change from 100% Na^+-rich to 50% Na^+-rich solution and back.

(B) IPSCs in a BC-PC synapse under control conditions (left), loading presynaptic terminals with 10 mM EGTA (middle), and loading presynaptic terminals with 10 mM BAPTA (right) at P9. Top traces represent APs; center traces represent IPSC amplitudes before loading; bottom traces represent IPSC amplitudes 60 min after loading.

(C) Plot of IPSC peak amplitude against experimental time for control, 10 mM EGTA, and 10 mM BAPTA loading by pipette perfusion in P7–9 synapses. Gray vertical bar indicates the time when loading starts.

(D) Summary bar graph of the effects of EGTA and BAPTA on synaptic transmission at P7–9 synapses.

(E and G) Plots of IPSC peak amplitude against experimental time for 10 mM EGTA (E) and 10 mM BAPTA (G) loading by pipette perfusion in P7–9 (gray), P14–16 (red), and P21–23 synapses (cyan).

(F and H) Summary bar graphs of the effects of EGTA (F) and BAPTA (H) on synaptic transmission at BC-PC synapses at different developmental stages. See also Figures S1–S5 and Table S1.

synaptic transmission at all developmental stages (Figures 3G and 3H; Table S1). Taken together, our results suggest developmental tightening of channel-sensor coupling[3] independently of any switch in Ca^{2+} channel subtype.

Changes in bouton and AZ numbers and in nanoscopic AZ structure

We next attempted to obtain insight into the mechanisms underlying changes in the number of functional release sites, N. Although the functional release site is a widely used concept, the structural correlate remains elusive.[42–44] To examine the structural properties of BC-PC synapses during synaptic maturation, we combined light microscopy (LM) and EM analysis (Figure 4; Table S2). Analysis was performed at P7–9, P14–16, and P21–23, developmental time points identical to those used in our biophysical experiments. We first determined the number of boutons per connection, using a triple labeling procedure (Figures 4A and 4B). BCs were filled with biocytin via whole-cell recording and labeled with Alexa Fluor-conjugated streptavidin (5, 5, and 6 biocytin-filled BCs, respectively). Synaptic boutons were identified using antibodies against vesicular GABA transporters (VGAT) and postsynaptic $GABA_A$ receptor alpha-1 subunits ($GABA_A$ α1). LM analysis including both somata and proximal dendrites of PCs revealed that the number of boutons per connection increased from 6.55 ± 0.64 at P7–9 to 8.40 ± 1.09 at P14–16, and 9.00 ± 0.95 at P21–23 (11, 10, and 10 PCs; p = 0.1126). Thus, the BC-PC synapse is a multi-bouton connection throughout development (Figure 4E).

Next, we determined the number of AZs per bouton, using serial-section EM on perfusion-fixed brain samples (Figures 4C, 4D, and 4F). BC-PC synapses were unequivocally identified, based on their morphological characteristics and location.

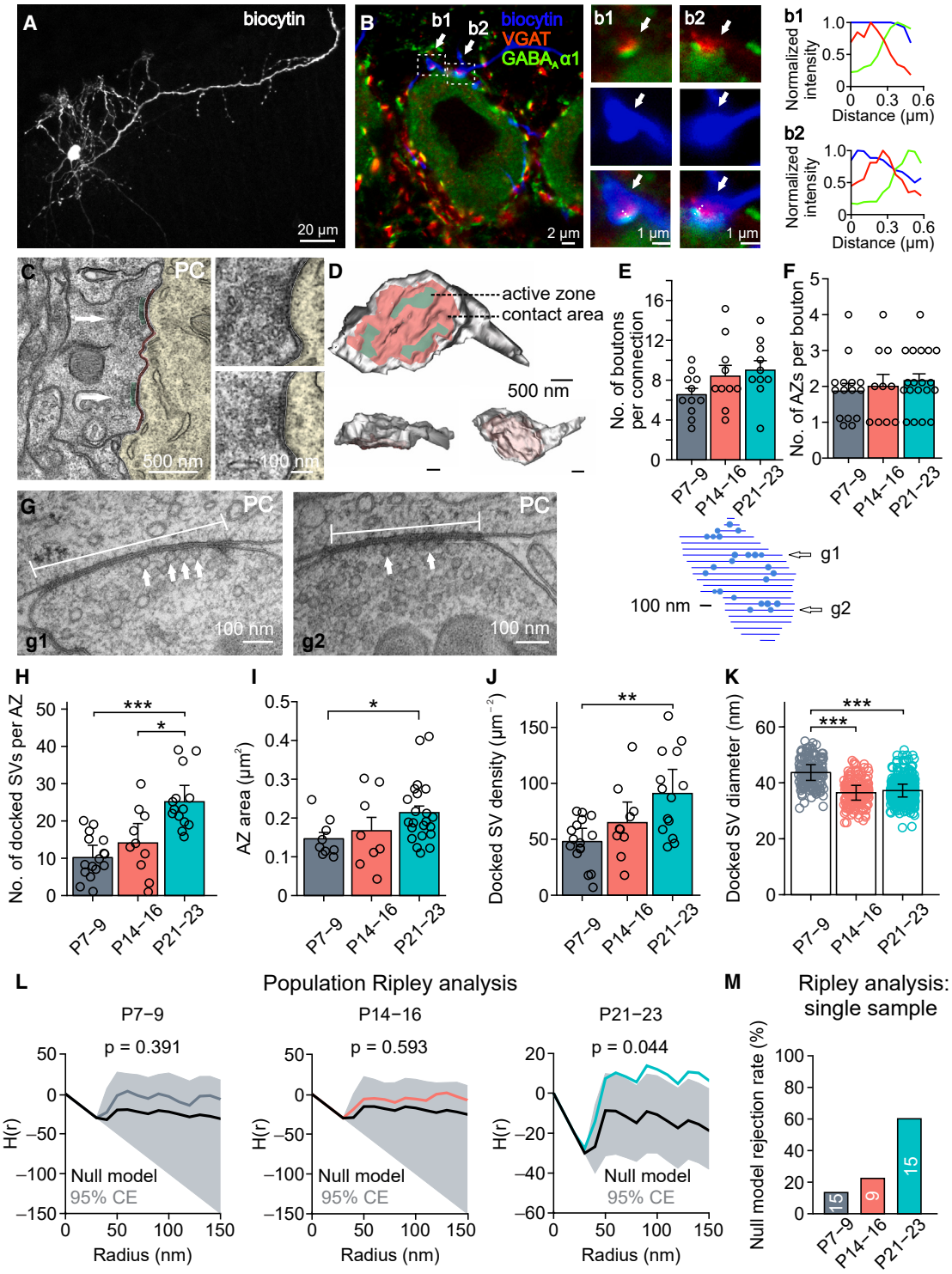

Figure 4. Number of boutons, active zones (AZs), and docked vesicles at BC-PC synapses during development

(A) Confocal maximum intensity projection of BC at P14 filled with biocytin during recording and labeled using Alexa Fluor-conjugated streptavidin.

(B) Example confocal fluorescence micrographs of biocytin-labeled BC terminals and immunolabeling for VGAT and GABA$_A$ α1 subunit in a BC-PC synapse at P14. White arrows indicate two boutons. Individual fluorescent signals were converted into red, green, and blue pseudocolors to improve clarity. Dashed lines indicate pixels used for intensity profile plots (right).

(legend continued on next page)

Evaluation of the AZ number in fully reconstructed boutons revealed 1.87 ± 0.22 AZs per bouton at P7–9, 2.00 ± 0.33 AZs per bouton at P14–16, and 2.16 ± 0.19 AZs per bouton at P21–23 (15, 10, and 19 fully reconstructed boutons; $p = 0.5371$). Thus, the majority of GABAergic boutons contained one to three AZs, independently of the developmental stage (Figure 4F).

Finally, we analyzed the nanoscopic structure of the AZs in more detail (Figures 4G–4K). To accurately determine the number of docked vesicles, we performed cryo-fixation of acute brain slices, which avoids confounding effects of chemical fixation,[45] and reconstructed entire AZs using serial section EM. The number of docked vesicles per AZ substantially increased during development, from 10.2 ± 1.4 at P7–9 to 14.1 ± 2.8 at P14–16, and 25.1 ± 2.0 at P21–23 (16, 10, and 14 AZs; $p < 0.0001$). The AZ area also significantly increased, from 0.15 ± 0.02 μm^2 at P7–9 to 0.17 ± 0.04 μm^2 at P14–16, and 0.21 ± 0.02 μm^2 at P21–23 (9, 8, and 22 AZs; $p = 0.0474$). Thus, the overall AZ area at BC-PC synapses appeared larger than at excitatory synapses[46] and other inhibitory synapses.[47] In parallel, the density of docked vesicles significantly increased from 48.0 ± 5.1 μm^{-2} at P7–9 to 64.9 ± 10.1 μm^{-2} at P14–16, and 90.9 ± 10.0 μm^{-2} at P21–23 ($p = 0.0082$). This indicates that the increase in the total number of docked vesicles per AZ is caused by a combination of both increase in AZ area and increase in vesicle density. Finally, we found that the diameter of synaptic vesicles decreased slightly, but significantly, during synaptic maturation (Figure 4K), which may explain the declining quantal size (Figure 2F).

To determine the distribution of docked vesicles within AZs, we analyzed nearest neighbor distance (NND) distributions of docked synaptic vesicles and compared them to simulated random distributions (Figure S6). NND analysis revealed that vesicles were non-randomly distributed at all three developmental stages ($p < 0.001$; Figures S6A–S6D). To distinguish between clustering and dispersion, we performed Ripley's H(r) function analysis (Figures 4L and 4M).[16,48] At both P7–9 and P14–16, maximal H(r) values were not significantly different in measured and randomized data (15 and 9 AZs; $p = 0.39$ and 0.59, respectively), and the proportion of individual AZs with significant maximal H(r) was small (13.3% for P7–9 and 22.2% for P14–16). In contrast, at P21–23 synapses, maximal H(r) values were significantly higher than in randomized data (15 AZs; $p = 0.04$), and the proportion of individual AZs with significant vesicle clustering was much larger (60.0%; $p < 0.05$; Figure 4M). These results suggest that the distribution of docked synaptic vesicles at AZs changes from a more random to a more clustered configuration during development.

Clustering of presynaptic Ca^{2+} channels

To determine the coupling nanotopography, we analyzed the distribution of presynaptic Ca^{2+} channels by means of FRL, a diffusion-free method with single-molecule resolution and unique sensitivity (Figure 5).[21,49–51] BC-PC synapses were ideal for this analysis because transmitter release was exclusively mediated by P/Q-type Ca^{2+} channels (Figures 1I–1N). This allowed us to quantitatively analyze presynaptic Ca^{2+} channel numbers and localization by immunolabeling with anti-$Ca_V2.1$ α_{1A} antibodies,[16] which labeled presynaptic Ca^{2+} channels with high efficiency (77.6%; STAR Methods and Li et al.[52]) and specificity (minimal labeling in $Ca_V2.1$ $\alpha_{1A}^{-/-}$ mice; Figure S7). GABAergic synapses were identified by immunolabeling for VGAT, which was detected, albeit with low density, in the plasma membrane of GABAergic terminals (Figures 5A–5C).[53] This was particularly important early in development, when glutamatergic axons occasionally form synapses with PC somata.[54] For identification of AZs, we applied antibodies against the AZ marker proteins Rab3a-interacting molecule (RIM); E-, L-, K-, and S-rich protein (ELKS); and neurexin in a mix (STAR Methods). AZs were delineated drawing a polygon around the outermost immunoparticles for both $Ca_V2.1$ and the AZ marker proteins (Figure S8).[51] FRL analysis revealed that the number of $Ca_V2.1$ particles per AZ significantly increased during maturation (Figure 5D). In parallel, the AZ area increased as well (Figure 5E), resulting in similar particle densities throughout development (Figure 5F). These results reveal a largely constant Ca^{2+} channel density in AZs of GABAergic BC-PC synapses.

FRL analysis further revealed that immunoparticles for $Ca_V2.1$ in AZs of BC terminals were non-randomly distributed (Figures 5G, 5H, and S9). The measured NND was significantly smaller than the corresponding simulated value, suggesting clustering of the channels ($p < 0.001$; Figure S9).[51] To further evaluate this, we performed Ripley's H(r) function analysis (Figures 5G

(C) Transmission electron micrograph of a BC bouton at P14. Left, low-magnification view; contact area color-coded in pink, AZ area in green. Right, high-magnification view of AZs (white arrows in left panel). PC soma color-coded in yellow.
(D) 3D reconstruction of a BC bouton at P9. Contact area between BC terminal and PC soma is depicted in pink, AZ area in green. View from top, side, and bottom, respectively.
(E and F) Summary bar graphs of the number of boutons emerging from a single BC and terminating in the perisomatic area of a single PC (from confocal immunohistochemistry analysis; E) and the number of AZs per bouton (from serial section EM analysis; F).
(G) Transmission electron micrographs (left) and corresponding reconstruction of docked vesicle distribution from serial sections (right, blue circles) of an AZ of a BC-PC synapse at P21. Sections (left) correspond to arrows g1 and g2 (right).
(H–K) Summary bar graphs of number of docked synaptic vesicles per AZ (H), AZ area (I), docked synaptic vesicle density (J), and docked synaptic vesicle diameter (K) at P7–9, P14–16, and P21–23 respectively. Circles represent data from individual connections, boutons, AZs, or vesicles. Bars indicate mean ± SEM.
(L) Ripley H-function analysis of docked vesicle distribution in individual AZs for P7–9 (left), P14–16 (center), and P21–23 age group (right) AZs. Gray, red, and cyan curves represent the edge-corrected H(r) function for 15, 9, and 15 AZs, respectively. The black line represents the mean H(r) function calculated from 100 null model point pattern simulations from each AZ. The gray shaded area represents the 95% confidence envelope (CE). Population p value was calculated using a maximum difference test.
(M) Ripley H-function analysis of docked vesicle distribution in individual AZs revealed that the null model was rejected (maximum difference test) for 13.3% of P7–9, 22.2% of P14–16, and 60.0% of P21–23 AZs.
Data in (C)–(F) and (I) were obtained from chemically fixed tissue; data in (G), (H), (J), and (K)–(M) were obtained from cryofixed tissue. See also Figure S6 and Tables S2 and S3.

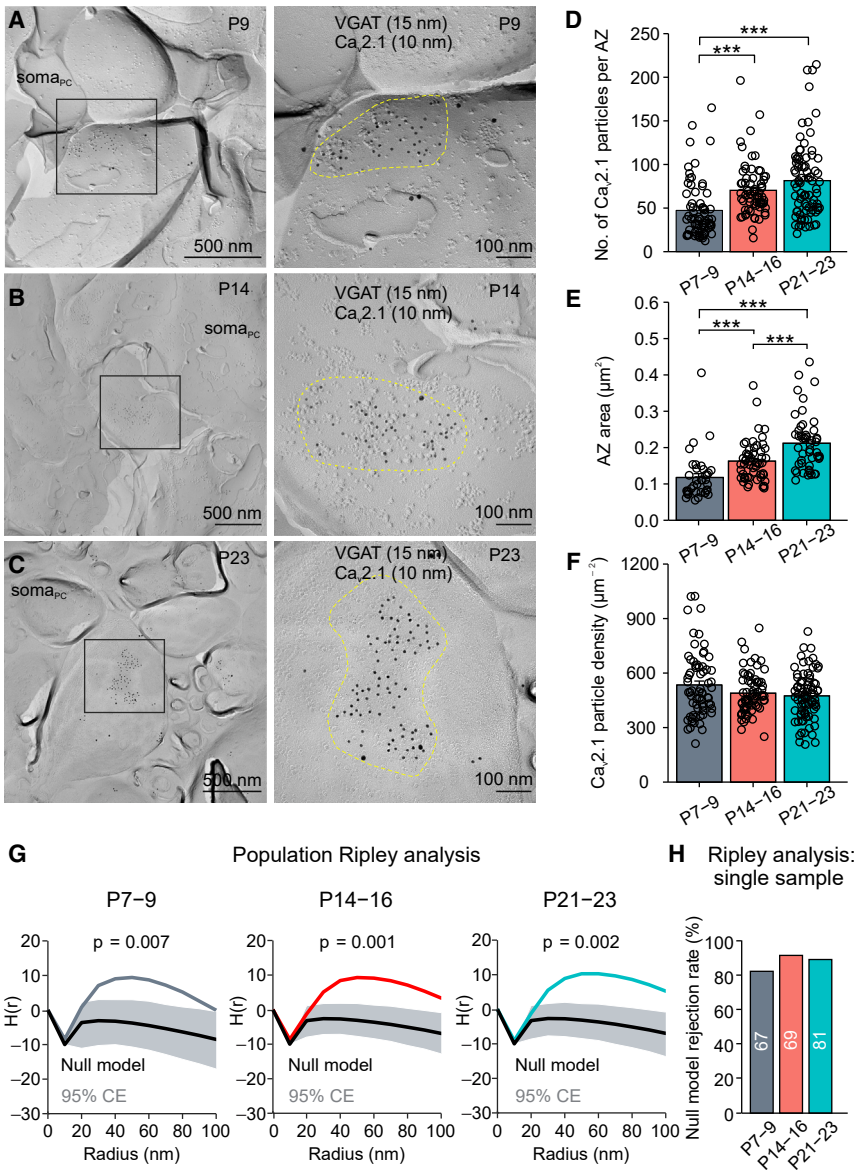

Figure 5. Nanoclusters of presynaptic Ca^{2+} channels in AZs of BC terminals revealed by freeze-fracture replica labeling (FRL)

(A–C) FRL of presynaptic Ca^{2+} channels in AZs at P9 (A), P14 (B), and P23 (C), respectively. 15-nm gold particles represent VGAT immunoreactivity; 10-nm gold particles label presynaptic $Ca_v2.1$ Ca^{2+} channels. BC terminals were identified by location near PC soma and VGAT expression. Putative AZ boundaries are indicated by yellow dashed lines. Right panels show zoomed images from the black rectangular boxes in left panels.

(D–F) Summary bar graphs of number of $Ca_v2.1$ particles per AZ (D), putative AZ area (E), and corresponding particle density in AZs (F). Circles represent data from individual AZs; bars indicate mean ± SEM.

(G) Ripley H-function analysis of $Ca_v2.1$ gold particle distribution across the population of P7–9 (left), P14–16 (center), and P21–23 AZs (right). Gray, red, and cyan curves represent the edge-corrected H(r) function for 67, 69, and 81 AZs, respectively. The black line represents the mean H(r) function calculated from 100 null model point pattern simulations from each AZ. The gray shaded area represents the 95% confidence envelope (CE). Population p value was calculated using a maximum difference test.

(H) Ripley H-function analysis of $Ca_v2.1$ gold particle distribution in individual AZs revealed that the null model was rejected (maximum difference test) for 82.1% of P7–9, 91.3% of P14–16, and 88.9% of P21–23 AZs. See also Figures S7–S9 and Table S2.

and 5H).[16,48] Population analysis revealed a prominent positive peak and a significant difference from the null model for all developmental stages (67, 69, and 81 AZs; p = 0.007, 0.001, and 0.002, respectively; Figure 5G). Analysis of null model rejection rate in individual AZs corroborated this conclusion (rejection for >80% of AZs at three developmental stages; $p < 0.05$; Figure 5H). Thus, presynaptic Ca^{2+} channels in BC-PC synapses were significantly clustered at all developmental time points.

To determine the number of Ca^{2+} channel clusters and analyze their properties, we used a "density-based spatial clustering of applications with noise" (DBSCAN) algorithm (Figure 6). We found that the number of clusters per AZ increased significantly during development (2.91 ± 0.19 at P7–9, 4.38 ± 0.23 at P14–16, and 4.64 ± 0.23 at P21–23; 67, 69, and 81 AZs; $p < 0.001$; Figures 6G–6I and 6M), whereas the average number of particles per cluster remained almost constant (15.6 ± 1.1 at P7–9, 15.4 ± 1.0 at P14–16, and 16.9 ± 1.0 at P21–23; 194, 299, and 373 clusters; p = 0.44; Figures 6J–6L and 6N). The spacing of channels within clusters, as quantified by NND, was 20.86 ± 0.29 nm at P7–9, 22.90 ± 0.25 nm at P14–16, and 23.27 ± 0.21 nm at P21–23 (Figure 6O). In contrast, the distance between adjacent clusters was much wider, 143.7 ± 3.5 nm at P7–9, 146.2 ± 2.7 nm at P14–16, and 159.8 ± 3.1 nm at P21–23 (Figure 6P). Thus, whereas individual channels within a given cluster were tightly packed, clusters within the same AZ were widely separated.

Analysis of EM and FRL data allowed us to further compute the stoichiometric ratios of the channel-vesicle coupling. On average, the number of docked vesicles associated with a Ca^{2+} channel cluster was 3.50 at P7–9, 3.22 at P14–16, and 5.42 at P21–23. Hence, BC-PC synapses show an increasing excess of the number of docked synaptic vesicles over the number of Ca^{2+} channel clusters.

Changes in Ca^{2+} domain structure during development

Our results provide detailed information about p_R, sensitivity of release to Ca^{2+} chelators, type and distribution of presynaptic Ca^{2+} channels, and numbers of synaptic vesicles. Taken

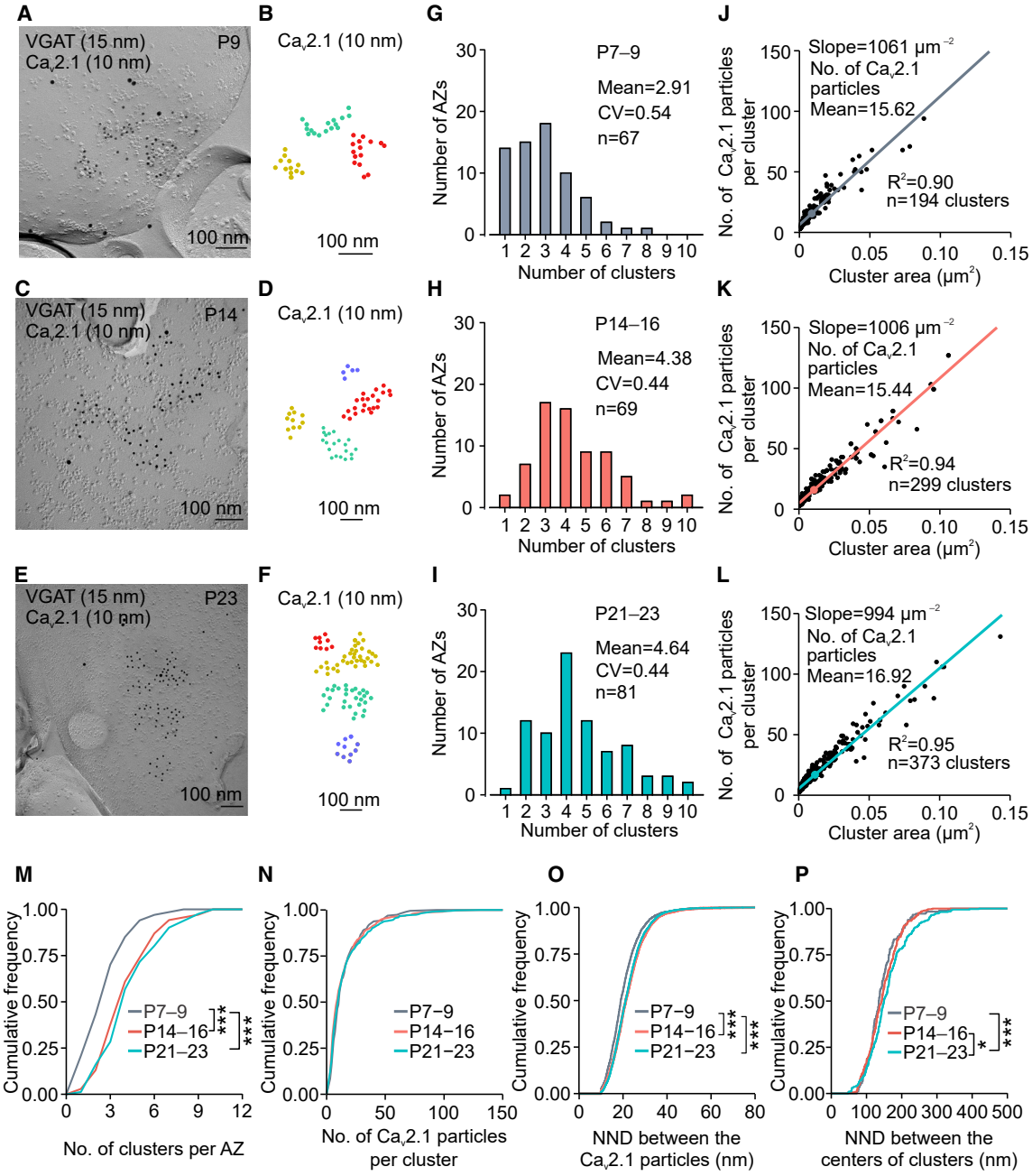

Figure 6. Developmental changes in number and properties of presynaptic Ca^{2+} channel clusters

(A–F) Distributions of Ca$_v$2.1 clusters in representative AZs from the P7–9 (A and B), P14–16 (C and D), and P21–23 age groups (E and F). Original EM micrographs are shown in (A), (C), and (E) and positions of gold particle labeling Ca$_v$2.1, color-coded according to cluster allocation in (B), (D), and (F). Single scattered particles not allocated to clusters were omitted from the analysis.

(G–I) Distribution histograms for the number of Ca$_v$2.1 clusters per AZ at P7–9 (G), P14–16 (H), and P21–23 age groups (I).

(J–L) Plots of Ca$_v$2.1 gold particle number per cluster against cluster area at P7–9 (J), P14–16 (K), and P21–23 age groups (L). Gray, red, and cyan filled circles indicate mean values.

(M and N) Cumulative distributions of the number of Ca$_v$2.1 clusters per AZ (M) and the number of Ca$_v$2.1 particles per cluster (N) for P7–9 (gray), P14–16 (red), and P21–23 age groups (cyan).

(O and P) Cumulative distributions of nearest neighbor distance (NND) values between Ca$_v$2.1 particles within a cluster (O) and between the centers of Ca$_v$2.1 clusters (P) for P7–9 (gray), P14–16 (red), and P21–23 age groups (cyan), respectively. The NND between the centers of clusters was calculated by averaging coordinates of all particles in individual clusters. See also Figures S7 and S8 and Table S2.

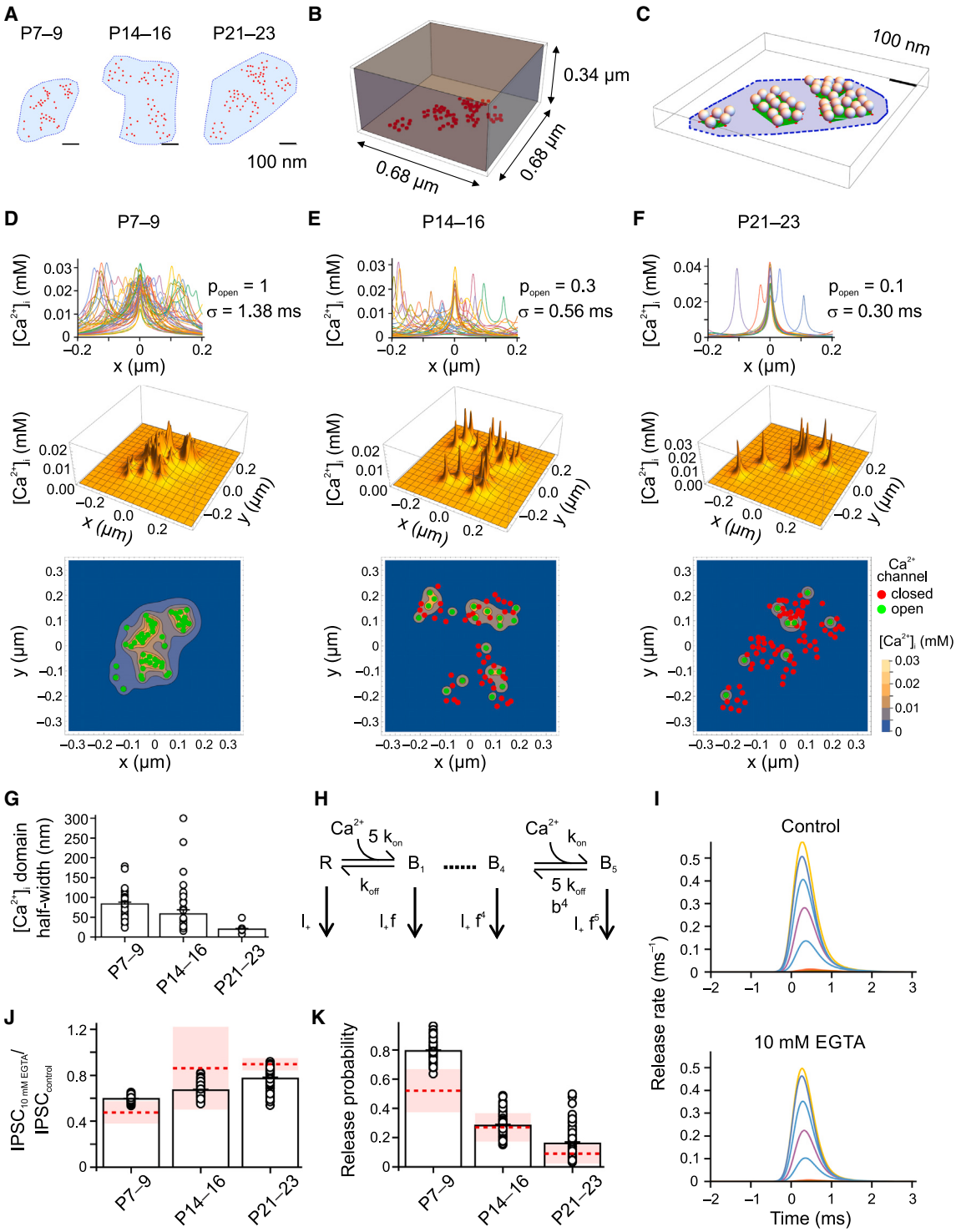

Figure 7. Sharpening of Ca^{2+} domains in cerebellar BC terminals during development

(A) Topography of three representative AZs from the P7–9, P14–16, and P21–23 age groups. Blue, AZ area; red, presynaptic Ca^{2+} channels.

(B) Schematic illustration of simulations of buffered diffusion of Ca^{2+}. The full set of partial differential equations was solved assuming a three-dimensional spatial grid with 5-nm resolution. Gray cube, simulated volume. For details, see STAR Methods.

(C) Model of AZ in which vesicles were attached to the presynaptic membrane opposite to nanoclusters of presynaptic Ca^{2+} channels. Spheres, synaptic vesicles; red dots, presynaptic Ca^{2+} channels; green areas, convex hull around Ca^{2+} channel clusters. Vesicles were attached at 5 nm vertical distance from the plasma membrane, consistent with the distance of docked vesicles.

(legend continued on next page)

together, these data constrain the coupling configuration. To fully exploit this information, we generated a realistic model of Ca^{2+} diffusion and sensor activation at BC terminals (Figure 7). Duration and amplitude of the presynaptic Ca^{2+} flux were constrained by our presynaptic recordings (Figure S4) and previous analysis of gating and single-channel conductance of P/Q-type Ca^{2+} channels.[52,56–59] Buffered diffusion of Ca^{2+} was modeled by numerical solution of the full set of partial differential equations in three dimensions, assuming a fixed Ca^{2+} buffer, a low-affinity endogenous mobile Ca^{2+} buffer, and a high-affinity exogenous mobile Ca^{2+} buffer (EGTA or BAPTA; see STAR Methods).[3,6,7,15,60] Finally, transmitter release was computed using a Ca^{2+} sensor model for synaptotagmin-2, the putative Ca^{2+} sensor of exocytosis at the BC-PC synapse.[55,61–63]

First, we simulated Ca^{2+} domains around Ca^{2+} channels assuming realistic distributions, including their non-random localization (Figure 7A). Intracellular Ca^{2+} concentration was plotted in two dimensions parallel to the AZ. Presynaptic Ca^{2+} flux was represented by Gaussian functions with standard deviations σ of 1.38 ms, 0.56 ms, and 0.3 ms, to account for differences in presynaptic AP shape (Figure S4E). Peak open probability of presynaptic Ca^{2+} channels was assumed as 1, 0.3, and 0.1, respectively (Figures S4F and S5). Whereas Ca^{2+} domains around individual Ca^{2+} channels and Ca^{2+} channel clusters merged in young synapses, individual Ca^{2+} domains were much better separated in mature synapses (Figures 7D–7F). On average, the width of Ca^{2+} domains at half-maximal amplitude decreased from 83.4 ± 4.5 nm (P7–9) to 58.5 ± 10.2 nm (P14–16), and 19.6 ± 2.1 nm (P21–23; $p < 0.0001$; Figure 7G). These results indicate a switch from merged Ca^{2+} microdomains, which cover the entire AZ, to isolated Ca^{2+} nanodomains, which are spatially more confined. Thus, the assumed reduction of Ca^{2+} channel open probability, suggested by the reduction in presynaptic AP duration, markedly changed the shape of the Ca^{2+} domains (Figures 7D–7F, bottom).

Next, we simulated the effects of these different Ca^{2+} domains on transmitter release (Figures 7H and 7I). Vesicles were put at random locations at Ca^{2+} channel clusters (corresponding to a cluster area "CA" model, see below), and the Ca^{2+} concentration at the corresponding location was used to drive the release sensor model (Figure 7H).[55] Simulations were performed in control conditions (0.1 mM EGTA) and in the presence of 10 mM EGTA and 10 mM BAPTA to predict the effects of the Ca^{2+} chelators.[15] Furthermore, the simulated release rates with 0.1 mM EGTA were used to estimate release probability, delay, and decay time constant of transmitter release. Although the model was highly constrained, it reasonably predicted both EGTA sensitivity and release probability (Figures 7J and 7K).

Developmental transformation of coupling nanotopography

To infer the coupling topography, we quantitatively compared the ability of several Ca^{2+} channel-vesicle coupling models to describe our experimental observations (including experimental EGTA, BAPTA, p_R, delay, and decay time constant of release data; Figure 8). In particular, we examined a cluster area model ("CA") in which vesicles were put on top of Ca^{2+} channel cluster areas, a cluster perimeter model ("CP") in which the vesicles were positioned along cluster perimeters,[21] a model in which vesicles were randomly positioned over the entire AZ ("RAZ"), and a model in which vesicles were randomly assigned to the entire presynaptic membrane ("RPM"). Furthermore, we tested three different exclusion zone models ("CAEZ," "RAZEZ," and "RPMEZ"; Figure 8A).[13] To assess the ability of the models to reproduce the experimental data, we selected a representative AZ from each age group and simulated 100 AZ configurations with stochastic Ca^{2+} channel activation and random vesicle positioning. We then compared the distributions of the minus log-likelihood values, providing a metric of the ability of the model to describe the experimental observations. Whereas the CP model resembles the previously described perimeter model,[21] the RAZEZ model shows similarities to the previously used exclusion zone model.[13,16]

In the representative AZ from the P7–9 age group, the RAZEZ model best described the experimental data, followed by RAZ, CP, CAEZ, CA, RPM, and RPMEZ models ($p < 0.001$; Figure 8B, left; Figure S11). In contrast, in the AZ from the P21–23 age group, the CP model produced the best fit, followed by CA, CAEZ, RAZ, RAZEZ, RPM, and RPMEZ models ($p < 0.001$; Figure 8B, right; Figure S11). In the P14–16 age group, the distribution was more similar to the P21–23 than to the P7–9 age group (Figure 8B, center), suggesting that a substantial transformation in coupling topography may occur between the young and medium age groups (i.e., in the range P10–13).

(D–F) Intracellular Ca^{2+} concentration 5 nm away from the plasma membrane and 0.2 ms after the peak of the presynaptic Ca^{2+} inflow for P7–9 (D), P14–16 (E), and P21–23 (F) AZs. Top, "line scans" of Ca^{2+} concentration through all Ca^{2+} channels in the x direction (y = 0, z = 5 nm), with x = 0 corresponding to the channel center. Different colors indicate different Ca^{2+} channels. Center, 3D plots of Ca^{2+} domains. Bottom, contour plots of Ca^{2+} concentration; points indicate Ca^{2+} channels (red, closed; green, activated). Standard deviation σ of presynaptic Ca^{2+} flux: 1.38 ms, 0.56 ms, and 0.3 ms; open probability of presynaptic Ca^{2+} channels: 1, 0.3, and 0.1, respectively.

(G) Summary bar graph of width of Ca^{2+} domains at half-maximal amplitude for the example AZs from the P7–9, P14–16, and P21–23 age groups. Circles, individual Ca^{2+} domains; bars, mean ± SEM (n = 49, 38, and 16).

(H and I) Random positioning of synaptic vesicles opposite to Ca^{2+} channel clusters explains nanodomain coupling and developmental changes. Transmitter release rate was computed using the Ca^{2+} sensor-release model of Lou et al.[55] (H). Release rate was computed in control (I, top) and in 10 mM EGTA (I, bottom) for a representative synapse from the P21–23 age group. Different colors represent release rates for individual vesicles at different locations.

(J and K) Summary bar graphs of simulated EGTA effects (J) and release probability (K) for representative AZs from the P7–9, P14–16, and P21–23 age groups. Data in P7–9 were generated by 100 random vesicle placement patterns; data in P14–16 and P21–23 were generated by 10 random channel activation patterns combined with 10 random vesicle placement patterns (CA model). Circles, individual instances of random positioning; bars, mean ± SEM. Red dashed lines, mean experimental values; light red shaded area, 95% confidence band. See also Figure S10 and Table S4.

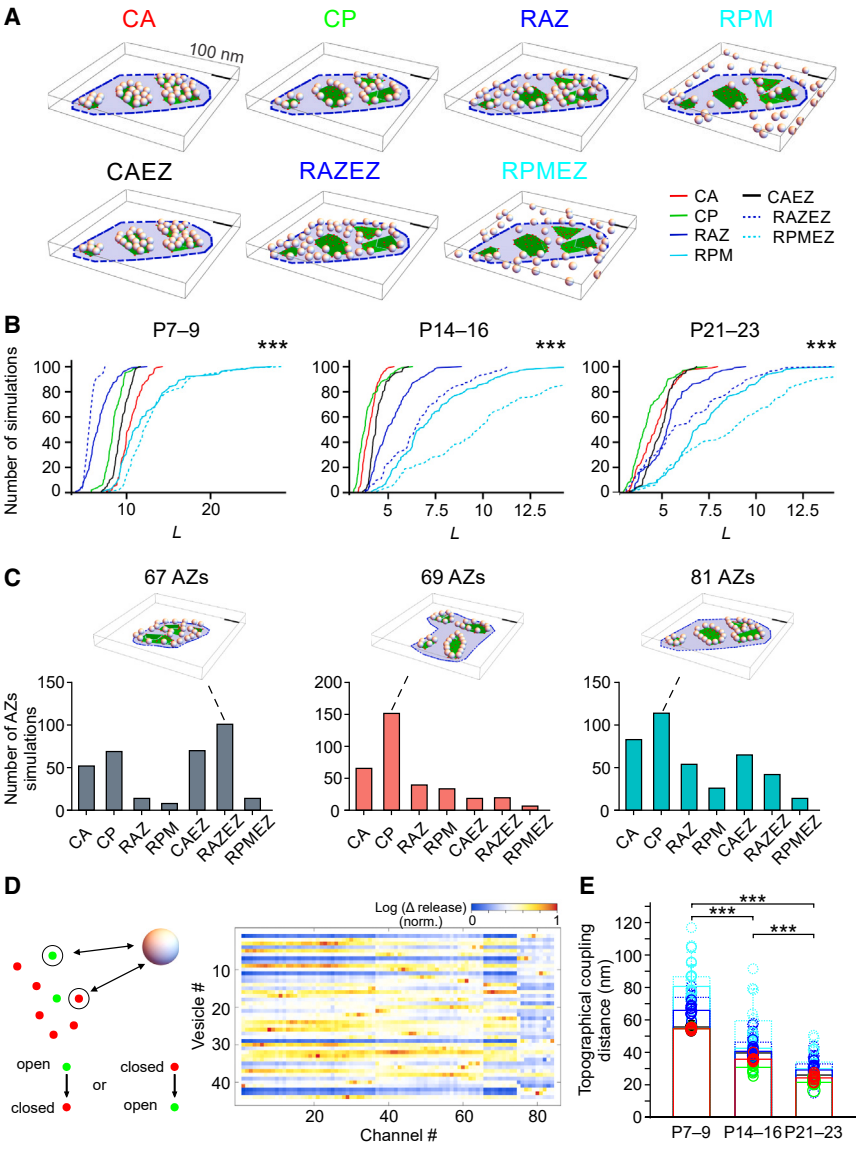

Figure 8. Change of Ca^{2+} channel-vesicle coupling from random to clustered nanotopography during development

(A) Three-dimensional depiction of different Ca^{2+} channel-vesicle coupling models. CA, vesicle attachment to the entire Ca^{2+} channel cluster area; CP, vesicle attachment to cluster perimeters; RAZ, vesicle attachment to whole AZ; RPM, vesicle attachment to entire presynaptic membrane; CAEZ, vesicle attachment to cluster area with exclusion zone (5 nm around each channel); RAZEZ, vesicle attachment to AZ with exclusion zone; RPMEZ, vesicle attachment to presynaptic membrane with exclusion zone. Red, Ca^{2+} channels; green, Ca^{2+} channel cluster area; blue, AZ area. AZ from P21–23 age group.

(B) Comparison of coupling topography models in P7–9 (left), P14–16 (center), and P21–23 age groups (right). Cumulative distribution of minus log-likelihood score (including EGTA, BAPTA, p_R, delay, and time course of release); lower values indicate better fit. Red, CA model; green, CP model; blue, RAZ model; cyan, RPM model; black, CAEZ model; blue dashed, RAZEZ model; cyan dashed, RPMEZ model.

(C) Histograms of the best-fit model in P7–9 (left), P14–16 (center), and P21–23 age groups (right). Histograms show the distribution for the entire set of reconstructed active zones (67, 69, and 81 AZs). For each AZ, 5 random synaptic vesicle placement patterns were simulated. Insets on top show the models with the highest abundance in the histograms.

(D) Direct estimation of "topographical coupling distance." Left, schematic illustration of the approach. Topographical coupling distance was computed as the mean of the pairwise distance matrix multiplied with the release relevance matrix to define weights. For details, see STAR Methods. Right, release relevance matrix for a synapse from the P21–23 age group and the CA model. Color scale indicates fractional contribution (red, high contribution; blue, low contribution).

(E) Estimates of topographical coupling distance for the three age groups and all tested models. Same color code as in (A). See also Figure S11 and Table S4.

The results derived from three representative AZs suggest a developmental change in the coupling configuration. To test this hypothesis more generally, we simulated Ca^{2+} domains and transmitter release in all morphologically analyzed AZs and determined the best-fit model in each case (67, 69, and 81 AZs, respectively; Figure 8C). In the P7–9 age group, the RAZEZ often provided the best fit, whereas the other models did less frequently (Figure 8C, left). In the P21–23 age group, the CP showed highest frequency (Figure 8C, right). In the P14–16 age group, the distribution was more similar to the P21–23 than to the P7–9 age group. Distributions of best-fit models were significantly different among age groups ($p < 0.001$; χ^2 test). Collectively, structural and modeling results suggest that developmental processes not only result in a reduction in average coupling distance[17–21] but also a change in coupling nanotopography.

Modeling also allowed us to determine the topographical coupling distance between Ca^{2+} channels and synaptic vesicles in the three age groups (Figures 8D and 8E). For each channel-vesicle pair in each model, we first determined the coupling distance in x-y dimension, resulting in a "distance matrix". We then determined the contribution of each channel to the release of each vesicle by channel silencing or activation, resulting in a "release relevance matrix" (Figure 8D, right). Finally, we determined the mean topographical coupling distance, multiplying each distance value with the corresponding release relevance as a weight factor. We found that the average topographical coupling distance was 63.5 ± 0.5 nm at P7–9, 36.4 ± 0.4 nm at P14–16, and 26.3 ± 0.5 nm at P21–23 ($p < 0.001$ for all models; Figure 8E). Thus, our combined functional-structural-computational approach directly demonstrates shortening of the topographical coupling distance during development.

DISCUSSION

To determine the nanotopography and stoichiometry of coupling at an inhibitory synapse, we combined biophysical analysis (paired recording, presynaptic recording, and pipette perfusion), structural measurements (serial-section EM and FRL), and modeling of Ca^{2+} diffusion and release sensor activation. This combined approach offered unprecedented insights into the relation between structure and function of a central synapse. Our results suggest that developmental processes not only result in a reduction of the source-sensor coupling distance, but also a transformation in the coupling nanotopography from more random to more clustered. Thus, presynaptic signaling developmentally approaches a point-to-point configuration, optimizing speed, reliability, and energy efficiency of synaptic transmission.

Ca^{2+} channel subtype and activation during development

Direct recording from BC terminals revealed that the presynaptic AP undergoes substantial shortening during synaptic maturation. This is reminiscent of previous results at the calyx of Held.[22] In contrast, transmitter release at BC-PC synapses constantly relies on P/Q-type Ca^{2+} channels. This is different from several other synapses, including the calyx, in which early in development, transmitter release depends on P/Q-, N-, and R-type Ca^{2+} channels, whereas later in development, release only relies on P/Q-type channels.[19,23,29] Thus, at BC-PC synapses, presynaptic APs of decreasing duration act on the same Ca^{2+} channel subtype, implying a reduction in the efficacy of activation of presynaptic Ca^{2+} channels during synaptic maturation.[52,57] However, as the peak amplitude of the presynaptic AP may also change during development,[34,64] the efficacy of Ca^{2+} channel activation can only be roughly estimated (Figure S4F).

Our results suggest that the high efficacy of Ca^{2+} channel activation in young BC-PC synapses may be similar to that in the calyx of Held and the hippocampal mossy fiber bouton,[56,57] whereas the low efficacy of Ca^{2+} channel activation in mature BC-PC synapses more closely resembles the squid giant synapse or the frog neuromuscular junction.[65,66] As a corollary, in the immature synapse Ca^{2+} channels are opened largely deterministically, whereas in the mature synapse Ca^{2+} channels are activated more stochastically.[67] Stochastic Ca^{2+} channel activation in the mature synapse may explain why only few Ca^{2+} channels are necessary to trigger transmitter release.[66,68–70]

Developmental transformation of Ca^{2+} channel-vesicle coupling

A decrease of the sensitivity to the slow intracellular Ca^{2+} chelator EGTA during development was reported at several synapses.[17–19,21] This has been interpreted as a decrease in the average coupling distance between Ca^{2+} source and release sensor.[3] However, our results reveal that the developmental changes in the coupling are more complex. We found that presynaptic Ca^{2+} channels were clustered in the AZ at all developmental time points, as reported for other synapses.[21,51] Synaptic vesicles were also non-randomly distributed, but clustering was only significant in mature synapses.

To determine the precise coupling configuration, we compared different nanotopography models against the experimental data (Figure 8). In mature synapses, the CP model, in which vesicles were attached to cluster perimeters, provided the best fit to our experimental observations, although the variability among AZs was substantial. Models in which vesicles were positioned to entire active zones were statistically inferior, and exclusion zones did not improve the fit. In contrast, in young synapses the RAZEZ model, in which vesicles were put to entire AZs with an exclusion zone, was superior (Figure 8C).[13] Taken together, our results suggest that developmental processes not only result in a reduction of the coupling distance[17–19,21] but rather in a transformation in the coupling topography from more random to more clustered. In intermediate synapses, the distribution was more similar to the P21–23 than to the P7–9 age group, implying that the transformation occurs between P10 and P13. Recent work suggested exclusion zone coupling at cerebellar parallel fibers versus perimeter coupling in stellate cell synapses.[16] Our results highlight the importance of these coupling configurations[13,21] and extend the previous findings by showing not only synapse-specific differences but also developmental regulation.

Our findings have implications for the molecular interactions between Ca^{2+} channels and release sensors. The CP model (best-fit model at P21–23) implies attraction between channels and sensors, while the RAZEZ model (best-fit model at P7–9) may suggest repulsion. Thus, intermolecular interactions may switch from repulsive to attractive during development. Attractive forces may be explained by the abundant presynaptic protein RIM, which binds to the vesicle protein Rab3 via zinc-finger domains and to the C terminus of presynaptic Ca^{2+} channels via PDZ domains.[71,72] Furthermore, RIM-binding proteins (RIM-BPs) bind to both RIM and the Ca^{2+} channel C terminus. Additionally, Munc13-3 may tighten the coupling complex.[73] Recent work suggested different machineries for clustering of Ca^{2+} channels and synaptic vesicles. Whereas RIM and RIM-BP are critically important for Ca^{2+} channel clustering, Liprin-α and the protein tyrosine phosphatase PTPσ seem to be more relevant for vesicle docking and priming.[74] Thus, a developmental sequence of expression of these proteins may contribute to the transformation of the coupling configuration.

Repulsive forces are more difficult to explain. It was suggested that septin 5 may increase the coupling distance, acting as a spacer that separates source and sensor from each other.[75] However, whether septin 5 is expressed at BC-PC synapses and whether it is downregulated during development is, at present, unclear.[76] Other molecular factors generating repulsion remain to be identified.

Developmental change in the number of functional release sites

The number of functional release sites, N, is a key factor that determines the efficacy of the synapse.[31] But what is the structural correlate of N?[44] Our combined functional and structural analysis provides a tentative answer to this fundamental question. Traditionally, it was thought that synaptic boutons per connection represent the structural correlates of functional release

sites.[42,77] However, it has also been suggested that the AZ represents the structural correlate.[78] Furthermore, there are well-documented examples of multi-vesicular release from single AZs,[79] raising the possibility of additional substructure of the AZ. At the BC-PC synapse, the number of functional release sites greatly exceeds the number of synaptic boutons per connection (Table S3). Early in development, the functional N agrees with the total number of AZs. However, later in development, the functional N exceeds the number of AZs and coincides better with the number of presynaptic Ca^{2+} channel clusters (Table S3). Thus, the structural correlate of the functional N is not constant but may change during development.

How do the changes in the structural correlates of functional N relate to the changes in the coupling configuration? Early in development, the loosely coupled vesicles may "see" Ca^{2+} channel inflow throughout the entire AZ, so that the AZ may act as a unit (Figure 7D). In contrast, later in development, the tightly coupled vesicles may selectively detect Ca^{2+} inflow from the nearest Ca^{2+} channels, so that the release process in the AZ is more fragmented (Figure 7F). A corollary of our results is that the interpretation of the number of functional release sites may differ between excitatory synapses (which often show microdomain coupling)[7] and inhibitory synapses (which frequently employ nanodomain coupling).[3] Combined biophysical and structural analysis at other synapses will be needed to test this hypothesis.

Whether release units at BC-PC synapses are aligned with clusters of postsynaptic $GABA_A$ receptors to form "nanocolumns"[80] remains to be determined. If so, our results may call for a redefinition of the term "synapse." This term was classically used, based on physiological studies, to describe the entire junction between two neurons,[81] and later, based on anatomical work, for a presynaptic terminal attached to its somatodendritic target element.[42,77] Our results suggest that a new definition based on nanotopographical criteria (e.g., presynaptic Ca^{2+} channel clusters with attached vesicles, or Ca^{2+} nanodomains) may be more appropriate.

Functional significance of coupling nanotopography for inhibitory synaptic transmission

Inhibitory synapses play a key role in several higher network functions, such as feedforward and feedback inhibition, pattern separation by winner-takes-all computations,[82] and fast rhythmic activity, such as network oscillations in the gamma frequency range.[83] For all these functions, the speed of inhibition is critically important. Furthermore, speed and efficiency have to be maintained during high-frequency activity, a hallmark property of GABAergic neurons *in vivo*.[84,85] How the requirements for speed and efficacy at inhibitory synapses can be integrated into single AZs remains enigmatic.

Our results suggest that the coupling nanotopography may explain how these requirements are implemented. In the mature synapse, clustered configurations (CA and CP) may offer functional advantages over random configurations (RPM and RPMEZ). The clustered nanotopography enables tight coupling between vesicles and the nearest neighbor Ca^{2+} channels, which maximizes the speed of inhibitory synaptic transmission.[6] Furthermore, the clustered nanotopography allows accommodation of a large number of vesicles to their docking sites, leading to a high vesicle-to-channel stoichiometric ratio. Large numbers of docked vesicles will be important to ensure fast and sustained transmitter release during *in vivo*-like repetitive activity at GABAergic synapses.[84,85] Additionally, stochastic Ca^{2+} channel activation in combination with low Ca^{2+} channel numbers will minimize multivesicular release at single AZs or single Ca^{2+} channel clusters.[79] This may save vesicles, contributing to both sustained efficacy and energy efficiency of synaptic transmission.[24] Finally, stochastic Ca^{2+} channel activation will minimize presynaptic Ca^{2+} inflow, further contributing to the energy efficiency. Thus, clustered nanotopography at mature GABAergic synapses provides unique functional advantages to inhibitory synaptic transmission, explaining its critical contribution to higher-order network computations.

STAR★METHODS

Detailed methods are provided in the online version of this paper and include the following:

- KEY RESOURCES TABLE
- RESOURCE AVAILABILITY
  - Lead contact
  - Materials availability
  - Data and code availability
- EXPERIMENTAL MODEL AND STUDY PARTICIPANT DETAILS
- METHOD DETAILS
  - Cerebellar slice preparation
  - Paired recordings
  - Presynaptic recordings from GABAergic terminals
  - Immunohistochemistry
  - Patch pipette perfusion
  - Bouton Ca^{2+} imaging
  - Data acquisition and analysis
  - Serial section EM and image analysis
  - Freeze-fracture replica labeling (FRL)
  - Modeling of nanodomain coupling based on realistic coupling topographies
  - Conventions and statistics

SUPPLEMENTAL INFORMATION

Supplemental information can be found online at https://doi.org/10.1016/j.neuron.2023.12.002.

ACKNOWLEDGMENTS

We thank Drs. David DiGregorio and Erwin Neher for critically reading an earlier version of the manuscript, Ralf Schneggenburger for helpful discussions, Benjamin Suter and Katharina Lichter for support with image analysis, Chris Wojtan for advice on numerical solution of partial differential equations, Maria Reva for help with Ripley analysis, Alois Schlögl for programming, and Akari Hagiwara and Toshihisa Ohtsuka for anti-ELKS antibody. We are grateful to Florian Marr, Christina Altmutter, and Vanessa Zheden for excellent technical assistance and to Eleftheria Kralli-Beller for manuscript editing. This research was supported by the Scientific Services Units (SSUs) of ISTA (Electron Microscopy Facility, Preclinical Facility, and Machine Shop). The project received funding from the European Research Council (ERC) under the European Union's Horizon 2020 research and innovation program (grant agreement no. 692692), the Fonds zur Förderung der Wissenschaftlichen Forschung

(Z 312-B27, Wittgenstein award; P 36232-B), all to P.J., and a DOC fellowship of the Austrian Academy of Sciences to J.-J.C.

AUTHOR CONTRIBUTIONS

Conceptualization, P.J.; methodology, all authors; electrophysiology, J.-J.C., C.C., and I.A.; structural analysis and modeling, W.A.K., J.-J.C., and P.J.; writing—original draft, P.J.; writing—review & editing, all authors; funding acquisition, P.J. and J.-J.C.; resources, all authors; supervision, P.J.

DECLARATION OF INTERESTS

P.J. is member of the advisory board of *Neuron*.

Received: October 25, 2022
Revised: July 12, 2023
Accepted: December 5, 2023
Published: January 11, 2024

REFERENCES

1. Abbott, L.F., and Regehr, W.G. (2004). Synaptic computation. Nature *431*, 796–803.
2. Lisman, J.E., Raghavachari, S., and Tsien, R.W. (2007). The sequence of events that underlie quantal transmission at central glutamatergic synapses. Nat. Rev. Neurosci. *8*, 597–609.
3. Eggermann, E., Bucurenciu, I., Goswami, S.P., and Jonas, P. (2012). Nanodomain coupling between Ca^{2+} channels and sensors of exocytosis at fast mammalian synapses. Nat. Rev. Neurosci. *13*, 7–21.
4. Südhof, T.C. (2012). The presynaptic active zone. Neuron *75*, 11–25.
5. Wadel, K., Neher, E., and Sakaba, T. (2007). The coupling between synaptic vesicles and Ca^{2+} channels determines fast neurotransmitter release. Neuron *53*, 563–575.
6. Bucurenciu, I., Kulik, A., Schwaller, B., Frotscher, M., and Jonas, P. (2008). Nanodomain coupling between Ca^{2+} channels and Ca^{2+} sensors promotes fast and efficient transmitter release at a cortical GABAergic synapse. Neuron *57*, 536–545.
7. Vyleta, N.P., and Jonas, P. (2014). Loose coupling between Ca^{2+} channels and release sensors at a plastic hippocampal synapse. Science *343*, 665–670.
8. Adler, E.M., Augustine, G.J., Duffy, S.N., and Charlton, M.P. (1991). Alien intracellular calcium chelators attenuate neurotransmitter release at the squid giant synapse. J. Neurosci. *11*, 1496–1507.
9. Arai, I., and Jonas, P. (2014). Nanodomain coupling explains Ca^{2+} independence of transmitter release time course at a fast central synapse. Elife *3*, e04057.
10. Ohana, O., and Sakmann, B. (1998). Transmitter release modulation in nerve terminals of rat neocortical pyramidal cells by intracellular calcium buffers. J. Physiol. *513*, 135–148.
11. Kawaguchi, S.Y., and Sakaba, T. (2017). Fast Ca^{2+} buffer-dependent reliable but plastic transmission at small CNS synapses revealed by direct bouton recording. Cell Rep. *21*, 3338–3345.
12. Meinrenken, C.J., Borst, J.G.G., and Sakmann, B. (2002). Calcium secretion coupling at calyx of Held governed by nonuniform channel-vesicle topography. J. Neurosci. *22*, 1648–1667.
13. Keller, D., Babai, N., Kochubey, O., Han, Y., Markram, H., Schürmann, F., and Schneggenburger, R. (2015). An exclusion zone for Ca^{2+} channels around docked vesicles explains release control by multiple channels at a CNS synapse. PLoS Comput. Biol. *11*, e1004253.
14. Wang, L.Y., Fedchyshyn, M.J., and Yang, Y.M. (2009). Action potential evoked transmitter release in central synapses: insights from the developing calyx of Held. Mol. Brain *2*, 36. https://molecularbrain.biomedcentral.com/articles/10.1186/1756-6606-2-36.
15. Nakamura, Y., Reva, M., and DiGregorio, D.A. (2018). Variations in Ca^{2+} influx can alter Ca^{2+}-chelator-based estimates of Ca^{2+} channel-synaptic vesicle coupling distance. J. Neurosci. *38*, 3971–3987.
16. Rebola, N., Reva, M., Kirizs, T., Szoboszlay, M., Lőrincz, A., Moneron, G., Nusser, Z., and DiGregorio, D.A. (2019). Distinct nanoscale calcium channel and synaptic vesicle topographies contribute to the diversity of synaptic function. Neuron *104*, 693–710.
17. Fedchyshyn, M.J., and Wang, L.Y. (2005). Developmental transformation of the release modality at the calyx of Held synapse. J. Neurosci. *25*, 4131–4140.
18. Baur, D., Bornschein, G., Althof, D., Watanabe, M., Kulik, A., Eilers, J., and Schmidt, H. (2015). Developmental tightening of cerebellar cortical synaptic influx-release coupling. J. Neurosci. *35*, 1858–1871.
19. Bornschein, G., Eilers, J., and Schmidt, H. (2019). Neocortical high probability release sites are formed by distinct Ca^{2+} channel-to-release sensor topographies during development. Cell Rep. *28*, 1410–1418.e4.
20. Wang, L.Y., Neher, E., and Taschenberger, H. (2008). Synaptic vesicles in mature calyx of Held synapses sense higher nanodomain calcium concentrations during action potential-evoked glutamate release. J. Neurosci. *28*, 14450–14458.
21. Nakamura, Y., Harada, H., Kamasawa, N., Matsui, K., Rothman, J.S., Shigemoto, R., Silver, R.A., DiGregorio, D.A., and Takahashi, T. (2015). Nanoscale distribution of presynaptic Ca^{2+} channels and its impact on vesicular release during development. Neuron *85*, 145–158.
22. Taschenberger, H., and von Gersdorff, H. (2000). Fine-tuning an auditory synapse for speed and fidelity: developmental changes in presynaptic waveform, EPSC kinetics, and synaptic plasticity. J. Neurosci. *20*, 9162–9173.
23. Iwasaki, S., and Takahashi, T. (2001). Developmental regulation of transmitter release at the calyx of Held in rat auditory brainstem. J. Physiol. *534*, 861–871.
24. Taschenberger, H., Leão, R.M., Rowland, K.C., Spirou, G.A., and von Gersdorff, H. (2002). Optimizing synaptic architecture and efficiency for high-frequency transmission. Neuron *36*, 1127–1143.
25. Pouzat, C., and Hestrin, S. (1997). Developmental regulation of basket/stellate cell → Purkinje cell synapses in the cerebellum. J. Neurosci. *17*, 9104–9112.
26. Caillard, O., Moreno, H., Schwaller, B., Llano, I., Celio, M.R., and Marty, A. (2000). Role of the calcium-binding protein parvalbumin in short-term synaptic plasticity. Proc. Natl. Acad. Sci. USA *97*, 13372–13377.
27. Eggermann, E., and Jonas, P. (2012). How the 'slow' Ca^{2+} buffer parvalbumin affects transmitter release in nanodomain-coupling regimes. Nat. Neurosci. *15*, 20–22.
28. Cajal, S.R. (1995). Histology of the Nervous System. Translated by Swanson N., and Swanson L.W (Oxford University Press).
29. Iwasaki, S., and Takahashi, T. (1998). Developmental changes in calcium channel types mediating synaptic transmission in rat auditory brainstem. J. Physiol. *509*, 419–423.
30. Randall, A., and Tsien, R.W. (1995). Pharmacological dissection of multiple types of Ca^{2+} channel currents in rat cerebellar granule neurons. J. Neurosci. *15*, 2995–3012.
31. Katz, B. (1969). The Release of Neural Transmitter Substances (Liverpool University Press).
32. Clements, J.D., and Silver, R.A. (2000). Unveiling synaptic plasticity: a new graphical and analytical approach. Trends Neurosci. *23*, 105–113.
33. Rowan, M.J.M., Tranquil, E., and Christie, J.M. (2014). Distinct Kv channel subtypes contribute to differences in spike signaling properties in the axon initial segment and presynaptic boutons of cerebellar interneurons. J. Neurosci. *34*, 6611–6623.
34. Rowan, M.J.M., DelCanto, G., Yu, J.J., Kamasawa, N., and Christie, J.M. (2016). Synapse-level determination of action potential duration by K^+ channel clustering in axons. Neuron *91*, 370–383.

35. Schneggenburger, R., Meyer, A.C., and Neher, E. (1999). Released fraction and total size of a pool of immediately available transmitter quanta at a calyx synapse. Neuron *23*, 399–409.

36. Rizzoli, S.O., and Betz, W.J. (2005). Synaptic vesicle pools. Nat. Rev. Neurosci. *6*, 57–69.

37. Jones, M.V., Jonas, P., Sahara, Y., and Westbrook, G.L. (2001). Microscopic kinetics and energetics distinguish $GABA_A$ receptor agonists from antagonists. Biophys. J. *81*, 2660–2670.

38. Ragozzino, D., Woodward, R.M., Murata, Y., Eusebi, F., Overman, L.E., and Miledi, R. (1996). Design and *in vitro* pharmacology of a selective gamma-aminobutyric $acid_C$ receptor antagonist. Mol. Pharmacol. *50*, 1024–1030.

39. Collin, T., Chat, M., Lucas, M.G., Moreno, H., Racay, P., Schwaller, B., Marty, A., and Llano, I. (2005). Developmental changes in parvalbumin regulate presynaptic Ca^{2+} signaling. J. Neurosci. *25*, 96–107.

40. Woehler, A., Lin, K.H., and Neher, E. (2014). Calcium-buffering effects of gluconate and nucleotides, as determined by a novel fluorimetric titration method. J. Physiol. *592*, 4863–4875.

41. Schmidt, H., Brown, E.B., Schwaller, B., and Eilers, J. (2003). Diffusional mobility of parvalbumin in spiny dendrites of cerebellar Purkinje neurons quantified by fluorescence recovery after photobleaching. Biophys. J. *84*, 2599–2608.

42. Redman, S. (1990). Quantal analysis of synaptic potentials in neurons of the central nervous system. Physiol. Rev. *70*, 165–198.

43. Pulido, C., and Marty, A. (2017). Quantal fluctuations in central mammalian synapses: Functional role of vesicular docking sites. Physiol. Rev. *97*, 1403–1430.

44. Holler, S., Köstinger, G., Martin, K.A.C., Schuhknecht, G.F.P., and Stratford, K.J. (2021). Structure and function of a neocortical synapse. Nature *591*, 111–116.

45. Korogod, N., Petersen, C.C.H., and Knott, G.W. (2015). Ultrastructural analysis of adult mouse neocortex comparing aldehyde perfusion with cryo fixation. Elife *4*, e05793.

46. Rollenhagen, A., Sätzler, K., Rodríguez, E.P., Jonas, P., Frotscher, M., and Lübke, J.H.R. (2007). Structural determinants of transmission at large hippocampal mossy fiber synapses. J. Neurosci. *27*, 10434–10444.

47. Gjoni, E., Aguet, C., Sahlender, D.A., Knott, G., and Schneggenburger, R. (2018). Ultrastructural basis of strong unitary inhibition in a binaural neuron. J. Physiol. *596*, 4969–4982.

48. Ripley, B.D. (1977). Modelling spatial patterns. J. R. Stat. Soc. B *39*, 172–192.

49. Masugi-Tokita, M., and Shigemoto, R. (2007). High-resolution quantitative visualization of glutamate and GABA receptors at central synapses. Curr. Opin. Neurobiol. *17*, 387–393.

50. Holderith, N., Lorincz, A., Katona, G., Rózsa, B., Kulik, A., Watanabe, M., and Nusser, Z. (2012). Release probability of hippocampal glutamatergic terminals scales with the size of the active zone. Nat. Neurosci. *15*, 988–997.

51. Miki, T., Kaufmann, W.A., Malagon, G., Gomez, L., Tabuchi, K., Watanabe, M., Shigemoto, R., and Marty, A. (2017). Numbers of presynaptic Ca^{2+} channel clusters match those of functionally defined vesicular docking sites in single central synapses. Proc. Natl. Acad. Sci. USA *114*, E5246–E5255.

52. Li, L., Bischofberger, J., and Jonas, P. (2007). Differential gating and recruitment of P/Q-, N-, and R-type Ca^{2+} channels in hippocampal mossy fiber boutons. J. Neurosci. *27*, 13420–13429.

53. Althof, D., Baehrens, D., Watanabe, M., Suzuki, N., Fakler, B., and Kulik, Á. (2015). Inhibitory and excitatory axon terminals share a common nanoarchitecture of their $Ca_V2.1$ (P/Q-type) Ca^{2+} channels. Front. Cell. Neurosci. *9*, 315.

54. Ichikawa, R., Yamasaki, M., Miyazaki, T., Konno, K., Hashimoto, K., Tatsumi, H., Inoue, Y., Kano, M., and Watanabe, M. (2011). Developmental switching of perisomatic innervation from climbing fibers to basket cell fibers in cerebellar Purkinje cells. J. Neurosci. *31*, 16916–16927.

55. Lou, X., Scheuss, V., and Schneggenburger, R. (2005). Allosteric modulation of the presynaptic Ca^{2+} sensor for vesicle fusion. Nature *435*, 497–501.

56. Borst, J.G.G., and Sakmann, B. (1998). Calcium current during a single action potential in a large presynaptic terminal of the rat brainstem. J. Physiol. *506*, 143–157.

57. Bischofberger, J., Geiger, J.R.P., and Jonas, P. (2002). Timing and efficacy of Ca^{2+} channel activation in hippocampal mossy fiber boutons. J. Neurosci. *22*, 10593–10602.

58. Weber, A.M., Wong, F.K., Tufford, A.R., Schlichter, L.C., Matveev, V., and Stanley, E.F. (2010). N-type Ca^{2+} channels carry the largest current: implications for nanodomains and transmitter release. Nat. Neurosci. *13*, 1348–1350.

59. Sheng, J., He, L., Zheng, H., Xue, L., Luo, F., Shin, W., Sun, T., Kuner, T., Yue, D.T., and Wu, L.G. (2012). Calcium-channel number critically influences synaptic strength and plasticity at the active zone. Nat. Neurosci. *15*, 998–1006.

60. Smith, G.D. (2001). Modeling local and global calcium signals using reaction-diffusion equations. In Computational Neuroscience, E. de Schutter, ed. (CRC Press), pp. 49–85.

61. Sun, J., Pang, Z.P., Qin, D., Fahim, A.T., Adachi, R., and Südhof, T.C. (2007). A dual-Ca^{2+}-sensor model for neurotransmitter release in a central synapse. Nature *450*, 676–682.

62. Chen, C., Arai, I., Satterfield, R., Young, S.M., Jr., and Jonas, P. (2017). Synaptotagmin 2 is the fast Ca^{2+} sensor at a central inhibitory synapse. Cell Rep. *18*, 723–736.

63. Chen, C., Satterfield, R., Young, S.M., Jr., and Jonas, P. (2017). Triple function of Synaptotagmin 7 ensures efficiency of high-frequency transmission at central GABAergic synapses. Cell Rep. *21*, 2082–2089.

64. Begum, R., Bakiri, Y., Volynski, K.E., and Kullmann, D.M. (2016). Action potential broadening in a presynaptic channelopathy. Nat. Commun. *7*, 12102.

65. Augustine, G.J. (1990). Regulation of transmitter release at the squid giant synapse by presynaptic delayed rectifier potassium current. J. Physiol. *431*, 343–364.

66. Shahrezaei, V., Cao, A., and Delaney, K.R. (2006). Ca^{2+} from one or two channels controls fusion of a single vesicle at the frog neuromuscular junction. J. Neurosci. *26*, 13240–13249.

67. Tarr, T.B., Dittrich, M., and Meriney, S.D. (2013). Are unreliable release mechanisms conserved from NMJ to CNS? Trends Neurosci. *36*, 14–22.

68. Stanley, E.F. (1993). Single calcium channels and acetylcholine release at a presynaptic nerve terminal. Neuron *11*, 1007–1011.

69. Bucurenciu, I., Bischofberger, J., and Jonas, P. (2010). A small number of open Ca^{2+} channels trigger transmitter release at a central GABAergic synapse. Nat. Neurosci. *13*, 19–21.

70. Scimemi, A., and Diamond, J.S. (2012). The number and organization of Ca^{2+} channels in the active zone shapes neurotransmitter release from Schaffer collateral synapses. J. Neurosci. *32*, 18157–18176.

71. Kaeser, P.S., Deng, L., Wang, Y., Dulubova, I., Liu, X., Rizo, J., and Südhof, T.C. (2011). RIM proteins tether Ca^{2+} channels to presynaptic active zones via a direct PDZ-domain interaction. Cell *144*, 282–295.

72. Han, Y., Kaeser, P.S., Südhof, T.C., and Schneggenburger, R. (2011). RIM determines Ca^{2+} channel density and vesicle docking at the presynaptic active zone. Neuron *69*, 304–316.

73. Kusch, V., Bornschein, G., Loreth, D., Bank, J., Jordan, J., Baur, D., Watanabe, M., Kulik, A., Heckmann, M., Eilers, J., and Schmidt, H. (2018). Munc13-3 is required for the developmental localization of Ca^{2+} channels to active zones and the nanopositioning of $Ca_V2.1$ near release sensors. Cell Rep. *22*, 1965–1973.

74. Emperador-Melero, J., Andersen, J.W., Metzbower, S.R., Levy, A.D., Dharmasri, P.A., de Nola, G., Blanpied, T.A., and Kaeser, P.S. (2023). Molecular definition of distinct active zone protein machineries for Ca^{2+} channel clustering and synaptic vesicle priming. bioRxiv. https://doi.org/10.1101/2023.10.27.564439.

75. Yang, Y.M., Fedchyshyn, M.J., Grande, G., Aitoubah, J., Tsang, C.W., Xie, H., Ackerley, C.A., Trimble, W.S., and Wang, L.Y. (2010). Septins regulate developmental switching from microdomain to nanodomain coupling of Ca^{2+} influx to neurotransmitter release at a central synapse. Neuron *67*, 100–115.

76. Paul, A., Cai, Y., Atwal, G.S., and Huang, Z.J. (2012). Developmental coordination of gene expression between synaptic partners during GABAergic circuit assembly in cerebellar cortex. Front. Neural Circuits *6*, 37.

77. Silver, R.A., Lübke, J., Sakmann, B., and Feldmeyer, D. (2003). High-probability uniquantal transmission at excitatory synapses in barrel cortex. Science *302*, 1981–1984.

78. Schikorski, T., and Stevens, C.F. (1997). Quantitative ultrastructural analysis of hippocampal excitatory synapses. J. Neurosci. *17*, 5858–5867.

79. Rudolph, S., Tsai, M.C., von Gersdorff, H., and Wadiche, J.I. (2015). The ubiquitous nature of multivesicular release. Trends Neurosci. *38*, 428–438.

80. Tang, A.H., Chen, H., Li, T.P., Metzbower, S.R., MacGillavry, H.D., and Blanpied, T.A. (2016). A trans-synaptic nanocolumn aligns neurotransmitter release to receptors. Nature *536*, 210–214.

81. Sherrington, C.S. (1897). In Textbook of Physiology, 7th ed., *volume 3*, M. Foster and C.S. Sherrington, eds. (Macmillan), p. 929. https://search.worldcat.org/title/1045302366.

82. Guzman, S.J., Schlögl, A., Espinoza, C., Zhang, X., Suter, B.A., and Jonas, P. (2021). How connectivity rules and synaptic properties shape the efficacy of pattern separation in the entorhinal cortex–dentate gyrus–CA3 network. Nat. Comput. Sci. *1*, 830–842.

83. Hu, H., Gan, J., and Jonas, P. (2014). Fast-spiking, parvalbumin+ GABAergic interneurons: from cellular design to microcircuit function. Science *345*, 1255263.

84. Lapray, D., Lasztoczi, B., Lagler, M., Viney, T.J., Katona, L., Valenti, O., Hartwich, K., Borhegyi, Z., Somogyi, P., and Klausberger, T. (2012). Behavior-dependent specialization of identified hippocampal interneurons. Nat. Neurosci. *15*, 1265–1271.

85. Jörntell, H., and Ekerot, C.F. (2003). Receptive field plasticity profoundly alters the cutaneous parallel fiber synaptic input to cerebellar interneurons *in vivo*. J. Neurosci. *23*, 9620–9631.

86. Guzman, S.J., Schlögl, A., and Schmidt-Hieber, C. (2014). Stimfit: quantifying electrophysiological data with Python. Front. Neuroinform. *8*, 16.

87. Kremer, J.R., Mastronarde, D.N., and McIntosh, J.R. (1996). Computer visualization of three-dimensional image data using IMOD. J. Struct. Biol. *116*, 71–76.

88. Sakaba, T. (2008). Two Ca^{2+}-dependent steps controlling synaptic vesicle fusion and replenishment at the cerebellar basket cell terminal. Neuron *57*, 406–419.

89. Hu, H., and Jonas, P. (2014). A supercritical density of Na^{+} channels ensures fast signaling in GABAergic interneuron axons. Nat. Neurosci. *17*, 686–693.

90. Sasaki, T., Matsuki, N., and Ikegaya, Y. (2012). Targeted axon-attached recording with fluorescent patch-clamp pipettes in brain slices. Nat. Protoc. *7*, 1228–1234.

91. Yamashita, M., Kawaguchi, S.Y., Hori, T., and Takahashi, T. (2018). Vesicular GABA uptake can be rate limiting for recovery of IPSCs from synaptic depression. Cell Rep. *22*, 3134–3141.

92. Schindelin, J., Arganda-Carreras, I., Frise, E., Kaynig, V., Longair, M., Pietzsch, T., Preibisch, S., Rueden, C., Saalfeld, S., Schmid, B., et al. (2012). Fiji: an open-source platform for biological-image analysis. Nat. Methods *9*, 676–682.

93. Mishra, R.K., Kim, S., Guzman, S.J., and Jonas, P. (2016). Symmetric spike timing-dependent plasticity at CA3-CA3 synapses optimizes storage and recall in autoassociative networks. Nat. Commun. *7*, 11552.

94. Pernía-Andrade, A.J., Goswami, S.P., Stickler, Y., Fröbe, U., Schlögl, A., and Jonas, P. (2012). A deconvolution-based method with high sensitivity and temporal resolution for detection of spontaneous synaptic currents in vitro and in vivo. Biophys. J. *103*, 1429–1439.

95. Silver, R.A., Momiyama, A., and Cull-Candy, S.G. (1998). Locus of frequency-dependent depression identified with multiple-probability fluctuation analysis at rat climbing fibre–Purkinje cell synapses. J. Physiol. *510*, 881–902.

96. Hefft, S., and Jonas, P. (2005). Asynchronous GABA release generates long-lasting inhibition at a hippocampal interneuron-principal neuron synapse. Nat. Neurosci. *8*, 1319–1328.

97. Neher, E. (2015). Merits and limitations of vesicle pool models in view of heterogeneous populations of synaptic vesicles. Neuron *87*, 1131–1142.

98. Starborg, T., Kalson, N.S., Lu, Y., Mironov, A., Cootes, T.F., Holmes, D.F., and Kadler, K.E. (2013). Using transmission electron microscopy and 3View to determine collagen fibril size and three-dimensional organization. Nat. Protoc. *8*, 1433–1448.

99. Borges-Merjane, C., Kim, O., and Jonas, P. (2020). Functional electron microscopy, ''Flash and Freeze,'' of identified cortical synapses in acute brain slices. Neuron *105*, 992–1006.e6.

100. Cardona, A., Saalfeld, S., Schindelin, J., Arganda-Carreras, I., Preibisch, S., Longair, M., Tomancak, P., Hartenstein, V., and Douglas, R.J. (2012). TrakEM2 software for neural circuit reconstruction. PLoS One *7*, e38011.

101. Fujimoto, K. (1995). Freeze-fracture replica electron microscopy combined with SDS digestion for cytochemical labeling of integral membrane proteins. Application to the immunogold labeling of intercellular junctional complexes. J. Cell Sci. *108*, 3443–3449.

102. Kaufmann, W.A., Kleindienst, D., Harada, H., and Shigemoto, R. (2021). High-resolution localization and quantitation of membrane proteins by SDS-digested freeze-fracture replica labeling (SDS-FRL). In Receptor and Ion Channel Detection in the Brain, *169* (Neuromethods), pp. 267–283.

103. Möbius, W., Cooper, B., Kaufmann, W.A., Imig, C., Ruhwedel, T., Snaidero, N., Saab, A.S., and Varoqueaux, F. (2010). Electron microscopy of the mouse central nervous system. Methods Cell Biol. *96*, 475–512.

104. Ester, M., Kriegel, H.P., Sander, J., and Xu, X. (1996). A density-based algorithm for discovering clusters in large spatial databases with noise. In Proc. 2nd Int. Conf. KDD (AAAI Press), pp. 226–231.

105. Eguchi, K., Montanaro, J., Le Monnier, E., and Shigemoto, R. (2022). The number and distinct clustering patterns of voltage-gated calcium channels in nerve terminals. Front. Neuroanat. *16*, 846615.

106. Wang, X.J., and Buzsáki, G. (1996). Gamma oscillation by synaptic inhibition in a hippocampal interneuronal network model. J. Neurosci. *16*, 6402–6413.

107. Naraghi, M., and Neher, E. (1997). Linearized buffered Ca^{2+} diffusion in microdomains and its implications for calculation of $[Ca^{2+}]$ at the mouth of a calcium channel. J. Neurosci. *17*, 6961–6973.

108. Neher, E. (1998). Usefulness and limitations of linear approximations to the understanding of Ca^{++} signals. Cell Calcium *24*, 345–357.

109. Nägerl, U.V., Novo, D., Mody, I., and Vergara, J.L. (2000). Binding kinetics of calbindin-D_{28k} determined by flash photolysis of caged Ca^{2+}. Biophys. J. *79*, 3009–3018.

110. Kochubey, O., Han, Y., and Schneggenburger, R. (2009). Developmental regulation of the intracellular Ca^{2+} sensitivity of vesicle fusion and Ca^{2+}-secretion coupling at the rat calyx of Held. J. Physiol. *587*, 3009–3023.

STAR★METHODS

KEY RESOURCES TABLE

REAGENT or RESOURCE	SOURCE	IDENTIFIER
Antibodies		
Guinea pig Polyclonal anti-VGAT	Synaptic Systems	Cat # 131 004; RRID: AB_887873
Rabbit Polyclonal anti-$GABA_A$ receptor α1 subunit	Synaptic Systems	Cat # 224 203; RRID: AB_2232180
Guinea pig Polyclonal anti-$Ca_v2.1$ α_{1A}	Synaptic Systems	Cat # 152 205; RRID: AB_2619842
Rabbit Polyclonal anti-RIM 1/2	Synaptic Systems	Cat # 140 203; RRID: AB_887775
Rabbit Polyclonal anti-ELKS	provided by Akari Hagiwara and Toshihisa Ohtsuka, Yamanashi University Medical School, Japan	N/A
Rabbit Polyclonal anti-neurexin	provided by Masahiko Watanabe, Hokkaido University School of Medicine, Japan	N/A
Mouse Monoclonal anti-VGAT	Synaptic Systems	Cat # 131 011; RRID: AB_887872
Goat anti-guinea pig IgG:10nm immunogold conjugate	British Biocell International (BBI), Cardiff	Cat # EM.GAG10; RRID: AB_2892072
Goat anti-rabbit IgG:2nm immunogold conjugate	British Biocell International (BBI), Cardiff	Cat # EM.GAR2
Goat anti-mouse IgG:15nm immunogold conjugate	British Biocell International (BBI), Cardiff	Cat # EM.GMHL15; RRID: AB_2715551
Goat anti-rabbit Alexa Fluor 488	Invitrogen	Cat # A-11034; RRID: AB_2576217
Goat anti-guinea pig Alexa Fluor 405	Abcam	Cat # ab175678; RRID: AB_2827755
Chemicals, peptides, and recombinant proteins		
NaCl	VWR (Merck)	Cat # 1.06404
Sucrose	Sigma-Aldrich	Cat # 16104
$NaHCO_3$	VWR (Merck)	Cat # 1.06329
D-glucose	VWR (Merck)	Cat # 1.08342
KCl	VWR	Cat # 26764.232
Na_2HPO_4	VWR (Merck)	Cat # 1.06580
NaH_2PO_4	VWR (Merck)	Cat # 1.06346
$CaCl_2$	VWR (Merck)	Cat # 1.02382
$MgCl_2$	Sigma-Aldrich	Cat #M9272
HEPES	Sigma-Aldrich	Cat #H3375
EGTA	Sigma-Aldrich	Cat #E0396
BAPTA	Sigma-Aldrich	Cat # A4926
Na_2ATP	Sigma-Aldrich	Cat # A3377
NaGTP	Sigma-Aldrich	Cat #G8877
QX-314 bromide	TOCRIS	Cat # 1014
Biocytin	Invitrogen	Cat #B1592
Alexa Fluor 488	Thermo Fisher Scientific	Cat # A10436
Alexa Fluor 594	Thermo Fisher Scientific	Cat # A10438
Streptavidin Alexa Fluor 647 conjugate	Invitrogen	Cat #S32357
ω-agatoxin IVa	Bachem (Switzerland)	Cat # H-1544
ω-conotoxin GVIa	Bachem (Switzerland)	Cat # H-6615
SNX-482	Peptides International	Cat # PCB-4363-S
Bovine serum albumin (BSA)	Sigma-Aldrich	Cat # A9647
BSA Alexa Fluor 488 conjugate	Invitrogen	Cat # A13100

(*Continued on next page*)

Continued

REAGENT or RESOURCE	SOURCE	IDENTIFIER
TEA	Sigma-Aldrich	Cat #T2265
4-AP	Sigma-Aldrich	Cat # 275875
Paraformaldehyde	TAAB	Cat # P001/1
Triton X-100	Sigma-Aldrich	Cat #X100
Polyvinylpyrrolidone (PVP)	Sigma-Aldrich	Cat # PVP10
Glutaraldehyde	Electron Microscopy Sciences	Cat # 16220
Osmium tetroxide	Electron Microscopy Sciences	Cat # 19130
Polyethylene glycol 2000	VWR (Merck)	Cat # 8.21037
Glycine	VWR	Cat # 24403.298
Glycerol	Sigma-Aldrich	Cat #G5516
Picric acid solution (saturated)	Sigma-Aldrich	Cat #P6744
Sodium dodecyl sulfate (SDS)	Sigma-Aldrich	Cat #L3771
Tannic acid	Sigma-Aldrich	Cat # 403040
Polyvinyl Formal Resin	Electron Microscopy Sciences	Cat # 15800
Tris(hydroxymethyl)amino methane	VWR (Merck)	Cat # 1.08387
Durcupan ACM Resin Single component A	Sigma-Aldrich	Cat # 44611
Durcupan ACM Resin Single component B	Sigma-Aldrich	Cat # 44612
Durcupan ACM Resin Single component C	Sigma-Aldrich	Cat # 44613
Durcupan ACM Resin Single component D	Sigma-Aldrich	Cat # 44614
Uranyl acetate	Serva	Cat # 77870.02
Lead (II) nitrate	Sigma-Aldrich	Cat # 228621
Acetone, HPLC grade	ChemLab	Cat # CL00.0172
TPMPA	TOCRIS	Cat # 1040
CGP 55845 hydrochloride	TOCRIS	Cat # 1248
Fluo-5F pentapotassium salt	Invitrogen	Cat #F14221
Experimental models: Organisms/strains		
C57BL/6J wild-type mice	Charles River Germany (from The Jackson Laboratory)	RRID:IMSR_JAX:000664
Software and algorithms		
Multiclamp (version 2.1.0.16; version 2.2.2.2)	Axon Instruments/Molecular Devices	https://www.moleculardevices.com/
Igor Pro (version 6.3)	WaveMetrics	https://www.wavemetrics.com/
Stimfit (version 0.15.8)	Guzman et al., 2014[86]	PMID: 24600389
Radius Software	EMSIS	https://www.emsis.eu/products/software/radius/
Fiji (ImageJ version 1.53c)	NIH, Open source	https://fiji.sc/
IMOD 4.11	Kremer et al., 1996[87]	https://bio3d.colorado.edu/imod/
MATLAB 2020	MathWorks	https://www.mathworks.com/
R (4.1.0)	The R Project for Statistical Computing	https://www.rproject.org/
CorelDRAW 2019	CorelDRAW	https://www.coreldraw.com/en
Mathematica 11,12,13	Wolfram Research	https://www.wolfram.com/mathematica/
Other		
Borosilicate glass (2 mm OD/1 mm ID)	Hilgenberg	Cat # 1807542
Leaded glass (1.65 mm OD/1.1 mm ID)	World Precision Instruments	Cat # PG10165-4

RESOURCE AVAILABILITY

Lead contact

Further information and requests for resources should be directed to and will be fulfilled by the Lead Contact, Peter Jonas (peter.jonas@ist.ac.at).

Materials availability

This study did not generate new unique reagents.

Data and code availability

Original data, analysis programs, and computer code were stored in the scientific repositories of the Institute of Science and Technology Austria (ISTA). Any additional information required to reanalyze the data reported in this work paper is available from the lead contact upon request.

EXPERIMENTAL MODEL AND STUDY PARTICIPANT DETAILS

C57BL/6J mice were used for this study. Experiments were performed in strict accordance with institutional, national, and European guidelines for animal experimentation and were approved by the Bundesministerium für Bildung, Wissenschaft und Forschung (A. Haslinger, Vienna).

METHOD DETAILS

Cerebellar slice preparation

Paired recordings were performed between synaptically connected BCs and PCs in the cerebellum at three developmental time points (P7–9, P14–16, and P21–23). The BC-PC synapse was particularly suitable for the combined biophysical and structural analysis of developmental changes. First, it is highly amenable to a mechanistic analysis of synaptic transmission, because of perisomatic location and high synaptic connectivity.[9] Second, in comparison to hippocampus and neocortex, interneuron diversity in the cerebellum is more limited, making it easier to trace developmental changes. Finally, it undergoes substantial functional changes during development.[25]

Slices were cut from the cerebellum of C57BL/6 mice of either sex in the three age groups. After decapitation, the brain was rapidly dissected out and immersed in ice-cold slicing solution containing: 87 mM NaCl, 25 mM $NaHCO_3$, 2.5 mM KCl, 1.25 mM NaH_2PO_4, 10 mM D-glucose, 75 mM sucrose, 0.5 mM $CaCl_2$, and 7 mM $MgCl_2$ (pH 7.4 in 95% O_2/5% CO_2, ~325 mOsm). Parasagittal 250-μm-thick cerebellar slices from the vermis region were cut using a VT1200 vibratome (Leica Microsystems). After ~20 min incubation at ~35°C, the slices were stored at room temperature (RT). Slices were used for maximally 5 h after dissection. Experiments were performed at 21°C–24°C.

Paired recordings

During experiments, slices were superfused with a bath solution containing: 125 mM NaCl, 2.5 mM KCl, 25 mM $NaHCO_3$, 1.25 mM NaH_2PO_4, 25 mM D-glucose, 2 mM $CaCl_2$, and 1 mM $MgCl_2$ (pH 7.4 in 95% O_2/5% CO_2, ~325 mOsm). To investigate the relationship between IPSC peak amplitude and $[Ca^{2+}]_o$, different combinations of $[Ca^{2+}]_o$/$[Mg^{2+}]_o$ were used (0.7/2.3, 2/1, 4/1, and 10/1 mM). In the age group of 21–23 days, 1 mM TEA and 0.05 mM 4-AP were added to the 10/1 mM combination of $[Ca^{2+}]_o$/$[Mg^{2+}]_o$ to further enhance release probability. Paired recordings from synaptically connected BCs and PCs were performed as described previously.[9,25–27,88] Intracellular solution used for presynaptic BCs contained: 125 mM K-gluconate, 20 mM KCl, 10 mM HEPES, 10 mM phosphocreatine, 2 mM $MgCl_2$, 0.1 mM EGTA, 2 mM ATP, 0.4 mM GTP, and 0.2% biocytin (pH adjusted to 7.28 with KOH, ~310 mOsm). For experiments using Ca^{2+} chelators, 0.1 mM EGTA was replaced by 10 mM EGTA or 10 mM BAPTA; the concentration of K-gluconate was reduced accordingly to maintain osmolarity. Presynaptic pipette resistance was 8–10 MΩ. Intracellular solution for postsynaptic PCs contained: 140 mM KCl, 10 mM HEPES, 2 mM $MgCl_2$, 10 mM EGTA, 2 mM ATP, and 2 mM QX-314 (pH adjusted to 7.28 with KOH, ~313 mOsm). To achieve minimal postsynaptic series resistance, leaded glass (PG10165-4, WPI) was used to fabricate large tip-sized recording pipettes. Postsynaptic pipette resistance was 0.8–1.5 MΩ, resulting in a series resistance of 3–8 MΩ. Experiments in which series resistance changed by > 3 MΩ were discarded. BCs were recorded under current clamp conditions. For P7–9 synapses, no holding current was applied. For P14–16 and P21–23 age groups, a hyperpolarizing holding current of ~ –50 pA was injected to maintain the resting membrane potential at ~–65 mV and to avoid spontaneous AP generation. PCs were recorded in the voltage-clamp configuration with a holding potential of −70 mV. To evoke presynaptic APs, single pulses or trains of 10 pulses at 50 Hz (400 pA, 4 ms) were injected into the presynaptic BC every 4 s or 20 s, respectively. In a subset of variance-mean analysis experiments (Figure S3), 300 μM of the low-affinity competitive $GABA_A$ receptor antagonist TPMPA was added to the bath solution. As TPMPA has fast binding and unbinding rates ($k_{on} \sim 5 \times 10^6$ M^{-1} s^{-1}; $k_{off} \sim 2000$ s^{-1}), this is expected to minimize receptor saturation and desensitization.[37] Miniature IPSCs (mIPSCs, Table S1) were recorded in pharmacological isolation in the presence of 1 μM TTX, 10 μM CNQX, and 20 μM D-AP5. Peptide toxins were applied using a recirculation system with a peristaltic pump (Ismatec, Germany). The total volume of the system was ~5 mL, and the solution was equilibrated with 95% O_2/5% CO_2. Bovine serum albumin (BSA, Sigma-Aldrich, St. Louis, MI) was added at a concentration of 0.5 mg mL^{-1} to prevent adsorption of peptides to the surfaces of the perfusion system. ω-agatoxin IVa and ω-conotoxin GVIa were from Bachem (Switzerland), and SNX-482 was from Peptides International.

Presynaptic recordings from GABAergic terminals

BC boutons were patched using the following experimental strategy.[89,90] First, a somatic whole-cell recording was obtained, using BC internal solution containing Alexa Fluor 488 (100 μM, Invitrogen). Second, after ~20 min of recording, the fluorescently labeled boutons were visualized in the PC layer with a Leica TCS SP5 confocal microscope (equipped with a DFC365FX camera, a Leica HCX APO L 20x/1.0W objective, and an argon laser, excitation wavelength of 488 nm). Exposure time was minimized to avoid phototoxicity and photobleaching. The bouton pipettes were coated with BSA Alexa Fluor 488 conjugate (0.02%, Invitrogen) solution for ~20 s while keeping a positive intrapipette pressure during vertical dipping to prevent the pipette tips from clogging. Finally, confocal and infrared differential interference contrast (IR-DIC) images were compared and boutons were patched in the cell-attached configuration guided by confocal images.

Immunohistochemistry

After recording, slices were fixed by immersion in phosphate buffer (PB; 0.1 M, pH 7.4) containing 4% formaldehyde at 4°C overnight. After 3 times wash in PB, slices were embedded in 4% agarose and further sectioned into 50-μm-thick slices. For cryo-protection, slices were immersed in 30% sucrose in PB for 2 h at 4°C. Slices were further frozen above liquid nitrogen and thawed in PB to increase penetration of reagents. For immunolabeling, slices were first washed 3 times in PB and immersed in 10% normal goat serum (NGS) and 0.4% Triton X-100 in PB for 1 h at RT to block nonspecific binding. The slices were then incubated in rabbit polyclonal anti-$GABA_A$ receptor α1 primary antibody (5 μg mL^{-1}, Synaptic Systems, cat# 224 203) and guinea pig polyclonal anti-VGAT primary antibody (1:200, Synaptic Systems, cat# 131 004) for 48 h at 4°C in PB with 5% NGS and 0.4% Triton X-100. After washing 3 times in PB, slices were further incubated in PB containing 5% NGS, 0.4% Triton X-100, streptavidin Alexa Fluor 647 conjugate (4 μg mL^{-1}, Invitrogen, cat# S32357), goat anti-rabbit Alexa Fluor 488 (10 μg mL^{-1}, Invitrogen, cat# A-11034), and goat anti-guinea pig Alexa Fluor 405 (10 μg mL^{-1}, Abcam, cat# ab175678) for 2 h at RT. Slices were then washed in PB and mounted in Prolong Gold antifade embedding medium (Invitrogen). Fluorescence images were acquired using a Zeiss LSM 800 inverted microscope with sequential scanning of fluorescence signals using an oil objective (63x/1.4). Confocal images were analyzed with Fiji open source software.

Patch pipette perfusion

Ca^{2+} chelators were loaded into presynaptic BCs by pipette perfusion, as described previously,[6] using a custom-made two-port pipette holder and parts of the 2PK + pipette perfusion kit (ALA Scientific Instruments, Westbury, NY). Presynaptic pipettes were filled with a small volume (2–4 μL) of intracellular solution. Chelators were applied through one port via a flexible quartz tubing (100 μm outer diameter) coated with polyamide. To minimize exchange times, the end of the tubing was positioned closely to the pipette tip. The other end was connected to a ~0.6 mL reservoir with chelator-containing solution. To deliver the chelators to the pipette, positive pressure was applied to the reservoir and a compensatory negative pressure was applied at the second port of the pipette holder (which was also used for suction during seal formation and transition from cell-attached into whole-cell mode). Both positive and negative pressure were generated by a pressure/vacuum pump system and precisely controlled using two independent pressure regulators (2–5 mm Hg). To ensure stable long-term recordings, 3 mM GABA was added to the presynaptic internal solution.[91] Control experiments with mock application of a solution with 0.1 mM EGTA revealed that the rundown of evoked IPSCs during long-lasting recordings was only minimal (to 100.4% of control value; Figures 3C and 3D). Given the small magnitude of rundown, no correction was made. To minimize diffusion time, pipette perfusion experiments were made from closely spaced pairs (BC-PC intersomatic distance <50 μm).

Bouton Ca^{2+} imaging

Imaging of BC boutons (Figure S5) was performed using a Leica TCS SP5 confocal microscope (equipped with a Leica HCX APO L 20x/1.0W objective). First, BCs were filled with Fluo-5F (200 μM) and Alexa Fluor 594 (80 μM) via somatic whole-cell patch pipettes. To allow for a proper equilibration of the dyes, fluorescent signals were measured ~40 min after break-in. Excitation wavelength was 488 nm (argon laser, intensity was set at 0.5%) for Fluo-5F and 561 nm for Alexa Fluor 594 (diode pumped solid state laser, intensity was set at 0.05%). Fluorescence signals were detected by two photomultiplier tubes (PMTs) at fixed PMT voltages, and detection range was 500 nm–550 nm for Fluo-5F and 600 nm–650 nm for Alexa Fluor 594. Boutons were searched in the PC layer and were identified as varicosities with diameter >2 times that of the adjacent axons. Line scan imaging was performed in the center of boutons, and the zoom factor was set such that pixel size was 90 nm. To enable simultaneous measurements from boutons at slightly different focal planes, the pinhole size was increased to 2 Airy units. Fluorescent transients were elicited by single APs evoked by brief somatic current pulses and recorded in line scans at 700 Hz temporal resolution. Each bouton was recorded 3 to 5 times.

Intracellular Ca^{2+} transients were extracted with Fiji[92] and further analyzed with custom-made MATLAB code (Matlab 2020, Mathworks). The Ca^{2+}-dependent green fluorescence was normalized to the Ca^{2+}-insensitive red fluorescence and expressed as $\Delta G(t)/R$, where G(t) is the fluorescence in the green channel for each time point and R is the mean fluorescence signal in the red channel over each recording epoch. Baseline fluorescence was measured in a 50-ms time window before stimulation, and peak fluorescence was determined in a 10-ms time window after stimulation. Care was taken to avoid phototoxic damage; experiments in which the resting green fluorescence increased by > 20% during recording were excluded from analysis. As background was minimal, no correction was performed. Ca^{2+} transients shown in figures represent averages of 5 individual consecutive line scans. The decay phase of the Ca^{2+} transients was fit by a double-exponential function, and the time constant was given as amplitude-weighted average decay time

constant; components with negative amplitudes were set to 0. The average decay time constant of the Ca^{2+} transients was ~100 ms, consistent with the relatively low affinity of Fluo-5F (Figure S5).[93]

Data acquisition and analysis

Data were acquired with a Multiclamp 700B amplifier (Axon Instruments/Molecular Devices), low-pass filtered at 10 kHz, and sampled at 20 or 50 kHz using a CED 1401plus interface (Cambridge Electronic Design). Data were analyzed with Stimfit 0.15.8, Igor Pro 6.3 (Wavemetrics), Mathematica 13.2 (Wolfram Research), or R 4.1.0 (the R project for statistical computing). For BC recording, resting membrane potential was determined immediately after transition into the whole-cell configuration. Single AP parameters (peak amplitude, half-duration, and maximal rate of rise and decay) were measured from the AP threshold determined as the first point in the voltage trajectory in which the slope exceeded 20 V s^{-1}. Membrane potentials reported in the text were not corrected for liquid junction potentials. For BC-PC recording, functional properties of unitary IPSCs were determined from averages of 10–50 individual traces including failures. Synaptic latency (from the peak of the presynaptic AP to the onset of the IPSC), rise time (20%–80% of IPSC peak amplitude), and the proportion of failures were determined from 100 to 800 traces using Stimfit software.[86] The IPSC decay time constant (single-exponential fit) was determined from single IPSCs. To quantify multiple-pulse depression, traces were averaged and the amplitude of each IPSC in a train was measured from the baseline directly preceding the rising phase. mIPSCs (Table S1) were detected using a template matching algorithm and verified by visual inspection.[94]

For analysis of quantal parameters, multiple probability fluctuation analysis was used.[32] Mean and variance of IPSC peak amplitude were determined from stationary epochs. Variance-mean data were then fit with the equation

$$\sigma^2 = I\,q - I^2/N, \quad \text{(Equation 1a)}$$

where σ^2 is variance, I is mean current, q is quantal size, and N is the number of functional release sites. Variance-mean data were also fit with equations including type 1 (intrasite) and type 2 (intersite) quantal variability

$$\sigma^2 = \left(I\,q - I^2/N\right)\left(1+CV_{q2}{}^2\right) + I\,q\,CV_{q1}{}^2 = I\,q\left(1+CV_{q1}{}^2+CV_{q2}{}^2\right) - I^2/N\left(1+CV_{q2}{}^2\right), \quad \text{(Equation 1b)}$$

where CV_{q1} and CV_{q2} represent the coefficients of variation of type 1 and type 2 variability, respectively.[95] Thus, the basic structure of the variance-mean relation was maintained, with linear scaling factors for q ($1 + CV_{q1}2 + CV_{q2}2$) and N ($(1 + CV_{q2}2)^{-1}$). As corrections were relatively small for plausible values of CV, and N was only affected by CV_{q2}, Equation 1a was used for final analysis. Additionally, variance-mean data were also fit with equations using a baseline noise term. As introducing this term gave only minimal differences in the estimated parameters and the best-fit value was close to 0, it was omitted in the final analysis. Finally, release probability at 2 mM $[Ca^{2+}]_o$ was computed as $p_R = I_{2\ mM}/(N\,q)$.

To determine the time course of quantal release, average unitary IPSCs were deconvolved from average quantal IPSCs.[9,96] Quantal events were detected in the decay phase after a train of 10 APs using the template matching procedure, and converted into an idealized waveform with instantaneous rise and exponential decay. Time course of quantal release was computed by dividing the Fourier transforms of unitary and quantal IPSCs, and computing the inverse Fourier transform (Figure S1C).

To determine vesicular pool size and refilling rate, IPSC amplitudes during a 100-Hz train of 50 stimuli were subjected to cumulative release analysis.[35] IPSC peak amplitude values were normalized by $IPSC_1$, averaged across cells, and cumulatively plotted against stimulus number. The last ten data points were fit by linear regression. The size of the RRP was determined from intersection of the regression line with the ordinate, whereas refilling rate was determined from the slope.[35] For obtaining absolute numbers of RRP size and refilling rate, estimated values were multiplied by the quantal content of $IPSC_1$. For P7–9 and P14–16 synapses, the depression under control conditions was >50%, fulfilling a previously specified criterion for this analysis.[97] For P21–23 synapses, however, the extent of depression was less; thus, pool analysis was performed in high-p_R conditions with 4 mM extracellular Ca^{2+} (Figure S2).

Serial section EM and image analysis

For the analysis of the number of AZs per bouton, brains of animals (C57BL/6 mice P7–9, n = 4; P14–16, n = 4; P21–23, n = 4) were perfusion-fixed with PB containing 2% formaldehyde, 2.5% glutaraldehyde, and 15% saturated picric acid solution. Serial sagittal sections from cerebellum were sliced at 50 μm with a VT1200 vibratome and processed according to a previously published protocol[98] with modifications. Briefly, sections were washed in PB and treated with 0.2% tannic acid in PB two times 45 min each at RT. Sections were postfixed and stained with 2% osmium tetroxide in PB for 40 min at RT and 1% uranyl acetate in water overnight at 4°C. They were further contrast-enhanced with Walton's lead aspartate for 30 min at 60°C, dehydrated in graded ethanol and anhydrous acetone, and embedded in epoxy resin following the manufacturer's instructions (Durcupan ACM, Sigma-Aldrich).

For the analysis of the number of docked vesicles per AZ, high-pressure freezing (HPF) of acute slice preparations was performed with a Leica EM ICE high-pressure freezing apparatus (Leica Microsystems) as previously described.[99] After slicing and recovery, slices were mounted in sapphire-metal ring sandwiches. For mounting, a bottom sapphire disk (diameter 6 mm, thickness 120 μm; Wohlwend, Sennwald, Switzerland) was placed on the middle plate of a clear cartridge. Next, a spacer ring (outer diameter 6 mm, inner diameter 4 mm; thickness 200 μm) was put on top of the sapphire disk, adding a drop of extracellular bath solution containing 15% of the cryoprotectant polyvinylpyrrolidone. Subsequently, the tissue sample was transferred using a paintbrush. Finally,

a second sapphire disk with identical dimensions was put on top to form a sandwich. Freeze substitution and embedding were done as previously described.[99]

For serial sectioning, samples were sliced at either 40 nm (number of docked vesicle analysis in cryofixed samples) or 80 nm (number of AZ analysis in chemically fixed samples) using a UC7 ultramicrotome (Leica Microsystems) and a 4-mm Ultra 35° diamond knife (Diatome). Ribbons of sections were mounted onto Formvar-coated copper slot grids, and examined in a Tecnai 10 transmission electron microscope (T10 TEM; Thermo Fisher Scientific) operated at 80 kV accelerating voltage. Images were recorded with a Megaview III CCD camera and Radius acquisition software (both EMSIS).

BC boutons and AZs were selected for three-dimensional reconstruction from serial section electron micrographs based on completeness and optimal angle of sectioning. Serial images were aligned and relevant structures were traced and measured with Fiji/TrakEM2 software.[100] Perimeters of AZs were drawn according to close and parallel apposition of the pre- and postsynaptic membrane, and presence of amorphous electron-dense material in the cleft. Three-dimensional reconstruction of AZs was performed using custom-made MATLAB software. Vesicles were classified as docked when the distance between vesicular and presynaptic plasma membrane was <5 nm, consistent with previous criteria for classification of vesicular pools.[99] Three-dimensional reconstruction of boutons was performed using the ETomo software of the IMOD software package, version IMOD 4.11.[87] For model scaling, the z scale was set as the section thickness divided by the pixel size of the respective electron micrograph. For calculation of the AZ surface area, the object was meshed within the 3Dmod software using the standard parameters.

Freeze-fracture replica labeling (FRL)

FRL was performed with some modifications to the original method.[101,102] Brains of animals (C57BL/6 mice P7–9, n = 3; P14–16, n = 3; P21–23, n = 3) were perfusion-fixed with PB containing 2% formaldehyde and 15% saturated picric acid solution. Sagittal sections from cerebellum were cut at 140 μm with a VT1200 vibratome and cryoprotected by immersion in 30% glycerol in PB overnight at 4°C. Samples were rapidly frozen by use of the high-pressure freezing machine HPM 010 and fractured by a double-replica method in the freeze-etching device BAF 060 (Leica Microsystems) as described before.[103] In brief, fractured faces were replicated by evaporation of carbon (rotating) by means of an electron beam gun positioned at a 90° angle to a thickness of 5 nm for immobilization of macromolecules. They were then shadowed unidirectionally with platinum-carbon at a 60° angle (thickness 2 nm) and strengthened by evaporation of carbon to a thickness of 20 nm from a 90° angle (rotating). Samples were brought to atmospheric pressure and thawed to RT in Tris-buffered saline (TBS; 50 mM, 0.9% NaCl, pH 7.4). Tissue not immobilized in the replica membrane was solubilized in a medium containing 2.5% sodium dodecyl sulfate (SDS) and 20% sucrose in 15 mM TBS, pH 8.3, on a shaking platform for 48 h at 60°C. Replicas were treated for another 12 h at 37°C and kept at RT in the same solution.

For immunolabeling, replicas were washed in TBS and incubated in 5% BSA in TBS for 1 h at RT to block nonspecific binding. Subsequently, antibodies were applied sequentially in TBS containing 2% BSA. Replicas were first incubated with guinea pig polyclonal anti-$Ca_v2.1$ α_{1A} primary antibodies (2 μg mL^{-1}; Synaptic Systems, cat# 152 205), and reacted with goat anti-guinea pig secondary antibodies conjugated to 10-nm gold particles. Replicas were then incubated with a cocktail of AZ marker proteins including rabbit polyclonal anti-RIM1/2 antibodies (2 μg mL^{-1}; Synaptic Systems, cat# 140 203), rabbit polyclonal anti-ELKS antibodies (2 μg mL^{-1}; provided by Akari Hagiwara and Toshihisa Ohtsuka, Yamanashi University Medical School, Japan), and rabbit polyclonal anti-neurexin antibodies (1 μg mL^{-1}; provided by Masahiko Watanabe, Hokkaido University School of Medicine, Japan), and reacted with goat anti-rabbit secondary antibodies conjugated to 2-nm gold particles.[51] Finally, replicas were incubated with mouse monoclonal anti-VGAT antibodies (4 μg mL^{-1}; Synaptic Systems cat# 131 011), and reacted with goat anti-mouse secondary antibodies conjugated to 15-nm gold particles. All primary antibodies and gold-conjugated secondary antibodies (1:30, BBI Solutions) were each applied overnight at 15°C. The specificity of the $Ca_v2.1$ antibody was confirmed by testing cerebellar tissue samples from $Ca_v2.1$ $\alpha_{1A}^{-/-}$ mice (Figure S7). Replicas were then washed in water, mounted onto Formvar-coated 100-line copper grids, and examined in a Tecnai 12 TEM (Thermo Fisher Scientific) operated at 120 kV and equipped with a Veleta CCD camera (EMSIS). Images were acquired and analyzed using Radius (EMSIS) and Fiji software (distributed under the General Public License, GPL).

For identification of BC AZs, we set the following criteria: (1) presence of immunoparticles labeling AZ marker proteins (2 nm) and VGAT (15 nm; minimum 2 particles), (2) aggregates of intramembrane particles, and (3) direct proximity to postsynaptic PC plasma membrane. AZs were delineated according to the following principles: (1) demarcation of AZs drawing a polygon based on the outmost immunoparticles for $Ca_v2.1$ (10-nm gold particles) and RIM-ELKS-neurexin (2-nm gold particles; Miki et al., 2017). (2) Inclusion of an outer rim of 20 nm as antibodies can freely rotate around the epitope.[102] The dimension of this rim results from the size of antibodies applied (IgGs with approximately 8 nm each) and the size of the immunoparticle itself (radius of the gold particle). (3) Elimination of cases where a single gold particle or the center of an individual particle cluster was >100 nm away from the nearest particle cluster to avoid spurious delineation of AZs by isolated RIM-ELKS-neurexin particles. The threshold of 100 nm was derived from the longest distance between neighboring RIM-ELKS-neurexin clusters inside AZs. Distances were calculated using macros in R 4.1.0 (the R project for statistical computing). The x and y coordinates of immunoparticles were recorded and extracted in Fiji, the distances from each particle to every other particle were calculated, and the smallest value was assigned as the NND for each particle.

Clustering of particles was analyzed by comparing cumulative distributions of NNDs between real data from experimental measurements and simulated data generated by a random point process. Statistical significance was assessed using a

Wilcoxon-Mann-Whitney test. In addition, clustering of particles was analyzed using the Ripley method.[16,48] Ripley's K function was computed as:

$$K(r) = \lambda^{-1}\sum_{i\neq j}\omega_{ij}{}^{-1}\, I(d_{ij} < r) \,/\, N, \qquad \text{(Equation 2)}$$

where λ is average point density, $\omega_{i,j}$ is a weight factor for edge correction, I is an indicator function that counts the number of points within a radius r (taking a value of 1 if its operand is true and 0 otherwise), and N is number of points in the pattern. After correction for edge effects, $H(r)$ was computed from $K(r)$ as $H(r) = \sqrt{\frac{K(r)}{\pi}} - r$. Values $H(r) > 0$ may indicate clustering, while values $H(r) < 0$ may suggest dispersion. $H(r)$ curves were first obtained for individual AZs and then pooled for all AZs of each developmental time period. Statistical significance was assessed using a maximum deviation test, comparing experimental against Monte Carlo-simulated data.[16] To specifically test for clustering, only positive deviations were considered. For random positioning of Ca^{2+} channels, points were simulated on the AZ plane with 10 nm minimal distance. For random positioning of vesicles, spheres were distributed within single sections with 30 nm minimal distance.

To define clusters of particles, we applied DBSCAN to our replica data.[104] To obtain quantitative criteria for separating particles in the same versus different clusters, we plotted, for each particle, the 2-nearest neighbor graph for an individual AZ, and then identified the onset point of each graph as ϵ. We found that most of the ϵ were located in the range between mean +2 SD and mean +3 SD of the NND. The mean ϵ was 40.3 nm, 41.1 nm, and 40.9 nm for the P7–9, P14–16, and P21–23 age groups, respectively. The minimal number of points in each cluster was set to 3, based on the $Ca_v2.1$ particle background labeling on knockout mice tissue (Figure S7).[51] The NND between clusters was estimated by determining the shortest distance between cluster centers.

Labeling efficacy of the $Ca_v2.1$ antibody used in the present study was estimated in control experiments at hippocampal mossy fiber synapses, in which direct presynaptic Ca^{2+} current recordings,[52] serial-section EM data,[46] and FRL data (O.K., unpublished) are all available.[105] Functional analysis revealed 2007 Ca^{2+} channels of all types and 1324 P/Q-type Ca^{2+} channels per mossy fiber terminal.[52] Serial-section EM gave a total AZ area of 3.33 μm^2, a total presynaptic surface area of 75.5 μm^2, and an extrasynaptic surface area of 72.2 μm^2 (75.5 μm^2 − 3.33 μm^2; P28).[46] Finally, FRL analysis revealed $Ca_v2.1$ particle densities of 279 μm^{-2} inside the AZ and 1.36 μm^{-2} outside the AZ (O.K., unpublished). Taken together, this gives a total number of P/Q immunoparticles of 1027 per mossy fiber terminal (AZ density × AZ area + extrasynaptic density × extrasynaptic area), corresponding to a labeling efficiency of 77.6% (1027/1324). This is higher than a previous estimate based on optical fluctuation analysis (~40%).[16]

Modeling of nanodomain coupling based on realistic coupling topographies

Ca^{2+} diffusion and binding to buffers was modeled solving the full set of partial differential equations of the reaction-diffusion problem in three dimensions, including all necessary boundary and initial conditions.[3,6,7,15,60] The main partial differential equations were

$$\frac{\partial[Ca]}{\partial t} = D_{Ca}\left(\frac{\partial^2[Ca]}{\partial x^2}+\frac{\partial^2[Ca]}{\partial y^2}+\frac{\partial^2[Ca]}{\partial z^2}\right) - k_{on}\,[Ca][B_i]+k_{off}\left([B_i]_{tot} - [B_i]\right), \qquad \text{(Equation 3)}$$

$$\frac{\partial[B_i]}{\partial t} = D_B\left(\frac{\partial^2[B_i]}{\partial x^2}+\frac{\partial^2[B_i]}{\partial y^2}+\frac{\partial^2[B_i]}{\partial z^2}\right) - k_{on}\,[Ca]\,[B_i]+k_{off}\left([B_i]_{tot} - [B_i]\right), \qquad \text{(Equation 4)}$$

and

$$\frac{\partial[B_{fix}]}{\partial t} = - k_{on}\,[Ca]\,[B_{fix}]+k_{off}\left([B_{fix}]_{tot} - [B_{fix}]\right), \qquad \text{(Equation 5)}$$

where $[Ca]$ is the free Ca^{2+} concentration, t is time, x, y, and z are spatial coordinates, and D_{Ca} is the diffusion coefficient for Ca^{2+}. Furthermore, $[B_i]$ is the free mobile buffer concentration, k_{on} the binding rate, k_{off} the unbinding rate, $[B_i]_{tot}$ the total mobile buffer concentration, and D_B the diffusion coefficient of the buffer. Finally, $[B_{fix}]$ is the free fixed buffer concentration, and $[B_{fix}]_{tot}$ is the total fixed buffer concentration.

Near the Ca^{2+} sources, the boundary conditions were given as

$$\frac{\partial[Ca]}{\partial z} = D_{Ca}\,\sigma(t,x,y) \text{ for } z\rightarrow 0, \qquad \text{(Equation 6)}$$

where $\sigma(t, x, y)$ is the flux density.

Otherwise, the boundary conditions were

$$\frac{\partial[Ca]}{\partial x} = \frac{\partial[B_i]}{\partial x} = 0 \text{ for } x\rightarrow x_{min} \text{ or } x_{max}, \qquad \text{(Equation 7a)}$$

$$\frac{\partial[Ca]}{\partial y} = \frac{\partial[B_i]}{\partial y} = 0 \text{ for } y \rightarrow y_{min} \text{ or } y_{max}, \quad \text{(Equation 7b)}$$

$$\frac{\partial[Ca]}{\partial z} = \frac{\partial[B_i]}{\partial z} = 0 \text{ for } z \rightarrow z_{max}, \quad \text{(Equation 7c)}$$

and

$$\frac{\partial[B_i]}{\partial z} = 0 \text{ for } z \rightarrow 0. \quad \text{(Equation 7d)}$$

This set of partial differential equations was numerically solved with NDSolve of Mathematica 11.3, 12.2, 13.0, or 13.1 running under a Windows 10 operating system, using the IDA method and the GMRES implicit solver of Mathematica. The spatial grid resolution was 5 nm, and the total number of grid points was 1,295,061. For analysis of multiple random Ca^{2+} channel activation patterns and AZs, computations were performed on a high-performance computing cluster (ISTA-HPC), using x86_64 (64bit Intel/AMD) CPUs, GNU/Linux Debian11 operating system, and Mathematica 13.0.

Ca^{2+} influx during an AP was represented by a Gaussian function. The standard deviation was set according to the shape of the presynaptic APs and the gating properties of presynaptic P/Q-type Ca^{2+} channels (Figure S4).[52] APs were simulated using a Wang-Buzsáki excitability model of GABAergic interneurons,[106] with gating scaling factors ϕ and K^+ conductance $\overline{g_K}$ varied over a wide range. Simulated APs were applied as stimuli to models of P/Q-type Ca^{2+} channels, and Ca^{2+} current half-duration was plotted against AP half-duration and analyzed by linear regression. The peak amplitude of the current through a single Ca^{2+} channel was set to 0.13 pA.[52,58,59] The diffusion coefficient for Ca^{2+} was assumed as $D_{Ca} = 220\ \mu m^2\ s^{-1}$ throughout.

The standard parameters of our model were as follows (Table S4): for the fixed buffer, the rates were chosen as $k_{on} = 1 \times 10^8\ M^{-1}\ s^{-1}$ and $k_{off} = 10{,}000\ s^{-1}$; the total concentration was set to 4 mM.[21] For the endogenous mobile buffer (with ATP-like binding properties), the rates were chosen as $k_{on} = 5 \times 10^8\ M^{-1}\ s^{-1}$ and $k_{off} = 100{,}000\ s^{-1}$, the concentration was set to 0.27 mM, and the diffusion coefficient was $D_B = 200\ \mu m^2\ s^{-1}$. For the exogenous buffer EGTA, the rates were assumed as $k_{on} = 1 \times 10^7\ M^{-1}\ s^{-1}$ and $k_{off} = 0.7\ s^{-1}$ (affinity 70 nM); for the exogenous buffer BAPTA, the rates were taken as $k_{on} = 4 \times 10^8\ M^{-1}\ s^{-1}$ and $k_{off} = 88\ s^{-1}$ (affinity 220 nM).[12,107–109] The diffusion coefficient was set as $D_{EGTA} = D_{BAPTA} = 220\ \mu m^2\ s^{-1}$.

Buffer concentrations were assumed to be uniform. The resting Ca^{2+} concentration was set to 40 nM.[39] Initial conditions were calculated according to mass action law. Ca^{2+} channels were represented as disks with 5 nm radius. Cytoplasmic volume around an AZ was represented as a cuboid with 0.68 μm × 0.68 μm width and 0.34 μm height (Figure 7B). Experimentally determined Ca^{2+} channel coordinates were shifted and rotated to optimize insertion into the cuboid. Mathematically, a system in which a single AZ is surrounded by a small volume with reflective boundaries would be equivalent to a system in which multiple AZs are surrounded by a larger volume without boundaries. Thus, the model was consistent with our morphological data. Ca^{2+} extrusion mechanisms were not modeled, since the kinetics of these processes is more than an order of magnitude slower than the fast Ca^{2+} transients following single APs examined here. As BCs express the Ca^{2+}-binding protein PV, a buffer with PV-like properties[27,39] was added in a subset of simulations (Figure S10). As simulations were computationally expensive and differences were minimal, we have not routinely included PV-like buffers in our model.

Finally, the release rate was computed using an allosteric model of transmitter release, previously established at the calyx of Held.[55] As both BC-PC and calyx synapses involve synaptotagmin-2 as a Ca^{2+} sensor,[61–63] the use of a model from a different synapse was justified, although subtle developmental differences in affinity cannot be excluded.[110] Total simulation time was 10 ms.

The occupancies for the different states of the model were obtained by solving the corresponding first-order ordinary differential equations with a Q matrix approach. The location of the Ca^{2+} sensor was varied in x and y direction, whereas in z direction the sensor was placed 5 nm below the surface of the plasma membrane. For simulation of fixed Ca^{2+} channel activation patterns (P7–9), a single pattern of Ca^{2+} channel activation was used together with 100 patterns of random synaptic vesicle placement. For simulation of stochastic Ca^{2+} channel activation (P14–16 and P21–23), 10 random activation patterns were combined with 10 random patterns of synaptic vesicle placement for each representative example AZ.[21] For simulation of all AZs (67, 69, and 81 AZs), 5 random synaptic vesicle placement patterns were generated. Vesicles were randomly placed on cluster areas, cluster perimeters, AZs, and presynaptic membrane, using the RandomPoint function of Mathematica. For CA and CP model, the area of a circle with double radius was subtracted for each positioned vesicle, and vesicle positioning was iteratively continued until the available area was empty. The mean numbers of attached vesicles were 22 and 19, 37 and 31, and 42 and 34, respectively. For RAZ and RPM model, the same number of vesicles as in the CA model was distributed over a larger area. Finally, a likelihood score was determined, which describes the probability of a model given the experimental data. Specifically, the minus log likelihood score was computed as

$$L = -\ln \Pi\, P(x_{mod}|x_{exp}) =$$
$$-\ln\left[P(r_{EGTA,mod}|r_{EGTA,exp}) \times P(r_{BAPTA,mod}|r_{BAPTA,exp}) \times P(p_{R,mod}|p_{R,exp}) \times P(\delta_{tcr,mod}|\delta_{tcr,exp}) \times P(\tau_{tcr,mod}|\tau_{tcr,exp})\right], \quad \text{(Equation 8)}$$

where x is a given synaptic parameter, mod indicates modeling data, exp denotes experimental values, r_{EGTA} and r_{BAPTA} are chelator-to-control current ratios, δ_{tcr} is the delay, and τ_{tcr} is the decay time constant of the time course of release. P distributions $P(x_{mod} \mid x_{exp})$ were represented by normal distributions based on experimental data (means taken from each age group; standard deviations averaged across age groups; peaks normalized to 1). Release probability p_R was computed as $p_R = \xi_{max}/I_+ f^5$ (Table S4),[55] where ξ_{max} is maximal release rate. Delay δ_{tcr} was measured from peak of Ca^{2+} flux to peak of release. τ_{tcr} was obtained by fitting a monoexponential function to the decay of the release period. Weights were set to 1 for r_{EGTA} and r_{BAPTA}, and 0.5 for p_R, δ, and τ_{tcr} to account for smaller reliability in kinetic measurements. *L* values were computed for each random pattern in each model, and cumulative distributions were compared between models using a Wilcoxon-Mann-Whitney test.

To determine the mean topographical coupling distance, the following procedure was used (Figure 8D, left). For each channel-vesicle pair, the physical distance in x-y plane was measured, resulting in a distance matrix. Each channel's fractional contribution to the release rate was probed by either activating the channel (if closed) or inactivating the channel (if open), resulting in a release relevance matrix. Finally, the weighted mean distance was computed, using the release relevance matrix to derive the weight factors. Thus, the topographical coupling distance was obtained as $\sum_{i=1}^{m}\sum_{j=1}^{n} r(i,j)\, d(i,j) / \sum_{i=1}^{m}\sum_{j=1}^{n} r(i,j)$, where *r*(i, j) is the fractional contribution of Ca^{2+} channel i to the release of vesicle j, *d*(i, j) is the distance in x-y plane between Ca^{2+} channel i and vesicle j, *m* is the total number of Ca^{2+} channels, and *n* is the total number of vesicles.

Conventions and statistics

All values were reported as mean ± standard error of the mean (SEM). Statistical significance was tested using a Kruskal-Wallis test, followed by a Wilcoxon rank-sum test/Mann-Whitney U-test with Bonferroni correction, unless specified differently. Differences with $p < 0.05$ were considered significant. In the text, p values indicate the results from Kruskal-Wallis test. In the figures, brackets with *, **, and *** labels indicate the results from Wilcoxon-Mann-Whitney test (representing $p < 0.05$, $p < 0.01$, and $p < 0.001$, respectively). In the tables, both values are given. Throughout the paper, P7–9 data are indicated in gray, P14–16 data in red, and P21–23 data in cyan. In bar graphs, circles represent data from individual experiments, and bars indicate mean ± SEM, unless specified differently. In total, data included in the present paper were from 197 BC-PC paired recordings, 5 BC soma-soma recordings, 15 BC bouton-soma recordings, and 20 BC recordings for imaging. 13 paired recordings at P14 were taken from a previous publication.[9]